Precision Predictions
for W^+W^- Scattering at the LHC

Dissertation zur Erlangung des
naturwissenschaftlichen Doktorgrades
der Julius-Maximilians-Universität Würzburg

vorgelegt

von

Robert Franken
aus Hamburg

Würzburg, 2024

Eingereicht am: _____
bei der Fakultät für Physik und Astronomie

1. Gutachter: Prof. Dr. Ansgar Denner

2. Gutachter: Prof. Dr. Raimund Ströhmer

3. Gutachter: –

der Dissertation

Vorsitzende(r): Prof. Dr. Vladimir Hinkov

1. Prüfer: Prof. Dr. Ansgar Denner

2. Prüfer: Prof. Dr. Raimund Ströhmer

3. Prüfer: Prof. Dr. Karl Mannheim

im Promotionskolloquium

Tag des Promotionskolloquiums: 26. Juni 2024

Doktorurkunde ausgehändigt am: _____

Abstract

In this thesis we examine the vector boson scattering (VBS) process pp → $e^+\nu_e\mu^-\bar{\nu}_\mu$jj + X (short: W^+W^- scattering) at NLO accuracy in two experimental setups by performing a Monte Carlo analysis of a 13 TeV LHC run. W^+W^- scattering shows similarities and differences compared to the scattering of other vector bosons. We present a detailed description of the types of appearing subprocesses and background processes. We give insight into our code which solves the problems we are faced within W^+W^- scattering. This is especially the presence of the Higgs-boson resonance in the fiducial phase-space region. Particular attention is dedicated to the permutation of resonances. The integrated signal cross section at LO $\mathcal{O}\left(\alpha^6\right)$ amounts to 2.6988(3) fb and 1.5322(2) fb, respectively, in the two experimental setups. The LO QCD-induced background of $\mathcal{O}\left(\alpha_s^2\alpha^4\right)$ amounts to 6.9115(9) fb and 1.6923(3) fb. The EW corrections to the signal are −11.4% and −6.7%, the QCD corrections amount to −5.2% and −23.0%. The EW corrections to the background are −8.3% and −5.3%, the QCD corrections amount to −30.3% and −77.6%. Our results for the QCD corrections and the QCD-induced background include a large uncertainty from varying the renormalisation and factorisation scale, and we discuss improvements for future calculations. We show the differential cross sections with unique features of W^+W^- scattering compared to other VBS processes and investigate in particular the subprocess of Higgs-boson production by using a modified version of our setups.

Abstract

In dieser Arbeit untersuchen wir den Vektorboson-Streuprozess (VBS-Prozess) pp → $e^+\nu_e\mu^-\bar{\nu}_\mu$jj + X (kurz: W^+W^--Streuung) auf nächstführender Ordnung in zwei Versuchsanordnungen, indem wir eine Monte-Carlo-Analyse des LHC-Betriebs bei 13 TeV durchführen. W^+W^--Streuung zeigt Gemeinsamkeiten mit der und Unterschiede zur Streuung anderer Vektorbosonen. Wir stellen eine detaillierte Beschreibung der Arten auftauchender Subprozesse und Hintergrundprozesse vor und geben Einsicht in unseren Code, der die Probleme löst, vor die wir im Rahmen der W^+W^--Streuung gestellt wurden. Dies ist insbesondere die Präsenz der Higgs-Boson-Resonanz im Bezugsphasenraum. Besonderes Augenmerk wird auf die Permutation der Resonanzen gelegt. Wir präsentieren den integrierten Wirkungsquerschnitt. Der integrierte Wirkungsquerschnitt des Signals beträgt 2,6988(3) fb beziehungsweise 1,5322(2) fb auf führender Ordnung $\mathcal{O}\left(\alpha^6\right)$ in den beiden experimentellen Setups. Der QCD-Hintergrund auf führender Ordnung $\mathcal{O}\left(\alpha_s^2\alpha^4\right)$ beträgt 6,9115(9) fb bzw. 1,6923(3) fb. Die elektroschwachen Korrekturen zum Signal belaufen sich auf −11,4% bzw. −6,7%, die QCD-Korrekturen auf −5,2% bzw. −23,0%. Die elektroschwachen Korrekturen zum Hintergrund sind −8,3% bzw. −5,3%, die QCD-Korrekturen −30,3% bzw. −77,6%. Unsere Ergebnisse für die QCD-Korrekturen und den QCD-induzierten Hintergrund enthalten eine große Unsicherheit durch die Variation der Renormierungs- und Faktorisierungsskala und wir diskutieren Verbesserungen für zukünftige Rechnungen. Wir zeigen die differentiellen Wirkungsquerschnitte mit Eigenheiten von W^+W^--Streuung verglichen mit anderen VBS-Prozessen und betrachten insbesondere den Subprozess der Higgs-Boson-Produktion, indem wir eine modifizierte Version unserer Versuchsanordnungen verwenden.

Contents

1 Introduction

> When I began my physical studies, and I sought my honourable teacher Philipp von Jolly for advice about the conditions and prospects of my studies, he described physics as a highly developed science, which [...] would soon receive its final stable form. There might be a mote or a vesicle to check and classify in one or another corner, but the system stands safely, and theoretical physics approaches noticeably that grade of perfection, which, for example, geometry has for centuries.
> – Max Planck, 1924 [1]

In the middle and late 19$^{\text{th}}$ century, everything was fine. Gravitation was known for centuries, electromagnetism and thermodynamics were primarily understood in the last few decades, and atoms were some massive billiard balls that could form molecules or salts but had no interior life. However, within only a span of 50 years, everything was about to change.

In 1902, Rutherford and Soddy found that a newly discovered phenomenon, radioactivity, was able to transmute atoms from one element to another [2]. In their words, they discovered a process

$$\text{Th} \longrightarrow \text{ThX} \longrightarrow \text{some gas},$$
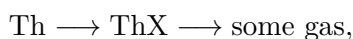
which we would write in modern notation as

$$^{228}\text{Th} \longrightarrow {}^{224}\text{Ra} \longrightarrow {}^{220}\text{Rn}.$$
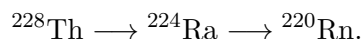
With this discovery, the "unbreakable" atom was literally shattered. Knowing the existence of electrons, which were already discovered in 1897 by Thomson, Rutherford postulated after his scattering experiments in 1909 the existence of an atomic nucleus and predicted in 1920 the existence of uncharged nucleons [3]. In the 1930s, even more particles with masses smaller than the hydrogen atom popped up: positrons, muons, and pions; in the 1940s, kaons joined.

Apart from the problem of sorting all of these new particles, physicists had an additional struggle with the conservation of energy and momentum. They were well-established facts in classical physics and new developments such as special and general relativity or quantum mechanics did not affect them. In contrast, Noether's newly discovered theorem grounded them even more. On the other hand, the conservation laws seemed to be violated in some radioactive processes. In α-decays, the radiated α-particles always have the same energy, as one would expect in a $1 \to 2$ decay process. In β-decays, the radiated β-particles do not, but show a continuous energy spectrum. This could only be resolved by Pauli by introducing a third participant in the interaction, which was soon called the neutrino.

As the years passed by, physicists were eager to find a mathematical description of β-decays. Fortunately, with the development of quantum mechanics, special relativity, and their unification, quantum field theory, we possess the armamentarium to tackle these problems in the standard model of elementary particle physics (SM). It does not only bring order to the particle zoo; it also describes three kinds of forces: electromagnetic, weak, and strong interaction.

The SM is one of the experimentally most well-tested theories of modern physics. It describes our surrounding world at microscopically small length and very high energy scales with astonishing precision. The plethora of all known forms of matter can be described with only 12 elementary particles (and their corresponding antiparticles), and six additional particles mediate the forces. Theoretical predictions made by the SM are regularly confirmed by particle physics experiments all over the world.

Alas, we are far away from Jolly's hybris in the 19$^{\text{th}}$ century. We know that the aforementioned gravitation eludes the description of the SM, and even worse, general relativity as a mathematical description of gravitation is mathematically incompatible with quantum field theory. Speaking of gravitation, we also know that astronomical measurements seem to require gravitationally interacting, not yet discovered particles, which cannot be members of either elementary or composite particles from the SM.

One class of discussed candidates for these particles are the hypothetical WIMPs, weakly interacting massive particles [4, 5]. They also come across when discussing supersymmetric extensions of the SM. All of these new theories have one thing in common: With the introduction of new weakly interacting particles, the predictions of the SM in its electroweak (EW) sector are changed. There are two routes for testing the existence of hypothetical particles: direct measurement, in which the particles have to be produced on-shell, and they or their decay products are detected, or indirect measurement, in which we probe the SM at very high accuracy and try to detect any deviations from its predictions.

Although direct searches of non-SM particles at the Large Hadron Collider (LHC) were not successful [6], the LHC has become more and more capable of measuring cross sections with high precision due to data collected in the course of the last few years. One of its most outstanding achievements was indeed the discovery of a new SM particle in 2012, the Higgs boson [7, 8]. The Higgs mechanism [9–13], which postulates the existence of this boson, is an essential building block of the EW sector. Some new physics models beyond the SM revolve around the introduction of a second Higgs doublet instead of a single one [14]. Interactions with those new particles would also alter experimental results compared to SM predictions.

In this thesis, we investigate a process that is directly connected to the EW sector of the SM and especially to the Higgs boson. The class of processes it belongs to is called vector boson scattering (VBS), and the particular process is opposite-sign W^+W^- scattering.

VBS processes have relatively small cross sections and disappear in front of an overwhelmingly large background unless a set of appropriate phase-space cuts on the final state of the measured events is applied. Nevertheless, due to the immense amount of collected data, the LHC was able to detect VBS signals in the past few years for a set of two leptonically decaying weak vector bosons combined with the occurrence of two jets. Same-sign W^+W^+ [15–19], WZ [20–22] and ZZ scattering [23–25] have been observed by ATLAS and CMS in the last decade. At last, the observation of opposite-sign W^+W^- scattering has first been claimed and verified by CMS in 2021 and 2022, respectively [26–28].

With more and more experimental measurements, precise theoretical predictions of the cross sections of VBS processes become increasingly important. There have been theoretical studies of VBS processes for more than a decade, which mainly focussed on QCD corrections. For opposite-sign W^+W^- scattering, QCD corrections became available between 2006 and 2012 [29–31]. Parton shower matching followed soon after that [32, 33]. The EW corrections have been neglected so far for W^+W^- scattering. This thesis is part of a series of studies in which special attention is given to EW corrections to VBS processes and which started in 2017 with the calculation of both differential and integrated cross sections of W^+W^+ scattering at next-to-leading order (NLO) accuracy [34, 35]. It continued with the completion of a complete analysis of W^+Z [36] and ZZ scattering [37, 38]. A paper containing next-to-leading order corrections to parts of opposite-sign W^+W^- scattering neglecting the QCD background using the results of this thesis has been published in 2022 [39].

This thesis finalises the research of the paper mentioned above [39] by presenting the entire theoretical leading order (LO) and next-to-leading order cross sections for W^+W^- scattering in two different experimental setups. We used Monte Carlo integration techniques of our in-house multi-channel integrator Bbmc to simulate scattering events at the LHC and a combination of the matrix element generator Recola [40, 41] and the Collier library [42, 43] to calculate integrated and differential cross sections from our events.

The thesis is split into four parts. In Section 2, we recapitulate the theoretical foundations forming the base of our research. Special attention is given to the Higgs mechanism and the Glashow–Weinberg–Salam theory of EW interactions. We also recapitulate the concepts of NLO calculations with the help of some basic examples and present the Catani–Seymour formalism, which handles them for numeric integrators. In Section 3, we present the concrete process of W^+W^- scattering. This includes a description of all orders of the coupling constants which contribute to our process at leading and next-to-leading order. We also give insights into the

code we used to simulate the process and show occurring problems within Bbmc when we first tried to compute the process, as well as our solutions for these problems. In Section 4, we introduce the simulated experimental setups and present our results for the cross sections. This is done at the level of integrated and differential cross sections, where we first show all LO contributions and, afterwards, the different LO contributions with their corresponding NLO corrections separately. As a final step, we present the dependence of our differential cross section on the used renormalisation and factorisation scale. The last part is a very brief outlook for possible future improvements in Section 5.

2   Theoretical foundations

2.1   Electroweak symmetry breaking

Since the purpose of this thesis is the investigation of the phenomenology of VBS, we begin with a recapitulation of the EW interaction as a theoretical basis. We start, therefore, with a brief historical overview of the first successful theories, and we present their problems both from a physical and a mathematical viewpoint.

This leads us to the very beginning, the Fermi theory and its inability to reproduce the correct energy and angular dependence of the cross section. The next theory we present is the simple $V - A$ theory, which can solve these physical problems but cannot be formulated as a gauge theory, unlike the theories of electromagnetism and strong interaction. In this course, we briefly recapitulate the concept of gauge invariance, which will lead us to the theory of Glashow, Weinberg, and Salam. Special attention is given to the process of mass generation by the Higgs mechanism.

2.1.1   About energy-momentum conservation and neutrinos

As we already stated in the introduction, β-decay posed a serious problem for physicists in the early 20th century. It was known that a mother nucleus (M) decayed into some daughter nucleus (D) and emitted a light particle, which is a simple two-particle decay. Consider a generic reaction

$$M \longrightarrow D + R$$

and calculate the energy spectrum of the radiated particle (R). It is straightforward; we have to place ourselves in the centre-of-mass system with the mother nucleus at rest and use energy-momentum conservation. Without loss of generality, we may assume that the radiated particle is emitted in x_1-direction:

$$\begin{pmatrix} m_{\text{M}} \\ 0 \\ 0 \\ 0 \end{pmatrix} = \begin{pmatrix} \sqrt{m_{\text{D}}^2 + p_{\text{D}}^2} \\ p_{\text{D}} \\ 0 \\ 0 \end{pmatrix} + \begin{pmatrix} \sqrt{m_{\text{R}}^2 + p_{\text{R}}^2} \\ p_{\text{R}} \\ 0 \\ 0 \end{pmatrix}. \tag{1}$$

Neglecting the small mass of the radiated particle, some arithmetic leads to

$$p_{\text{R}} = \frac{m_{\text{M}}^2 - m_{\text{D}}^2}{2m_{\text{M}}}. \tag{2}$$

After this reasoning, we expect a sharp energy peak of the radiated particles in our spectrometers. This is, in fact, the case for an α-particle: All α-emitters have characteristic decay energies [44]. Surprisingly, emitted β-particles show a continuous energy spectrum instead [45], which contradicts our results and hence energy-momentum conservation.

To solve this puzzle, Pauli postulated in a letter a yet unknown, uncharged light particle [46], which we call nowadays an electron-antineutrino.[1] Since no apparatus at that time was technically able to detect and prove the existence of the particle, and hence none of its characteristics was measurable, this was a shocking assumption. Pauli did not dare to publish his ideas, but it was the only solution for the problem. For some β-decay, one could now write:

$$M \longrightarrow D + e^- + \bar{\nu}_{\text{e}}. \tag{3}$$

With the additional particle, we moved from a two-particle decay to a three-particle decay, which gives us more free parameters for our equations. The third particle can absorb momentum

---

[1]We will conveniently drop the discrimination between different types of neutrinos and antineutrinos in the written text if there are no ambiguities.

in a second spatial dimension. There are, hence, three equations – one for energy and two for momentum – and five free variables – the absolute values of the three momenta and two independent angles. The energy of the electron is not fixed any more but can be expressed as a continuous function of two free parameters. Let us assume the process takes place in the x_1, x_2-plane, the electron is emitted in the x_1-direction, the angle between the momenta of daughter particle and electron is ϕ_D and the angle between the momenta of electron and neutrino is ϕ_ν. We depict this graphically in Figure 2.1. Then, energy-momentum conservation tells us, neglecting electron and neutrino mass,

$$\begin{pmatrix} m_M \\ 0 \\ 0 \\ 0 \end{pmatrix} = \begin{pmatrix} \sqrt{m_D^2 + p_D^2} \\ p_D \cos \phi_D \\ p_D \sin \phi_D \\ 0 \end{pmatrix} + \begin{pmatrix} p_e \\ p_e \\ 0 \\ 0 \end{pmatrix} + \begin{pmatrix} p_\nu \\ p_\nu \cos \phi_\nu \\ p_\nu \sin \phi_\nu \\ 0 \end{pmatrix}. \tag{4}$$

Some calculation leads to

$$p_e = \frac{m_M^2 - m_D^2 - 2m_M p_\nu}{2(m_M + p_\nu \cos \phi_\nu)} \tag{5}$$

for the electron momentum as a function of neutrino momentum and angle between the two particles. Since electron and neutrino are interchangeable labels in this calculation, the maximum electron energy is achieved when the neutrino momentum is zero and takes the value calculated in (2). Vice versa, the minimum electron energy is zero in this approximation.
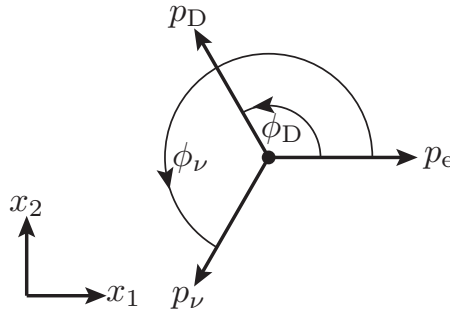
Figure 2.1: Geometry of the beta decay

2.1.2   Matrix elements and cross sections

Although the introduction of the neutrino explains why the energy spectrum of β-particles is continuous, it does not explain the shape of the energy distribution. We will not calculate this distribution since we are more interested in scattering than in decay processes in the course of this thesis. Still, we will move on to the more generic topic of matrix elements and cross sections.

Suppose we do a particle physics experiment and collide two proton beams, which is exactly what we are going to simulate in the second part of this thesis. We are then interested in the number of scattering events in some time interval $\mathrm{d}N/\mathrm{d}t$. This quantity will depend on the experimental design – especially the particle densities, the intersection area, and the length of the beams. We collect all of these technical parameters and call the result the luminosity L. If we factor off the luminosity, the remainder is the "physical" quantity named cross section, σ, which is independent of the experimental setup. We write this in the differential form

$$\mathrm{d}\frac{\mathrm{d}N}{\mathrm{d}t} = L \, \mathrm{d}\sigma. \tag{6}$$

For a derivation of a formula for the cross section we refer to any QFT textbook, e. g. [47]. We just write it down for massless initial-state particles in the centre-of-mass frame since we are

only interested in the high-energy limit in this thesis (and for the introductory examples, this simplifying assumption is sufficient):

$$\mathrm{d}\sigma = \frac{1}{2s}|\mathcal{M}|^2\mathrm{d}\Gamma, \tag{7}$$

where s is the centre-of-mass energy, $\mathcal{M}$ is the matrix element and $\mathrm{d}\Gamma$ the Lorentz-invariant final-state phase-space element. It is given in four space-time dimensions by

$$\mathrm{d}\Gamma = \left(\prod_f \int \frac{\mathrm{d}^3 p_f}{(2\pi)^3}\frac{1}{2E_f}\right)(2\pi)^4\delta^{(4)}(p_1 + p_2 - \sum_f p_f), \tag{8}$$

where the index f runs over all final-state particles, and the initial-state particles are labelled with 1 and 2.

For a $2 \to 2$ process, the phase-space integral simplifies drastically, and we obtain the formula

$$\frac{\mathrm{d}\sigma}{\mathrm{d}\Omega} = \frac{1}{64\pi^2 s}|\mathcal{M}|^2 \tag{9}$$

as the connection between the differential cross section (with respect to the solid angle in the centre-of-mass frame) and the matrix element. We will revisit the phase-space integral in space-time dimensions different from four, especially for a $2 \to 3$ process in Section 2.2.1.

The matrix element is defined via the $\mathcal{S}$-matrix that is the Heisenberg operator which mediates between the asymptotic initial and final Schrödinger states:

$$\langle i(t = -\infty)|f(t = \infty)\rangle_\mathrm{S} = \langle i|\mathcal{S}|f\rangle_\mathrm{H} \equiv \langle i|1 + \mathrm{i}\mathcal{T}|f\rangle_\mathrm{H}. \tag{10}$$

It is given by stripping off the four-momentum conservation factor from the interaction part

$$\langle i|\mathcal{T}|f\rangle_\mathrm{H} = (2\pi)^4\delta^{(4)}(p_1 + p_2 - \sum_f p_f)\mathcal{M}. \tag{11}$$

The matrix element contains all information about the scattering process independent of external influences. It can be directly connected to the Lagrangian and to Feynman diagrams. We again refer to [47] for the derivation. We are not interested in polarised cross sections in the course of this thesis, so we will always sum over the final-state spins and helicities and average over the initial-state ones.

2.1.3   Historical theories of the weak interaction: Fermi and $V - A$ theory

With the tools to calculate cross sections at hand, we can go back to the problem with the neutrinos. In quantum field theory, we need a Lagrangian to calculate matrix elements to predict the cross sections. The first one to develop a successful theory for the β-decay, and therefore founding the field of (electro-)weak interactions, was Enrico Fermi [48–50]. In modern language, he introduced the following Lagrangian to explain the beta decay, including the neutrino $(\mathrm{n} \to \mathrm{p}^+ + \mathrm{e}^- + \bar{\nu}_\mathrm{e})$:

$$\mathcal{L}_\mathrm{Fermi} = \mathrm{i}\bar{\psi}_i\slashed{\partial}\psi_i - \left(\frac{G_\mathrm{F}}{\sqrt{2}}(\bar{\psi}_1\gamma^\mu\psi_2)(\bar{\psi}_3\gamma_\mu\psi_4) + \mathrm{h.c.}\right) \tag{12}$$

The first term is a sum over different fermions, which is the kinetic part, and the second is a contact interaction between four different fermions at one single point in space-time, where the matching fermions had to be put in "by hand". The factor of $\sqrt{2}$ accompanying the coupling constant G_F is conventional. This Lagrangian cannot only describe decays but also scattering processes. Let us hence consider the so-called inverse β-decay, in which an antineutrino collides with a proton to form a neutron and a positron:
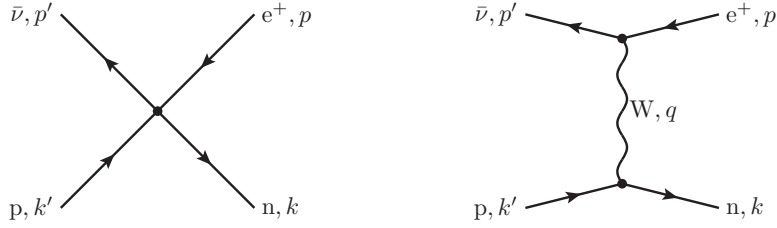
$$\bar{\nu}_\mathrm{e} + \mathrm{p} \longrightarrow \mathrm{e}^+ + \mathrm{n}.$$

Figure 2.2: Feynman diagrams for $\bar{\nu}\mathrm{p} \to \mathrm{e}^+\mathrm{n}$ scattering in Fermi (left) and $V - A$ theory (right)

In fact, this is the process in which the neutrino had been discovered [51, 52]. The corresponding Feynman diagram is given in Figure 2.2.

We may use Fermi's theory to calculate the cross section. The matrix element follows directly from the Lagrangian as

$$\mathcal{M} = \frac{G_\mathrm{F}}{\sqrt{2}} \bar{v}_{\bar{\nu}_\mathrm{e}}(p')\gamma^\alpha v_{\bar{\mathrm{e}}}(p) \bar{u}_\mathrm{p}(k')\gamma_\alpha u_\mathrm{n}(k), \tag{13}$$

if we identify the four fermions correctly and assign momenta to them. Taking the absolute square and averaging yields after applying Casimir's trick [53] and some Dirac algebra

$$|\bar{\mathcal{M}}|^2 = \frac{1}{4}\sum |\mathcal{M}|^2 = \frac{1}{8}G_\mathrm{F}^2 \, \mathrm{Tr}(\slashed{p}'\gamma^\alpha \slashed{p}\gamma^\beta)\, \mathrm{Tr}(\slashed{k}'\gamma_\alpha \slashed{k}\gamma_\beta) = 4G_\mathrm{F}^2 \left[(pk)(p'k') + (pk')(kp')\right]. \tag{14}$$

The products of four-momenta can be rewritten into the centre-of-mass energy and the scattering angle θ in the centre-of-mass frame as

$$|\bar{\mathcal{M}}|^2 = G_\mathrm{F}^2(s^2 + u^2) = \frac{G_\mathrm{F}^2}{2}s^2 \left(\frac{5}{2} - \cos\theta + \frac{1}{2}\cos^2\theta\right). \tag{15}$$

Plugging this into equation (9) and integrating over the solid angle, the differential and integrated cross sections are

$$\frac{\mathrm{d}\bar{\sigma}}{\mathrm{d}\Omega} = \frac{G_\mathrm{F}^2}{128\pi^2}s \left(\frac{5}{2} - \cos\theta + \frac{1}{2}\cos^2\theta\right), \qquad \bar{\sigma} = \frac{G_\mathrm{F}^2}{12\pi}s. \tag{16}$$

With the Fermi theory at hand, physicists were able to calculate these weak cross sections for the first time. Despite its success in the first decades, the result is incorrect. There are two problems: First, the predicted cross section grows with s. In those days, this was not noticeable in experiments since high-energy particle colliders were futuristic and typical energies in β-decays are at the order of some few MeV. Nowadays, such behaviour is excluded by experiments. Instead, this posed a more severe problem from a theoretical viewpoint. Such behaviour violates unitarity. It is a fact that all individual transition probabilities from some initial state to a specific final state must be positive and have to sum up to one. This is impossible when the integrated cross section grows faster than $\ln^2 s$, which is called the Froissart bound [54]. Second, the prediction of the differential cross section and the angular dependence was simply wrong.

Additionally, the Fermi theory is not renormalisable, which does not spoil the correctness of its predictions – gravitation is also not renormalisable after all –, but it is nevertheless a small blemish. Renormalisability of a theory is needed to calculate higher-order corrections (see Section 2.2), and a necessary condition at the Lagrangian level is the non-negativity of the dimension of all appearing coupling constants. By simple dimensional analysis, the Fermi constant has a mass dimension of -2.

The issue of the infinitely growing cross section and the non-renormalisability could be resolved by interpreting the Fermi theory as an effective theory that was only valid in the low-energy limit. The solution was the introduction of two heavy, charged bosons, which were called W for "weak" and mediated the interaction like photons mediate the electromagnetic

interaction. Nevertheless, even if we introduce some heavy, charged photon and incorporate its propagator into the theory, it is not able to predict the correct angular behaviour. The necessary input came from another side, the decay of kaons, formerly known as θ- and τ-particles[2], which seemed to be distinct particles decaying into two or three pions respectively. The different final states have opposite parity, but the θ and τ had identical properties otherwise. Lee and Yang hence discussed a possible parity violation of the weak interaction [55]. This was later confirmed by the Wu experiment [56] and the new theory was given the name "vector minus axial vector" $(V - A)$ theory, which introduced chiral currents [57].

For this, consider a decomposition of spinors into two orthogonal left- and right-handed chirality states, which are eigenstates of the fifth Dirac matrix γ^5. The projection operators

$$P_{\mathrm{L}} = \frac{1 - \gamma^5}{2} \qquad P_{\mathrm{R}} = \frac{1 + \gamma^5}{2}, \tag{17}$$

form a complete set of orthogonal projections since

$$P_{\mathrm{L}}P_{\mathrm{L}} = P_{\mathrm{L}}, \qquad P_{\mathrm{R}}P_{\mathrm{R}} = P_{\mathrm{R}}, \qquad P_{\mathrm{R}}P_{\mathrm{L}} = P_{\mathrm{L}}P_{\mathrm{R}} = 0, \qquad P_{\mathrm{L}} + P_{\mathrm{R}} = 1. \tag{18}$$

With these operators, we can decompose any Dirac spinor as

$$\psi = P_{\mathrm{L}}\psi + P_{\mathrm{R}}\psi \equiv \psi_{\mathrm{L}} + \psi_{\mathrm{R}}, \tag{19}$$

and (vector) currents have the property not to mix states of different chirality:

$$\bar{\psi}\gamma^\mu\psi = \bar{\psi}_{\mathrm{L}}\gamma^\mu\psi_{\mathrm{L}} + \bar{\psi}_{\mathrm{R}}\gamma^\mu\psi_{\mathrm{R}}. \tag{20}$$

In the $V - A$ theory, there are two electrically charged heavy vector bosons mediating the weak interactions. These bosons only couple to currents of left-handed chirality. Merging these two fixes of the Fermi theory, we arrive at the Proca Lagrangian (called after Proca's work introducing a massive spin-1 particle long before $V - A$ [58]) for a massive boson

$$\mathcal{L}_{\mathrm{Proca},V-A} = W^{\mu\pm}(\Box + M_{\mathrm{W}}^2)W_\mu^\mp + \mathrm{i}\bar{\psi}_i\slashed{\partial}\psi_i - \left(g\bar{\psi}_1\slashed{W}^+\frac{1 - \gamma^5}{2}\psi_2 + \mathrm{h.c.}\right) \tag{21}$$

with some coupling constant g. We are now going to calculate the cross section for the inverse β-decay again with this Lagrangian and the corresponding Feynman diagram also shown in Figure 2.2. The same steps as before lead to the matrix element

$$\mathcal{M} = g^2\bar{u}_{\nu_e}(p')\gamma^\alpha\frac{1 - \gamma^5}{2}u_e(p)\frac{\mathrm{i}g_{\alpha\beta}}{q^2 - M_{\mathrm{W}}^2}\bar{u}_\mu(k')\gamma^\beta\frac{1 - \gamma^5}{2}u_{\nu_\mu}(k), \tag{22}$$

where $q = p' - p$ is the momentum transfer between the two fermion lines. After a slightly more complicated computation, the result for the averaged squared matrix element is

$$|\bar{\mathcal{M}}|^2 = g^4 s^2\frac{1}{(q^2 - M_{\mathrm{W}}^2)^2} = g^4 s^2\frac{1}{(\frac{s}{2}(1 + \cos\theta) + M_{\mathrm{W}}^2)^2}. \tag{23}$$

Inserting this expression into the formula for the differential cross section (9) and integrating over the solid angle, we obtain

$$\bar{\sigma} = g^4\frac{1}{16\pi}\frac{s}{M_{\mathrm{W}}^2(M_{\mathrm{W}}^2 + s)}. \tag{24}$$

Hence, at small energies $s \ll M_{\mathrm{W}}^2$, the cross section can be approximated by

$$\bar{\sigma} = g^4\frac{s}{16\pi M_{\mathrm{W}}^4} + \mathcal{O}(1), \tag{25}$$

---

[2]Not to be confused with τ-leptons.

which resembles the energy dependence of the Fermi theory.[3] On the other hand, in the high-energy limit $s \gg M_{\mathrm{W}}^2$, the cross section becomes constant with

$$\bar{\sigma} = \frac{g^4}{16\pi M_{\mathrm{W}}^2} + \mathcal{O}\left(\frac{M_{\mathrm{W}}^2}{s}\right) \tag{27}$$

without violating the unitarity bounds. In fact, the $V - A$ theory with a massive intermediate boson predicts the correct differential and integrated cross section for the inverse β-decay at LO. Nevertheless, this comes with a price. The theory is not gauge-invariant any more, which we discuss in detail in the following section. Furthermore, we introduced new particles, and we need a consistent description of how those charged bosons interact with photons. Although we rescued the inverse β-decay from being unitarity-violating, we show in Section 2.1.7 that a theory only containing W bosons is also inconsistent.

2.1.4   Towards a gauge theory of electroweak interaction

Unfortunately, the Proca Lagrangian cannot be embedded into a gauge-invariant prescription. We emphasise this concept of gauge invariance, especially since it can be proven that all unitarity-preserving renormalisable theories are necessarily gauge theories [59]. To clarify the concept, we go one step back to classical electrodynamics and quantum mechanics. Recall that states in non-interacting quantum mechanics are invariant under a global phase rotation

$$\psi(\vec{x}, t) \rightarrow \psi'(\vec{x}, t) = e^{iq\alpha}\psi(\vec{x}, t), \tag{28}$$

since the Schrödinger equation and all physical quantities are invariant under this transformation, which is called a global gauge transformation (we include the factor q for convenience). On the other hand, the Schrödinger equation is not invariant under a local gauge transformation, in which the parameter α depends on time and space, because this produces terms proportional to $\partial_t\alpha$, $\nabla\alpha$ and $\nabla^2\alpha$ in the primed version of the equation. Classical electrodynamics also has this feature of gauge invariance. We can add a spatial derivative of an arbitrary function $\alpha(\vec{x}, t)$ to the vector potential $\vec{A}$ and a temporal derivative to the electric potential ϕ without changing the electric and magnetic field,

$$\vec{A}(\vec{x}, t) \rightarrow \vec{A}'(\vec{x}, t) = \vec{A}(\vec{x}, t) - \nabla\alpha, \qquad \phi(\vec{x}, t) \rightarrow \phi'(\vec{x}, t) = \phi(\vec{x}, t) - \partial_t\alpha. \tag{29}$$

These two a priori completely different features astonishingly combine after we put electrodynamics and quantum mechanics together. The principle of minimal coupling to describe a wave function that interacts with an electromagnetic field leads to the Pauli equation

$$i(\partial_t + iq\phi)\psi = \frac{(i\nabla - q\vec{A})^2}{2m}\psi. \tag{30}$$

After combining the two gauge prescriptions of quantum mechanics and electrodynamics, the Pauli equation is covariant under a local gauge transformation if we identify the parameter q that appears in the quantum mechanical phase rotation with the electric charge. The terms

---

[3]We must not directly identify $G_{\mathrm{F}} = \sqrt{\frac{3}{4}}\frac{g^2}{M_{\mathrm{W}}^2}$, since we combined the two improvements. If we calculated the Fermi theory with the correct $V - A$ structure, and thus the correct angular dependence, we would obtain $|\bar{\mathcal{M}}|^2 = 2G_{\mathrm{F}}^2 s^2$ and $\bar{\sigma} = \frac{G_{\mathrm{F}}^2}{8\pi}s$, hence

$$G_{\mathrm{F}} = \frac{1}{\sqrt{2}}\frac{g^2}{M_{\mathrm{W}}^2}. \tag{26}$$

We additionally note that the Fermi constant in the context of $V - A$ theory is usually redefined such that the factors of $\frac{1}{2}$ in the projection operators are absorbed into the Fermi constant, which results in $G_{\mathrm{F}} = \frac{1}{4\sqrt{2}}\frac{g^2}{M_{\mathrm{W}}^2}$. The latter definition is also used in equation (271).

emerging from the gauge transformation of the electromagnetic potentials in the Pauli equation counteract the terms that come from taking the derivatives in the Schrödinger equation.

Mathematically speaking, the phase rotation of the wave function corresponds to a transformation under the one-dimensional unitary group $U(1)$, which can be represented by complex numbers with an absolute value of one. We say that electrodynamics is invariant under a $U(1)$ symmetry. This property became a guiding principle in physics: Forces are connected to symmetries by transformations under Lie groups.

A Lie group is a differentiable manifold that is in close relation to a Lie algebra. Introducing these objects, we refer for proofs to [60, 61]. Lie algebras are vector spaces with one inner operation, the Lie bracket $[A, B]$, which is bilinear, antisymmetric[4] and obeys the Jacobi identity $[A, [B, C]] + [B, [C, A]] + [C, [A, B]] = 0$. We do not have to go too much into the mathematical details for our purpose and we will restrict ourselves to the vector space of endomorphisms, which can be represented by $n \times n$ matrices. Then the Lie bracket is simply the commutator $[A, B] = AB - BA$. Lie algebras can be characterised by their structure constants: If some T^a form a basis of the Lie algebra, then every element in the algebra can be written as a linear combination of basis elements, and we define the structure constants f_c^{ab} as coefficients

$$[T^a, T^b] = \mathrm{i} f_c^{ab} T^c. \tag{31}$$

The structure constants are antisymmetric in their upper indices since the commutator is antisymmetric. If all structure constants vanish, the Lie algebra is Abelian. The structure constants uniquely define a Lie algebra. We remark that the Jacobi identity can be written in terms of the structure constants as

$$[T^a, [T^b, T^c]] + [T^b, [T^c, T^a]] + [T^c, [T^a, T^b]] = 0 \quad \Leftrightarrow \quad f_e^{ad} f_d^{bc} + f_e^{bd} f_d^{ca} + f_e^{cd} f_d^{ab} = 0. \tag{32}$$

The structure constants themselves satisfy the Lie algebra. Define the matrices $(T_{\mathrm{ad}}^a)_{ce}$ via

$$(T_{\mathrm{ad}}^a)_{ce} = -\mathrm{i} f_e^{ac}, \tag{33}$$

then the identity

$$([T_{\mathrm{ad}}^a, T_{\mathrm{ad}}^b])_{ce} = \mathrm{i} f_d^{ab} (T_{\mathrm{ad}}^d)_{ce} \tag{34}$$

holds, as can be derived from the Jacobi identity. We call these new matrices T_{ad}^a the adjoint representation of the algebra.

The connection between Lie groups and algebras comes via the matrix exponential: Every element of the group U can be obtained as matrix exponential of a linear combination of basis elements of the Lie algebra T^a, which are hence called the generators of the group:

$$U = \exp(\mathrm{i} \alpha^a T^a). \tag{35}$$

The α^a are real numbers, and the factor of i is a convention to assure that the T^a are Hermitian for the groups of our interest. Vice versa, the generators of a Lie group can be deduced from the group elements via differentiation:

$$T^a = -\mathrm{i} \left. \frac{\partial U}{\partial \alpha^a} \right|_{\alpha=0}. \tag{36}$$

In the following, we only deal with unitary and special unitary Lie groups. The unitary group in n dimensions $U(n)$ is defined as a group that can be represented by $n \times n$ matrices, which leaves, operating on objects of dimension n, the complex scalar product invariant. We call this

---

[4]We implicitly assume that all mathematical objects are objects over the real or complex numbers and not over exotic fields.

representation the defining or fundamental representation of the group. This means, for any $U \in U(n)$, they obey

$$\langle a|b \rangle = \langle Ua|Ub \rangle = \langle a|U^\dagger U|b \rangle \quad \Rightarrow \quad U^\dagger U = 1. \tag{37}$$

Since the determinant is multiplicative, it follows that $|\det U| = 1$. However, each unitary group has a normal subgroup, the $SU(n)$. The $SU(n)$ is defined as the matrices contained in $U(n)$ with $\det U = 1$. Each element of $U(n)$ (for $n \geq 2$) can be written as a product of an element of $SU(n)$ and $U(1)$, which is, as discussed above, a complex phase factor. A priori, a complex $n \times n$ matrix has $2n^2$ free parameters. The unitarity condition, however, leads to n^2 equations to fulfil, and hence the dimension of $U(n)$ is $\dim U(n) = n^2$. The dimension of $SU(n)$ is subsequently $\dim SU(n) = n^2 - 1$ because of additionally constraining the determinant. It can be shown that the generators of $U(n)$ are hermitian matrices, and the generators of $SU(n)$ are additionally traceless.

From this fundamental representation of the group, we may construct the fundamental representation of the algebra, calculate the structure constants, construct the adjoint representation of the algebra, and from thereon the adjoint representation of the group.

The fundamental representation of the group acts on an n-dimensional vector ψ via matrix multiplication:

$$\psi \to \psi' = U\psi; \tag{38}$$

the adjoint representation acts on $n \times n$-matrices A via

$$A \to A' = UAU^{-1}. \tag{39}$$

At last, we shall mention the trivial representation of any group in which all group elements are represented by 1. The operation of the trivial representation can also be described as "nothing happens".

The connection between Lie groups and forces is a powerful tool. Physicists are able to ask: If we assume gauge invariance under a specific Lie group, which implications for the force will we receive? The construction of a gauge-invariant theory is now straightforward. We assume that the fermions transform in the fundamental representation. Our goal is that the free Lagrangian

$$\mathcal{L}_{\text{free}} = \mathrm{i}\bar{\psi}\slashed{\partial}\psi, \tag{40}$$

from which the free Dirac equation follows, remains invariant under a transformation

$$\psi \to \psi' = e^{\mathrm{i}gT^a\alpha^a}\psi = U\psi, \tag{41}$$

where we introduced an additional yet arbitrary parameter g compared to equation (35). Like in the base case of the Schrödinger equation, the free Lagrangian is not invariant because the derivative also acts on the α^a. To solve this formally, we replace the derivative ∂^μ with a covariant derivative D^μ and require

$$\mathcal{L}' = \mathrm{i}\bar{\psi}U^{-1}D'^\mu U\psi = \mathrm{i}\bar{\psi}U^{-1}UD^\mu\psi = \mathcal{L} \tag{42}$$

$$\Leftrightarrow \quad D'^\mu U\psi = UD^\mu\psi. \tag{43}$$

To this end, we have to introduce an additional term by writing

$$D^\mu = \partial^\mu + \mathrm{i}gT^aA^{\mu a} \tag{44}$$

and determine the transformation properties of A^μ. We recognise that the correct behaviour is

$$T^aA^{\mu a} \to T^aA'^{\mu a} = UT^aA^{\mu a}U^{-1} - \frac{\mathrm{i}}{g}(\partial^\mu U)U^{-1}, \tag{45}$$

hence, $A = T^a A^a$ must transform in the adjoint representation, or

$$A^{\mu a} \to A'^{\mu a} = A^{\mu a} + \partial^\mu \alpha^a - g f_c^{ab} \alpha^b A^{\mu c} + \mathcal{O}\left(\alpha^2\right). \tag{46}$$

The second and last step is to introduce dynamics for the vector fields $A^{\mu a}$. We, therefore, extend the Lagrangian with more Lorentz invariant terms that behave well under the gauge transformation. Since we would like to stay in a renormalisable regime, we restrict ourselves to terms with a mass dimension of four or lower. There are two more allowed terms, and both of them contain the expression

$$[D^\mu, D^\nu] = -\mathrm{i}g(\partial^\mu T^a A^{\nu a} - \partial^\nu T^a A^{\mu a}) - g^2 A^{\mu b} A^{\nu c}[T^b, T^c]. \tag{47}$$

Let us define

$$F^{\mu\nu a} = (\partial^\mu A^{\nu a} - \partial^\nu A^{\mu a}) + g f_a^{bc} A^{\mu b} A^{\nu c} \tag{48}$$

with

$$F^{\mu\nu a} T^a = -\frac{1}{\mathrm{i}g}[D^\mu, D^\nu]. \tag{49}$$

The allowed terms in the Lagrangian are then $F^{\mu\nu a} F_{\mu\nu a}$ and $\varepsilon^{\alpha\beta\mu\nu} F_{\alpha\beta}^a F_{\mu\nu}^a$. The latter, however, can be rewritten in terms of a total derivative and does not contribute to the equations of motion so we will ignore it.

We can shortly cross-check whether this prescription is consistent with classical electrodynamics when we set our underlying group to be $U(1)$. $U(1)$ has dimension one, so there is one generator, which is proportional to the one-dimensional unit matrix, $T^a = 1$. With this replacement, we receive the usual quantum mechanics gauge transformation in (41), the structure constants vanish because of the Abelian nature, $f_a^{bc} = 0$, and subsequently the (relativistic) electromagnetic transformation law from (46) and the usual electromagnetic field strength tensor $F^{\mu\nu}$ in (48) are recovered. Besides the number of gauge bosons, the main difference between Abelian and non-Abelian gauge theories is the appearance of the structure constants. For non-Abelian symmetry groups, the structure constants are non-zero and lead to additional terms in the Lagrangian, which are tri- and quadrilinear in the gauge bosons and describe interactions between gauge bosons. Especially, the strong force found its description in quantum chromodynamics based on an $SU(3)$ gauge group.

We now transfer these thoughts to the theory of weak interaction at this stage of history, the Proca Lagrangian from (21). In the beginning, we have to incorporate the different behaviour concerning left- and right-handed currents. If we apply a transformation as in (41) on the fermions, the kinetic term transforms as

$$\mathrm{i}\bar{\psi}\slashed{\partial}\psi \to \mathrm{i}\bar{\psi}'\slashed{\partial}\psi' = \mathrm{i}\bar{\psi}\slashed{\partial}\psi - g\bar{\psi}T^a(\slashed{\partial}\alpha^a)\psi, \tag{50}$$

but the interaction term comes with an expression $\bar{\psi}_1 \slashed{W} P_{\mathrm{L}} \psi_2$. This is the only term capable of counteracting the emerging term from the gauge transformation, but it contains a projection operator P_{L}. No possible transformation law of the W bosons can invert this P_{L} because P_{L} projects to a subspace; the information about the orthogonal subspaces is lost after applying the projection and cannot be restored by any means (mathematically rigorous: P_{L} has determinant zero). Any transformation law of the fermions must hence already involve this projection. The solution becomes obvious when we split the fermions into their projections on the left- and right-handed chirality subspaces. The (fermionic) Lagrangian is

$$\mathcal{L}_{\mathrm{fermion}} = \mathrm{i}(\psi_{\mathrm{L}}\slashed{\partial}\psi_{\mathrm{L}} + \psi_{\mathrm{R}}\slashed{\partial}\psi_{\mathrm{R}}) - g\psi_{\mathrm{L}}T^a\slashed{W}^a\psi_{\mathrm{L}}. \tag{51}$$

If we now assume that only the left-handed parts undergo the gauge transformation and the right-handed part remains invariant,

$$\psi_{\mathrm{L}} \to \psi'_{\mathrm{L}} = e^{\mathrm{i}g T^a \alpha^a}\psi_{\mathrm{L}}, \quad \psi_{\mathrm{R}} \to \psi'_{\mathrm{R}} = \psi_{\mathrm{R}}, \tag{52}$$

then only the first kinetic term in the Lagrangian is affected by the transformation, and we reach

$$\mathcal{L}'_{\text{fermion}} = \mathcal{L}_{\text{fermion}}. \tag{53}$$

Nevertheless, there are still two problems. At first, although we could clarify the gauge dependence of the fermionic part, the W bosons are – in contrast to photons and gluons – massive, and this bosonic mass term in the Lagrangian transforms as

$$m_{\text{W}}^2 W^{\mu a} W_\mu^a \to m_{\text{W}}^2 W'^{\mu a} W_\mu'^a = m_{\text{W}}^2 \left(W^{\mu a} W_\mu^a - 2 W^{\mu a} \partial_\mu \alpha^a + (\partial_\mu \alpha^a)^2 \right). \tag{54}$$

These two new terms cannot be compensated by any other term in the Lagrangian. Second, the W bosons are charged, in contrast to gluons, so there must be some connection between the weak interaction and the electromagnetic one, which the Proca Lagrangian does not account for. There should be some term containing a contraction of

$$W^{\mu a} W^{\nu b} A^\rho \tag{55}$$

(accompanied by a derivative because of dimensionality), but the photon A is completely decoupled from the W bosons in the Proca theory since they belong to two different transformations. On the other hand, charge conservation forbids trilinear terms in W in the Lagrangian since this would mean an interaction of three charged W bosons, but we find a term proportional to

$$f_a^{bc} W^{\mu b} W^{\nu c} (\partial_\mu W_\nu^a) \tag{56}$$

in the expansion of $F^{\mu\nu a} F_{\mu\nu a}$. If this were correct, it would imply that the structure constants are either totally antisymmetric or zero. The problem is that there is neither a two-dimensional Lie group with totally antisymmetric structure constants nor a non-trivial Abelian Lie group.

The first issue implies that we cannot simply put a mass term by hand into a gauge-invariant Lagrangian, but the mass must be generated dynamically; the second one leads the way directly to a unification of the weak and the electromagnetic interaction into a theory of electroweak interaction.

2.1.5 The Higgs Mechanism

Spontaneous symmetry breaking via the Higgs mechanism [9–13] is able to generate the mass term. As we derived in the previous section, gauge invariance forbids the introduction of a priori massive gauge bosons to the theory. We must assume massless particles and find a way to introduce a term only proportional to W^2 in a gauge-invariant way that we can identify as a mass term afterwards. In this section, we will produce a massive photon from a massless one as Abelian $U(1)$ example and see in the next one how this works out for W bosons.

When we start with the massless photon, it has two degrees of freedom, whereas when we end up with a massive one, it has three. Somewhere along the way, it has to acquire one degree of freedom. Let us incorporate an additional scalar field ϕ to the theory and couple the photon to the scalar (hence, we need a charged and thus complex scalar with two additional degrees of freedom). The Lagrangian for this theory would be

$$\mathcal{L} = (D^\mu \phi)^\dagger (D_\mu \phi) + \mu^2 \phi^\dagger \phi - \lambda (\phi^\dagger \phi)^2 \tag{57}$$

plus kinetic terms for the photon. This Lagrangian contains all renormalisable terms in ϕ, which are gauge-invariant under a $U(1)$ transformation. The potential

$$\mathcal{V} = -\mu^2 \phi^\dagger \phi + \lambda (\phi^\dagger \phi)^2 \tag{58}$$

describes the scalar self-interaction and its mass (note that $U(1)$ gauge invariance does not forbid massive scalars or fermions). If the mass term μ^2 is negative, then we would simply add an additional particle, and nothing special happens since we recover the Klein–Gordon equation

$$(\Box - \mu^2)\phi = 0 + \text{interaction}. \tag{59}$$

However, if $\mu^2 > 0$, this particle would have an imaginary mass, which is clearly unphysical.

Let us investigate the case of $\mu^2 > 0$ in more detail. We immediately recognise that the potential $\mathcal{V}$ is not a parabola any more since the $\phi^\dagger\phi$ term dominates the $(\phi^\dagger\phi)^2$ term for small $\phi^\dagger\phi$. It instead becomes a form of the iconic "Mexican hat" with a local maximum at the origin and a minimum symmetrically around the origin with a distance of

$$(\phi^\dagger\phi)_{\text{min}} = \frac{\mu^2}{2\lambda} \equiv \frac{v^2}{2}. \tag{60}$$

However, in nature, the field is (at zero temperature[5]) expected to be in its ground state rather than in some excited state, which means at the point of minimal potential energy. This point is in the case of our ϕ not at zero, but at its *vacuum expectation value v*. Since it is not possible to uniquely determine the phase of ϕ the ground state, we may decide that $\langle\phi\rangle = \langle\phi^\dagger\rangle = \frac{v}{\sqrt{2}}$.

Let us now reparametrise the scalar sector via a change of variables

$$\phi, \phi^\dagger \to h, \varphi \tag{61}$$

with

$$\phi = \frac{v+h}{\sqrt{2}} e^{\mathrm{i}\frac{\varphi}{v}}. \tag{62}$$

Both h and φ have zero expectation value, $\langle h \rangle = \langle \varphi \rangle = 0$, and are real, thus uncharged, scalar quantities. If we insert this into the Lagrangian, we obtain

$$\mathcal{L} = \frac{1}{2}\partial_\mu\varphi\partial^\mu\varphi + \frac{1}{2}\partial_\mu h\partial^\mu h - \frac{1}{2}\mu^2 h^2 - \frac{q^2 v^2}{2}A_\mu A^\mu - qvA_\mu\partial^\mu\varphi + \dots, \tag{63}$$

where the dots represent terms of higher order in the field variables. Not only the h field has now a real mass μ (note the sign change in front of μ^2 from (57) to (63)), but also the photon in this model acquired one of value qv. This means we started from a gauge-invariant theory, but the true vacuum state is not gauge-invariant any more – the gauge symmetry has been broken. Other things happening in the model are the following: There is one massless scalar boson φ, which is called a Goldstone boson. These Goldstone bosons always appear when the original symmetry is spontaneously broken [63]. Besides various interaction terms, there remains a strange expression in the Lagrangian: It seems as if the Goldstone boson would have the property to convert into a vector boson and vice versa via the term $qvA_\mu\partial^\mu\varphi$. However, his term can be gauged away and hence must not result in physical consequences. Consider the gauge transformation

$$\phi \to \phi' = e^{\mathrm{i}\frac{\alpha}{v}}\phi, \quad \text{and} \quad A^\mu \to A'^\mu = A^\mu + \frac{1}{qv}\partial^\mu\alpha, \tag{64}$$

then this gauge transformation acts on the new fields as

$$\varphi \to \varphi' = \varphi - \alpha \qquad h \to h' = h \tag{65}$$

If we choose a gauge with $\alpha = \varphi$, then the Goldstone mode is identically zero. The h field cannot be gauged away since it is invariant under gauge transformations.

We have now transformed a complex scalar ϕ and a massless vector with two degrees of freedom each to a real scalar h with one and a massive vector with three degrees of freedom. The remaining particle h is called a Higgs boson and appears immanently in spontaneously broken gauge theories.

Additionally, something happens with the electric charge when the symmetry is broken. We recall that a charged scalar must be a complex quantity: Mathematically transforming a scalar

---

[5]We are always assuming zero temperature. Using quantum field theory at finite temperatures, it can be shown that there is a transition between the unbroken and the broken phase, which occurs at $T \approx 159.5\,\text{GeV} \approx 2 \times 10^{15}\,\text{K}$ [62], a temperature far from accessible except in the early universe.

to its antiparticle is done via complex conjugation. If the scalar were real, it would be its own antiparticle, which is a contradiction to its charge quantum number. However, the new h boson is a real quantity by construction and thus should not interact with the photon any more. Having a look at some of the interaction terms in the Lagrangian,

$$\mathcal{L} = 2hA^\mu \partial_\mu \varphi - \frac{1}{2}q^2(2vh + h^2)^2 A^\mu A_\mu - \frac{\lambda}{4}(4vh^3 + h^4) + \dots, \tag{66}$$

this is not the case. The Higgs boson still couples to photons in a strange way, proportional to q^2, but this quantity cannot be connected to the classical electric charge any more. In fact, there is no such quantity as classical "charge" any more. According to the Fabri–Picasso theorem, any conserved charge operator must annihilate the vacuum [64], but the charge operator of spontaneously broken symmetries does not fulfil the criterion. Let us calculate $Q|\Omega\rangle$ for a spontaneously broken $U(1)$. The charge operator is proportional to the generator of $U(1)$, which is the one-dimensional unit matrix, $Q = 1$, and the vacuum state is the one-dimensional vector $|\Omega\rangle = v/\sqrt{2}$. Hence

$$Q|\Omega\rangle = \frac{v}{\sqrt{2}} = |\Omega\rangle \neq 0. \tag{67}$$

2.1.6 The Glashow–Weinberg–Salam theory of electroweak interactions

We now go back to the real world, in which we do not have to generate masses for the photon but for the two W bosons. First, we have to embed them into a gauge theory. Therefore, let us take the $SU(2)$, which is the smallest Lie group with a dimension larger than two with $\dim SU(2) = 3$. The structure constant of $SU(2)$, the totally antisymmetric Levi–Civita symbol, $f_a^{bc} = \varepsilon^{bc}{}_a$, prevents interactions between two identical bosons and a third one. Still, it allows the interaction between three different bosons, of which one is positively and one is negatively charged, while the third is neutral. Unfortunately, this third boson cannot be the photon: Electrodynamics is already connected to a $U(1)$ symmetry, which acts both on the left- and right-handed fermions, whereas the third boson of $SU(2)$, like the W, would only interact with the left-handed ones.

Nevertheless, let us set up a particle zoo and assign some quantum numbers. We need a left-handed fermion doublet, which transforms in the fundamental representation of $SU(2)$, which we will denote as $SU(2)_\mathrm{L}$ for clarification. As $SU(2)_\mathrm{L}$ gauge fields, we need three vector fields $W^{\mu a}$. Furthermore, we introduce a vector boson for the $U(1)$ to incorporate electromagnetism and a right-handed set of fermions. Both left- and right-handed fermions should transform in the fundamental representation of the $U(1)$, but the right-handed fermions should transform as singlets in the trivial representation of the $SU(2)_\mathrm{L}$. At last, we introduce a complex scalar to break the gauge symmetry of the theory spontaneously. Since the $SU(2)_\mathrm{L}$ bosons should become massive, the $SU(2)_\mathrm{L}$ has to be broken, and the scalar must be a doublet under the $SU(2)_\mathrm{L}$. With these ingredients, the gauge boson of the electromagnetic $U(1)$ and those of the weak $SU(2)_\mathrm{L}$ do not interact with each other, just like the gluons of the $SU(3)$ and the photons do not interact. This is not what we want. Let instead also the scalar transform under the $U(1)$. Such a $U(1)$ will not be the electromagnetic $U(1)$, as we will see in a moment.

The $SU(2)_\mathrm{L}$ has three generators, the Pauli matrices σ^a, and hence three charges. Since the Pauli matrices do not commute, not all of the $SU(2)_\mathrm{L}$ charges can be measured independently. Let us take $T^3 = \frac{1}{2}\sigma^3$ as the preferred charge and call it the "third component of the weak isospin". T^3 is a diagonal matrix with eigenvalues $\pm\frac{1}{2}$, so let us build the left-handed fermions as eigenstates of T^3 with $T^3|u\rangle = \frac{1}{2}|u\rangle$ and $T^3|d\rangle = -\frac{1}{2}|d\rangle$. The fermion states should couple to the gauge bosons with a coupling strength g. Furthermore, $U(1)$ has one generator, the unit matrix I and one charge. Let us call this charge the "weak hypercharge" Y and the group $U(1)_Y$ to distinguish it from the electromagnetic $U(1)_\mathrm{em}$. The hypercharge Y can be an a priori arbitrary number for each particle, whereas the normalisations of the T^a are fixed by the condition $[T^a, T^b] = \mathrm{i}\varepsilon^{abc}T^c$. The gauge boson of $U(1)_Y$ shall be called B^μ, and the fermions should couple to it with coupling strength g'. A tabular overview is given in Table 2.1. Let

us emphasise that the weak hypercharge and the third component of the weak isospin can be measured simultaneously since T^3 and Y commute and there are simultaneous eigenstates of T^3 and Y.

	ψ_L	ψ_R	$W^{\mu a}$	B^μ	ϕ
$U(1)_Y$	F	F	T	A	F
$SU(2)_\mathrm{L}$	F	T	A	T	F

Table 2.1: Overview of the particle content in the GWS theory and their transformation properties under the gauge groups. F stands for transformation in the fundamental representation, A for the adjoint representation, and T for the trivial representation.

With these ingredients, we get the Glashow–Weinberg–Salam (GWS) Lagrangian [65–67]

$$\mathcal{L}_\mathrm{GWS} = -\frac{1}{4}F^{\mu\nu a}F^a_{\mu\nu} - \frac{1}{4}G^{\mu\nu}G_{\mu\nu} + \mathrm{i}\bar{\psi}_\mathrm{L}\slashed{D}\psi_\mathrm{L} + \mathrm{i}\bar{\psi}_\mathrm{R}\slashed{D}\psi_\mathrm{R}$$
$$+ (D^\mu\phi)^\dagger(D_\mu\phi) + \mu^2\phi^\dagger\phi - \lambda(\phi^\dagger\phi)^2, \tag{68}$$

where $F^{\mu\nu a}$ is the field strength tensor of the $SU(2)_\mathrm{L}$, $G^{\mu\nu}$ is the field strength tensor of the $U(1)_Y$ and D^μ is the covariant derivate, which can be written as

$$D^\mu = \partial^\mu + \mathrm{i}gT^aW^{\mu a} + \mathrm{i}g'YB^\mu, \tag{69}$$

when acting on an $SU(2)_\mathrm{L}$ doublet ψ_L, ϕ and

$$D^\mu = \partial^\mu + \mathrm{i}g'YB^\mu, \tag{70}$$

when acting on an $SU(2)_\mathrm{L}$ singlet ψ_R.

Let us focus on the covariant derivatives of the Higgs field ϕ. Whilst the weak isospins are fixed by the structure constants of $SU(2)$, we can freely choose a normalisation of Y by fixing $Y_\mathrm{H} = \frac{1}{2}$, which simplifies the upcoming expressions.[6] The Abelian model can be straightforwardly generalised, and the Higgs field acquires a vacuum expectation value at $\langle\phi^\dagger\phi\rangle = \mu^2/(2\lambda) = v^2/2$. We choose as a convention

$$\langle\phi\rangle = \begin{pmatrix} 0 \\ \frac{v}{\sqrt{2}} \end{pmatrix}, \tag{71}$$

such that we reparametrise the two-component Higgs field in four real scalars h, φ^a

$$\phi = \begin{pmatrix} 0 \\ \frac{v+h}{\sqrt{2}} \end{pmatrix} e^{\mathrm{i}\frac{T^a\varphi^a}{v}}, \tag{72}$$

which is just the generalisation of the results in the previous section for $SU(2)$ with a Higgs doublet and three generators. As we also saw in the last section, we may choose again a gauge, in which $\varphi^a = 0$. Then, the covariant derivative acts on the Higgs doublet as

$$(D^\mu\phi)^\dagger(D_\mu\phi) = \frac{v^2}{2}\begin{pmatrix} 0 & 1 \end{pmatrix}(gT^aW^{\mu a} + g'\tfrac{1}{2}B^\mu)(gT^bW^b_\mu + g'\tfrac{1}{2}B_\mu)\begin{pmatrix} 0 \\ 1 \end{pmatrix} + \mathcal{O}(h, \partial^\mu h) \tag{73}$$

$$= \frac{g^2v^2}{8}\begin{pmatrix} 0 & 1 \end{pmatrix}\begin{pmatrix} W^{\mu 3} + \frac{g'}{g}B^\mu & W^{\mu 1} - \mathrm{i}W^{\mu 2} \\ W^{\mu 1} + \mathrm{i}W^{\mu 2} & -W^{\mu 3} + \frac{g'}{g}B^\mu \end{pmatrix}^2\begin{pmatrix} 0 \\ 1 \end{pmatrix} + \mathcal{O}(h, \partial^\mu h) \tag{74}$$

$$= \frac{g^2v^2}{8}\left[(W^{\mu 1})^2 + (W^{\mu 2})^2 + (\tfrac{g'}{g}B^\mu - W^{\mu 3})^2\right] + \mathcal{O}(h, \partial^\mu h), \tag{75}$$

---

[6]This is just a convention. For example, going back to classical electrodynamics, we could say the electron has not charge $q = -1$, but $q' = -2$. This would not change physics if we rescaled all other charges also by a factor of 2, the Coulomb constant by $\varepsilon' = 4\varepsilon$ et cetera.

where the kinetic terms and the coupling to the remaining Higgs boson have been left out. With this method, we achieved two massive W bosons with masses $M_{\mathrm{W}} = \frac{gv}{2}$ and a third term, which is not diagonal in the $U(1)_Y$ gauge field B^μ and the third $SU(2)_{\mathrm{L}}$ field $W^{\mu 3}$. We can fix this last issue by mixing the B and the W^3 fields to diagonalise the matrix into two mass eigenstates

$$A^\mu = \sin\theta_{\mathrm{w}} W^{\mu 3} + \cos\theta_{\mathrm{w}} B^\mu \qquad Z^\mu = \cos\theta_{\mathrm{w}} W^{\mu 3} - \sin\theta_{\mathrm{w}} B^\mu, \tag{76}$$

where

$$\theta_{\mathrm{w}} = \arctan\frac{g'}{g} \tag{77}$$

is the weak mixing angle. The inverse transformation is

$$B^\mu = \cos\theta_{\mathrm{w}} A^\mu - \sin\theta_{\mathrm{w}} Z^\mu \qquad W^{\mu 3} = \sin\theta_{\mathrm{w}} A^\mu + \cos\theta_{\mathrm{w}} Z^\mu. \tag{78}$$

With this rotation, the covariant derivative for the Higgs field becomes

$$(D^\mu \phi)^\dagger (D_\mu \phi) = \frac{g^2 v^2}{8} \left[(W^{\mu 1})^2 + (W^{\mu 2})^2 + \frac{1}{\cos^2\theta_{\mathrm{w}}} (Z^\mu)^2 \right] + \mathcal{O}(h, \partial^\mu h). \tag{79}$$

Especially, there is one massive Z boson and one massless A boson. The remaining questions are: Is the A really the photon, and how do we recover the electric charge, which is a conserved quantity in nature?

To answer these questions, we look at the Fabri–Picasso theorem again. Recall that the charge operator of all conserved charges must annihilate the vacuum state $\begin{pmatrix} 0 & v/\sqrt{2} \end{pmatrix}$. Out of the generators of measurable $SU(2)$ and $U(1)$ charges, we can, besides normalisation, build exactly one hermitian generator that fulfils the criterion:

$$Q = T^3 + Y = \begin{pmatrix} 1 & 0 \\ 0 & 0 \end{pmatrix}. \tag{80}$$

The Lie algebra with only one generator Q has structure constants zero ($[Q, Q] = 0Q$). This means, the group $SU(2)_{\mathrm{L}} \times U(1)_Y$ is broken down to the desired $U(1)$ symmetry. We still have to check whether it has the correct properties, i. e. not differentiating between left- and right-handed currents and the correct coupling to the W bosons.

We would like to formulate the $SU(2)_{\mathrm{L}}$ fermion doublets in terms of their electric charge eigenstates (the singlets are trivial). This implies, the coupling to the photon should not mix them. Let us start with the right-handed fermions, which interact with the A and the Z fields via

$$\mathrm{i}\bar{\psi}_{\mathrm{R}} \slashed{D} \psi_{\mathrm{R}} = \mathrm{i}\bar{\psi}_{\mathrm{R}} \slashed{\partial} \psi_{\mathrm{R}} - g' Y \bar{\psi}_{\mathrm{R}} \slashed{B} \psi_{\mathrm{R}} = \mathrm{i}\bar{\psi}_{\mathrm{R}} \slashed{\partial} \psi_{\mathrm{R}} - g' Y \cos\theta_{\mathrm{w}} \bar{\psi}_{\mathrm{R}} \slashed{A} \psi_{\mathrm{R}} + g' Y \sin\theta_{\mathrm{w}} \bar{\psi}_{\mathrm{R}} \slashed{Z} \psi_{\mathrm{R}}. \tag{81}$$

Since T^3 does not act on ψ_{R}, we have for the right-handed singlets the identification $Q = Y$ proportional to the unit matrix and need for a consistent description of electromagnetism and the unified theory as a relation between the coupling constants

$$e = g' \cos\theta_{\mathrm{w}} = g \sin\theta_{\mathrm{w}}. \tag{82}$$

With this, we can rewrite

$$\mathrm{i}\bar{\psi}_{\mathrm{R}} \slashed{D} \psi_{\mathrm{R}} = \mathrm{i}\bar{\psi}_{\mathrm{R}} \slashed{\partial} \psi_{\mathrm{R}} - e\bar{\psi}_{\mathrm{R}} Q \slashed{A} \psi_{\mathrm{R}} + e \tan\theta_{\mathrm{w}} \bar{\psi}_{\mathrm{R}} Q \slashed{Z} \psi_{\mathrm{R}}. \tag{83}$$

The left-handed fermions interact in a more complicated way via

$$\mathrm{i}\bar{\psi}_{\mathrm{L}} \slashed{D} \psi_{\mathrm{L}} = \mathrm{i}\bar{\psi}_{\mathrm{L}} \slashed{\partial} \psi_{\mathrm{L}} - \begin{pmatrix} \bar{u}_{\mathrm{L}} & \bar{d}_{\mathrm{L}} \end{pmatrix} (g T^3 \slashed{W}^3 + g' Y \slashed{B}) \begin{pmatrix} u_{\mathrm{L}} \\ d_{\mathrm{L}} \end{pmatrix} + \dots \tag{84}$$

$$= \mathrm{i}\bar{\psi}_{\mathrm{L}} \slashed{\partial} \psi_{\mathrm{L}} - e \begin{pmatrix} \bar{u}_{\mathrm{L}} & \bar{d}_{\mathrm{L}} \end{pmatrix} Q \slashed{A} \begin{pmatrix} u_{\mathrm{L}} \\ d_{\mathrm{L}} \end{pmatrix} \tag{85}$$

$$- e \begin{pmatrix} \bar{u}_{\mathrm{L}} & \bar{d}_{\mathrm{L}} \end{pmatrix} (\cot\theta_{\mathrm{w}} T^3 - \tan\theta_{\mathrm{w}} Y) \slashed{Z} \begin{pmatrix} u_{\mathrm{L}} \\ d_{\mathrm{L}} \end{pmatrix} + \dots \tag{86}$$

with the A and Z fields, where we already replaced g, g', T^3, and Y by e and Q in the terms proportional to A. We remark that Q is not proportional to the unit matrix in this expression but given by equation (80). Hence, we see that the A field truly couples equally both to the left- and right-handed fermions, and we identify it with the photon. Apart from the photon, there is another boson that has to be neutral, like the photon. In contrast to the photon, the Z boson is massive and couples with different strengths to the left- and right-handed fermions. Its coupling to left-handed fermions is not proportional to the electric charge of the fermions, and the Z boson may interact with neutrinos.

Remember that at this step, Q is an operator, and its eigenvalues are yet arbitrary since the eigenvalues of Y are arbitrary. Especially, while we could simply assign $Q\psi_\mathrm{R} = q\psi_\mathrm{R}$ and define the singlet fields, we still have to prove that the interplay between the photon and the $W^{1,2}$ fields reproduces the relevant terms in the old Proca Lagrangian as well as the correct electromagnetic coupling to the physical $\mathrm{W}^\pm$ bosons.

	$\psi_L = \begin{pmatrix} \nu_\mathrm{L} \\ \mathrm{e}_\mathrm{L} \end{pmatrix}$	$\psi_Q = \begin{pmatrix} \mathrm{u}_\mathrm{L} \\ \mathrm{d}_\mathrm{L} \end{pmatrix}$	$\psi_e = \mathrm{e}_\mathrm{R}$	$\psi_u = \mathrm{u}_\mathrm{R}$	$\psi_d = \mathrm{d}_\mathrm{R}$	$\phi = \begin{pmatrix} 0 \\ \frac{v+h}{\sqrt{2}} \end{pmatrix} e^{\mathrm{i}\frac{T^a \varphi^a}{v}}$
T^3	$\begin{pmatrix} +1/2 \\ -1/2 \end{pmatrix}$	$\begin{pmatrix} +1/2 \\ -1/2 \end{pmatrix}$	0	0	0	$\begin{pmatrix} +1/2 \\ -1/2 \end{pmatrix}$
Y	$-1/2$	$+1/6$	-1	$+2/3$	$-1/3$	$+1/2$
Q	$\begin{pmatrix} 0 \\ -1 \end{pmatrix}$	$\begin{pmatrix} +2/3 \\ -1/3 \end{pmatrix}$	-1	$+2/3$	$-1/3$	$\begin{pmatrix} +1 \\ 0 \end{pmatrix}$

Table 2.2: Charge assignments to SM fields. We slightly abuse the notation by denoting the eigenvalues of the operators with the name of the operator in this table. The third component of the weak isospin T^3 is determined by the eigenvalues of the $SU(2)$ generator $T^3 = \frac{1}{2}\sigma^3$ and the weak hypercharge Y is chosen such that the electric charge $Q = T^3 + Y$ gets the values that are observed in classical electrodynamics. In the SM, all charges of the right-handed neutrinos are zero, making them sterile particles and decoupling them from the SM particle content, so we do not include them in this table. We show in Section 2.2.6 that this is, up to normalisation, the only assignment of quantum numbers that is possible in a self-consistent quantum field theory if we require non-zero hypercharges for all fields.

Of course, we *know* what particles hide behind u_L and d_L as eigenstates of Q and what their eigenvalues have to be. We summarise the assignment of charges in Table 2.2. Let us use this knowledge for a moment to determine what to do with the two W^1 and W^2 fields and come back to the problem in Section 2.2.6. To be able to reproduce the terms proportional to $W^\pm$ in the Proca Lagrangian, we must ensure that the left-handed doublet couples proportionally to

$$\begin{pmatrix} \bar{u}_\mathrm{L} & \bar{d}_\mathrm{L} \end{pmatrix} \begin{pmatrix} 0 & W^+ \\ W^- & 0 \end{pmatrix} \begin{pmatrix} u_\mathrm{L} \\ d_\mathrm{L} \end{pmatrix} + \dots \tag{87}$$

to them. It is, hence, clear that we have to define the charge eigenstates

$$W^{\mu\pm} = \frac{1}{\sqrt{2}}(W^{\mu 1} \mp \mathrm{i}W^{\mu 2}). \tag{88}$$

Furthermore, we define

$$T^\pm = \frac{1}{\sqrt{2}}(T^1 \pm \mathrm{i}T^2), \tag{89}$$

so we can write

$$T^a W^{\mu a} = T^+ W^{\mu +} + T^- W^{\mu -} + T^3 W^{\mu 3} \tag{90}$$

$$= T^+ W^{\mu +} + T^- W^{\mu -} + T^3 \sin\theta_\mathrm{w} A^\mu + T^3 \cos\theta_\mathrm{w} Z^\mu. \tag{91}$$

To check whether the bosons that we identified as physical charged W bosons couple correctly to the photon, we have a look at the field strength tensors. The terms in $G^{\mu\nu}$ do not lead to any couplings since $U(1)$ is Abelian. On the other hand, because of the mixing of the W^3 and B fields, the photon couples to the $W^{1,2}$ and Z fields via the terms in $F^{\mu\nu a}$. Remember that the field strength tensor can be written as

$$F^{\mu\nu a}T^a = \frac{1}{\mathrm{i}g}[D^\mu, D^\nu], \tag{92}$$

and the interaction terms are determined by $g[W^{\mu a}T^a, T^b W^{\nu b}]$. In the unbroken basis, this resembled the structure constants of $SU(2)_\mathrm{L}$, but let us check the couplings in the broken phase. The relevant term is

$$g[T^3 \sin\theta_\mathrm{w} A^\mu, T^\pm W^{\nu\pm}] = eA^\mu W^{\nu\pm}[T^3, T^\pm] = \pm eA^\mu W^{\nu\pm}T^\pm. \tag{93}$$

Hence, the photon couples correctly to the charged W bosons, and the GWS theory is consistent with our desires.[7]

Let us summarise: The GWS theory is able to unify the electromagnetic and the weak forces into one EW force. With the GWS theory and the Higgs mechanism to spontaneously break the EW $SU(2)_\mathrm{L} \times U(1)_Y$ symmetry to a $U(1)_\mathrm{em}$ symmetry, it provides a way to generate massive charged W bosons that couple only to left-handed currents, and a massless A boson (the photon) that couples equally to left- and right-handed currents, without violating gauge invariance. On top, it historically *predicted* the existence of two additional particles: a massive, uncharged vector boson Z which couples differently to left- and right-handed currents and a massive, uncharged scalar boson H.

Historically, the discovery of the Z boson in 1973 [68] was a strong confirmation of the GWS theory, and the discovery of the H boson in 2012 [7, 8] is generally seen as a milestone of modern physics.

2.1.7   Unitarity preservation in the GWS theory

Although the $V - A$ theory could solve the problem of unitarity violation in $2 \to 2$ scattering processes with four external fermions, it introduced the W bosons as new particles. With the additional particle content, new problems also emerge. In this section, we show that both Z and H bosons are needed for a consistent description.

Since the W bosons are massive, they can be longitudinally polarised, in contrast to the massless photon:

$$W_0^\mu = W_0\epsilon_0^\mu e^{\mathrm{i}px} = W_0\frac{1}{M_\mathrm{W}}\left(p^\mu - \frac{M_\mathrm{W}^2}{pq}q^\mu\right)e^{\mathrm{i}px} \tag{94}$$

is a valid solution of the Proca equation

$$\partial_\nu(\partial^\nu W^\mu - \partial^\mu W^\nu) + M_\mathrm{W}^2 W^\mu = 0 \tag{95}$$

for an arbitrary choice of a light-like auxiliary vector q, which is not perpendicular to p [69] (especially it satisfies the Lorenz condition $\partial_\nu W^\nu = 0$). We may also loosen the constraint of light-likeness on q if we normalise ϵ_0 appropriately afterwards to $\epsilon^2 = -1$. Unlike the transverse polarisations, the expression for ϵ_0 scales with the momentum of the particle. This scaling leads to problems for unitarity for the scattering of or into longitudinally polarised vector bosons in the high-energy limit. We emphasise that the Goldstone boson equivalence theorem [59, 70, 71], which we will introduce in this section, is, as its name suggests, based on the existence of Goldstone bosons, which appear only after spontaneous symmetry breaking, hence only in theories with

---

[7]Mathematically rigorous, we can find the eigenvalues and eigenstates of Q in the Lie algebra, $qX = [Q, X]$, which gives the same results $X = T^1 \pm \mathrm{i}T^2$ without physical motivation up to a normalisation constant.

scalar bosons in its particle content. It is not applicable in the $V - A$ theory. We will see how the Higgs boson fixes the unitarity problems, and the Goldstone boson equivalence theorem simplifies calculations.

First, we show briefly that the Z boson is needed for a consistent theory by studying the energy dependence of the process

$$\nu_e \bar{\nu}_e \to W_0^+ W_0^-.$$

Although without being of any practical relevance – the cross section is far too small to be measured nowadays and even in the far future – it leads to the unitarity-violating catastrophe. Without a Z boson, there is only one single Feynman diagram; it is a t-channel exchange of an electron, shown on the left-hand side of Figure 2.3. The matrix element is

$$\mathcal{M}_t = \bar{v}(p_1) \frac{g}{\sqrt{2}} \gamma_\mu \frac{1 - \gamma^5}{2} \frac{\slashed{q}}{q^2} \frac{g}{\sqrt{2}} \gamma_\nu \frac{1 - \gamma^5}{2} u(p_2) \epsilon_0^{*\mu}(k_1) \epsilon_0^{*\nu}(k_2). \tag{96}$$

Calculating the squared matrix element is quite tedious since it involves a trace of up to 12 Dirac matrices. We do not need to do the full calculation for our estimate since we can rely on power counting: The external fermionic spinors scale as $\sqrt{p}_1$ and $\sqrt{p}_2$, respectively, the longitudinal polarisation vectors as k_1 and k_2. Taking the square leads to a plethora of terms containing various products of those kinematic variables. This is counteracted by the fermionic propagator, which scales as $1/q$. Each of those variables scales as $\sqrt{s}$ for its part; hence we arrive at

$$|\bar{\mathcal{M}}_t|^2 \sim \frac{p_1 p_2 k_1^2 k_2^2}{q^2} \sim \frac{\sqrt{s}\sqrt{s}ss}{s} \sim s^2 \tag{97}$$

(the expressions k_i^2 must not be taken literally as $k_i^\mu k_{i,\mu} = M_W^2$ here). Constructing the cross section via equation (9) removes one further power of s from the numerator, so $\sigma \sim s$. This again violates the Froissart bound. We conclude that we need an additional particle mediating the interaction via the s-channel to exactly cancel the LO terms in s^2, shown on the right-hand side of Figure 2.3.[8] A detailed computation with full results is given in [72].
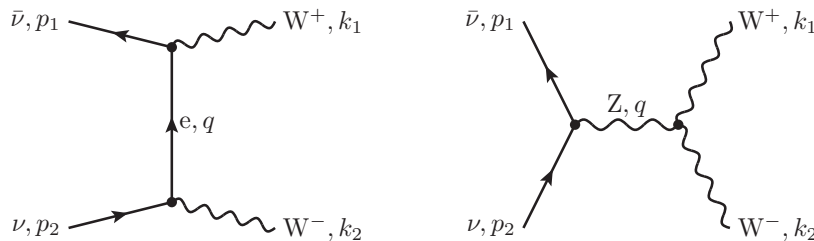

Figure 2.3: Feynman diagrams for $\nu\bar{\nu} \to W^+W^-$ scattering

In the second calculation, we show why only adding the Z boson to the theory is not sufficient. In contrast to the last process, the one we use now is relevant in nature and lies exactly at the heart of this thesis: it is W^+W^- vector boson scattering,

$$W_0^+ W_0^- \to W_0^+ W_0^-. \tag{98}$$

Without the Higgs boson, there are five diagrams to compute: Both s- and t-channel exchanges of a photon or a Z boson, respectively, and the quartic vertex. The corresponding Feynman

---

[8]We feel obliged to remark that the propagator of the Z boson in the s channel scales as $1/q^2$, in contrast to the fermionic propagator in the t channel which scales as $1/q$. This different scaling is compensated by the triple vector boson coupling that leads to an additional momentum factor in the numerator.

diagrams are shown in subdiagrams (a), (b), and (e) of Figure 3.1. The s-channel matrix element takes the form

$$\mathcal{M}_s^{\gamma,Z} = \mathrm{i}c_{\gamma,Z}\epsilon_1^\mu\epsilon_2^\nu\epsilon_3^{*\rho}\epsilon_4^{*\sigma}g_{\alpha\beta} \tag{99}$$
$$\times \left[-g^{\mu\nu}(p_2-p_1)^\alpha + g^{\nu\alpha}(p_2+q)^\mu - g^{\alpha\mu}(q+p_1)^\nu\right] \tag{100}$$
$$\times \left[-g^{\rho\sigma}(p_4-p_3)^\beta + g^{\sigma\beta}(p_4+q)^\rho - g^{\beta\rho}(q+p_3)^\sigma\right], \tag{101}$$

where

$$c_\gamma = \frac{g^2\sin^2\theta_{\mathrm{w}}}{s} \qquad \text{and} \qquad c_Z = \frac{g^2\cos^2\theta_{\mathrm{w}}}{s-M_Z^2} \tag{102}$$

emerge from the photon and Z boson vertex and propagator factors. The t-channel matrix element is similar with the appropriate replacements in the momentum factors and $s \leftrightarrow t$ in the denominator of the propagator. The matrix element with a quartic coupling is

$$\mathcal{M}_{4\mathrm{W}} = \mathrm{i}g^2\epsilon_1^\mu\epsilon_2^\nu\epsilon_3^{*\rho}\epsilon_4^{*\sigma}\left[2g_{\mu\rho}g_{\nu\sigma} - g_{\mu\nu}g_{\rho\sigma} - g_{\mu\sigma}g_{\nu\rho}\right]. \tag{103}$$

Note that we use the so-called Feynman gauge in this calculation, which simplifies the propagators. The drawback of the Feynman gauge is, in principle, the reappearance of Goldstone bosons in our expressions. We are, however, free of them in this particular case since there is no triple vertex with two W bosons and a Goldstone boson φ_Z. Although we are interested in the high-energy limit, we will keep the Z masses in the denominator to be able to perform a correct Taylor expansion afterwards.

The strategy is now to plug in the explicit expressions for all ϵ_i after we have conveniently chosen the auxiliary vectors q_i. Of course, the final result must not depend on this choice. Instead of a lengthy calculation, we quote the results from [72][9]:

$$\mathcal{M}_s^{\gamma,Z} = -\mathrm{i}c_{\gamma,Z}\frac{s^3+2s^2t+8M_{\mathrm{W}}^2st}{4M_{\mathrm{W}}^4} + \mathcal{O}(1), \tag{104}$$

$$\mathcal{M}_t^{\gamma,Z} = -\mathrm{i}c_{\gamma,Z}\frac{s^2t^3+2s^3t^2-8M_{\mathrm{W}}^2s^3t-24M_{\mathrm{W}}^2s^2t^2}{4M_{\mathrm{W}}^4(s-4M_{\mathrm{W}}^2)^2} + \mathcal{O}(1), \tag{105}$$

$$\mathcal{M}_{4\mathrm{W}} = \mathrm{i}g^2\frac{s^4+4s^3t+s^2t^2-12M_{\mathrm{W}}^2s^3-28M_{\mathrm{W}}^2s^2t}{4M_{\mathrm{W}}^4(s-4M_{\mathrm{W}}^2)^2} + \mathcal{O}(1). \tag{106}$$

Each of these five matrix elements shows divergences of $\mathcal{O}(s^2)$ and $\mathcal{O}(s)$ (recall that $t = \mathcal{O}(s)$ and $c_{\gamma,Z} = \mathcal{O}(s^{-1})$). We now perform an expansion for the high-energy limit in the variables $M_{\mathrm{W}}^2, M_Z^2 \ll s,t$:

$$\frac{1}{(s-4M_{\mathrm{W}}^2)^2} = \frac{1}{s^2} + \frac{8M_{\mathrm{W}}^2}{s^3} + \mathcal{O}\left(\frac{M_{\mathrm{W}}^4}{s^4}\right), \qquad \frac{1}{s-M_Z^2} = \frac{1}{s} + \frac{M_Z^2}{s^2} + \mathcal{O}\left(\frac{M_Z^4}{s^3}\right). \tag{107}$$

The product of these two terms, with s replaced by t in one term, appears in $\mathcal{M}_t^Z$ in the denominators:

$$\frac{1}{(s-4M_{\mathrm{W}}^2)^2}\frac{1}{t-M_Z^2} = \frac{1}{s^2t} + \frac{8M_{\mathrm{W}}^2}{s^3t} + \frac{M_Z^2}{s^2t^2} + \mathcal{O}\left(\frac{M^4}{s^5}\right). \tag{108}$$

Multiplying and adding everything together, we finally end up with

$$\mathcal{M}_s^\gamma + \mathcal{M}_s^Z + \mathcal{M}_t^\gamma + \mathcal{M}_t^Z + \mathcal{M}_{4\mathrm{W}} = \mathrm{i}g^2\frac{s+t}{M_{\mathrm{W}}^2} - \mathrm{i}g^2\frac{3M_Z^2\cos^2\theta_{\mathrm{w}}}{4M_{\mathrm{W}}^4}(s+t) + \mathcal{O}(1). \tag{109}$$

---

[9]We note that this source uses a convention that "eats up" a factor of the imaginary unit i in a not clearly defined step of the process of calculating the matrix elements, which we restore for our results. The missing factor can be seen most easily by comparing sub-equation 6 of equation (39) in the source material to our equation (103), which is identical to line 3 of Figure 1 in the source material.

The leading terms of $\mathcal{O}\left(s^2\right)$ have disappeared due to cancellations in the gauge sector, but the matrix element still diverges with $\mathcal{O}\left(s\right)$. As in the previous cases, then the cross section also diverges at $\mathcal{O}\left(s\right)$ and violates unitarity. Hence, only the gauge sector is not sufficient for unitarity preservation. Fortunately, the GWS theory provides us with an additional particle, the Higgs boson, that can be exchanged both via s- and t-channel, which is shown in subdiagrams (c) and (d) of Figure 3.1. Again, we quote the results [72]:

$$\mathcal{M}_s^{\mathrm{H}} = -\mathrm{i}g^2 \frac{s}{4M_{\mathrm{W}}^2} + \mathcal{O}(1) \tag{110}$$

$$\mathcal{M}_t^{\mathrm{H}} = -\mathrm{i}g^2 \frac{t}{4M_{\mathrm{W}}^2} + \mathcal{O}(1). \tag{111}$$

Adding all of these seven terms, the final result is

$$\mathcal{M} = \frac{3}{4}\mathrm{i}g^2 \left(1 - \frac{M_{\mathrm{Z}}^2 \cos^2 \theta_{\mathrm{w}}}{M_{\mathrm{W}}^2}\right) \frac{s+t}{M_{\mathrm{W}}^2} + \mathcal{O}(1) \tag{112}$$

and this result does not diverge if and only if $M_{\mathrm{Z}} \cos \theta_{\mathrm{w}} = M_{\mathrm{W}}$, which is a prediction of the GWS theory. The quintessence of this reasoning is the following: First, a theory without Z and Higgs boson is inconsistent. Second, even with some additional particles, we need large cancellations between different terms in the matrix elements to guarantee a consistent description; a gauge theory can exactly provide the required relations.

We conclude this chapter with an excursus to the Goldstone boson equivalence theorem. In the GWS theory with spontaneous symmetry breaking, we can express matrix elements with longitudinally polarised gauge bosons in the high energy limit by replacing them with their corresponding Goldstone boson:

$$\mathcal{M}(A_0^\mu, \dots) = -\mathrm{i}\mathcal{M}(\varphi, \dots) + \mathcal{O}\left(\frac{M_{\mathrm{W}}}{\sqrt{s}}\right). \tag{113}$$

The reasoning behind this is that the gauge bosons appear massless in the high-energy limit. Since they have received their mass by "eating up" the unphysical Goldstone boson, it takes over the role of the third polarisation. We may now compute the matrix element of the process $\mathrm{W}_0^+ \mathrm{W}_0^- \to \mathrm{W}_0^+ \mathrm{W}_0^-$ again in the high-energy limit. After the lengthy calculations in this section, which we have not carried out, it turns out to be almost trivial since we only have to calculate the scattering amplitude of four scalars $\varphi_0^+ \varphi_0^- \to \varphi_0^+ \varphi_0^-$ by replacing the vector bosons with their Goldstone boson counterparts (and modifying the couplings). Then, the s-channel matrix elements for the Goldstone bosons are simply

$$\mathcal{M}_s^{\gamma,\mathrm{Z}} = \mathrm{i}\tilde{c}_{\gamma,\mathrm{Z}}(t-u) \tag{114}$$

$$\mathcal{M}_s^{\mathrm{H}} = -\mathrm{i}\frac{g^2}{4} \frac{M_{\mathrm{H}}^4}{M_{\mathrm{W}}^2} \frac{1}{s - M_{\mathrm{H}}^2}, \tag{115}$$

where

$$\tilde{c}_\gamma = \frac{g^2 \sin^2 \theta_{\mathrm{w}}}{s} \qquad \text{and} \qquad \tilde{c}_{\mathrm{Z}} = g^2 \left(\frac{\cos^2 \theta_{\mathrm{w}} - \sin^2 \theta_{\mathrm{w}}}{2 \cos \theta_{\mathrm{w}}}\right)^2 \frac{1}{s - M_{\mathrm{Z}}^2}, \tag{116}$$

and the t-channel matrix elements are obtained by replacing $s \leftrightarrow t$. In contrast to the full calculation, we may safely set the Z mass to zero in the propagator. The quartic contribution is a constant:

$$\mathcal{M}_{4\varphi_W} = -\mathrm{i}\frac{g^2}{2} \frac{M_{\mathrm{H}}^2}{M_{\mathrm{W}}^2}. \tag{117}$$

We recognise that none of these terms shows divergent behaviour. The terms of $\mathcal{O}(1)$, which we omitted in the above full calculation, are simply the sum over these seven contributions.

Nevertheless, we can also show that the Higgs boson is a crucial ingredient for the Goldstone boson equivalence theorem by decoupling it from the theory. We, therefore, send its mass to infinity, which is not forbidden by the theorem since it only assumes $M_\text{W}^2 \ll s$. In such a hypothetical limit, the parts of the matrix element involving photon or Z boson exchange are of $\mathcal{O}(1)$, whereas

$$\mathcal{M}_{4\varphi W} + \mathcal{M}_s^\text{H} + \mathcal{M}_t^\text{H} = -\mathrm{i}\frac{g^2}{2}\frac{M_\text{H}^2}{M_\text{W}^2} - \mathrm{i}\frac{g^2}{4}\frac{M_\text{H}^4}{M_\text{W}^2}\left(\frac{1}{s - M_\text{H}^2} + \frac{1}{t - M_\text{H}^2}\right) + \mathcal{O}(1) \qquad (118)$$

$$= \mathrm{i}g^2\frac{s + t}{4M_\text{W}^2} + \mathcal{O}(1). \qquad (119)$$

This is precisely the result without the presence of the Higgs boson in the full calculation.

In fact, it can be shown that the Higgs mass cannot be arbitrarily large to preserve unitarity in the GWS theory. As Lee, Quigg, and Thacker have shown in a detailed analysis with all longitudinal or scalar $2 \to 2$ processes [73, 74], the Higgs boson mass must not exceed

$$M_\text{H}^\text{crit} = 8\sqrt{\frac{\pi}{3}}\frac{M_\text{W}}{g} = \sqrt{\frac{8\pi\sqrt{2}}{3G_\text{F}}} \approx 1\,\text{TeV}. \qquad (120)$$

2.2 Next-to-leading order calculations

In the previous section, we investigated general aspects of the theory. When we calculated matrix elements and cross sections to illustrate them with examples, we always implicitly used LO calculations in perturbation theory. Our objective of this thesis is, however, to present calculations of W^+W^- scattering at NLO accuracy. In this section, we give a brief overview of NLO effects and calculate some simple examples.

In quantum-field-theoretical perturbation theory, we expand in the coupling constants g or g_s. In Feynman diagrams, factors of g or g_s are always connected to vertices; triple vertices correspond to one power of g or g_s, quartic vertices to factors of g^2 or g_s^2. Pictorially, an expansion in the coupling constants hence corresponds to an expansion in the number of vertices of the Feynman diagrams. Alternatively, there can be more quartic vertices than in corresponding LO diagrams. This can lead to two effects: One additional power of g or g_s leads to the emission of an additional particle. Two powers of either g or g_s may also lead to the emission of two additional particles, but also to a closed particle loop.

Processes with additional external particles are called real corrections, such with closed particle loops virtual corrections. Real-correction diagrams and LO diagrams are summarised as tree-level diagrams. While virtual corrections correspond to the same process, it might be questionable why we also have to include processes with additional particles and, hence, another final-state particle content. We motivate this a priori from an experimental point of view: A real particle detector has only a finite momentum and position resolution. Similarly, two particles emitted in the same line of flight will be reconstructed as only one object. A process that we can observe is therefore always a process of all detected particles accompanied by an indeterminate number of additional collinear and soft particles.

We will see in the course of this chapter that these soft and/or collinear particles cause so-called infrared (IR) singularities in the cross sections, which means the real-emission cross sections are divergent. To be able to quantify the singularities, we start this section with the concept of dimensional regularisation. Not only the real but also the virtual corrections show IR-divergent behaviour. It turns out that the IR singularities from real and virtual corrections exactly cancel each other and the final result is IR-finite. For practical computations, this cancellation can be handled by the Catani–Seymour dipole formalism, which is an integral component of our Monte Carlo integration. However, there are also other types of singularities, the so-called ultraviolet (UV) singularities, which only stem from virtual corrections. We have to introduce the concept of renormalisation to handle them since they are in contrast to the IR divergences not cancelled by other physical structures.

At last, we examine the concept of anomalies, which may result from chiral symmetries like the left-handed $SU(2)_L$ of the GWS theory. This is more of a theoretical question that does not directly connect to our calculations. We show that the GWS theory is anomaly-free only if certain conditions on quantum numbers are met, which restricts deviations from the SM in these quantities.

2.2.1 Dimensional regularisation

Our surrounding world, as we recognise it, has four space-time dimensions d. In quantum field theory, it turns out that these four space-time dimensions cause troubles in the calculation of NLO corrections, and we would sometimes like to use a variable number of dimensions. For our calculations to be meaningful in the end, we should be able to take the limit $d \to 4$ continuously. In practice, we shift this dependence to a small parameter ε and write $d = 4 - 2\varepsilon$ and take the limit of $\varepsilon \to 0$. The factor of 2 is purely convenience, and we will specify when we have to take the limit from above ($\varepsilon \to 0^+$) or from below ($\varepsilon \to 0^-$). This method is called dimensional regularisation [75]. This is only a mathematical tool and does not resemble the physical reality since we still use four-dimensional Minkowski vectors, four Dirac matrices, et cetera. However, there are some slight changes to familiar results in the Lorentz algebra, the Dirac algebra and phase-space integrals, which we introduce as necessary basics.

Recall that the identity $g^{\mu\nu}g_{\mu\nu} = 4$ is only valid in four space-time dimensions, and the generalisation for an arbitrary number of d dimensions is

$$g^{\mu\nu}g_{\mu\nu} = d. \tag{121}$$

Since this result is used to derive expressions for the contraction of Dirac matrices, they are also subject to change in a different number of dimensions. In an arbitrary dimension, they are [47]

$$\gamma^\alpha \gamma^\nu \gamma_\alpha = (2 - d)\gamma^\nu, \tag{122}$$

$$\gamma^\alpha \gamma^\nu \gamma^\rho \gamma_\alpha = 4g^{\nu\rho} - (4 - d)\gamma^\nu \gamma^\rho \tag{123}$$

$$\gamma^\alpha \gamma^\nu \gamma^\rho \gamma^\sigma \gamma_\alpha = -2\gamma^\sigma \gamma^\rho \gamma^\nu \gamma_\alpha + (4 - d)\gamma^\nu \gamma^\rho \gamma^\sigma, \tag{124}$$

and reduce to the usual expressions in the limit $d \to 4$.

Furthermore, we have to take care of the dimension of the components of the Lagrangian in space-time dimensions different from four. Space and time still have dimension minus one, mass, momentum, and energy have dimension one and the action $S = \int \mathrm{d}^d x \mathcal{L}$ is dimensionless. Hence, the Lagrangian has mass dimension $[\mathcal{L}] = d$, and we can infer from the kinetic terms in the Lagrangian that the fields have dimensions

$$[A] = \frac{d-2}{2}, \qquad [\psi] = \frac{d-1}{2}, \tag{125}$$

and from the interaction term, we conclude that the coupling gains the mass dimension

$$[e] = \frac{4-d}{2}. \tag{126}$$

We redefine

$$e \to \mu^{\frac{4-d}{2}} e \tag{127}$$

with an arbitrary parameter of mass dimension μ, which we call the renormalisation scale, to ensure that the electric charge remains a dimensionless quantity. The physical relevance of this parameter becomes clear in the following examples. Also, for these quantities, the limit $d \to 4$ results in the familiar expressions.

Next, we have to define what we understand under an integral over a non-integer space-time dimension. For a vector k_E, which is defined in a Euclidean d-dimensional space-time, we generalise the integration in four-dimensional polar coordinates as

$$\int \frac{\mathrm{d}^4 k_E}{(2\pi)^4} = \int \frac{\mathrm{d}\Omega_4}{(2\pi)^4} \int \mathrm{d}k_E \, k_E^3 \quad \rightarrow \quad \int \frac{\mathrm{d}^d k_E}{(2\pi)^d} = \int \frac{\mathrm{d}\Omega_d}{(2\pi)^d} \int \mathrm{d}k_E \, k_E^{d-1}, \tag{128}$$

where the integral over the solid angle is given by

$$\int \frac{\mathrm{d}\Omega_d}{(2\pi)^d} = \frac{1}{(2\pi)^d} \frac{2\pi^{d/2}}{\Gamma(d/2)} = \frac{1}{2^{d-1}\pi^{d/2}\Gamma(d/2)}. \tag{129}$$

The formula for the angular integration can be derived from a d-dimensional generalisation of the integration over a real power of a Gaussian curve instead of an integer,

$$(\sqrt{\pi})^d = \left(\int_{-\infty}^{\infty} \mathrm{d}x \, e^{-x^2} \right)^d = \int \mathrm{d}^d r \, e^{-r^2}, \tag{130}$$

and the definition of the Gamma function. The conversion between Euclidean and Minkowski vectors can be achieved by Wick-rotating the k^0 component in the complex plane $k^0 \equiv i k_E^0$ while leaving $k^i = k_E^i$ unaltered. This change of variables results in quadratic expressions in picking up a minus sign

$$k^2 = (k^0)^2 - \vec{k}^2 \rightarrow -(k_E^0)^2 - \vec{k}_E^2 = -k_E^2 \tag{131}$$

and the integration measure picks up an imaginary unit due to the zeroth component, $\mathrm{d}^4 k = i\,\mathrm{d}^4 k_E$.

The expressions for phase-space integrals generalise equation (8) for an arbitrary number of space-time dimensions. We write down the two- and three-particle Lorentz-invariant phase spaces explicitly:

$$\int_2 \mathrm{d}\Gamma_d = (2\pi)^{2-d} \int \frac{\mathrm{d}^{d-1} p_3}{2E_3} \frac{\mathrm{d}^{d-1} p_4}{2E_4} \delta^{(d)}(p_3 + p_4 - q); \tag{132}$$

$$\int_3 \mathrm{d}\Gamma_d = (2\pi)^{3-2d} \int \frac{\mathrm{d}^{d-1} p_3}{2E_3} \int \frac{\mathrm{d}^{d-1} p_4}{2E_4} \int \frac{\mathrm{d}^{d-1} p_5}{2E_5} \delta^{(d)}(p_3 + p_4 + p_5 - q), \tag{133}$$

where the final-state particles are labelled with $3, 4$ and 5, and the sum of the initial-state momenta is q. It is, however, convenient in the case of the three-particle final state to perform a change of variables

$$x_i = \frac{2 p_i q}{q^2} \tag{134}$$

to integrate out the angular dependence. The initial-state xs fulfil $x_1 + x_2 = 2$ and momentum conservation translates to $x_3 + x_4 + x_5 = 2$. The calculation of the new phase-space measure is rather involved, already for three massless final-state particles, and we quote the result [76]:

$$\int_3 \mathrm{d}\Gamma_d = \left(\frac{s}{4\pi} \right)^{d-4} \frac{s}{128\pi^3 \Gamma(d-2)}$$
$$\times \int_0^1 \mathrm{d}x_3 \mathrm{d}x_4 \mathrm{d}x_5 \left[\frac{1}{(1-x_3)(1-x_4)(1-x_5)} \right]^{2-d/2} \delta(x_3 + x_4 + x_5 - 2). \tag{135}$$

We will need these expressions when calcluating the real corrections.

2.2.2   Virtual corrections

In the following, we want to give a glimpse of concepts that appear when NLO corrections are taken into account. Therefore we start with a simple example and work our way through the appearing difficulties. The example process we use is

$$e^+e^- \to \mu^+\mu^-$$

and we restrict ourselves to pure QED corrections. Already, with this restriction, there are three new types of diagrams compared to the LO calculation: We can connect both initial- or final-state fermions with a photon, leading to two triangle diagrams. We can also insert a fermion loop into the LO photon propagator or a photon emission and absorption by the same fermion, leading to five different self-energy diagrams.[10] At last, we can connect the initial- and final-state fermions with an additional photon in two different ways, leading to two box diagrams. We present an example for each of these diagram types in Figure 2.4.
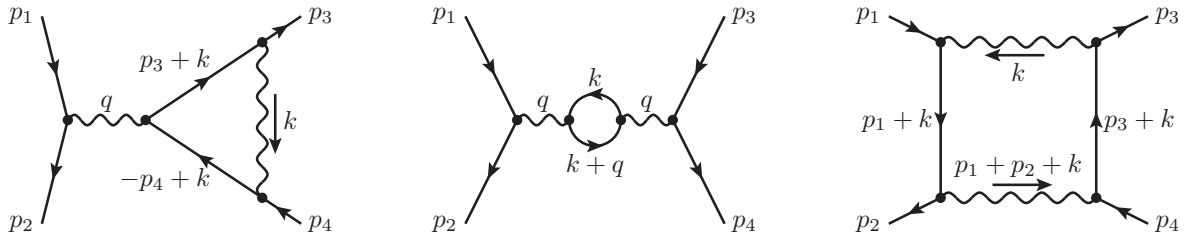
Figure 2.4: The three types of loop diagrams in $e^+e^- \to \mu^+\mu^-$ scattering with momentum assignment. k is the loop momentum to be integrated over, q is fixed by momentum conservation. We use the convention that the momentum flow of fermionic propagators is always parallel to the fermionic flow; the loop momentum flow of bosons is indicated by arrows for clarity (but irrelevant for the computation).

We remind of the important fact that the momenta of internal particles in Feynman diagrams are a priori indeterminate and we had to integrate over all of them in the calculation of matrix elements. However, energy and momentum have to be conserved at each vertex, which leads to delta functions to completely determine all internal four-momenta in the case of tree-level diagrams but not in the case of loop diagrams. We may prove this in analogy to Euler's polyhedron formula, which states

$$\#\text{vertices} - \#\text{edges} + \#\text{faces} = 2.$$

We are tempted to directly identify the faces with loops, the edges with propagators and the vertices with vertices, but this is not correct. External particles are also edges, and their endpoints are also vertices in the Eulerian sense. However, there are exactly as many endpoints as external particles, and thus, the difference between Eulerian vertices and edges is identical to the difference between physical vertices and propagators. Furthermore, the outside face of the graph is not a loop. We, therefore, end with the slightly modified version

$$\#\text{vertices} - \#\text{propagators} + \#\text{loops} = 1. \tag{136}$$

Hence, for tree-level diagrams, there is one propagator less than there are vertices. One delta function of the vertices is used up for overall energy–momentum conservation between initial and final states, and the others exactly match the number of propagators. However, if there is at least

---

[10]Of these five diagrams only the self-energy of the internal photon propagator contributes to the matrix element due to the LSZ reduction formula [77] after the fields are properly renormalised.

one loop, then the delta functions are not sufficient any more to determine all propagators.[11] Respecting energy–momentum conservation at each vertex, we labelled the integration parameter four-momentum, which we have to integrate over, with k in Figure 2.4. We explicitly state that this integration variable does not have to obey the on-shell condition.

With this in mind, we can write down the matrix element of the final-state triangle diagram, assuming massless fermions, as

$$\mathcal{M} = \bar{v}(p_2)(\mathrm{i}e\gamma^\mu)u(p_1)\frac{-\mathrm{i}g_{\mu\nu}}{q^2}\bar{u}(p_3)\left[\int\frac{\mathrm{d}^4k}{(2\pi)^4}(\mathrm{i}e\gamma^\rho)\mathrm{i}\frac{\not{p}_3+\not{k}}{(p_3+k)^2}(\mathrm{i}e\gamma^\nu)\mathrm{i}\frac{-\not{p}_4+\not{k}}{(p_4-k)^2}(\mathrm{i}e\gamma^\sigma)\frac{-\mathrm{i}g_{\rho\sigma}}{k^2}\right]v(p_4). \tag{137}$$

The difference between the LO and the NLO expression is the NLO vertex factor

$$\mathrm{i}e\Gamma^\nu = -e^3\int\frac{\mathrm{d}^4k}{(2\pi)^4}\frac{\gamma^\rho(\not{p}_3+\not{k})\gamma^\nu(\not{p}_4-\not{k})\gamma_\rho}{(p_3+k)^2k^2(p_4-k)^2}, \tag{138}$$

whereas at LO, the vertex factor was $\mathrm{i}e\gamma^\nu$. The NLO vertex contains an integral expression which we are not able to carry out immediately. This can be seen as follows: There are terms in the integrand that scale as k^{-4} for large k. The integral measure d^4k in the form of four-dimensional polar coordinates after Wick rotation scales as $k^3\mathrm{d}k$, which leads to a logarithmically divergent integral. However, this is only a problem in space-time dimensions equal or greater than four, and we can make use of dimensional regularisation: In $4-2\varepsilon$ dimensions, $\varepsilon > 0$, the integral is executable. Restoring our four-dimensional world by taking the limit $\varepsilon \to 0$, we end up with a divergence in ε.

Applying the modified Dirac algebra (122) and (124) the vertex factor reads

$$\mathrm{i}e\Gamma^\nu = -e^3\mu^{4-d}\int\frac{\mathrm{d}^dk}{(2\pi)^d}\frac{-2(\not{p}_4-\not{k})\gamma^\nu(\not{p}_3+\not{k})+(4-d)(\not{p}_3+\not{k})\gamma^\nu(\not{p}_4-\not{k})}{(p_3+k)^2k^2(p_4-k)^2}. \tag{139}$$

These integrals are generally solved by introducing Feynman parameters, which is rewriting the denominator as

$$\frac{1}{(p_3+k)^2k^2(p_4-k)^2} = 2\int_0^1\mathrm{d}x\mathrm{d}y\mathrm{d}z\,\frac{\delta(x+y+z-1)}{[x(p_3+k)^2+yk^2+z(p_4-k)^2]^3} \tag{140}$$

$$= 2\int_0^1\mathrm{d}x\mathrm{d}y\mathrm{d}z\,\frac{\delta(x+y+z-1)}{[k^2+2k(xp_3-zp_4)]^3} \tag{141}$$

$$= 2\int_0^1\mathrm{d}x\mathrm{d}y\mathrm{d}z\,\frac{\delta(x+y+z-1)}{[(k+xp_3-zp_4)^2+xzs]^3}. \tag{142}$$

We may now shift the integration parameter $k^\mu \to k'^\mu = k^\mu + xp_3^\mu - zp_4^\mu$ for a simplified denominator depending only on k'^2.

Of course, we have to shift the integration parameter in the numerator as well. At first sight, this blows up the expression. However, we can use the Dirac equation $\not{p}_4v(p_4) = \bar{u}(p_3)\not{p}_3 = 0$, since both external fermions are on-shell and in the expression for the matrix element, we are going to sandwich $\mathrm{i}e\Gamma^\mu$ between those two spinors. With a slight abuse of mathematical

---

[11]To be precise, the polyhedron formula is only valid for planar graphs. However, one-loop graphs are always planar. Let us now start with a planar graph and keep the number of external particles fixed. An additional vertex will divide an existing propagator into two, and we are forced to introduce an additional propagator that must either merge with a triple to a quartic vertex or produce a second additional vertex (which then subsequently splits another propagator into two). In both cases, the difference between the number of vertices and propagators is lowered by one after the complete procedure. Alternatively, a new propagator might also be inserted between two already existing vertices, lowering the difference between the numbers of vertices and propagators by one. In all cases, there is one more integral to carry out. The difference between a planar and a non-planar graph is only in the number of resulting loops. For non-planar graphs, there is no simple connection "number of loops equals the number of integrals".

notation, we pretend that we can omit those factors already in the expression of the vertex factor. Furthermore, any term proportional to an odd power of k' vanishes after integration since they are antisymmetric under the exchange $k' \to -k'$, but the denominator and the integration region are symmetric. With this, we arrive at

$$-2(\not{p}_4 - \not{k})\gamma^\nu(\not{p}_3 + \not{k}) + (4 - d)(\not{p}_3 + \not{k})\gamma^\nu(\not{p}_4 - \not{k})$$
$$= -(2 - d)\not{k}'\gamma^\nu\not{k}' + [-2(1 - x)(1 - z) + (4 - d)xz]\not{p}_4\gamma^\nu\not{p}_3 + \dots \tag{143}$$

for the numerator, where the dots represent the parts which vanish after integration or according to the Dirac equation.

For the first term, we use the identity $\int \mathrm{d}^d k'\, k'^\alpha k'^\beta = \int \mathrm{d}^d k'\, \frac{1}{d} g^{\alpha\beta} k'^2$. For the last, we use the Dirac algebra to anticommute the $\not{p}_3$ to the left, after which we can use the Dirac equation again. Finally, this leads to

$$i e \Gamma^\nu = -2e^3 \mu^{4-d} \gamma^\nu \int_0^1 \mathrm{d}x\mathrm{d}y\mathrm{d}z\, \delta(x + y + z - 1)$$
$$\times \int \frac{\mathrm{d}^d k'}{(2\pi)^d} \frac{\frac{(2-d)^2}{d} k'^2 + [(2 - d)xz + 2x + 2z - 2]\, s}{[k'^2 + xzs]^3}. \tag{144}$$

As a last step before the integration, we Wick-rotate k' and change to polar coordinates. The final integral expression is

$$i e \Gamma^\nu = -2e^3 \mu^{4-d} \gamma^\nu \int_0^1 \mathrm{d}x\mathrm{d}y\mathrm{d}z\, \delta(x + y + z - 1)$$
$$\times \int \frac{\mathrm{d}\Omega_d}{(2\pi)^d} \int \mathrm{d}k'_\mathrm{E}\, i k'^{d-1}_\mathrm{E} \frac{-\frac{(2-d)^2}{d} k'^2_\mathrm{E} + [(2 - d)xz + 2x + 2z - 2]\, s}{[-k'^2_\mathrm{E} + xzs]^3}. \tag{145}$$

Formally, we could have written down everything so far in four dimensions despite the integrals not being well-defined. Since we are now at the point to carry out the integrals, this is a good point to talk about the divergence of the vertex function again. For small k'_E, the denominator is a constant, and we can only run into trouble from the Feynman parameter integration. This gives rise to the IR divergences. For large k'_E, the first term of the numerator combined with the integral measure and the denominator scales as $\mathrm{d}k_\mathrm{E}\, k_\mathrm{E}^{d-1+2-6} = \mathrm{d}k_\mathrm{E}\, k_\mathrm{E}^{d-5}$, the second term as $\mathrm{d}k_\mathrm{E}\, k_\mathrm{E}^{d-7}$. For large momenta, the second term is well-defined (UV-finite), but the first one is UV-divergent. Hence, we calculate these two objects separately.

UV-divergent terms   We carry out the integration of the first term in d dimensions and set $d = 4 - 2\varepsilon$:

$$i e \Gamma^\nu = -2i e \gamma^\nu \int_0^1 \mathrm{d}x\mathrm{d}y\mathrm{d}z\, \delta(x + y + z - 1) \frac{\mu^{2\varepsilon}}{(4\pi)^{2-\varepsilon}} \Gamma(\varepsilon) \left(\frac{1}{-xzs}\right)^\varepsilon + \text{UV-finite.} \tag{146}$$

We are now also able to integrate the Feynman parameters. Since the integrand (except the delta function) does not depend on y, the integration over y is trivial, and we can rewrite the integration boundaries as

$$\int_0^1 \mathrm{d}x \int_0^1 \mathrm{d}z \int_0^1 \mathrm{d}y\, \delta(x + y + z - 1) = \int_0^1 \mathrm{d}x \int_0^{1-x} \mathrm{d}z. \tag{147}$$

Hence

$$i e \Gamma^\nu = i e \gamma^\nu \frac{e^2}{8\pi^2} \left(\frac{4\pi\mu^2}{-s}\right)^\varepsilon \frac{\Gamma(\varepsilon)\Gamma^2(2 - \varepsilon)}{\Gamma(3 - 2\varepsilon)} + \text{UV-finite.} \tag{148}$$

The critical term in this expression is $\Gamma(\varepsilon)$ with a single pole at $\varepsilon = 0$, while the other terms are not problematic as they have a well-defined limit as $\varepsilon \to 0$.

IR-divergent terms   Let us now carry out the integration of the second term in d dimensions. By simple power-counting, the integral over k'_E is well-defined, and we could write down a result also in $d = 4$ dimensions. However, the integrals over the Feynman parameters cause problems in four dimensions. To see this, we also rewrite the triple integral over the parameters as a double integral and arrive at

$$\mathrm{i}e\Gamma^\nu = \mathrm{i}e^3\mu^{4-d}\gamma^\nu \int_0^1 \mathrm{d}x \int_0^{1-x} \mathrm{d}z \frac{\Gamma(3-d/2)}{(4\pi)^{d/2}} \frac{[(2-d)xz + 2x + 2z - 2]s}{(-xzs)^{3-d/2}} + \text{UV-divergent}. \quad (149)$$

The z-integral diverges at the lower bound of integration for $d \leq 4$ since the last term in the numerator is constant in z while the denominator scales as $z^{3-d/2}$. In contrast to the UV-divergent term, the problematic space-time dimensions are on the other "side" of the critical point $d = 4$. This might tempt us to use a definition of the IR-regulator ε_IR different from the UV-regulator ε_UV from the previous section. However, to avoid confusion, we instead use the same convention $d = 4 - 2\varepsilon$ for the IR-regulator but have to take care of the non-standard limit $\varepsilon_\mathrm{IR} \to 0^-$, approaching zero from below, in contrast to $\varepsilon_\mathrm{UV} \to 0^+$. We will make this differentiation between the two limits in using the subscripts whenever necessary.

   Carrying out the integral over the Feynman parameters and substituting the d-dependence with ε leads to the result

$$\mathrm{i}e\Gamma^\nu = \mathrm{i}e \frac{e^2}{16\pi^2}\gamma^\nu \left(\frac{4\pi\mu^2}{-s}\right)^\varepsilon \frac{\Gamma(\varepsilon)\Gamma(-\varepsilon)\Gamma(2-\varepsilon)}{\Gamma(2-2\varepsilon)} \frac{\varepsilon^2+2}{1-\varepsilon} + \text{UV-divergent}. \quad (150)$$

Compared to the UV-singularity, there is a double pole at $\varepsilon = 0$ because of the two factors $\Gamma(\varepsilon)$ and $\Gamma(-\varepsilon)$.

   It may seem as if we seperated the IR- and UV-divergent terms from each other, but this is not the case. In fact, the UV-divergent term also contains a hidden IR singularity from the lower integration bound of the Feynman parameters, although it is encoded in ε_UV instead of ε_IR. This is an artefact of dimensional regularisation, and we come back to the problem in the course of renormalisation.

Other virtual contributions   As stated above, there are other contributions to the virtual correction than the calculated final-state triangle correction. The calculation of the initial-state triangle correction is similar to the final-state one and modifies the other vertex factor. The photon self-energy also leads to a UV singularity, which we do not calculate here. The virtual correction modifies the propagator and is given by

$$\frac{-\mathrm{i}g_{\mu\nu}}{q^2} \longrightarrow \frac{-\mathrm{i}G_{\mu\nu}}{q^2} = \frac{-\mathrm{i}g_{\mu\rho}}{q^2} \int \frac{\mathrm{d}^4k}{(2\pi)^4} \frac{-\mathrm{Tr}\left[(-\mathrm{i}e\gamma^\rho)\mathrm{i}(\slashed{k})(-\mathrm{i}e\gamma^\sigma)\mathrm{i}(\slashed{k}+\slashed{q})\right]}{k^2(k+q)^2} \frac{-\mathrm{i}g_{\sigma\nu}}{q^2} \quad (151)$$

in Feynman gauge. The underlying argument is identical to the case of the triangle corrections and relies on simple power-counting of the integration variable k: The integrand scales as k^{-2}, the integration measure as $k^3\mathrm{d}k$. However, the Ward identity preserves the term from being quadratically divergent and softens it to a logarithmic one. It is, hence, conceptually identical to the triangle correction discussed above. On the other hand, the self-energy is not IR divergent.

   The box diagrams, whose matrix elements are given by

$$\mathcal{M} = \int \frac{\mathrm{d}^4k}{(2\pi)^4} \bar{v}(p_2)(\mathrm{i}e\gamma^\rho)\mathrm{i}\frac{\slashed{p}_1 + \slashed{k}}{(p_1+k)^2}(\mathrm{i}e\gamma^\mu)u(p_1)\bar{u}(p_3)(\mathrm{i}e\gamma^\nu)\mathrm{i}\frac{\slashed{p}_3 + \slashed{k}}{(p_3+k)^2}(\mathrm{i}e\gamma^\sigma)v(p_4)$$
$$\times \frac{-\mathrm{i}g_{\mu\nu}}{k^2} \frac{-\mathrm{i}g_{\rho\sigma}}{(p_1+p_2+k)^2}, \quad (152)$$

and an analogous expression for the crossed version are not UV-divergent at all since the integral scales as d^4k/k^6 for large k. Their IR divergences cancel against the real IR divergence from the

interference of initial- and final-state radiation, which we will not show explicitly here since it is conceptually identical to our example. In contrast to the other types of loop diagrams, the box correction also does not simply modify a vertex or a propagator.

In the following, we will pretend as if there was only one virtual correction, namely the final-state triangle correction since it is sufficient to present the concepts.

Virtual cross section   When doing perturbation theory at NLO, one-loop diagrams contribute to the cross section via interference with tree-level diagrams. To make the calculations easier, we recall that the spin-summed matrix element factorised into a production and decay part, as we saw in equation (14).[12] We are now going to calculate the LO cross section and modify the calculations at the appropriate steps for the virtual corrections.

With the identity

$$\sum_{\lambda=\pm} \epsilon_\lambda^{*\mu}(q)\epsilon_\lambda^\nu(q) = -g^{\mu\nu} \tag{153}$$

as sum over the different polarisations of a photon, we can identify

$$\mathcal{M}(\mathrm{e^+e^-} \to \mu^+\mu^-) = \sum_{\lambda=\pm} \underbrace{\bar{v}(p_2)(\mathrm{i}e\gamma_\mu)u(p_1)\epsilon_\lambda^{*\mu}(q)}_{\mathcal{M}(\mathrm{e^+e^-}\to\gamma^*)} \frac{\mathrm{i}}{q^2} \underbrace{\bar{u}(p_3)(\mathrm{i}e\gamma_\nu)v(p_4)\epsilon_\lambda^\nu(q)}_{\mathcal{M}(\gamma^*\to\mu^+\mu^-)}. \tag{154}$$

When we calculate the cross section, we have to square the matrix element and integrate it over the phase space. Using Casimir's trick [53] for spinor-summation again, we can define an initial-state tensor $i^{\mu\alpha}$ and a final-state tensor $f^{\nu\beta}$

$$\bar{\sigma}_d(\mathrm{e^+e^-} \to \mu^+\mu^-) = \frac{1}{2s}\int \mathrm{d}\Gamma_d\,|\bar{\mathcal{M}}|^2 \equiv \frac{e^4}{2s^3}\mu^{8-2d}i^{\mu\alpha}f^{\nu\beta}g_{\alpha\beta}g_{\mu\nu} = \frac{e^4}{2s^3}\mu^{8-2d}i^{\mu\alpha}f_{\mu\alpha}, \tag{155}$$

where the initial-state tensor is defined as

$$i^{\mu\alpha} = \frac{1}{4}\mathrm{Tr}(\slashed{p}_2\gamma^\mu\slashed{p}_1\gamma^\alpha) = p_1^\mu p_2^\alpha + p_1^\alpha p_2^\mu - \frac{q^2}{2}g^{\mu\alpha}. \tag{156}$$

This is true in any dimension since manipulating the space-time dimension does not affect traces of Dirac matrices of non-chiral currents. We already absorbed the spin-averaging factor into i and factorised out the coupling constants. The phase-space integral is included directly in the final-state tensor:

$$f^{\nu\beta} = \int \mathrm{d}\Gamma_d\,\mathrm{Tr}(\slashed{p}_3\gamma^\nu\slashed{p}_4\gamma^\beta) = \int \mathrm{d}\Gamma_d\,\left(4p_3^\nu p_4^\beta + 4p_3^\beta p_4^\nu - 2q^2g^{\nu\beta}\right). \tag{157}$$

To simplify the calculations further, we realise that the final-state tensor must be of the form

$$f^{\mu\nu} = (q^\mu q^\nu - q^2 g^{\mu\nu})f(q^2) \tag{158}$$

because q is the only leftover variable after we integrate over p_3 and p_4, $f^{\mu\nu}$ must be a true Lorentz tensor since the phase-space integral is compatible with the Lorentz structure, and the Ward identity $q_\mu f^{\mu\nu} = 0$ has to hold [78]. A contraction the Lorentz indices yields for the scalar $f(q^2)$:

$$g_{\mu\nu}f^{\mu\nu} = q^2(1-d)f(q^2) \quad \Rightarrow \quad f(q^2) = \frac{1}{(1-d)q^2}g_{\mu\nu}f^{\mu\nu}. \tag{159}$$

---

[12]Precisely, we saw this for the four-fermion contact interaction. Nevertheless, we can insert a factor of $g_{\mu\nu}$ by hand into the equation to achieve the same tensor structure in the Fermi theory as in electromagnetism. The additional factor of s^{-1} from the propagator and other constants do not matter for this argument.

Hence,

$$i_{\mu\alpha} f^{\mu\alpha} = \frac{d-2}{2} q^4 f(q^2) = \frac{d-2}{2(1-d)} q^2 g_{\mu\alpha} f^{\mu\alpha}. \tag{160}$$

The phase-space integral is easy to execute with the use of equation (132) since all angular dependence vanishes in the contraction of the final-state tensor with the metric tensor

$$g_{\mu\alpha} f^{\mu\alpha} = -\int d\Gamma_d \, 2(d-2)s = -2(d-2)s \left(\frac{4\pi}{s}\right)^{2-d/2} \frac{2^{-d}}{\sqrt{\pi}\Gamma(d/2-1/2)}. \tag{161}$$

Collecting all pieces, setting $d = 4 - 2\varepsilon$ and applying Legendre's duplication formula for the Gamma function to get rid of the square root of π and the 4^ε, we arrive at

$$\bar{\sigma}_d = \frac{e^4}{\pi s} \mu^{2\varepsilon} (1-\varepsilon)^2 \left(\frac{4\pi\mu^2}{s}\right)^\varepsilon \frac{\Gamma(3-\varepsilon)}{\Gamma(5-2\varepsilon)}. \tag{162}$$

As a cross-check, the LO cross section reduces with $\Gamma(3)/\Gamma(5) = 1/12$ in four dimensions to the familiar expression

$$\sigma_{\mathrm{LO}} = \frac{e^4}{12\pi s}. \tag{163}$$

Since the virtual corrections modify the vertex only by a number, Γ^ν is still proportional to γ^ν, we can write

$$\Gamma^\nu = g(s,\mu,\varepsilon)\gamma^\nu \quad \Rightarrow \quad \mathcal{M}_{\mathrm{virt}} = g(s,\mu,\varepsilon)\mathcal{M}_{\mathrm{LO}}. \tag{164}$$

We note that the factor g does not depend on other kinematic variables than the total centre-of-mass energy squared s. The NLO contribution from the virtual corrections can be obtained by calculating

$$\sigma_{\mathrm{tot}} = \frac{1}{2s} \int d\Gamma_d (\mathcal{M}_{\mathrm{LO}} + \mathcal{M}_{\mathrm{virt}})(\mathcal{M}_{\mathrm{LO}}^* + \mathcal{M}_{\mathrm{virt}}^*), \tag{165}$$

where we truncate the NNLO contribution of $|\mathcal{M}_{\mathrm{virt}}|^2$ and subtract the LO cross section. Hence

$$\sigma_{\mathrm{virt}} = \frac{1}{2s} \int d\Gamma_d \left(\mathcal{M}_{\mathrm{LO}}\mathcal{M}_{\mathrm{virt}}^* + \mathcal{M}_{\mathrm{LO}}^*\mathcal{M}_{\mathrm{virt}}\right) = 2\,\mathrm{Re}(g)\sigma_{\mathrm{LO}}^d \tag{166}$$

is just the LO cross section multiplied with twice the real part of the vertex correction factor from equations (148) and (150). We recall that in both of these equations, an imaginary part stems from the factors

$$\left(\frac{4\pi\mu^2}{-s}\right)^\varepsilon = \left(\frac{4\pi\mu^2}{s}\right)^\varepsilon e^{i\pi\varepsilon} \quad \Rightarrow \quad \mathrm{Re}\, g(s,\mu,\varepsilon) = g(-s,\mu,\varepsilon)\cos(\pi\varepsilon). \tag{167}$$

Collecting everything, we get the cross section from the UV-divergent part of the virtual corrections

$$\sigma_{\mathrm{virt}}^{\mathrm{UV\text{-}div}} = \sigma_{\mathrm{LO}}^d \frac{e^2}{4\pi^2} \left(\frac{4\pi\mu^2}{s}\right)^\varepsilon \frac{\Gamma(\varepsilon)\Gamma^2(2-\varepsilon)}{\Gamma(3-2\varepsilon)} \cos(\pi\varepsilon) \tag{168}$$

$$= \sigma_{\mathrm{LO}} \frac{3e^2}{\pi^2} \mu^{2\varepsilon} \left(\frac{4\pi\mu^2}{s}\right)^{2\varepsilon} (1-\varepsilon)^2 \frac{\Gamma(3-\varepsilon)}{\Gamma(5-2\varepsilon)} \frac{\Gamma(\varepsilon)\Gamma^2(2-\varepsilon)}{\Gamma(3-2\varepsilon)} \cos(\pi\varepsilon) \tag{169}$$

and for the UV-finite part

$$\sigma_{\mathrm{virt}}^{\mathrm{UV\text{-}fin}} = \sigma_{\mathrm{LO}}^d \frac{e^2}{8\pi^2} \left(\frac{4\pi\mu^2}{s}\right)^\varepsilon \frac{\Gamma(\varepsilon)\Gamma(-\varepsilon)\Gamma(2-\varepsilon)}{\Gamma(2-2\varepsilon)} \frac{\varepsilon^2+2}{1-\varepsilon} \cos(\pi\varepsilon) \tag{170}$$

$$= \sigma_{\mathrm{LO}} \frac{3e^2}{2\pi^2} \mu^{2\varepsilon} \left(\frac{4\pi\mu^2}{s}\right)^{2\varepsilon} \frac{\Gamma(3-\varepsilon)}{\Gamma(5-2\varepsilon)} \frac{\Gamma(\varepsilon)\Gamma(-\varepsilon)\Gamma(2-\varepsilon)}{\Gamma(2-2\varepsilon)} (\varepsilon^2+2)(1-\varepsilon)\cos(\pi\varepsilon). \tag{171}$$
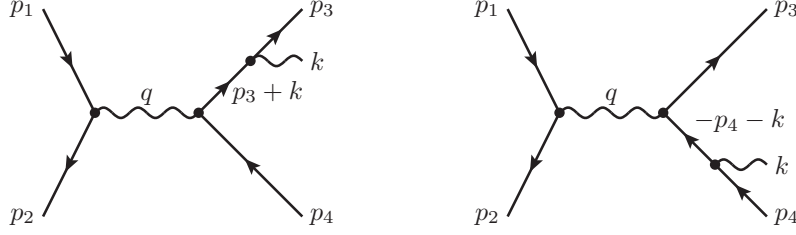
Figure 2.5: Feynman diagrams for final-state photon emission in $e^+e^- \to \mu^+\mu^-(+\gamma)$ scattering with momentum assignments. Note the minus signs on the right-hand diagram due to our momentum flow convention, in agreement with the relative minus signs in equations (172) and (173).

2.2.3   Real corrections

The other contribution at NLO is the emission of a real photon. Since we pretended in the calculations of the virtual corrections that the virtual photon only interacts with the final-state fermions, it is only straightforward and consistent to claim for our model calculation that only the final-state fermions can emit a real photon. The matrix element, whose corresponding Feynman diagrams are shown in Figure 2.5, reads

$$
\mathcal{M} = \bar{v}(p_2)(\mathrm{i}e\gamma^\mu)u(p_1)\frac{-\mathrm{i}g_{\mu\nu}}{q^2}
$$
$$
\times \bar{u}(p_3)\left[(\mathrm{i}e\gamma^\rho)\mathrm{i}\frac{\slashed{p}_3+\slashed{k}}{(p_3+k)^2}(\mathrm{i}e\gamma^\nu) - (\mathrm{i}e\gamma^\nu)\mathrm{i}\frac{\slashed{p}_4+\slashed{k}}{(p_4+k)^2}(\mathrm{i}e\gamma^\rho)\right]v(p_4)\epsilon^*_\rho(k). \tag{172}
$$

We calculate the cross section with the same strategy as in the previous section by dividing the calculations into a product of an initial-state tensor, which is identical to the initial-state tensor of the LO process, and a final-state tensor. In the case of real emission, it is

$$
f^{\mu\alpha} = \mu^{4-d}e^2\int \mathrm{d}\Gamma_d\,\mathrm{Tr}\left(\slashed{p}_3\left[\gamma^\rho\frac{\slashed{p}_3+\slashed{k}}{(p_3+k)^2}\gamma^\mu - \gamma^\mu\frac{\slashed{p}_4+\slashed{k}}{(p_4+k)^2}\gamma^\rho\right]\right.
$$
$$
\left.\times\slashed{p}_4\left[\gamma^\alpha\frac{\slashed{p}_3+\slashed{k}}{(p_3+k)^2}\gamma_\rho - \gamma_\rho\frac{\slashed{p}_4+\slashed{k}}{(p_4+k)^2}\gamma^\alpha\right]\right). \tag{173}
$$

Like in the other cases, we only need the contraction $f^{\mu\alpha}g_{\mu\alpha}$. After some Dirac algebra involving the modified identities (122), (123) and (124), as well as the identity (153), we arrive at

$$
g_{\mu\alpha}f^{\mu\alpha} = -\mu^{4-d}e^2\int \mathrm{d}\Gamma_d\left[2(d-2)^2\left(\frac{p_3k}{p_4k}+\frac{p_4k}{p_3k}\right)+4(d-2)s\frac{p_3p_4}{(p_3k)(p_4k)}\right]
$$
$$
+ (d-4)\times\mathrm{const.} \tag{174}
$$

after taking the traces. Because of our preparatory work on d-dimensional 3-particle phase-space integrals in equation (135), we rewrite the expression in terms of the x variables. We find for the contracted final-state tensor

$$
g^{\mu\alpha}f_{\mu\alpha} = -4e^2(d-2)\mu^{4-d}\int \mathrm{d}\Gamma_d\left[\frac{x_3^2+x_4^2+\frac{d-4}{2}x_5^2}{(1-x_3)(1-x_4)}\right]+(d-4)\times\mathrm{const.} \tag{175}
$$

The constant term vanishes for $d \to 4$, and we are safe to drop it already at this stage of the computation. Combining the leftover term with the integral measure and integrating out x_5 thanks to the delta distribution leads to

$$g^{\mu\alpha} f_{\mu\alpha} = -4e^2 \mu^{4-d} \left(\frac{s}{4\pi}\right)^{d-4} \frac{(d-2)s}{32\pi^3 \Gamma(d-2)}$$
$$\times \int_0^1 \mathrm{d}x_4 \int_{1-x_4}^1 \mathrm{d}x_3 \left[\frac{x_3^2 + x_4^2 + \frac{d-4}{2}(2-x_3-x_4)^2}{(1-x_3)^{3-d/2}(1-x_4)^{3-d/2}(-1+x_3+x_4)^{2-d/2}}\right]. \tag{176}$$

In this form, we realise that singularities arise for $d \leq 4$ at the upper bounds of integration in both x_3- or x_4-integrals. Physically, these regions correspond to the emission of a low-energetic photon or a photon collinear to one of the outgoing fermions. Let us investigate the case $x_3 \to 1$ to prove this statement:

$$1 - x_3 = \frac{q^2 - 2p_3 q}{q^2} = \frac{2p_4 k}{q^2} = \frac{2E_4 E_\gamma (1 - \cos\theta)}{q^2}, \tag{177}$$

where E_γ is the energy of the photon and θ is the angle between photon and particle 4. In the limit $x_3 \to 1$, either the photon has to be very soft, $E_\gamma = 0$, or the particles are collinear to each other, $\theta = 0$. According to these cases, the singularity is called a soft, collinear or soft-collinear singularity because a particle can become soft and collinear at the same time. We explicitly mention that the case $E_4 = 0$ is forbidden. It contradicts our assumption of being in the high-energy limit, in which we are allowed to set $p_4^2 = 0$, which we implicitly used to derive this result. In practice, we avoid the emission of low-energy fermions (outside of jets) with our event selection criteria (see Section 4.2).

Like in the case of the IR-divergent virtual contribution, the integration converges in more than four space-time dimensions. We hence set $d = 4 - 2\varepsilon_{\mathrm{IR}}$ with the limit $\varepsilon_{\mathrm{IR}} \to 0^-$ and drop the subscript. Unfortunately, the evaluation of the integral itself is very intricate since we have to deal with various hypergeometric functions. It does also not lead to further physical insights. We had to perform the integral, then follow the steps as in equation (160) to connect it to the initial-state tensor (which is identical in this NLO and LO process) and use equation (155) to merge it to a result for the cross section. Instead, we quote the result from [76] and rewrite it in our convention:

$$\sigma_{\mathrm{real}} = \frac{e^6}{16\pi^3 s} \mu^{2\varepsilon} \left(\frac{4\pi\mu^2}{s}\right)^{2\varepsilon} \frac{1-\varepsilon}{3-2\varepsilon}(1-2\varepsilon)\left[(\varepsilon-1)^2 + 1\right] \frac{\Gamma^2(-\varepsilon)\Gamma(2-\varepsilon)}{\Gamma(2-2\varepsilon)\Gamma(3-3\varepsilon)} \tag{178}$$

$$= \sigma_{\mathrm{LO}} \frac{3e^2}{4\pi^2} \mu^{2\varepsilon} \left(\frac{4\pi\mu^2}{s}\right)^{2\varepsilon} \frac{1-\varepsilon}{3-2\varepsilon}(1-2\varepsilon)\left[(\varepsilon-1)^2 + 1\right] \frac{\Gamma^2(-\varepsilon)\Gamma(2-\varepsilon)}{\Gamma(2-2\varepsilon)\Gamma(3-3\varepsilon)}. \tag{179}$$

We exhibit a double pole at $\varepsilon = 0$ due to the term $\Gamma^2(-\varepsilon)$ as for the IR-divergent virtual contribution.

Other real contributions   There are two other real emission contributions apart from squaring the final-state emission: the initial-state emission squared and the interference between those two processes. It can be shown that these three contributions do not influence each other's singularity structure: Suppose electron and muon coupled with two unrelated charges Q_{e} and Q_μ. The final-state loop is a process of $\mathcal{O}\left(Q_{\mathrm{e}} Q_\mu^3\right)$, which is interfered with the LO diagram of $\mathcal{O}\left(Q_{\mathrm{e}} Q_\mu\right)$. The only real correction leading to a cross section of the same order is obtained by squaring the final-state radiation diagrams of $\mathcal{O}\left(Q_{\mathrm{e}} Q_\mu^2\right)$. Similarly, the virtual box diagrams interfered with LO diagrams ($\mathcal{O}\left(Q_{\mathrm{e}}^2 Q_\mu^2\right) \times \mathcal{O}\left(Q_{\mathrm{e}} Q_\mu\right)$) are intertwined with the interference of initial- and final-state radiation ($\mathcal{O}\left(Q_{\mathrm{e}}^2 Q_\mu\right) \times \mathcal{O}\left(Q_{\mathrm{e}} Q_\mu^2\right)$) and the analogous statement is true for initial-state radiations. We are able to handle those contributions with the same strategies as the final-final contribution.

The emission of a soft or collinear particle is a necessary condition for the appearance of an IR singularity at the Feynman diagram level, but not a sufficient one. In our exemplary process, there is only the possibility of a photon emission from an external line. We have explicitly shown that the right-hand diagram of Figure 2.5 became singular under soft or collinear photon emission. This corresponded to the appearance of a singularity in the fermion propagator

$$\frac{-\mathrm{i}(\not{p}_4 - \not{k})}{(p_4 + k)^2} = \frac{-\mathrm{i}q^2(\not{p}_4 - \not{k})}{1 - x_3} \tag{180}$$

of equation (172), which has the same factor in its denominator as the problematic integral (176). However, suppose there is a more complicated process, and we attach an additional external photon to a propagator that scatters off or decays into hard particles. In that case, there is *no* singularity because the propagating particle is off-shell.

If an initial-state particle emits a photon, there is a singularity also connected to the propagator going on-shell. This happens when the photon is soft, as is in the case of final-state emission, or when the photon becomes collinear to the *incoming* particle.

2.2.4   Handling the singularities

A theory is only useful if it can predict measurable finite quantities. The last two sections, however, give the impression as if the opposite was the case in quantum field theory. Actually, this is not the case. Infinities at intermediate steps are not problematic as long as they cancel out in the final result. As we already discussed, the Gamma functions lead to single and/or double poles, and we receive contributions proportional to ε^{-2}, ε^{-1}, ε^0 and higher powers that vanish in taking the limit of $\varepsilon \to 0$. In the UV-divergent parts of the amplitude there were only single poles, whereas the IR-divergent parts also showed double poles. The omnipresent term $\mu^{2\varepsilon}$ is an artefact and will later drop out, whereas the equally omnipresent similar term $(4\pi\mu^2/s)^{2\varepsilon}$ plays a major role due to its dependence on s. We perform a series expansion in ε to the second power to investigate its influence due to interplay with the different poles:

$$\left(\frac{4\pi\mu^2}{s}\right)^{2\varepsilon} = 1 + 2\varepsilon \ln\left(\frac{4\pi\mu^2}{s}\right) + 2\varepsilon^2 \ln^2\left(\frac{4\pi\mu^2}{s}\right) + \mathcal{O}\left(\varepsilon^3\right). \tag{181}$$

In the case of a single pole, multiplying out the terms results in a constant single pole, logarithms of $4\pi\mu^2/s$ with a finite coefficient and constant finite terms. The squared logarithmic term vanishes. Like in the case of a potential, where we cannot measure the absolute values but only differences, the poles cancel each other when we calculate differences of quantities. In the logarithmic term, the dependence on the arbitrarily introduced parameter μ^2 cancels even when comparing quantities at different scales s because of $\ln(\mu^2/s_1) - \ln(\mu^2/s_2) = \ln(s_2/s_1)$. Hence, the single poles from UV divergences are good to handle, and we get rid of them by a procedure called renormalisation.

In contrast, if there is a double pole, like in the IR-divergent contributions, then the single poles in the final expression are not constant but are accompanied by the logarithmic term. Furthermore the squared logarithms survive and the parameter μ^2 does not cancel, since $\ln^2(\mu^2/s_1) - \ln^2(\mu^2/s_2) \neq \ln^2(s_2/s_1)$. Especially we are not able to renormalise these double poles and have to take care of them differently. Luckily, they vanish due to the Block–Nordsieck [79] and Kinoshita–Lee–Nauenberg theorems [80, 81].

Renormalisation   To handle the UV singularities, we use the concept of renormalisation. The core of this concept is very old and already used in classical electrodynamics when Dirac encountered a divergent integral leading to an infinite electron mass [82]. The idea is to view the quantities that appear in the fundamental physical objects as the Lagrangian, not as the observed quantities, but as some "bare" parameters. These bare parameters are infinitely large

themselves, but they have the correct properties to cancel out the divergent terms from higher-order perturbation theory. When adding the divergent integral quantities to the bare results, we arrive at a finite value. We will not go through the complete procedure of renormalisation, which would include the computation of propagator loops, but consider rewriting all bare parameters in the Lagrangian in terms of renormalised quantities and some renormalisation factor

$$\psi = \sqrt{Z_\psi}\psi_{\mathrm{R}}, \qquad A^\mu = \sqrt{Z_A}A_{\mathrm{R}}^\mu, \qquad e = Z_e e_{\mathrm{R}}. \tag{182}$$

Then, we can write

$$\mathcal{L} = e\bar{\psi}\slashed{A}\psi + \cdots = Z_\psi\sqrt{Z_A}Z_e e_{\mathrm{R}}\bar{\psi}_{\mathrm{R}}\slashed{A}_{\mathrm{R}}\psi_{\mathrm{R}} + \cdots = (1+\delta)e_{\mathrm{R}}\bar{\psi}_{\mathrm{R}}\slashed{A}_{\mathrm{R}}\psi_{\mathrm{R}} + \ldots, \tag{183}$$

where we shift the singular behaviour to δ. In our renormalised theory, there are two interaction terms in the Lagrangian, namely the well-known part $e_{\mathrm{R}}\bar{\psi}_{\mathrm{R}}\slashed{A}_{\mathrm{R}}\psi_{\mathrm{R}}$, which leads to the usual Feynman rules and the above infinities, and a new term $\delta e_{\mathrm{R}}\bar{\psi}_{\mathrm{R}}\slashed{A}_{\mathrm{R}}\psi_{\mathrm{R}}$. In terms of Feynman diagrams, the new term also corresponds to a vertex, and the Feynman rule for the vertex factor is just $\mathrm{i}e_{\mathrm{R}}\delta\gamma^\mu$, multiplying the conventional vertex factor by (the number) δ. At NLO, we can state for the matrix element (still assuming only a final-state triangle loop):

$$\mathcal{M}_{\mathrm{R}} = \bar{v}(p_2)(\mathrm{i}e_{\mathrm{R}}\gamma^\mu)u(p_1)\frac{-\mathrm{i}g_{\mu\nu}}{q^2}\bar{u}(p_3)(\mathrm{i}e_{\mathrm{R}}(\Gamma^\nu + \delta\gamma^\nu))v(p_4), \tag{184}$$

which has to be a finite quantity (we conveniently drop the index R hereafter).

However, there is a problem. This procedure only specifies that $\delta\gamma^\nu$ has to include the same divergent parts as Γ^ν, but it does not state anything about the finite parts of δ. This is done by a so-called renormalisation scheme. Let us first introduce the on-shell scheme, in which we recover the LO vertex factor in the low-energy limit without quantum corrections. This is a physical scheme which states that the electron charge at low energies is e. It imposes the renormalisation condition

$$\mathrm{i}e\,\Gamma^\nu|_{s=0} = \mathrm{i}e\gamma^\nu. \tag{185}$$

We do not focus on the finite part, but we may calculate the divergent part by referring to equation (145) for the unrenormalised one-loop vertex correction and set $s=0$ to obtain

$$-2e^2\frac{(2-d)^2}{d}\mu^{4-d}\gamma^\nu\int_0^1 \mathrm{d}x\mathrm{d}y\mathrm{d}z\delta(x+y+z-1)\int\frac{\mathrm{d}\Omega_d}{(2\pi)^d}\int\mathrm{d}k\,k^{d-5} + \delta^{\mathrm{OS}}\gamma^\nu = \gamma^\nu. \tag{186}$$

On the left-hand side, the k-integral is one of the scaleless integrals mentioned above. It does not converge in any dimension, because it diverges both in the IR and the UV region, but we can still calculate it using dimensional regularisation by splitting the integration region at some arbitrary point a:

$$\int_0^\infty \mathrm{d}k\,k^{d-5} = \int_0^a \mathrm{d}k\,k^{d-5} + \int_a^\infty \mathrm{d}k\,k^{d-5} = \int_0^a \mathrm{d}k\,k^{-1-2\varepsilon_{\mathrm{IR}}} + \int_a^\infty \mathrm{d}k\,k^{-1-2\varepsilon_{\mathrm{UV}}}$$

$$= -\frac{1}{2}\left(\frac{a^{-2\varepsilon_{\mathrm{IR}}}}{\varepsilon_{\mathrm{IR}}} - \frac{a^{-2\varepsilon_{\mathrm{UV}}}}{\varepsilon_{\mathrm{UV}}}\right) = -\frac{1}{2}\left(\frac{1}{\varepsilon_{\mathrm{UV}}} - \frac{1}{\varepsilon_{\mathrm{IR}}}\right) + \mathcal{O}\left(\varepsilon_{\mathrm{UV}}, \varepsilon_{\mathrm{IR}}\right). \tag{187}$$

It can be shown that these scaleless integrals vanish in dimensional regularisation [83]. This implies $\varepsilon_{\mathrm{UV}} = \varepsilon_{\mathrm{IR}}$, which is only allowed if we analytically continue the regions of convergence of our integrals that are only defined for $\varepsilon_{\mathrm{UV}} > 0, \varepsilon_{\mathrm{IR}} < 0$. Then, it is not possible to differentiate between the origin of the singularities any more. Inserting a zero in form of $\int \mathrm{d}k\,k^{d-5}$ shifts the $\varepsilon_{\mathrm{UV}}^{-1}$ poles to $\varepsilon_{\mathrm{IR}}^{-1}$ poles. However, we still maintain the different εs carefully for identifying the UV-divergent and the IR-divergent parts of the virtual cross section. These hidden IR singularities do not occur in other regularisation schemes. For a treatment with a finite photon mass regulator, where a $1/\varepsilon$ divergence corresponds to a $\log M_\gamma^2/s$, see, for example, [47] or [76]).

The integration of the Feynman parameters in (186) is trivial using equation (147), since they disappeared from the inner integral, and the expression for the solid angle is given in (129). We end up with

$$\frac{e^2}{16\pi^2}\left(\frac{(4\pi\mu^2)^{\varepsilon_{\mathrm{UV}}}}{\varepsilon_{\mathrm{UV}}}-\frac{(4\pi\mu^2)^{\varepsilon_{\mathrm{IR}}}}{\varepsilon_{\mathrm{IR}}}\right)+\delta^{\mathrm{OS}}(1+\mathcal{O}\left(\varepsilon_{\mathrm{UV}},\varepsilon_{\mathrm{IR}}\right))=1. \tag{188}$$

Solving for δ^{OS} results in

$$\delta^{\mathrm{OS}}=-\frac{e^2}{16\pi^2}\left(\frac{1}{\varepsilon_{\mathrm{UV}}}-\frac{1}{\varepsilon_{\mathrm{IR}}}\right)+\mathcal{O}\left(1\right). \tag{189}$$

In the course of this thesis and our computations, we use a different renormalisation scheme, which is called the modified minimal subtraction ($\overline{\mathrm{MS}}$) scheme. Preparatory, we introduce the minimal subtraction (MS) scheme, which simply *defines* the finite part of δ to be zero [84, 85], giving

$$\delta^{\mathrm{MS}}=-\frac{e^2}{16\pi^2}\left(\frac{1}{\varepsilon_{\mathrm{UV}}}-\frac{1}{\varepsilon_{\mathrm{IR}}}\right). \tag{190}$$

The divergent part is identical in all renormalisation schemes. Let us calculate the renormalised version of the formerly UV-divergent part of the virtual cross section. We start with appropriately modifying equation (164) to

$$\Gamma_{\mathrm{R}}^{\nu}=\Gamma^{\nu}+\delta\gamma^{\nu}=(g+\delta)\gamma^{\nu}\quad\Rightarrow\quad\mathcal{M}_{\mathrm{R,virt}}=(g+\delta)\mathcal{M}_{\mathrm{LO}}, \tag{191}$$

subsequently leading to

$$\sigma_{\mathrm{R,virt}}=2\operatorname{Re}(g+\delta)\sigma_{\mathrm{LO}}^{d}. \tag{192}$$

To simplify calculations, we insert a zero up to $\mathcal{O}\left(\varepsilon\right)$ into the counter term leading to the form

$$\delta^{\mathrm{MS}}=-\frac{e^2}{16\pi^2}\left[\left(\frac{4\pi\mu^2}{s}\right)^{\varepsilon_{\mathrm{UV}}}\frac{1}{\varepsilon_{\mathrm{UV}}}-\left(\frac{4\pi\mu^2}{s}\right)^{\varepsilon_{\mathrm{IR}}}\frac{1}{\varepsilon_{\mathrm{IR}}}\right]+\mathcal{O}\left(\varepsilon_{\mathrm{UV}},\varepsilon_{\mathrm{IR}}\right). \tag{193}$$

The finite terms of $\mathcal{O}\left(1\right)$ cancel each other in this expression. We then add the counter term to (168) and expand partially in $\varepsilon_{\mathrm{UV}}$ to obtain

$$\sigma_{\mathrm{R,virt}}^{\mathrm{UV\text{-}div}}=\sigma_{\mathrm{LO}}^{d}\frac{e^2}{8\pi^2}\left[\left(\frac{4\pi\mu^2}{s}\right)^{\varepsilon_{\mathrm{UV}}}(1-\gamma_{\mathrm{E}})+\left(\frac{4\pi\mu^2}{s}\right)^{\varepsilon_{\mathrm{IR}}}\frac{1}{\varepsilon_{\mathrm{IR}}}\right], \tag{194}$$

where γ_{E} is the Euler–Mascheroni constant. Its appearance is a remnant of Taylor expanding the Gamma function ($\Gamma(\varepsilon)=\varepsilon^{-1}-\gamma_{\mathrm{E}}+\mathcal{O}\left(\varepsilon\right)$).

By carefully retaining the different εs, we revealed the IR singularity in the UV-divergent part of the virtual cross section. The formerly UV-divergent virtual cross section is UV-finite after renormalisation because it contains no poles in $\varepsilon_{\mathrm{UV}}$ any more. Although the LO cross section in d dimensions is still ε-dependent, it is finite and we can take the limit $\varepsilon_{\mathrm{UV}}\to0^+$ in $\sigma_{\mathrm{R,virt}}^{\mathrm{UV\text{-}div}}$. This leads to

$$\sigma_{\mathrm{virt}}^{\mathrm{UV}}=\lim_{\varepsilon_{\mathrm{UV}}\to0^+}\sigma_{\mathrm{LO}}^{d}\frac{e^2}{8\pi^2}\left(\frac{4\pi\mu^2}{s}\right)^{\varepsilon_{\mathrm{UV}}}(1-\gamma_{\mathrm{E}})=\frac{e^2}{8\pi^2}(1-\gamma_{\mathrm{E}})\sigma_{\mathrm{LO}}. \tag{195}$$

A more common renormalisation scheme than the MS scheme is the $\overline{\mathrm{MS}}$ scheme. This scheme is based on the observation that the appearance of the Euler–Mascheroni constant serves no physical purpose. In fact, the γ_{E} in $\sigma_{\mathrm{virt}}^{\mathrm{UV}}$ will cancel against terms from the IR-divergent part of the virtual cross section and the real emission cross section. Furthermore, the 4π are an

omnipresent constant that originated from dimensionally regularising the integrand. $\overline{\text{MS}}$ removes both of them by a redefinition

$$\mu_{\text{MS}}^2 \to \mu_{\overline{\text{MS}}}^2 = 4\pi e^{-\gamma_{\text{E}}} \mu_{\text{MS}}^2. \tag{196}$$

In contrast to the on-shell scheme, neither the MS scheme nor the $\overline{\text{MS}}$ scheme are physical. They do not take care of the appearance of the parameter μ which we introduced way back as an arbitrary renormalisation scale without any physical meaning and μ_{MS} might appear in the final expressions. This may seem very concerning and sets up the stage for the renormalisation group equations, which we will not discuss here since this is a large topic which could fill entire books on its own and also has applications in solid-state physics. In the end, all observables must not depend on the renormalisation scale. Actually, each order of perturbation theory introduces new dependencies on μ_{MS}, but after summing up all orders, the dependence on μ_{MS} vanishes, and it is a major task to find a sensible scale at finite-order calculations [86, 87].

Bloch–Nordsieck and Kinoshita–Lee–Nauenberg theorems   The Bloch–Nordsieck theorem (for QED) and the (more general) Kinoshita–Lee–Nauenberg theorem state that physical predictions in the SM are IR-finite to all perturbative orders. Whilst the Bloch–Nordsieck theorem states that it is sufficient to sum over all possible final-state photons (if the electron is massive), the Kinoshita–Lee–Nauenberg theorem also requires summation over all degenerate initial states. This includes processes in which more than two particles scatter off each other. We are not going to prove or motivate the theorems here, but we show that the Bloch–Nordsieck theorem holds for our example case. Let us collect all leftover IR-divergent terms, which are the UV-finite part of the virtual cross section before renormalisation (171), the revealed IR singularity in the UV-divergent part in the second term of (194) and the real contribution of (179). We start with partially expanding (171) in ε:

$$\sigma_{\text{virt}}^{\text{UV-fin}} = \sigma_{\text{LO}} \frac{3e^2}{2\pi^2} \mu^{2\varepsilon} \left(\frac{4\pi\mu^2}{s}\right)^{2\varepsilon} \left[-\frac{1}{6\varepsilon^2} + \frac{3\gamma_{\text{E}} - 4}{9\varepsilon} + \frac{1}{108}\left(-131 + 96\gamma_{\text{E}} - 36\gamma_{\text{E}}^2 + 15\pi^2\right)\right]. \tag{197}$$

We do the same with the revealed IR singularity of (194) taking the d-dimensional LO cross section into account:

$$\sigma_{\text{virt}}^{\text{hidden IR}} = \sigma_{\text{LO}} \frac{e^2}{8\pi^2} \mu^{2\varepsilon} \left(\frac{4\pi\mu^2}{s}\right)^{2\varepsilon} \left[\frac{1}{\varepsilon} + \frac{2 - 3\gamma_{\text{E}}}{3}\right]. \tag{198}$$

Finally, we expand (179):

$$\sigma_{\text{real}} = \sigma_{\text{LO}} \frac{3e^2}{2\pi^2} \mu^{2\varepsilon} \left(\frac{4\pi\mu^2}{s}\right)^{2\varepsilon} \left[\frac{1}{6\varepsilon^2} + \frac{13 - 12\gamma_{\text{E}}}{36\varepsilon} + \frac{1}{216}\left(259 - 156\gamma_{\text{E}} + 72\gamma_{\text{E}}^2 - 30\pi^2\right)\right]. \tag{199}$$

Adding up all three contributions, all poles cancel. The result for the sum of all IR-divergent parts is finite and we can take the limit $\varepsilon \to 0^-$:

$$\sigma_{\text{real+virt}}^{\text{IR}} = \sigma_{\text{LO}} \frac{e^2}{8\pi^2} \mu^{2\varepsilon} \left(\frac{4\pi\mu^2}{s}\right)^{2\varepsilon} \left(\gamma_{\text{E}} + \frac{1}{2}\right) \to \sigma_{\text{LO}} \frac{e^2}{8\pi^2} \left(\gamma_{\text{E}} + \frac{1}{2}\right). \tag{200}$$

We explicitly mention that the Bloch–Nordsieck theorem is only valid for QED, not for the GWS theory with a spontaneously broken symmetry [88–90]. Although the divergences stemming from the massless photon as gauge boson of the residual $U(1)$ symmetry are cancelled, the terms of $\log^2 M_{\text{W}}^2/s$ survive. Although this is a general property, it is especially the case when we do not perform a fully inclusive study with radiated final-state W and Z bosons. These surviving terms are called Sudakov double logarithms.

NLO cross section   To calculate the renormalised NLO correction, we are only left with adding up the different parts from (195) and (200):

$$\sigma_{\text{real+virt}} = \sigma_{\text{virt}}^{\text{UV}} + \sigma_{\text{real+virt}}^{\text{IR}} = \frac{3e^2}{16}\sigma_{\text{LO}}. \tag{201}$$

Parton distribution functions and factorisation   In the context of the initial-state radiations, which we only briefly touched on here, we encounter collinear singularities that are regulated by the electron mass and lead to terms proportional to $\ln q^2/m_{\text{e}}^2$. Although they can become arbitrarily large, the electron mass may save our example process in QED. However, in QCD, gluons can be radiated off gluons and no mass term regulates the singularity. The phenomenon of singularities arising from particles collinear to the initial-state particle has to be interpreted differently than particles collinearly accompanying a final-state particle.

If we imagine two protons instead of an electron-positron pair as initial-state particles, the solution is obvious: A proton is a complicated bound state, and at high energies $q^2 \gg m_{\text{p}}^2$, the scattering process takes place between two constituting partons of the protons instead of the composite object. The residuals of the protons keep flying in the same direction. Similarly, one can imagine the electron in an NLO scattering process as a bound state of an electron-parton and a bundle of photons.

In general, such processes can be factorised as

$$\text{d}\sigma(p_1, p_2) = \sum_{i,j} \int \text{d}x_1 \text{d}x_2\, f_i(x_1)f_j(x_2)\, \text{d}\hat{\sigma}_{ij}(x_1 p_1, x_2 p_2), \tag{202}$$

where f_i and f_j are the so-called parton distribution functions (PDFs) that determine the possibility of finding a parton i or j inside the composite object and $\hat{\sigma}_{ij}$ is the partonic cross section. In QED, the electron PDFs can be calculated exactly order by order in perturbation theory, and we find for NLO $\text{e}^+\text{e}^- \to \mu^+\mu^-(+\gamma)$ scattering [91]

$$\text{d}\hat{\sigma}^{(0)} = \text{d}\sigma^{(0)} \tag{203}$$

$$\text{d}\hat{\sigma}^{(1)} = \text{d}\sigma^{(1)} - \left[\int \text{d}x_1 f_{\text{e}}^{(1)}(x_1)\text{d}\hat{\sigma}^{(0)}(x_1 p_1, p_2) + \int \text{d}x_2 f_{\text{e}}^{(1)}(x_2)\text{d}\hat{\sigma}^{(0)}(p_1, x_2 p_2)\right], \tag{204}$$

where a superscript (0) stands for the LO quantity and a (1) denotes the NLO correction. The expression (204) has the structure of a bare term plus a counter term that is able to cover all possible singularities. In fact, the mass singularities of initial-state QED radiation can be absorbed into the PDFs. For further information on electron PDFs, we refer to the cited source material.

In QCD, the PDFs already become relevant at LO because they are not able to be integrated out like in the QED case, where we know the initial condition $f_{\text{e}}^{(0)}(x) = \delta(1-x)$: At LO, an electron-particle consists of one electron-parton and it carries all of the momentum, but we do not know the constituents of the proton (except its valence quarks). The PDFs of a proton are quantities to be determined by measurement. They factorise the hard partonic scattering process off the soft, non-perturbative QCD stuff that happens when the proton breaks apart into its partons. Similar to the QED case, the singular behaviour can be absorbed by the PDFs, but additionally, we have to introduce an arbitrary mass parameter to regulate the collinear divergence. This parameter is called the factorisation scale μ_{F}. It is the energy scale at which we separate the hard from the soft process. Since it is non-physical like the renormalisation scale, the true physical cross section summed over all orders of perturbation theory is independent of the factorisation scale. At fixed order, however, there is a dependence on μ_{F}. Like in the case of the renormalisation scale, from which the renormalisation-group equations follow, there are differential equations that govern the evolution of the PDFs in dependence on the factorisation scale, the DGLAP equations [92–94].

2.2.5 The Catani–Seymour dipole formalism

As we have seen in the previous sections, the NLO calculations in perturbation theory can be performed analytically. However, the complexity of their computation, in addition to the sheer number of diagrams to consider, grows very fast with the number of external legs. A full computation for more complicated processes than simple examples is almost impossible. A much more effective way is the use of Monte Carlo methods to integrate cross sections numerically. In the first place, we need a program, which returns us the matrix element evaluated for a specific combination of initial- and final-state momenta, after which we discretely sum over all generated events, which lie in a specified region of the phase space. Unfortunately, such a program would always return nonsensical results when we make it analyse radiative corrections because, at some point, it will run into a singular region. A numerical integrator cannot know that the badly behaving real IR divergences cancel exactly against the bad behaviour from the virtual process with a different particle content *after* integration.

The Catani–Seymour (CS) dipole formalism [95, 96] (and its generalisation for QED by Dittmaier [97]) solves this problem. Its general idea is to introduce a counter term (not to be confused with the UV-regulating counter terms) for the real emission cross section at the phase-space point level:

$$\sigma^{\mathrm{NLO}} = \sigma^{\mathrm{virt}} + \sigma^{\mathrm{real}} = \int_n \mathrm{d}\sigma_{\mathrm{virt}} + \int_{n+1} \mathrm{d}\sigma_{\mathrm{real}} \tag{205}$$

$$= \int_n \left(\mathrm{d}\sigma_{\mathrm{virt}} + \int_1 \mathrm{d}\sigma_{\mathrm{C}} \right) + \int_{n+1} \left(\mathrm{d}\sigma_{\mathrm{real}} - \mathrm{d}\sigma_{\mathrm{C}} \right). \tag{206}$$

The idea behind the dipole formalism is to factorise the singular behaviour out of the $(n+1)$-particle matrix element

$$|\mathcal{M}_{n+1}(p_i, p_j, p_k, p_1, \ldots, p_{n+1})|^2 \to |\tilde{\mathcal{M}}_n(\tilde{p}_{ij}, \tilde{p}_k, p_1, \ldots, p_n)|^2 \otimes V_{ij,k}, \tag{207}$$

where the particles i and j are a pair of emitter and soft or collinear emitted particles, and k is a third so-called spectator particle. The crucial point of the dipole formalism is the factorisation in such a manner that the divergent parts are a process-independent expression, called the CS dipoles $V_{ij,k}$. The dipoles are convoluted with a process-dependent LO matrix element $\tilde{\mathcal{M}}_n$ with modified particle momenta $\tilde{p}_{ij}$ and $\tilde{p}_k$. This LO matrix element is called the reduced matrix element, and all quantities that are subject to the projection on the reduced n-particle phase space are denoted with a tilde. There are multiple dipoles to take care of each singular region, and their indices signal the combination of emitting, emitted and spectating particles. With this reasoning, we can write

$$\sigma^{\mathrm{NLO}} = \int_{n+1} \left[\mathrm{d}\sigma_{\mathrm{real}} - \sum_{i,j,k} \mathrm{d}\tilde{\sigma}_{\mathrm{LO}} \otimes V_{ij,k} \right] + \int_n \left[\mathrm{d}\sigma_{\mathrm{virt}} + \sum_{i,j,k} \mathrm{d}\tilde{\sigma}_{\mathrm{LO}} \otimes \int_1 \mathrm{d}V_{ij,k} \right] \tag{208}$$

$$\equiv \int_{n+1} \left[\mathrm{d}\sigma_{\mathrm{real}} - \sum_{i,j,k} \frac{\mathrm{d}\tilde{\Gamma}_{n+1}}{2\tilde{s}} D_{ij,k} \right] + \int_n \left[\mathrm{d}\sigma_{\mathrm{virt}} + \sum_{i,j,k} \frac{\mathrm{d}\tilde{\Gamma}_n}{2\tilde{s}} \mathcal{V}_{ij,k} \right]. \tag{209}$$

$\mathrm{d}\tilde{\Gamma}$ is the reduced phase space element. With this notation, we absorbed the convolution of the matrix elements and the dipoles into

$$D_{ij,k} = |\tilde{\mathcal{M}}_n|^2 \otimes V_{ij,k} \quad \text{and} \quad \mathcal{V}_{ij,k} = |\tilde{\mathcal{M}}_n|^2 \otimes \int_1 \mathrm{d}V_{ij,k}, \tag{210}$$

while we factored out the phase-space integration and the prefactor including the centre-of-mass energy of the reduced matrix element $\tilde{s}$ for converting the matrix element into the cross section. We define the convolution operator $\otimes$ such that any spin- and charge/colour-correlation is included into the convolution and not into the dipole $V_{ij,k}$. In the n-particle matrix element, the

momenta of the splitting particle (ij) and the spectator k get modified in a way such that both particles remain on-shell and overall momentum conservation is secured:

$$\tilde{p}_{ij}^2 = 0, \quad \tilde{p}_k^2 = 0, \qquad \tilde{p}_{ij} + \tilde{p}_k = p_i + p_j + p_k. \tag{211}$$
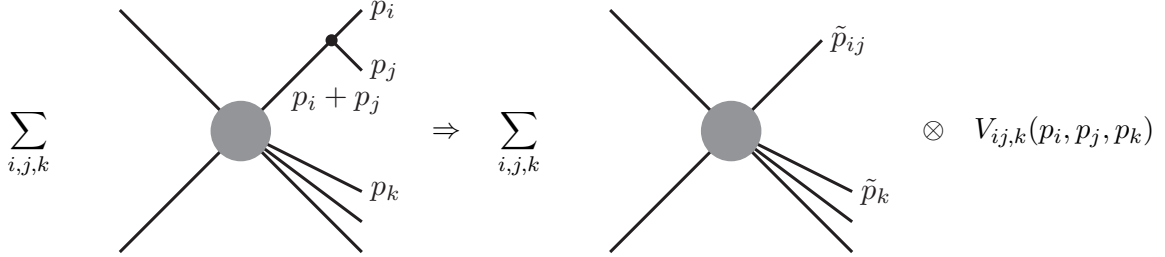
We show the concept pictorially in Figure 2.6.

Figure 2.6: Pictorial description of the CS dipole formalism. Note that the splitting can also occur in the initial state, as well as the spectator particle k can be an initial-state particle. The big grey blob denotes any kind of tree-level interaction. The factor $V_{ij,k}$ is independent of the type of interaction and depends only on the momenta and the types of particles i and j. There are different dipoles for initial- and final-state emission as well as initial- and final-state spectators.

In the course of this thesis, we cannot prove the existence of such universal dipole quantities nor write down all of them. The sheer amount of formulas – we need all kinds of possible massless three-particle splittings, the formalism differs within initial- and final-state emission, initial- and final-state spectators, and we need both the non-integrated and the integrated version – goes beyond the scope. We will hence stick exemplarily to our model process $e^+e^- \to \mu^+\mu^-\gamma$ with final-state photon emission in this section for a conceptual example and come back to the formalism in Section 3.2.3 and Section 3.2.4 when we discuss problems that arise in the implementation for W^+W^- scattering.

Therefore, let us introduce the dipole contributions for the final-state emitter, final-state spectator quark to quark-photon splitting. The convolution operator $\otimes$ reduces in the QED case to a simple multiplication operator containing the charge correlation [97],

$$|\tilde{\mathcal{M}}_n|^2 \otimes V_{ij,k} = |\tilde{\mathcal{M}}_n|^2 \frac{Q_i Q_k}{Q_i^2} V_{ij,k}. \tag{212}$$

With the appropriate dipole factor [95], this leads to

$$\sum_{k \neq i,j} D_{ij,k} = |\tilde{\mathcal{M}}_n|^2 \sum_{k \neq i,j} \frac{Q_i Q_k}{Q_i^2} V_{ij,k} \tag{213}$$

$$= \frac{1}{2p_i p_j} |\tilde{\mathcal{M}}_n|^2 \sum_{k \neq i,j} 2e^2 \mu^{2\varepsilon} \left[\frac{2}{1 - \tilde{z}_i(1 - y_{ij,k})} - (1 + \tilde{z}) - \varepsilon(1 - \tilde{z}_i) \right], \tag{214}$$

where

$$y_{ij,k} = \frac{p_i p_j}{p_i p_j + p_j p_k + p_k p_i} \quad \text{and} \quad \tilde{z}_i = \frac{p_i p_k}{p_j p_k + p_i p_k}. \tag{215}$$

Let us just investigate the soft limit as proof of concept, which is obtained by taking

$$p_j^\mu = \lambda p_\gamma^\mu, \quad \lambda \to 0 \tag{216}$$

and more simple than the collinear one. In this limit, the spin-summed dipole contribution reduces to

$$\sum_{k \neq i,j} D_{ij,k} = \frac{1}{\lambda^2} e^2 \mu^{2\varepsilon} |\tilde{\mathcal{M}}_n|^2 \frac{s}{(p_i p_\gamma)(p_j p_\gamma)} + \mathcal{O}(1).$$ (217)

Since we can ignore the initial-state contributions, we recall the final-state contribution of the LO matrix element from equation (161). In the following, we do not carry out the phase-space integration since we are only interested in the integrand – the squared matrix element –, leading to

$$\int_n d\tilde{\Gamma} \, |\tilde{\mathcal{M}}_n|^2 \sim g^{\mu\alpha} f_{\mu\alpha}^{\mathrm{LO}} = \int_n d\tilde{\Gamma} \left(-2(d-2)s\right),$$ (218)

and

$$\int_{n+1} d\tilde{\Gamma} \sum_{k \neq i,j} D_{ij,k} \sim \int_{n+1} d\tilde{\Gamma} \left(-2(d-2)\frac{1}{\lambda^2} e^2 \mu^{2\varepsilon} \frac{s^2}{(p_i p_\gamma)(p_j p_\gamma)}\right) + \mathcal{O}(1).$$ (219)

On the other hand, we recall the expression for the real matrix element from equation (174). Only the second term of the integrand is singular in the soft limit, leading to,

$$\int_{n+1} d\Gamma |\mathcal{M}_{n+1}|^2 \sim g^{\mu\alpha} f_{\mu\alpha}^{\mathrm{real}} = -\mu^{4-d} e^2 \int_{n+1} d\Gamma_d \left[4(d-2)s \frac{p_i p_k}{(p_i p_j)(p_k p_j)}\right] + \mathcal{O}(1)$$

$$= \int_{n+1} d\Gamma \left(-\frac{1}{\lambda^2} 2e^2(d-2)\mu^{2\varepsilon} \frac{s^2}{(p_i p_\gamma)(p_k p_\gamma)}\right) + \mathcal{O}(1)$$ (220)

with $d = 4 - 2\varepsilon$ and $2p_i p_k \to s$ in the soft limit.[13] The universal dipole splitting function, in combination with the process-dependent LO matrix element summing over all possible emitter-spectator pairs, perfectly mimics the emission of a soft photon. The difference of the real and the dipole contribution is hence free of soft singularities in $d = 4$ dimensions.

The integrated dipole contribution is [95]

$$\sum_{i,j,k} \frac{d\tilde{\Gamma}_n}{2\tilde{s}} \mathcal{V}_{ij,k} = \sum_{i,j,k} \frac{d\tilde{\Gamma}_n}{2\tilde{s}} |\tilde{\mathcal{M}}_n|^2 \frac{e^2}{8\pi^2} \left(\frac{4\pi\mu^2}{s}\right)^\varepsilon \frac{\Gamma^2(1-\varepsilon)}{\Gamma(1-3\varepsilon)} \left(\frac{1}{\varepsilon^2} + \frac{1}{\varepsilon} \frac{3+\varepsilon}{2(1-3\varepsilon)}\right)$$ (221)

$$= \frac{d\tilde{\Gamma}_n}{2\tilde{s}} |\tilde{\mathcal{M}}_n|^2 \frac{e^2}{4\pi^2} \left(\frac{4\pi\mu^2}{\tilde{s}}\right)^\varepsilon \left(\frac{1}{\varepsilon^2} + \frac{3-2\gamma_{\mathrm{E}}}{2\varepsilon} + \mathcal{O}(1)\right).$$ (222)

The summation yields a factor of 2 because there are two different configurations of emitter and spectator.

We compare this to the IR-divergent part of the virtual cross section. Since $\sigma_{\mathrm{virt}} = 2\,\mathrm{Re}(g + \delta)\sigma_{\mathrm{LO}}^d$ (c. f. (192)), we write down the expanded form of the one-loop vertex correction factor g of equation (150) combined with the IR-divergent part of the counter term from equation (190):

$$\sigma_{\mathrm{virt}}^{\mathrm{IR}} = 2\,\mathrm{Re}(g^{\mathrm{IR}} + \delta^{\mathrm{IR}}) \int \frac{d\Gamma_n}{2s} |\mathcal{M}_n|^2 = -\int \frac{d\Gamma_n}{2s} |\mathcal{M}_n|^2 \frac{e^2}{4\pi^2} \left(\frac{4\pi\mu^2}{s}\right)^\varepsilon \left[\frac{1}{\varepsilon^2} + \frac{3-2\gamma_{\mathrm{E}}}{2\varepsilon} + \mathcal{O}(1)\right].$$ (223)

As we see, the divergent terms cancel when adding the integrated dipole contribution to the virtual cross section.

---

[13]We explicitly note, to avoid confusion, that momentum k in equation (174) refers to the photon, which is the emitted particle j and not the spectating particle k in this context.

2.2.6   Excursus: anomaly cancellation and eigenvalues of Y

For a small excursus, we come back to the eigenvalues of the electric charge and weak hypercharge operators, which we introduced ad hoc in Table 2.2. In that chapter, we realised that there exists a relation $Q = T^3 + Y$ between the electric charge, the third component of the weak isospin and the weak hypercharge. While the values of the weak isospins of different particles in the weak isospin doublets are – up to rescaling – uniquely determined by the different eigenvalues of the $SU(2)$ group, and a $SU(2)$ singlet has no weak isospin, this is not the case for the weak hypercharge, which can a priori take arbitrary values. In this chapter, we are going to investigate, by NLO calculations, why the assignment of weak hypercharges (and subsequently electric charges) follows some constraints in nature.

Quantum field theories can suffer from anomalies, which means that a symmetry of the classical theory, to which the LO calculation corresponds, is spoiled by quantum effects. The $SU(2)_\mathrm{L}$ is a chiral symmetry that is connected to an anomaly at the one-loop level. In the GWS theory, there are corrections to triple vector couplings at the one-loop level by inserting a fermion triangle loop to the vertex, but let us start for simplicity with an Abelian theory and generalise our results. We constructed the GWS Lagrangian (68) such that it is invariant under the transformations

$$\psi \to \psi' = e^{\mathrm{i}\alpha}\psi \quad \text{and} \quad \psi \to \psi' = e^{\mathrm{i}\beta\gamma^5}\psi, \tag{224}$$

which leads according to Noether's theorem to the two conserved quantities

$$j_\mathrm{V}^\mu = \bar\psi\gamma^\mu\psi \quad \text{and} \quad j_\mathrm{A}^\mu = \bar\psi\gamma^\mu\gamma^5\psi. \tag{225}$$

In a quantum theory, we expect that the Ward identity for a gauge boson that couples to such a current holds.
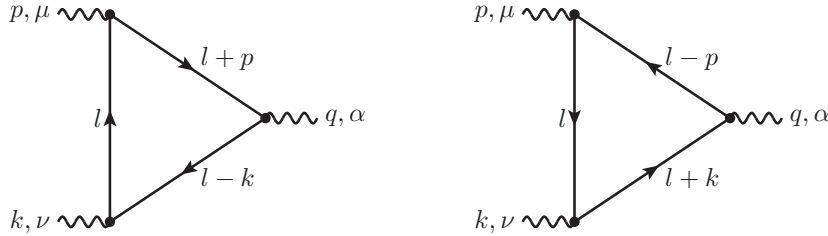
Figure 2.7: Triangle diagrams

We now consider a one-loop diagram, in which we have one axial vector coupling proportional to $\gamma^\alpha\gamma^5$ and two vector couplings proportional to γ^μ, γ^ν. Because of the closed fermion loop, we get a factor of -1 and have to take the trace, and the amputated matrix element, where we strip off the polarisation vectors, reads

$$\mathcal{M}^{\alpha\mu\nu} = g^3 \int \frac{\mathrm{d}^4 l}{(2\pi)^4} \gamma^\alpha\gamma^5 \frac{\slashed{l}+\slashed{p}}{(l+p)^2}\gamma^\mu\frac{\slashed{l}}{l^2}\gamma^\nu\frac{\slashed{l}-\slashed{k}}{(l-k)^2} + \{p,\mu \leftrightarrow k,\nu\}. \tag{226}$$

We show the corresponding Feynman diagrams in Figure 2.7. Let us now contract this matrix element with the corresponding momenta of the vector bosons. After some calculation, we find

$$q_\alpha\mathcal{M}^{\alpha\mu\nu} = 4\mathrm{i}\varepsilon^{\mu\nu\rho\sigma}\int \frac{\mathrm{d}^4 l}{(2\pi)^4}\left[\frac{l^\rho k^\sigma}{l^2(l+k)^2} + \frac{l^\rho p^\sigma}{l^2(l-p)^2}\right] + \{p,\mu \leftrightarrow k,\nu\}, \tag{227}$$

$$p_\mu\mathcal{M}^{\alpha\mu\nu} = -4\mathrm{i}\varepsilon^{\alpha\nu\rho\sigma}\int \frac{\mathrm{d}^4 l}{(2\pi)^4}\left[\frac{(l-p)^\rho(l+k)^\sigma}{(l-p)^2(l+k)^2} - \frac{(l-k)^\rho(l+p)^\sigma}{(l-k)^2(l+p)^2}\right]. \tag{228}$$

Note that the diagram on the right-hand side of Figure 2.7 is obtained from the diagram on the left-hand side by pairwise replacement of $p,\mu \leftrightarrow k,\nu$, leading to the symmetric expressions in (227). This symmetry is broken by contracting with p_μ in (228).

The first integral (227), connected to the axial current, is pretty simple because all terms depend only either on p or k. Since $\mathcal{M}$ must be a true Lorentz tensor and the only vector around in each summand is either p or k, the contraction must have the structure $q_\alpha \mathcal{M}^{\alpha\mu\nu} = \varepsilon^{\mu\nu\rho\sigma}(a_1 k^\rho k^\sigma + a_2 p^\rho p^\sigma) = 0$ because we contract a symmetric object with the totally antisymmetric Levi–Civita symbol.

In the second integral (228), connected to the vector current, we would like to regulate the divergence. The problem is that many regularisation procedures spoil current conservation and the Ward identity we want to prove here, and we cannot just use dimensional regularisation because, in this case, we would have to cautiously handle γ^5, which we have only properly defined in $d = 4$ dimensions. Nevertheless, it seems as if we had a loophole when we shift $l \to l' = l - \frac{p}{2} + \frac{k}{2}$ in the first and $l \to l'' = l - \frac{k}{2} + \frac{p}{2}$ in the second term. Under such a shift, the denominators stay finite, and the first integrand becomes

$$\frac{l'^\rho l'^\sigma - \frac{(p+k)^\rho}{2} l'^\sigma + l'^\rho \frac{(p+k)^\sigma}{2} - \frac{(p+k)^\rho}{2} \frac{(p+k)^\sigma}{2}}{\left(l'^2 + \frac{(p+k)^2}{4}\right)^2}. \tag{229}$$

The second one is similar. In this expression, the first and the last term become zero because of the contraction with the Levi–Civita symbol already before integration. The other ones vanish by symmetry arguments: There are only odd powers of l in the numerator after the shift and only even powers of l in the denominator, making the whole expression odd, which we integrate over a symmetrical region.

However, splitting the two divergent terms, freely manipulating the integration variables in different ways and meshing them somehow together, since the end justifies the means and we know which result to expect, feels more than hand-waving. Instead, we have to handle the terms in a mathematically proper way. In fact, there is a simple prescription, how to deal with linearly divergent integrals under a shift of the integration variable: We start with the shift mentioned above and throw away those terms that vanish due to the contraction with $\varepsilon^{\alpha\nu\rho\sigma}$. The terms linear in l' can be combined since they are antisymmetric in ρ and σ. The result is a function of the type

$$\Delta^{\rho\sigma} = \int \frac{\mathrm{d}^4 l}{(2\pi)^4} \left(f^{\rho\sigma}(l') - f^{\rho\sigma}(l' - a)\right) \tag{230}$$

with

$$f^{\rho\sigma}(l') = \frac{l'^\rho (p+k)^\sigma}{\left(l'^2 + \frac{(p+k)^2}{4}\right)^2} \quad \text{and} \quad a = p - k. \tag{231}$$

Wick-rotate the momentum (giving a factor of i) and Taylor-expand in a. Since all terms of order $l'^\rho l'^\sigma / l^4$ will vanish due to the contraction with the epsilon tensor, we can truncate the Taylor series at the first order. Afterwards, we use Gauss's theorem to rewrite the integral as surface integral evaluated at $l' \to \infty$. Hence

$$\Delta^{\rho\sigma} = \mathrm{i} \int \frac{\mathrm{d}^4 l}{(2\pi)^4} a^\mu \frac{\partial}{\partial l^\mu} f^{\rho\sigma} = \mathrm{i} a^\mu \int \frac{\mathrm{d}\Omega_4}{(2\pi)^4} \lim_{l \to \infty} l^2 l_\mu f^{\rho\sigma}. \tag{232}$$

Inserting $f^{\rho\sigma}$ and a^μ, we find with $l_\mu l^\rho = \frac{1}{4} l^2 g_\mu^\rho$ and $\int \mathrm{d}\Omega_4 = 2\pi^2$:

$$q_\alpha \mathcal{M}^{\alpha\mu\nu} = \frac{1}{4\pi^2} \varepsilon^{\mu\nu\rho\sigma} p^\rho k^\sigma \neq 0 \quad \text{and} \quad p_\mu \mathcal{M}^{\alpha\mu\nu} = k_\nu \mathcal{M}^{\alpha\mu\nu} = 0. \tag{233}$$

This result states that there is a Ward identity for the vector currents but not for the axial currents.

The existence of this anomaly at the loop level has a severe impact on the theory: If there is a conserved charge, then there has to be an exact local gauge symmetry and vice versa. This

gauge symmetry is (in the case of Abelian gauge theories) always accompanied by the Ward identity. What we have shown here is that one-loop corrections may spoil the Ward identity and, thus, the symmetry. So far we only investigated the vector and axial vector currents of a $U(1)$ symmetry. For the GWS theory in the unbroken phase, we can check whether we obtain such an anomaly by generalising our procedure to arbitrary gauge theories. This is done quite easily: At each vertex, a theory based on Lie groups picks up a factor of the generator T^a, which can be stripped off from the rest of the calculation. We can split this into the symmetric and the antisymmetric part

$$\text{Tr}(T^a T^b T^c) = \frac{1}{2}\text{Tr}([T^a, T^b]T^c) + \frac{1}{2}\text{Tr}(\{T^a, T^b\}T^c) = \mathrm{i}\frac{1}{2}T_R f^{abc} + \frac{1}{4}A_R d^{abc}. \qquad (234)$$

With the last equality, we further separated the two traces into a representation-dependent part T_R and A_R as well as an independent part f^{abc} and d^{abc}. T_R is called the index of the representation, and A_R is the anomaly coefficient. f^{abc} is the totally antisymmetric structure constant and d^{abc} is the totally symmetric anomaly constant. It is normalised such that $d^{abc} = 2\,\text{Tr}(\{T^a, T^b\}T^c)$ normalising $A_{\text{fund}} = 1$. The term proportional to the structure constant f^{abc} can be absorbed into a counter term if it is divergent since the triple gauge boson vertex is also proportional to f^{abc}. As its name suggests, the interesting term in this context is therefore the anomaly coefficient.

We also have to consider that there is more than one fermion that can flow through the loop. Left- and right-handed fermions contribute with a different sign because of the different sign in front of the γ^5 in the projection operator. In very generality, it can be shown that

$$q^\alpha j_\alpha^a \sim \left(\sum_{\text{left}} A_R d^{abc} - \sum_{\text{right}} A_R d^{abc} \right) \varepsilon^{\mu\nu\rho\sigma} F_{\mu\nu}^b F_{\rho\sigma}^c, \qquad (235)$$

in which j^α should be a conserved current. This is called the Adler–Bell–Jackiw anomaly [98, 99]. A non-chiral theory, where left- and right-handed particles transform in the same representation and have the same quantum numbers, is always anomaly free. This is especially the case for massive fermions, since the Dirac equation couples left- and right-handed fermions and forces them to have the same quantum numbers. QCD is also non-chiral and we do not have to worry about $SU(3)_c^3$ anomalies, when all three boson coupling to the fermion triangle are $SU(3)$ bosons. Since $\{T^a, T^b\} \sim \delta^{ab}$ for $SU(2)$ and $\text{Tr}(T^a) = 0$ for any $SU(N)$, a possible $SU(2)^3$ anomaly vanishes. Furthermore, any "mixed" anomaly with only one $SU(N)$ generator vanishes due to the tracelessness.

We are left with the combinations $SU(N)^2 U(1)$ and $U(1)^3$.[14] Hence, there are three non-trivial constraints within the SM and an additional one if we include gravitation. We summarise them in Table 2.3 [76, 102].

There are two sets of real solutions for these four nonlinear equations with six variables, parametrised by two arbitrary real numbers a and b. The first one is

$$Y_L = -\frac{a}{2} - b, \; Y_e = -a - b, \; Y_\nu = -b, \; Y_Q = \frac{a}{6} + \frac{b}{3}, \; Y_u = \frac{2a}{3} + \frac{b}{3}, \; Y_d = -\frac{a}{3} + \frac{b}{3}; \qquad (236)$$

the second one is

$$Y_Q = Y_L = 0, \; Y_u = a, \; Y_d = -a, \; Y_e = b, \; Y_\nu = -b. \qquad (237)$$

---

[14]This statement seems to be at odds with Furry's theorem [100, 101]; any graph containing a closed loop with only external photons vanishes if the number of photons, undoubtedly $U(1)$ gauge bosons, is odd. Furry's theorem, however, is only valid for *Dirac* fermions, not *Weyl* fermions, since it relies on $U(1)$ charge conjugation. For Weyl fermions, ψ_{L} and ψ_{R} are two independent quantities with a priori different quantum numbers (and in fact, the weak hypercharges of SM left- and right-handed fields differ).

Gauge groups	Constraint
$U(1)_Y^3$	$(2Y_L^3 - Y_e^3 - Y_\nu^3) + 3(2Y_Q^3 - Y_u^3 - Y_d^3) = 0$
$SU(3)_c^2 U(1)_Y$	$2Y_Q - Y_u - Y_d = 0$
$SU(2)_L^2 U(1)_Y$	$Y_L + 3Y_Q = 0$
$\text{gravity}^2 U(1)_Y$	$(2Y_L - Y_e - Y_\nu) + 3(2Y_Q - Y_u - Y_d) = 0$

Table 2.3: SM constraints on the weak hypercharge of particles. The subscripts L and Q denote left-handed leptons and quarks, the subscripts u, d, e and ν denote right-handed quarks of up- or down-type and right-handed electrons and neutrinos. There is a factor of 2 in front of the doublets since they contain two kinds of fermions and a factor of 3 in front of the quarks because of three different colours. Note that the factors of Y are emerging from the $U(1)$ generators in the anomaly constant d^{abc}.

Since we do not observe right-handed neutrinos that couple to the B field in nature, we have the constraint $Y_\nu = 0$ and must set $b = 0$ in both solutions.[15] The second solution would then describe a world in which only right-handed quarks would couple to the B field, which is also not what we observe. The leftover solution, with $a = 1$ as arbitrary normalisation, that can be absorbed by a redefinition of g', as mentioned above, is

$$Y_L = -\frac{1}{2}, \ Y_e = -1, \ Y_\nu = 0, \ Y_Q = \frac{1}{6}, \ Y_u = \frac{2}{3}, \ Y_d = -\frac{1}{3}, \tag{238}$$

in accordance with the electric charges that we know and with the values that we have stated in Table 2.2. Although we derived this result in perturbation theory via a one-loop calculation, it can be shown that it is a non-perturbative result, i. e. higher order corrections do not change it [103]. In other words, we have shown that the GWS theory, as it is realised in nature, is anomaly free. It is additionally the only anomaly-free solution in a world without right-handed neutrinos and all other particles having non-zero hypercharges.

---

[15]We add that the parameter choice $a = 0, b = 1$ leads to the solution

$$Y_Q = Y_u = Y_d = \tfrac{1}{3}, \quad Y_L = Y_e = Y_\nu = -1,$$

which are the baryon and lepton numbers. Although theoretically possible, we do not observe such an X boson converting quarks into leptons.

3   W$^+$W$^-$ scattering

Our objective in this thesis is the investigation of vector boson scattering. VBS is, as its name already tells, a process in which two (EW) vector bosons interact with each other and produce two outgoing vector bosons. The expression "W$^+$W$^-$ scattering" may, however, be slightly misleading since the W do not refer to incoming, but outgoing particles. In other words, we would like to investigate the process $VV \to$ W$^+$W$^-$, where V are two arbitrary vector bosons. All possible underlying Feynman diagrams at LO are shown in Figure 3.1.
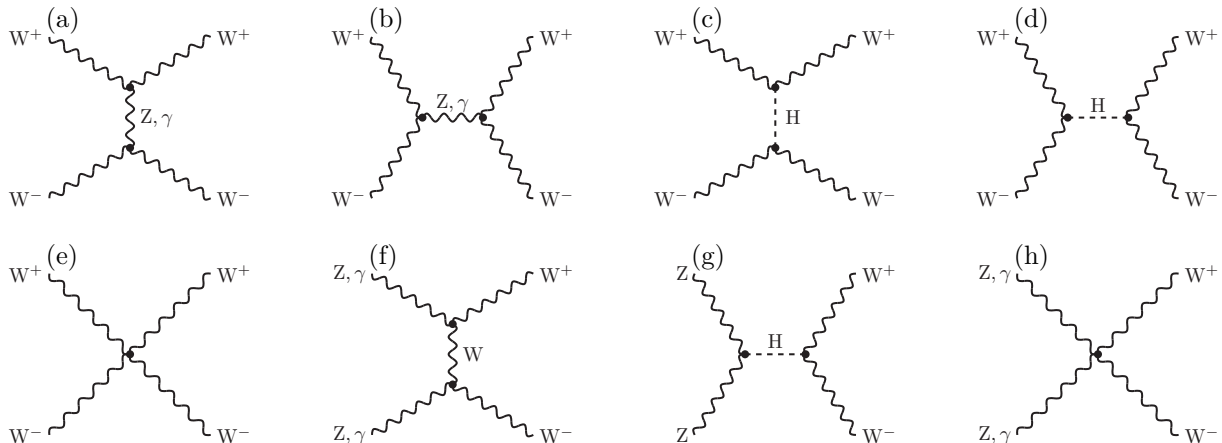
Figure 3.1: Feynman diagrams for the VBS subprocess VV $\to$ W$^+$W$^-$. Note that subfigures (a) and (b) encode two different diagrams, and subfigures (f) and (h) are three different ones.

As we already motivated in our small example in Section 2.1.7, there are *s*- and *t*-channel Z-, γ- and H-exchanges as well as the quartic term for the process W$^+$W$^- \to$ W$^+$W$^-$. Furthermore, there are neutral initial states ZZ, Zγ, $\gamma\gamma \to$ W$^+$W$^-$. All of them are featured by *t*-channel W-exchange and the quartic term; in the case of the ZZ initial state, there is additionally *s*-channel H exchange.

Alas, W bosons are unstable short-lived particles, and we can neither simply put them into a storage ring nor measure their properties in a particle detector. Hence we are faced with a more complicated process, in which the W bosons only appear as virtual particles and other diagrams than the ones above contribute as well.

3.1   Description of the process

The complete process we investigate is

$$\text{pp} \to \text{e}^+ \nu_\text{e} \mu^- \bar{\nu}_\mu \text{jj} + X. \tag{239}$$

We obtain this process out of the pure $VV \to$ W$^+$W$^-$ subprocess by the following considerations: At first, we need something to collide. Although processes in lepton colliders are theoretically much easier to describe, the colliders themselves are much more difficult to construct.[16] We therefore use an existing proton–proton collider. Protons are, however, a bound state, and in the hard scattering process, only two of their constituent partons interact. Since each of the partons has to emit a virtual vector boson and go out of the process again, they are seen in the detector as jets. When calculating the cross sections, we calculate it for each (physically allowed) combination of partons in the initial state and each combination of partons forming the final state jets separately and call this a partonic channel. We require two jets to avoid

---

[16]Because of synchrotron radiation, it is almost impossible to accelerate leptons to high energies comparable to the LHC. The most powerful accelerator so far was LEP with $\sqrt{s} = 209$ GeV [104]. For a planned linear lepton collider with $\sqrt{s} = 250$ GeV, see [105].

contamination with processes, in which a single jet is emitted. The outgoing Ws are decaying either hadronically or into lepton-neutrino pairs. If one or both of them decay hadronically, then we see more jets in the detector, but this final state is again contaminated with other processes as background. Therefore we restrict ourselves to a process with two oppositely charged leptons of different generations in the final state. In that case, it becomes more likely that these are decay products of two W-bosons, especially since the different generations exclude Z-decay or photon-splitting. The two corresponding neutrinos are not separately detectable and manifest themselves as missing transverse momentum in the event. We will abbreviate the leptonic content as 4ℓ in the following. At last, NLO corrections can produce additional photons or jets, which we denote by the X.

Although we may call this complete process still W^+W^- scattering and carefully choose a signal final state, there are lots of other processes which contribute to the same final state. Some of the underlying Feynman diagrams do not even include the presence of two W bosons. In some partonic channels, there are Feynman diagrams with VBS subprocesses appearing alongside background processes, which makes it impossible to separate the "signal" in theoretical calculations in a gauge-invariant way, and some other partonic channels are pure background.

There is, however, a separable background contribution, which we mention explicitly in some detail: $t\bar{t}$ production. As its name suggests, in this kind of process, a $t\bar{t}$ pair is, most likely via QCD processes, produced. Top quarks decay into a bottom quark and a lepton-neutrino pair of a specific generation approximately in $1/9$ of the cases [106]; hence leading in about 1% of the events to the same final-state signal as W^+W^- scattering. This background contribution is overwhelmingly large. Although using much more inclusive event selection criteria than we do (cf. Section 4.2), ATLAS measured the $t\bar{t}$ cross section to be $826\,\mathrm{pb}$ (sic!) [107]. Typical VBS cross sections, including the backgrounds, are at the one-digit femtobarn level, i. e. five orders of magnitude smaller, and we do not expect that applying even the harsh VBS cuts on $t\bar{t}$ production will have an influence drastic enough to curtail the background.

A method to get rid of all $t\bar{t}$ events is vetoing all events with a b-jet. From an experimental standpoint, this requires the b-tagging to work with 100% accuracy. Furthermore, we may also neglect contributions from initial-state bottom quarks: With the assumption of a diagonal CKM matrix, the only bottom quark induced processes consist of a $b\bar{b}$ annihilation, since there must not be any leftover bottom quarks in the final-state. These contributions are not only suppressed by our experimental setups but they are also double-suppressed by the PDFs. A rough estimate for the cross section $b\bar{b} \to 4\ell u\bar{u}$ yielded a contribution of few parts-per-billion compared to the total cross section at all orders.

In the following subsections, we have a closer look at the substructure of our process.

3.1.1   Leading order

Processes of four different orders in the coupling constants α and α_s contribute to the process (239) at leading order: $\mathcal{O}\left(\alpha^6\right)$, $\mathcal{O}\left(\alpha_\mathrm{s}\alpha^5\right)$ and $\mathcal{O}\left(\alpha_\mathrm{s}^2\alpha^4\right)$ are tree-level contributions; and the underlying Feynman diagrams are of $\mathcal{O}\left(g^6\right)$, $\mathcal{O}\left(g_\mathrm{s}g^5\right)$ and $\mathcal{O}\left(g_\mathrm{s}^2g^4\right)$. The orders $\mathcal{O}\left(\alpha^6\right)$ and $\mathcal{O}\left(\alpha_\mathrm{s}^2\alpha^4\right)$ can only be constructed out of diagrams of the orders $\mathcal{O}\left(g^6\right)$ or $\mathcal{O}\left(g_\mathrm{s}^2g^4\right)$ respectively, and we call them EW and QCD-induced contribution. The process of $\mathcal{O}\left(\alpha_\mathrm{s}\alpha^5\right)$ consists mainly of interfering EW and QCD-induced Feynman diagrams, and we call it the interference contribution for simplicity. However, there are also partonic channels, which are featured by diagrams of $\mathcal{O}\left(g_\mathrm{s}g^5\right)$. The last ingredient is the loop-induced contribution of $\mathcal{O}\left(\alpha_\mathrm{s}^4\alpha^4\right)$.

The electroweak process, $\mathcal{O}\left(\alpha^6\right)$ Ignoring the b-quarks, there are 60 different quark- and four photon-induced partonic channels contributing to the EW process of $\mathcal{O}\left(\alpha^6\right)$. There are four main categories of quark-induced Feynman diagrams which appear at tree-level of $\mathcal{O}\left(g^6\right)$:

- **VBS $\mathbf{ZZ \to W^+W^-}$ and $\gamma\gamma \to \mathbf{W^+W^-}$:** This is a part of our signal VBS process, which we explained above. There are two quark lines connecting the initial and final state, which

both emit a Z-boson or a photon in the *t*-channel. The Z-bosons or photons scatter off each other and emit *s*-channel W-bosons. In a partonic channel able to show these types of Feynman diagrams, there must be a quark of the same generation and the same weak isospin in the final state for each quark in the initial state since the emitted Z-bosons or photons neither changes generation nor weak isospin. As already stated above, the VBS subprocess is richer in Feynman diagrams in the case of Z-bosons than in the case of photons since we then also have *s*- and *t*-channel Higgs boson exchanges. Nevertheless, we abbreviate this type with ZZ $\rightarrow$ W$^+$W$^-$ hereafter. An example diagram is given in Figure 3.2 (a).

- **VBS W$^+$W$^-$ $\rightarrow$ W$^+$W$^-$:** Also part of the signal, the quark lines emit a W boson each. In contrast to ZZ $\rightarrow$ W$^+$W$^-$, the W changes the weak isospin, but, since we assume a diagonal CKM matrix, not the generation. Hence there must be a quark of the same generation and different weak isospin in the final state for each quark in the initial state. We present an example in Figure 3.2 (b).

- **WWW production:** This type is part of the irreducible EW background. In contrast to to signal, the quark lines connect only initial- or final-state particles. Three W bosons are emitted in the *s*-channel which then decay to the final-state particles. This especially means that the two final-state jets are also produced via *s*-channel boson exchange. We hence need a quark-antiquark pair of the same generation but different weak isospin in both initial and final state, but the generations of initial- and final-state quarks may differ. Figure 3.2 (c) serves as an example.

- **WWZ production:** This is the analogue of WWW production, but in addition to the two leptonically decaying W bosons a hadronically decaying Z boson (or photon) is emitted. The two quark-antiquark pairs in the initial and the final state must hence have identical generation and weak isospin each. We show such a case in Figure 3.2 (d).

In some partonic channels, the quark content fulfils multiple criteria. There are, for example, processes in which both ZZ $\rightarrow$ W$^+$W$^-$ and W$^-$W$^+$ $\rightarrow$ W$^+$W$^-$ scattering occur. An overview of the combinations of the different types with an exemplary channel each and the number of partonic channels falling into these combinations is given in Table 3.1. We explicitly state that each of our partonic channels falls in some of the above categories, i. e. there are no channels which show neither VBS nor triple vector boson production (3VP).

Apart from these main categories, there are miscellaneous background processes. Double vector boson production (WW production) is a background which appears in all partonic channels, exemplarily shown in Figure 3.2 (e). Depending on the partonic channel, there are more types of diagrams which we will not classify any further (see for few examples Figure 3.2 (f) – (h)).

The photon-induced channels are a minor background, and we expect them not to contribute in a sizeable manner. The $\mathcal{O}\left(g^6\right)$ Feynman diagrams need two photons in the initial state and are hence double PDF-suppressed. Although there are a variety of diagrams, of which one is shown in Figure 3.2 (i), we will not discuss them in detail. Further examples of Feynman diagram structures of $\mathcal{O}\left(g^6\right)$ (without explicit particle labels) can be inferred from Figure 3.15.

With all of these process types, W$^+$W$^-$ scattering offers a full spectrum of EW physics already at LO. There are triple and quartic gauge boson couplings in all partonic channels, and the Higgs boson is present in all quark-induced channels.

The QCD-induced process, $\mathcal{O}\left(\alpha_s^2\alpha^4\right)$ Since none of the QCD-induced processes is featured by VBS or 3VP, it makes no sense to classify the partonic channels of $\mathcal{O}\left(\alpha_s^2\alpha^4\right)$ in the same way as those of $\mathcal{O}\left(\alpha^6\right)$. Instead, we chose to divide the quark-induced processes after the appearing Mandelstam variable in the gluon propagator.

- **s-channel g exchange:** Requirement for an *s*-channel gluon exchange is the existence of a quark-antiquark-pair of the same generation in both the initial and the final state.
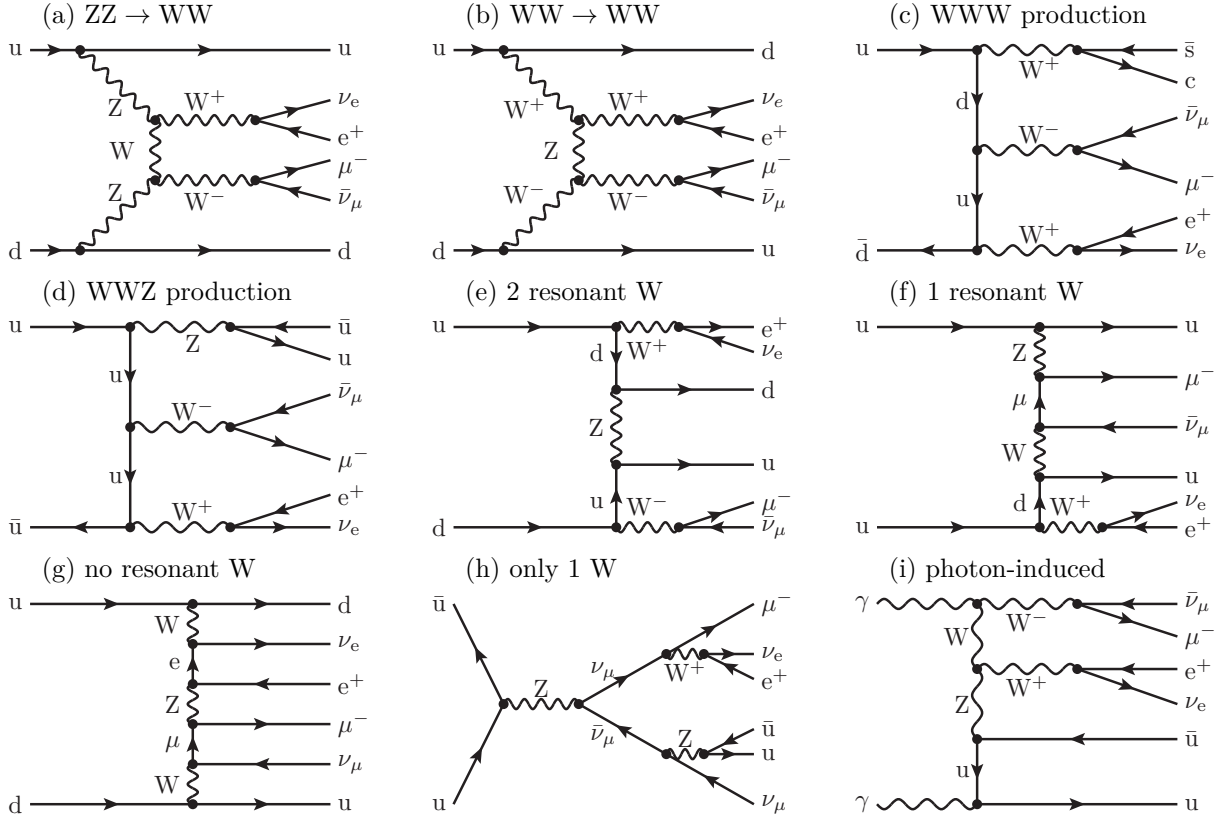
Figure 3.2: Examples of Feynman diagrams of $\mathcal{O}\left(g^6\right)$. Diagrams (a) and (b) are part of the signal, and (c) – (i) are EW background.

subtype	exemplary channel	# of channels
only ZZ $\to$ W$^+$W$^-$	uu $\to 4\ell$uu	24
only W$^+$W$^-$ $\to$ W$^+$W$^-$	us $\to 4\ell$dc	8
both W$^+$W$^-$/ZZ $\to$ W$^+$W$^-$	ud $\to 4\ell$ud	4
ZZ $\to$ W$^+$W$^-$ and WWW production	u$\bar{\text{d}}$ $\to 4\ell$u$\bar{\text{d}}$	4
ZZ $\to$ W$^+$W$^-$ and WWZ production	u$\bar{\text{u}}$ $\to 4\ell$u$\bar{\text{u}}$	8
only WWW production	u$\bar{\text{d}}$ $\to 4\ell$c$\bar{\text{s}}$	4
only WWZ production	u$\bar{\text{u}}$ $\to 4\ell$c$\bar{\text{c}}$	8
γ-induced	$\gamma\gamma \to 4\ell$u$\bar{\text{u}}$	4

Table 3.1: Categorisation of partonic channels at $\mathcal{O}\left(\alpha^6\right)$ according to appearing subprocesses.

They do not necessarily have to have corresponding weak isospins; in this case, we have to emit one W boson from the initial-state quark line and one from the final-state one. If they have the same weak isospin, however, this can be seen as a QCD-analogue of WWZ production, where the Z-boson is switched with a gluon.

- **t-channel g exchange:** For a t-channel gluon exchange, the quark lines connect initial- and final-state and, since the gluon does not change the generation, for each quark in the initial-state we need a quark of the same generation in the final-state. Since we may emit W bosons either both from the same quark line, not changing the weak isospin, or from different quark lines, the weak isospins of the final-state quarks can be identical or flipped compared to the initial state.

- **u-channel g exchange:** Almost identical to the t-channel exchange, we cross the two quark lines and therefore need two quarks or antiquarks of the same generation, but not a quark-antiquark-pair, in the final-state: If the weak isospins of the quarks are identical, then we may flip the lines after the emission of the W-bosons if they are different, then the number of emitted W-bosons from each quark line changes compared to the corresponding t-channel.

subtype	exemplary channel	# of channels
$4q$, only s-channel g exchange	u$\bar{\text{u}} \to 4\ell$c$\bar{\text{c}}$	12
$4q$, only t-channel g exchange	u$\bar{\text{c}} \to 4\ell$u$\bar{\text{c}}$	24
$4q$, both t- and u-channel g exchange	uu $\to 4\ell$uu	12
$4q$, both s- and t-channel g exchange	u$\bar{\text{u}} \to 4\ell$u$\bar{\text{u}}$	12
$qq \to 4\ell$gg	u$\bar{\text{u}} \to 4\ell$gg	4
g-induced	gg $\to 4\ell$u$\bar{\text{u}}$	12

Table 3.2: Categorisation of partonic channels at $\mathcal{O}\left(\alpha_\text{s}^2\alpha^4\right)$ according to appearing subprocesses.

Like in the case of the EW process, not all of these categories are mutually exclusive. The possible combinations of QCD-induced contributions with an exemplary channel and the number of channels are given in Table 3.2. Exemplary Feynman diagrams are presented in Figure 3.3 (a) and (b).
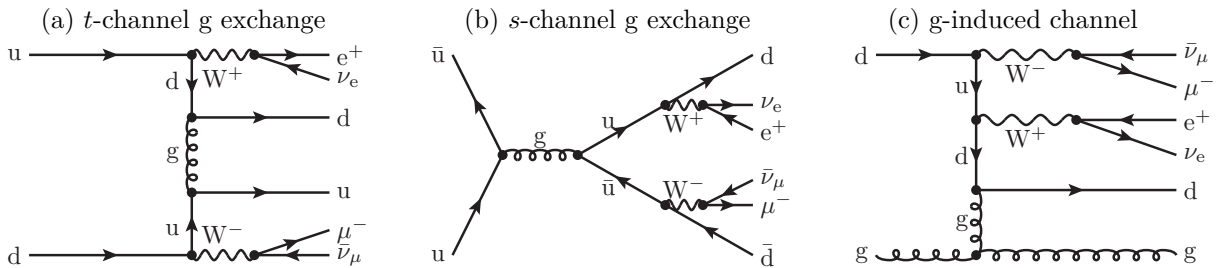
Figure 3.3: Examples of Feynman diagrams of $\mathcal{O}\left(g_\text{s}^2 g^4\right)$.

In contrast to the $\mathcal{O}\left(g^6\right)$ photon-induced channels, in which photons could only appear in the initial state, there are also diagrams of $\mathcal{O}\left(g_\text{s}^2 g^4\right)$ with one gluon in the initial- and the final-state each, which are hence "mixed" gluon-quark-induced channels. At last, there are the purely gluon-induced channels. In cases with two initial–state gluons, there is either an s-channel gluon exchange, accompanied by a triple gluon vertex, or a t-channel quark exchange. We do not classify these channels further and also summarise the mixed channels under the same category as gluon-induced processes. For an example diagram, see Figure 3.3 (c). Furthermore, there is a class of quark-induced channels with two gluons in the final state. These channels are always of the kind $q\bar{q} \to 4\ell$gg and diagrams with all Mandelstam variables contribute: s-channel gluon exchange as well as t- and u-channel quark exchange.

The interference contribution, $\mathcal{O}\left(\alpha_\text{s}\alpha^5\right)$ In the interference contribution, we mainly interfere the diagrams of $\mathcal{O}\left(g^6\right)$ and $\mathcal{O}\left(g_\text{s}^2 g^4\right)$. We may only interfere diagrams with the same particle content, so photon-induced diagrams of $\mathcal{O}\left(g^6\right)$ and the diagrams with external gluons of $\mathcal{O}\left(g_\text{s}^2 g^4\right)$ are not part of this order. Instead, there are additional non-interference partonic channels with Feynman diagrams of $\mathcal{O}\left(g_\text{s}g^5\right)$. All of these have exactly one gluon as an external particle and need a photon in the initial state because of fermion number conservation. We refer to those processes hence as photon-induced contributions. For an example diagram, consider Figure 3.2 (i) with the lower photon replaced by a gluon.

Concerning the purely quark-induced partonic channels, there are, however, fewer combinations possible than in the case of $\mathcal{O}\left(\alpha^6\right)$ or $\mathcal{O}\left(\alpha_s^2\alpha^4\right)$. Since we interfere different diagrams, we have exactly one gluon as an internal particle. As known from the colour algebra – the trace over an odd number of $SU(3)$ generators is zero –, only those contributions survive, in which we can construct a single closed quark line and we thus meet two quark-quark-gluon vertices going along the line. This is only possible if we can combine processes in which the jets are produced via propagators with different Mandelstam variables. Explicitly, this rules out all partonic channels, in which only s-channel or only t-channel gluon exchange occurs, because then the corresponding EW processes also feature only jets that are produced via s- or t-channel. Vice versa, channels with only WWZ or only WWW production are excluded, since all vector bosons in them appear also only in the s-channel.

When we classify the remaining channels, we may use either the same classification as for the EW contributions or the one for the QCD-induced contribution since the diagrams of $\mathcal{O}\left(g^6\right)$ and $\mathcal{O}\left(g_s^2 g^4\right)$ are on equal footing for the interference. However, there is no urgent need to choose in our case, since the interference contribution turns out to be negligible and does not need to be discussed in detail.

3.1.2 Loop-induced contributions

The loop-induced contributions take an exceptional position in our calculation. As their name suggests, there are no tree-level diagrams for partonic channels in this category. Hence, they are not one-loop corrections to some LO diagrams, as we discuss in the next subsection, but LO processes in their own right. However, they are of orders in the coupling constants that are even higher than the NLO corrections. In fact, there are three such loop-induced processes: $\gamma\gamma \to 4\ell gg$ at $\mathcal{O}\left(\alpha_s^2\alpha^6\right)$, $g\gamma \to 4\ell gg$ at $\mathcal{O}\left(\alpha_s^3\alpha^5\right)$ and $gg \to 4\ell gg$ at $\mathcal{O}\left(\alpha_s^4\alpha^4\right)$.

The corresponding Feynman diagrams are of $\mathcal{O}\left(g_s^2 g^6\right)$, $\mathcal{O}\left(g_s^3 g^5\right)$ and $\mathcal{O}\left(g_s^4 g^4\right)$ and are not interfered with tree-level diagrams, but diagrams of the same order. Since the gluons as final-state jets have to couple to some quark to be able to interact indirectly with the leptons, all of them are featured by a closed quark loop. We depict some diagrams for the loop-induced contributions in Figure 3.4.
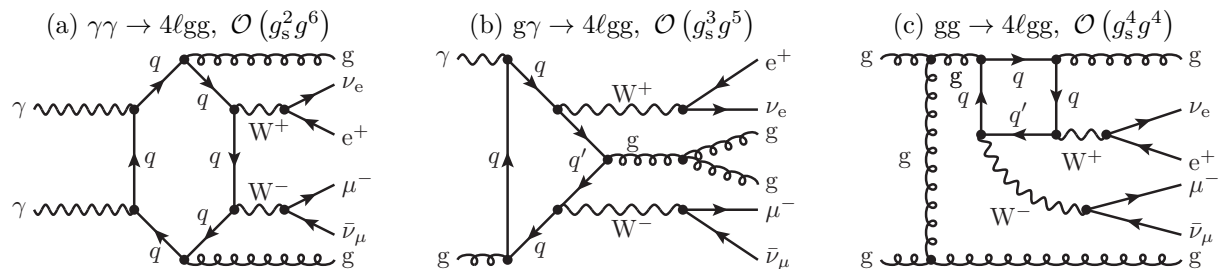
Figure 3.4: Examples of loop-induced Feynman diagrams for each appearing order.

We include especially the process with four external gluons. Although this process is of the same order as NNLO QCD corrections to the QCD-induced process, it is doubly enhanced: Gluons in the initial state have a larger PDF share than quarks and gluons in the final state have a larger colour multiplicity than quarks. Furthermore, assuming $\alpha_s^2 \approx \alpha$, processes of $\mathcal{O}\left(\alpha_s^4\alpha^4\right)$ are by naive power-counting expected to be larger than processes of $\mathcal{O}\left(\alpha^7\right)$, which we include as NLO correction in our calculations.[17]

While the corresponding loop-induced contribution of $\mathcal{O}\left(\alpha_s^3\alpha^5\right)$ is both enhanced by the gluon-PDF and suppressed by the photon-PDF, the $\mathcal{O}\left(\alpha_s^2\alpha^6\right)$ contribution is doubly suppressed. We hence expect their contribution to the cross section to be negligible and calculate them for reasons of completeness.

---

[17]A posteriori, it turned out that the loop-induced contributions are of the same size as the $\mathcal{O}\left(\alpha^7\right)$ corrections. We refer to the results in Table 4.3 and in Table 4.4 for numeric comparison.

In contrast to the LO processes, categorising the loop-induced contributions is futile since there is only one partonic channel per order of coupling constants. In fact, we even summarise all orders of loop-induced contributions into the same category since the process of $\mathcal{O}\left(\alpha_{\mathrm{s}}^4\alpha^4\right)$ is by far the most dominant contribution. In fact, when discussing the numeric results, we abbreviate the complete loop-induced contributions simply as contributions of $\mathcal{O}\left(\alpha_{\mathrm{s}}^4\alpha^4\right)$, unless stated otherwise.

3.1.3 Virtual corrections

As we sketched in Section 2.2.2 with a simple example, the virtual NLO corrections to a process are obtained by interfering tree-level diagrams of a given partonic channel with one-loop diagrams of the same partonic channel. Since a one-loop diagram contains exactly one more internal propagator than a tree-level diagram with the same external particle content, a loop diagram is two orders in the coupling constants g or g_{s} higher than a tree-level diagram for the same process. In our case there are hence loop diagrams of $\mathcal{O}\left(g^8\right)$, $\mathcal{O}\left(g_{\mathrm{s}}g^7\right)$, $\mathcal{O}\left(g_{\mathrm{s}}^2g^6\right)$, $\mathcal{O}\left(g_{\mathrm{s}}^3g^5\right)$ and $\mathcal{O}\left(g_{\mathrm{s}}^4g^4\right)$. Interfering them with the tree-level diagrams of $\mathcal{O}\left(g^6\right)$, $\mathcal{O}\left(g_{\mathrm{s}}g^5\right)$ and $\mathcal{O}\left(g_{\mathrm{s}}^2g^4\right)$ gives rise to contributions of four different orders: $\mathcal{O}\left(\alpha^7\right)$, $\mathcal{O}\left(\alpha_{\mathrm{s}}\alpha^6\right)$, $\mathcal{O}\left(\alpha_{\mathrm{s}}^2\alpha^5\right)$ and $\mathcal{O}\left(\alpha_{\mathrm{s}}^3\alpha^4\right)$.[18]

The diagrams of $\mathcal{O}\left(g^8\right)$ are purely EW corrections. Besides taking a tree-level diagram of $\mathcal{O}\left(g^6\right)$ and simply inserting a photon or a Z boson to connect two charged or weakly interacting particles, there is a plethora of new diagram types. For example, there are also closed fermion loops or more complicated loops involving additional insertions of W bosons. Additionally, there is the possibility to construct additional quartic vertices. We give some example diagrams in Figure 3.5. Interfering the electroweak loops with tree-level diagrams of $\mathcal{O}\left(g^6\right)$ leads to a contribution of $\mathcal{O}\left(\alpha^7\right)$, interfering them with diagrams of $\mathcal{O}\left(g_{\mathrm{s}}^2g^4\right)$ to one of $\mathcal{O}\left(\alpha_{\mathrm{s}}\alpha^6\right)$.
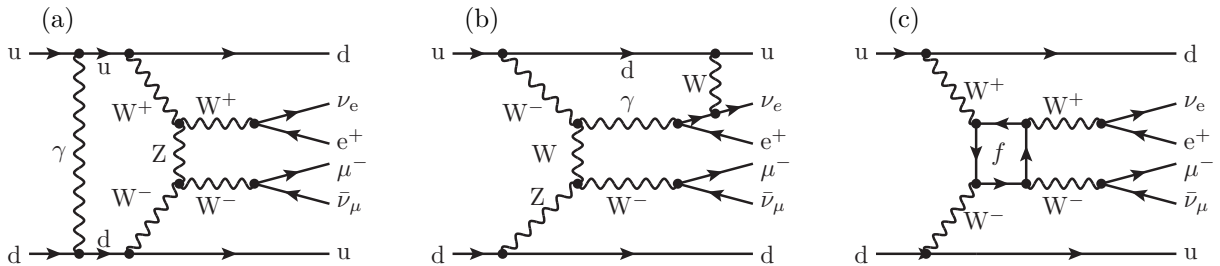
Figure 3.5: Examples of one-loop Feynman diagrams at $\mathcal{O}\left(g^8\right)$.

The diagrams of $\mathcal{O}\left(g_{\mathrm{s}}^4g^4\right)$ are pure QCD corrections to the QCD tree-level diagrams of $\mathcal{O}\left(g_{\mathrm{s}}^2g^4\right)$ like the diagrams of $\mathcal{O}\left(g^8\right)$ are for the electroweak case. The types of new Feynman diagrams are similar to those of $\mathcal{O}\left(g^8\right)$. Of course, we have fewer possibilities to integrate the leptonic part of our process into the new loops. Instead, we have more ways to play around with external gluons and may also include quartic gluon vertices, which are not present in LO diagrams. Example diagrams are shown in Figure 3.6. Combining these diagrams with tree-level diagrams of $\mathcal{O}\left(g^6\right)$ also leads to a contribution of $\mathcal{O}\left(\alpha_{\mathrm{s}}^2\alpha^5\right)$, combining them with such of $\mathcal{O}\left(g_{\mathrm{s}}^2g^4\right)$ leads to one of $\mathcal{O}\left(\alpha_{\mathrm{s}}^3\alpha^4\right)$.

The diagrams of $\mathcal{O}\left(g_{\mathrm{s}}g^7\right)$ and $\mathcal{O}\left(g_{\mathrm{s}}^3g^5\right)$ are those with one external gluon and must be derived from the tree-level diagrams of $\mathcal{O}\left(g_{\mathrm{s}}g^5\right)$. In the first case, it is a matter of an EW insertion, and in the latter one of a QCD insertion. The discussion is hence analogous as in the two former cases with a different tree-level base case. Both of these kinds of diagrams can only be interfered with diagrams of $\mathcal{O}\left(g_{\mathrm{s}}g^5\right)$ leading to a contribution of $\mathcal{O}\left(\alpha_{\mathrm{s}}\alpha^6\right)$ or $\mathcal{O}\left(\alpha_{\mathrm{s}}^2\alpha^5\right)$. Figure 3.7 depicts examples of diagrams of both of these orders.

---

[18]Let us here explicitly mention again that an odd power of g_{s} implies the presence of an external gluon. Such diagrams can only be interfered with diagrams with also an odd power of g_{s}, giving in total even powers of both g_{s} and g.
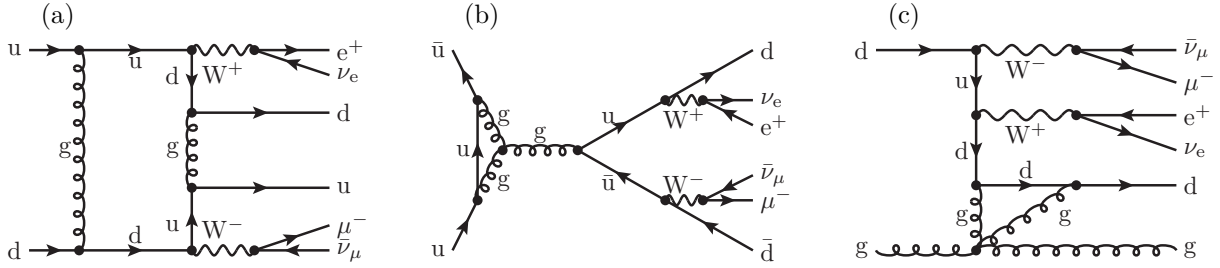
Figure 3.6: Examples of one-loop Feynman diagrams at $\mathcal{O}\left(g_{\mathrm{s}}^4 g^4\right)$.
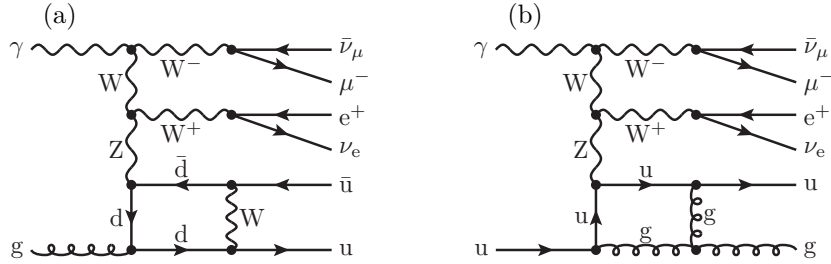
Figure 3.7: Examples of one-loop Feynman diagrams at $\mathcal{O}\left(g_{\mathrm{s}} g^7\right)$ and $\mathcal{O}\left(g_{\mathrm{s}}^3 g^5\right)$.

The last order of diagrams is $\mathcal{O}\left(g_{\mathrm{s}}^2 g^6\right)$. These diagrams are most interesting because, in contrast to the other cases, in which the type of correction could be clearly stated (either EW *or* QCD), the distinction in this case is sometimes impossible. Only looking at the order of coupling constants, these diagrams can be either QCD corrections to the $\mathcal{O}\left(g^6\right)$ diagrams or EW corrections to the $\mathcal{O}\left(g_{\mathrm{s}}^2 g^4\right)$ diagrams. Both perspectives are correct and sensible: Take, for example, an arbitrary $\mathcal{O}\left(g^6\right)$ diagram in which the two quark lines are connected with a photon. Inserting an additional gluon between those lines leads to the same diagram as inserting a photon to the same $\mathcal{O}\left(g_{\mathrm{s}}^2 g^4\right)$ diagram, in which the quarks are connected with a gluon. We depict this situation in Figure 3.8 (a). In fact, when we calculate the corresponding matrix element, we obtain both QED and QCD singularities. This shows that it is already impossible to differentiate between EW and QCD corrections at the level of some Feynman diagrams. Apart from diagrams with mixed singularities, there are such with only QED or only QCD singularities. Especially in partonic channels with external gluons, the two powers of g_{s} are already "used up", and we can only construct EW loops at this order, as we see explicitly in Figure 3.8 (b). Nevertheless, in other channels, there are also diagrams with pure EW or QCD loops. We refer to Figure 3.8 (c) for an example with a pure QCD loop. When interfered with a tree-level diagram of $\mathcal{O}\left(g^6\right)$ we produce a contribution of $\mathcal{O}\left(\alpha_{\mathrm{s}} \alpha^6\right)$, when interfered with one of $\mathcal{O}\left(g_{\mathrm{s}}^2 g^4\right)$, the result is of $\mathcal{O}\left(\alpha_{\mathrm{s}}^2 \alpha^5\right)$.
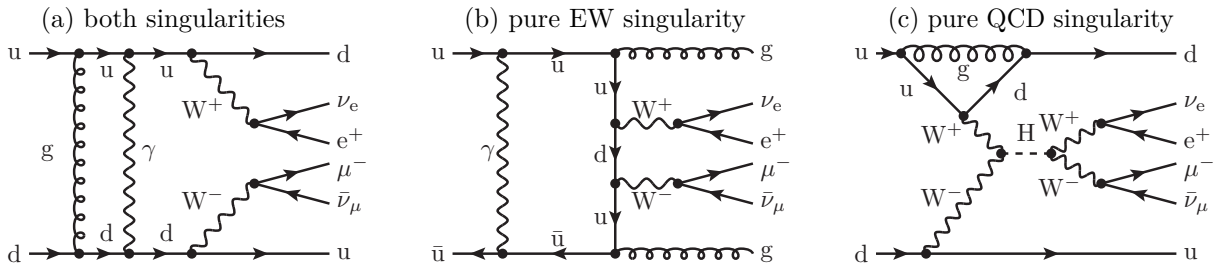
Figure 3.8: Examples of one-loop Feynman diagrams at $\mathcal{O}\left(g_{\mathrm{s}}^2 g^6\right)$.

We may hence summarise that the $\mathcal{O}\left(\alpha^7\right)$ virtual corrections are purely EW corrections to the EW process and $\mathcal{O}\left(\alpha_{\mathrm{s}}^3 \alpha^4\right)$ consists only of QCD corrections to the QCD-induced process. The other two orders are a mix of different contributions. Besides clear EW corrections from

the mixed gluon-photon-induced contributions, the process of $\mathcal{O}\left(\alpha_{\mathrm{s}}\alpha^6\right)$ is featured by interfering pure EW loops with QCD-induced LO diagrams as well as interfering indistinguishable mixed EW/QCD loops with EW LO diagrams. The $\mathcal{O}\left(\alpha_{\mathrm{s}}^2\alpha^5\right)$ is similar with exchanging EW $\leftrightarrow$ QCD. A pictorial description borrowed from papers of previous works on VBS [35] is presented in Figure 3.9.
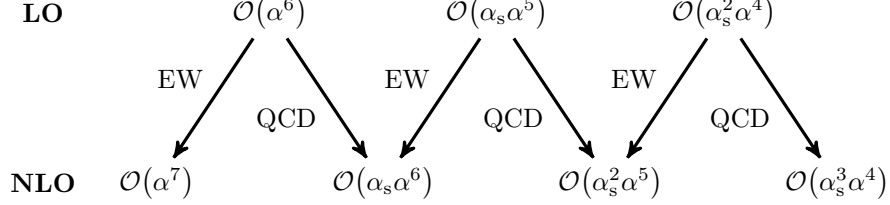
Figure 3.9: Pictorial description of interplay between LO and NLO for VBS [35].

3.1.4   Real emission

The other NLO contributions are real emission of photons or additional jets. An additional external particle rises the order of a corresponding LO contribution by one power of g or g_{s}, leading to four orders of Feynman diagrams with real emission in our process: $\mathcal{O}\left(g^7\right)$, $\mathcal{O}\left(g_{\mathrm{s}}g^6\right)$, $\mathcal{O}\left(g_{\mathrm{s}}^2g^5\right)$ and $\mathcal{O}\left(g_{\mathrm{s}}^3g^4\right)$. For reasons of bookkeeping, we differentiate the diagrams not only in their order of coupling constants but also in their jet multiplicity. These diagrams then have to be squared or interfered with real emission diagrams containing the same external particle content. This results, as in the case of the virtual corrections, in allowed contributions of $\mathcal{O}\left(\alpha^7\right)$, $\mathcal{O}\left(\alpha_{\mathrm{s}}\alpha^6\right)$, $\mathcal{O}\left(\alpha_{\mathrm{s}}^2\alpha^5\right)$ and $\mathcal{O}\left(\alpha_{\mathrm{s}}^3\alpha^4\right)$.

Processes with identical jet multiplicity as partonic channels at LO are easy to describe since they must have emitted a photon from some charged particle. We obtain them by taking a LO diagram and attaching one photon to all possible particles. Alternatively, we can modify an appropriate triple gauge-boson vertex to a quartic one. We present an example diagram in Figure 3.10 (a) and refer to Figure 3.2 and 3.3 with the imagination of an additional photon for further examples. These processes hence give rise to diagrams of $\mathcal{O}\left(g^7\right)$, $\mathcal{O}\left(g_{\mathrm{s}}g^6\right)$ and $\mathcal{O}\left(g_{\mathrm{s}}^2g^5\right)$. Although these diagrams are EW corrections, there is a possibility for a hidden QCD singularity at $\mathcal{O}\left(\alpha_{\mathrm{s}}\alpha^6\right)$ and $\mathcal{O}\left(\alpha_{\mathrm{s}}^2\alpha^5\right)$. We address this topic in Section 3.2.4.
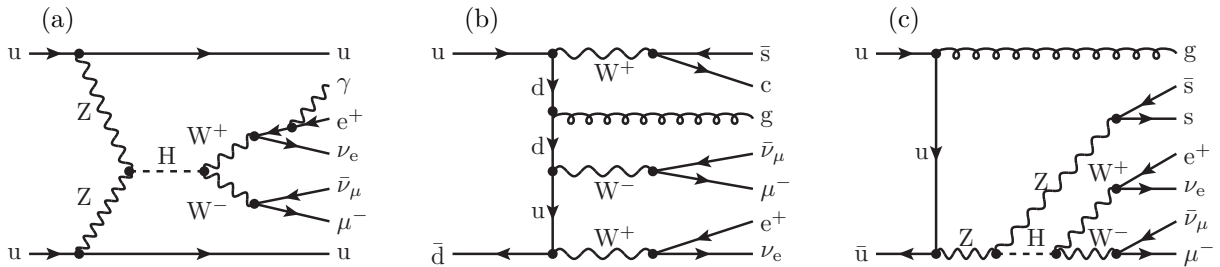
Figure 3.10: Examples of real photon emission at $\mathcal{O}\left(g^7\right)$ and real gluon emission at $\mathcal{O}\left(g_{\mathrm{s}}g^6\right)$. These types of emission are also possible for other orders in the coupling constants, depending on the order of the underlying LO diagram (here: $\mathcal{O}\left(g^6\right)$).

If the process has three jets, none, one, two or all three of them may be gluons, and the number of final-state quarks is the difference to the total number of jets. These processes cannot be unambiguously defined based on LO diagrams. Our discussion here is based on the appearing CS dipoles. There are four classes of them: 1) gluon splitting into two gluons (g $\rightarrow$ gg*), 2) gluon emission from a quark ($q \rightarrow$ gq^*), 3) quark emission from a quark ($q \rightarrow q$g*) and 4) quark emission from a gluon (g $\rightarrow qq^*$). Furthermore, the gluon can be replaced by a photon

except for case 1). However, multiple dipoles can appear in one partonic channel, which makes a one-to-one correspondence between the LO and NLO partonic channels impossible. We choose the convention that partonic channels that are obtained by adding a gluon to the final state compared to an existing LO partonic channel correspond to this particular LO channel.

With this convention, NLO partonic channels with at least one gluon in the final state are on a purely pictorial level obtained by taking an LO diagram of an LO partonic channel with one gluon less in the final state and attaching a gluon to any coloured particle or modifying an appropriate triple gauge vertex to a quartic one, like in case of photon emission. This leads to diagrams of $\mathcal{O}\left(g_{\mathrm{s}}g^6\right)$, $\mathcal{O}\left(g_{\mathrm{s}}^2g^5\right)$ and $\mathcal{O}\left(g_{\mathrm{s}}^3g^4\right)$. However, there might be many more singularities present than in that case. Because of the ambiguous nature of processes with less than three gluons in the final state, other singularities, both of QED and QCD type, emerge from interpreting the channel as quark radiation off an LO process with final-state gluons. We show this ambiguity in detail in Figure 3.11 and discuss it further in the caption. Two explicit example diagrams are given in Figure 3.10 (b) and (c). Further examples can be imagined out of the LO diagrams in Figure 3.2 and 3.3 with an additional gluon.
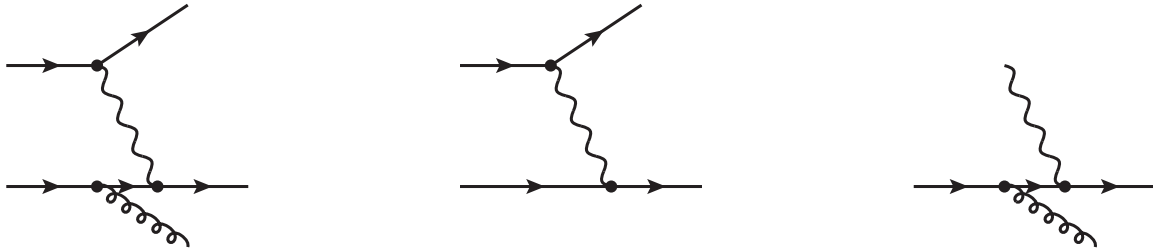
Figure 3.11: Impossibility of one-to-one correspondence between LO and NLO partonic channels. $qq \to 4\ell qq\mathrm{g}$ on the left is an NLO diagram of $\mathcal{O}\left(g_{\mathrm{s}}g^6\right)$ (we omit the leptonic part in the diagrams for clarity, since they do not play a role in this discussion). In our convention, it is assigned as a correction to the LO diagram $qq \to qq$ of $\mathcal{O}\left(g^6\right)$ (middle) via gluon radiation off one of the quarks. This gluon radiation leads to a QCD singularity when the internal quark propagator becomes on-shell. However, there is also a QED singularity present when the intermediate photon becomes on-shell; the same NLO process can also be interpreted as quark radiation off a quark. The corresponding LO diagram is $q\gamma \to q\mathrm{g}$ of $\mathcal{O}\left(g_{\mathrm{s}}g^5\right)$ (right). In fact, we need QCD and QED CS dipoles with both underlying Born processes to cancel all divergences.

The leftover processes are those with three quark jets. Because of fermion number conservation, there must be only one quark in the initial state, and the other initial-state particle has to be a boson. In our bookkeeping convention, partonic channels with three quark jets are hence counted as corrections to the photon/gluon-induced LO partonic channels. There are two possibilities for this initial-state boson: either it splits directly into a quark–antiquark pair or it interacts with other bosons and a quark–antiquark-pair is produced somewhere else in the process. In the case of direct splitting, one type of Feynman diagram is just obtained by crossing initial-state quark and final-state gluon or photon from initial-state gluon or photon emission. Another type of diagram is derived from LO diagrams with final-state gluons splitting into a quark-antiquark pair. There are, however, also diagrams that are not simply obtainable from modifying LO diagrams. Diagrams with three final-state quark jets are shown in Figure 3.12. Since the initial-state boson can be either a photon or a gluon, diagrams with three quark jets can be of $\mathcal{O}\left(g^7\right)$, $\mathcal{O}\left(g_{\mathrm{s}}g^6\right)$, $\mathcal{O}\left(g_{\mathrm{s}}^2g^5\right)$ or $\mathcal{O}\left(g_{\mathrm{s}}^3g^4\right)$.

Diagrams of $\mathcal{O}\left(g^7\right)$ contain only EW bosons: either an additional photon in the final state or a mixed photon-quark initial state. Hence, there are only QED singularities present, and we can identify partonic channels of $\mathcal{O}\left(\alpha^7\right)$, which can be uniquely constructed out of those diagrams, as pure EW corrections. With photon emission or a third jet and a mixed quark-photon initial state, the resulting partonic channels are of the type $qq \to 4\ell qq\gamma$ or $q\gamma \to 4\ell qqq$. Although we

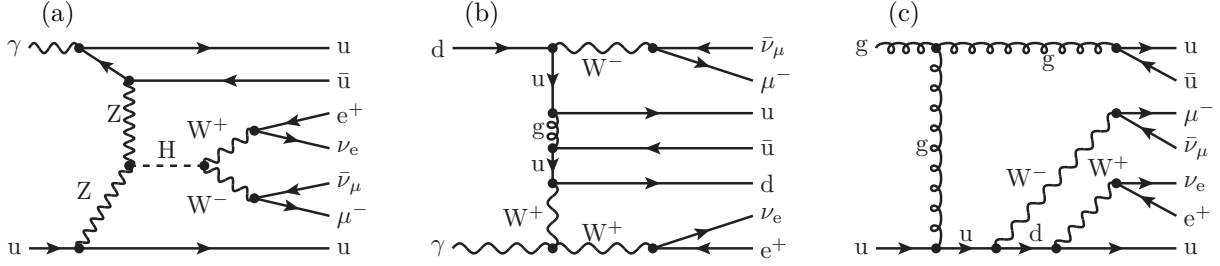Figure 3.12: Examples of real corrections with three quark jets at $\mathcal{O}\left(g^7\right)$, $\mathcal{O}\left(g_{\mathrm{s}}^2 g^5\right)$ and $\mathcal{O}\left(g_{\mathrm{s}}^3 g^4\right)$. An example for $\mathcal{O}\left(g_{\mathrm{s}} g^6\right)$ can be obtained by replacing the initial-state photon with a gluon in subfigure (a).

count the latter as corrections to the photon-induced process, they are not expected to show the typical behaviour of NLO quantities since they are strongly enhanced over the LO process of the same kind: At first, this process is not doubly suppressed by PDFs, since only one photon contributes. Second, depending on the explicit quark flavours, these new channels may include photon-induced VBS processes at NLO. An example diagram is shown in Figure 3.12 (a). We will recognise their effect in Section 4.3.3 when we investigate the NLO cross sections.

Similarly, channels of $\mathcal{O}\left(\alpha_{\mathrm{s}}^3 \alpha^4\right)$ can only be constructed out of diagrams of $\mathcal{O}\left(g_{\mathrm{s}}^3 g^4\right)$ and are pure QCD corrections to the QCD-induced process. Partonic channels of this order are $qq \to 4\ell qqg$, $qq \to 4\ell ggg$, $qg \to 4\ell qgg$, $qg \to 4\ell qqq$ and $gg \to 4\ell qqg$. We remark that Feynman rules forbid a channel $gg \to 4\ell ggg$ on tree-level.

Partonic channels of the other two orders $\mathcal{O}\left(\alpha_{\mathrm{s}} \alpha^6\right)$ and $\mathcal{O}\left(\alpha_{\mathrm{s}}^2 \alpha^5\right)$ consist both of interference contributions between Feynman diagrams of different orders ($\mathcal{O}\left(g^7\right) \times \mathcal{O}\left(g_{\mathrm{s}}^2 g^5\right)$ and $\mathcal{O}\left(g_{\mathrm{s}} g^6\right) \times \mathcal{O}\left(g_{\mathrm{s}}^3 g^4\right)$ respectively) and combinations of Feynman diagrams of the same order ($\left(\mathcal{O}\left(g_{\mathrm{s}} g^6\right)\right)^2$ and $\left(\mathcal{O}\left(g_{\mathrm{s}}^2 g^5\right)\right)^2$ respectively), like in the case of LO partonic channels. For $\mathcal{O}\left(\alpha_{\mathrm{s}} \alpha^6\right)$, the first case contains both a new interference between an EW process and a QCD-induced process and EW corrections to the LO interference. Although there are $\mathcal{O}\left(g_{\mathrm{s}}^2 g^5\right)$ diagrams with QCD singularities, they cannot be interfered with diagrams of $\mathcal{O}\left(g^7\right)$ (or the singularity is integrable, see section 3.2.5). In the second case, the diagrams of $\mathcal{O}\left(g_{\mathrm{s}} g^6\right)$ contain both QED and QCD singularities. They can be ambiguously seen as EW corrections to the interference or QCD corrections to the EW process. Partonic channels for $\mathcal{O}\left(\alpha_{\mathrm{s}} \alpha^6\right)$ are $qq \to 4\ell qq\gamma$, $qq \to 4\ell qqg$, $q\gamma \to 4\ell qqq$, $q\gamma \to 4\ell qg\gamma$, $\gamma\gamma \to 4\ell qqg$, $qg \to 4\ell qqq$ and $g\gamma \to 4\ell qq\gamma$. With appropriate replacements, the same reasoning is valid for $\mathcal{O}\left(\alpha_{\mathrm{s}}^2 \alpha^5\right)$ and the resulting partonic channels are obtained with the replacement $\gamma \leftrightarrow g$. Additionally, there are the partonic channels of type $q\gamma \to 4\ell qgg$ and $qq \to 4\ell gg\gamma$, since gluons form jets in contrast to photons.

The resulting picture is the same as in Figure 3.9 for the virtual corrections. The identical singularity structure is a necessity for them to be able to cancel order by order in the coupling constants.

3.2   Technical details

For our calculations, we make use of our in-house Monte Carlo event generator BBMC in combination with the matrix element generator RECOLA 1.4.0 [40, 41] and the one-loop library COLLIER 1.2.4 [43, 108–110]. For detailed information on RECOLA and COLLIER, we refer to the literature. Roughly speaking, their task is only to compute matrix elements: BBMC passes a set of momenta onto them and receives the corresponding matrix elements back. This includes "normal" tree-level and one-loop matrix elements for the LO process and the real and virtual corrections, as well as spin- and/or colour-correlated matrix elements, which are needed both for the subtracted and the integrated CS dipoles. The remainder is done by BBMC, which includes not only the generation of phase-space points and applying the event selection routine but also the identification of the dipole structure and the actual dipole subtraction, and the calculation

of the integrated and differential cross sections out of the information given by RECOLA and COLLIER as well as information stemming from the PDFs.

3.2.1 Momentum generation with BBMC

BBMC is a multi-channel Monte Carlo event generator which is based on the output of a certain number of random variables to generate phase-space points. However, a Monte Carlo integration with equally distributed (and even restricted to physically allowed) momenta of all of our final-state particles would be very inefficient. Therefore, BBMC is a *multi-channel* generator. The term "multi-channel" refers to the presence of multiple different so-called integration channels. In each of these, a set of a priori equally distributed random numbers is mapped to a set of momenta by using physical information which is taken from Feynman diagrams – by default, for a given partonic channel, each Feynman diagram corresponds to one integration channel. The first step for BBMC is hence constructing all possible tree-level Feynman diagrams for a given partonic channel and indexing them.[19] Generating the integration channels BBMC assigns a binary code to all external particles and propagators. When telling BBMC the process to compute, the appearing external particles are in a certain order in the input file. If i is the position of the external particle in that file, then the binary of the particle is 2^i, with the first two positions being used for the incoming particles. s-channel propagators are labelled back-to-front as follows: Their binaries are the sum of the binaries of their two decay particles. t-channel propagators[20] are afterwards labelled front-to-back: the first one is assigned the sum of the binaries of the incoming particle $i = 1$ and the binary of the s-channel propagator or final-state particle it shares a vertex with particle 1. Afterwards, this t-channel becomes the new incoming particle for labelling until the last vertex is reached: The sum of the binaries of all three lines at this vertex has to be $2^{i+1} - 1$. We demonstrate this procedure best by two examples in Figure 3.13.
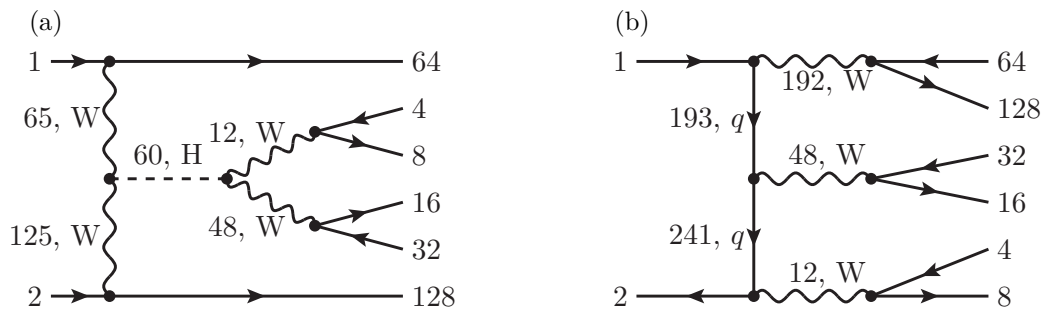
Figure 3.13: Two examples of integration channels (Feynman diagrams) for generic $qq \rightarrow$ $\mathrm{e}^+\nu_\mathrm{e}\mu^-\bar{\nu}_\mu qq$ scattering at $\mathcal{O}\left(\alpha^6\right)$ with assigned binary codes. Note that the binary codes of the particles and, hence, the priorities of the invariants depend on the ordering of the input.

For every set of momenta, a set of random numbers $\vec{x}$ with $0 < x_i < 1$ is generated by use of the random number generator RANLUX [111, 112]. The first of these random numbers is used to select an integration channel, the second and third ones to determine the partonic centre-of-mass energy $\hat{s}$ and the rest for the final-state momentum generation. If we are integrating the CS dipoles, additional random numbers are needed, which we will omit from the discussion in this chapter, since they do not affect the momenta.

---

[19] For the loop-induced contributions, BBMC also uses effective vertices. Quartic vertices are replaced with auxiliary particles connecting auxiliary triple vertices in the t channel.

[20] BBMC does not discriminate between t- and u-channel propagators. Suppose in some process t- and u-channel exchange are possible. In that case, different binaries are assigned to the two propagators .

At first, a specific integration channel i is picked by using the so-called channel weights α_i. These α_i do not necessarily have to be uniformly distributed, but a priori, the weight of each channel is identical; if N is the number of integration channels, then

$$\alpha_i^{\text{a priori}} = 1/N \quad \Rightarrow \quad \sum \alpha_i = 1. \tag{240}$$

The α_i are hence normalised such that they sum up to one. For some random number x_1, the channel i fulfilling the criterion $\sum_{j=1}^{i-1} \alpha_j < x_1 < \sum_{j=1}^{i} \alpha_j$ is chosen. Since the mapping of the random numbers to momenta is also not uniform, each of these channels has an individual probability density $g_i(\vec{x})$ for mapping the random numbers to a set of momenta.[21] The total probability density $g(\vec{x}) = \sum_i \alpha_i g_i(\vec{x})$ is still a well-defined probability density regardless of the distribution of the αs and the shape of the individual probability densities, since

$$\int_0^1 \mathrm{d}\vec{x}\, g(\vec{x}) = \int_0^1 \mathrm{d}\vec{x} \sum \alpha_i g_i(\vec{x}) = \sum \alpha_i \int_0^1 \mathrm{d}\vec{x}\, g_i(\vec{x}) = \sum \alpha_i = 1 \tag{241}$$

and $g(\vec{x})$ is non-negative and always smaller than one by definition. To see the benefit of a non-uniform distribution of integration channels, we are now artificially rewriting the integrated cross section as the expectation value of the so-called event weight $w(\vec{x})$

$$\sigma = \frac{1}{2s} \int \mathrm{d}\Gamma\, |\mathcal{M}|^2 = \int \mathrm{d}\vec{x} \frac{1}{2s} \frac{\mathrm{d}\Gamma}{\mathrm{d}\vec{x}} |\mathcal{M}|^2 \equiv \int \mathrm{d}\vec{x}\, w(\vec{x}) g(\vec{x}) = \langle w \rangle \tag{242}$$

with

$$w(\vec{x}) = \frac{1}{2s} \frac{\mathrm{d}\Gamma/\mathrm{d}\vec{x}}{g(\vec{x})} |\mathcal{M}|^2. \tag{243}$$

The probability density drops out of the expression of the cross section since it must not depend on the choice of mappings and channel weights. However, the integration error $\sqrt{\langle w^2 \rangle - \langle w \rangle^2}$ depends on the α_i and the g_i, since

$$\langle w^2 \rangle = \int \mathrm{d}\vec{x}\, g(\vec{x}) w^2(\vec{x}) = \int \mathrm{d}\vec{x} \frac{1}{g(\vec{x})} \left(\frac{1}{2s} \frac{\mathrm{d}\Gamma}{\mathrm{d}\vec{x}} |\mathcal{M}|^2 \right)^2. \tag{244}$$

Whilst the individual probability densities are fixed, it is possible to optimise the channel weights after a certain amount of accepted events. The procedure Bbmc uses is described in [113], and the optimisation is carried out after $100N \times 2^k, k \in \mathbb{N}$, accepted events. If we assume an a priori uniform distribution, the first optimisation hence occurs after each channel was picked 100 times on average.

After choosing an integration channel, Bbmc starts with the momentum generation by determining the momentum fractions of the incoming partons, which are assumed to be perfectly collinear to the beam axis. The momenta of the partons are directly derived from the centre-of-mass energy of the beam protons $\sqrt{s}$ via

$$p_1 = \begin{pmatrix} p_1 & 0 & 0 & p_1 \end{pmatrix} = x_2 \begin{pmatrix} \sqrt{s}/2 & 0 & 0 & \sqrt{s}/2 \end{pmatrix} \tag{245}$$

$$p_2 = \begin{pmatrix} p_2 & 0 & 0 & -p_2 \end{pmatrix} = x_3 \begin{pmatrix} \sqrt{s}/2 & 0 & 0 & -\sqrt{s}/2 \end{pmatrix}. \tag{246}$$

The partonic centre-of-mass energy squared is hence $\hat{s} = x_2 x_3 s$.

Afterwards, the final-state momenta are constructed as follows: At first, the s-channel invariants are determined. Therefore, we can divide the Feynman diagram into "decay chains": s-channel propagators of different decay chains are separated by t-channel propagators or emerge from the decay of the same mother particle. In the examples of Figure 3.13, there is one main decay chain (60-12/48) in the diagram on the left-hand side with two sub-chains (12,48), and

---

[21]We use the abbreviation $\vec{x}$ as argument, but in fact, we mean only $x_4, x_5, \ldots$ since the other three random numbers are already in use at this stage.

there are three independent decay chains (12,48,192) in the diagram on the right-hand side. Depending on their binaries, individual propagators and decay chains are said to have a specific priority that fixes their position in the sequence in which they are determined. By default, the priority decreases from back to front; the first invariant to be calculated is the one of the s-channel propagator with the smallest binary code.

Depending on physical constraints, any s-channel propagator in a diagram must have an s-value between some minimal $s_{\min}$ and a maximal $s_{\max}$. For each decay chain individually, s_i for some propagator with binary code i has to be larger than

$$s_{i,\,\min} = \left(\sum \sqrt{s_j} \right)^2, \tag{247}$$

when propagators j are its direct decay products. This bound is a direct consequence of energy-momentum conservation. Note that we define $s_j = m_j^2$ if the binary code j corresponds to an external particle. Since we calculate a process with only massless external particles, we reduce our discussion here without taking external masses into account in the formulae. Vice versa, the maximum of s_i does not only depend on the total centre-of-mass energy squared of the process but also on the values for s_k, that are already reserved for propagators in other decay chains with higher priority:

$$s_{i,\,\max} = \left(\sqrt{\hat{s}} - \sum \sqrt{s_k} \right)^2. \tag{248}$$

If there were massive final-state particles, then it would also depend on the minimal s-values of all other decay chains since a certain amount of energy is required to produce the massive external particle. Between these extrema, the actual s_i are determined using the random numbers for massive s-channel propagators via the formula

$$s_i^{m \neq 0} = m_i \Gamma_i \tan\left(x \arctan\left(\frac{s_{i,\,\max} - m_i^2}{m_i \Gamma_i} \right) + (1-x) \arctan\left(\frac{s_{i,\,\min} - m_i^2}{m_i \Gamma_i} \right) \right) + m_i^2, \tag{249}$$

where Γ_i is the decay width of the particle and x is the generic random variable. This function has a plateau around $s \approx m_i^2$, which is becoming larger as Γ_i becomes smaller. This means, the propagator is most likely mapped towards its resonance peak and the sharper the peak is, the more likely this mapping occurs. Massless s-channel invariants are mapped with

$$s_i^{m=0} = \left(x s_{\max}^{1-\nu} + (1-x) s_{\min}^{1-\nu} \right)^{\frac{1}{1-\nu}}, \quad \nu = 0.9. \tag{250}$$

The use of this specific ν-value is based on experience, and the function maps more likely to small values of s.

To demonstrate this routine and fill it with life, we use a small exemplary set of random numbers and the integration channel of Figure 3.13 (a). Let us say, $\vec{x} = \begin{pmatrix} x_1 & 0.4 & 0.7 & 0.9 & 0.1 & 0.6 & \dots \end{pmatrix}$ and $\sqrt{s} = 13 \text{ TeV}$. This leads to $\sqrt{\hat{s}} = 6.9 \text{ TeV}$. At first, the W boson with binary 12 is determined with

$$x_4 = 0.9, \quad \sqrt{s_{12,\min}} = 0 \text{ TeV}, \quad \sqrt{s_{12,\max}} = 6.9 \text{ TeV} \quad \Rightarrow \quad \sqrt{s_{12}} = 83.6 \text{ GeV}. \tag{251}$$

Since the minimal s-value of the s-channel propagator with next smallest binary 48 is independent of propagator 12 – propagator 12 is not a decay product of propagator 48 –, it remains unchanged. The maximal s-value is, however, affected since a certain amount of energy is used up by propagator 12 of a different sub-chain and cannot flow into propagator 48 any more. s_{48} is thus determined with

$$x_5 = 0.1, \quad \sqrt{s_{48,\min}} = 0 \text{ TeV}, \quad \sqrt{s_{48,\max}} = 6.8 \text{ TeV} \quad \Rightarrow \quad \sqrt{s_{48}} = 77.4 \text{ GeV}. \tag{252}$$

At last, the s-value of the propagator of the Higgs boson 60 is calculated. Since it has two decay products, whose invariant masses have been determined previously, it obtains a bound on its minimal s-value. However, the maximal s-value is only limited by the complete centre-of-mass energy:

$$x_6 = 0.6, \quad \sqrt{s_{60,\min}} = 160.9 \text{ GeV}, \quad \sqrt{s_{60,\max}} = 6.9 \text{ TeV} \quad \Rightarrow \quad \sqrt{s_{60}} = 203.2 \text{ GeV}. \tag{253}$$

The last s-channel invariant is not a free variable since it is fixed by energy-momentum conservation. After the s-channels, the t-channel invariants are determined. Then, the angular distribution of the outgoing momenta is determined with a set of random numbers in accordance with the previously given invariants. We leave out further explanations of this more lengthy procedure since it gives no significant insights into specific problems we had to face for W$^+$W$^-$-scattering.

With the information out of the generated momenta of final-state and intermediate particles in a specific channel, BBMC can calculate the probability g_i for exactly this outcome in each other channel. In practice, the generated momenta are first passed to the event selection routine, which checks whether they are inside our fiducial phase-space region to avoid unnecessary computation of probability densities. Afterwards, the momenta are passed to RECOLA for matrix element computations.

If we have to compute CS dipoles, BBMC also calculates the mapping from the $n+1$-particle phase space to the corresponding underlying n-particle Born phase spaces and passes them to RECOLA again for the computation of the reduced matrix elements. The dipole terms themselves are calculated by BBMC again. We mention explicitly that BBMC only uses the $n+1$-particle integration channels for constructing the momenta. Subsequently, only these channels and the event weight after applying the subtraction procedure are taken into account for the weight optimisation.

3.2.2   Permutation of resonances

For some processes, the default momentum generation procedure of BBMC does not produce optimal results and W$^+$W$^-$ scattering at $\mathcal{O}\left(\alpha^6\right)$ falls under this kind. The general problem is the fixed sequence of determining the s-channel invariants. It may happen that some internal particle only becomes resonant with a small probability, not because of physical constraints, but purely by specific construction of the mappings or, in some minor cases, by an unfortunate interplay between both factors. Describing this problem is fairly simple by example.

For the first case, let us reuse Figure 3.13 (a). Being one of *the* main ingredients for calling our process "W$^+$W$^-$ scattering", this statement explicitly demonstrates the importance of the issue. On the one hand, both s-channel W bosons in this integration channel have a higher priority than the Higgs boson because they emerge from its decay, and thus both have a smaller binary code than the Higgs boson. Since their invariants are the first to be determined, there is usually[22] sufficient centre-of-mass energy to map both of them preferably towards their resonance peak at

$$s_\mathrm{W}^+ \approx M_\mathrm{W}^2 \qquad s_\mathrm{W}^- \approx M_\mathrm{W}^2. \tag{254}$$

As a consequence, the Higgs boson is only very seldom mapped towards its resonance peak since

$$s_\mathrm{H} \approx 4M_\mathrm{W}^2 > M_\mathrm{H}^2. \tag{255}$$

We already performed a small example for one random phase-space point in the last section concerning this integration channel, in which we saw this behaviour. We show an example histogram of $\sqrt{s_\mathrm{H}}$ in Figure 3.14 in the channel. The bulk of generated events lies around $\sqrt{s_\mathrm{H}} = 2M_\mathrm{W} \approx 160\,\mathrm{GeV}$, only a fraction of less than 1% of the events lies around $\sqrt{s_\mathrm{H}} = M_\mathrm{H} \approx 125\,\mathrm{GeV}$. For all integration channels in W$^+$W$^-$ scattering, an s-channel Higgs boson must decay into two W bosons, so this is a general statement independent of the specific example. On the other hand,

---

[22]This statement becomes false, if the total centre-of-mass energy is below two times the W mass. Such a situation is excluded in our experimental setup since there must be enough energy inside the process to pass the invariant-mass cuts for the jets, which are defined in equations (284) and (292) of Section 4.2 to be at 400 GeV and 500 GeV respectively. BBMC uses this knowledge on cuts such that all events with lesser partonic centre-of-mass energy are dismissed right away. In fact, if the energy is just above the threshold and this integration channel is chosen, the most likely scenario will be: Both W bosons are mapped towards their resonances, then there is too little energy left for the jets, and the event is dismissed.

events with a resonant Higgs boson have, due to its very narrow decay width, a large matrix element and hence a strong impact on the integration stability, if they are not often hit.
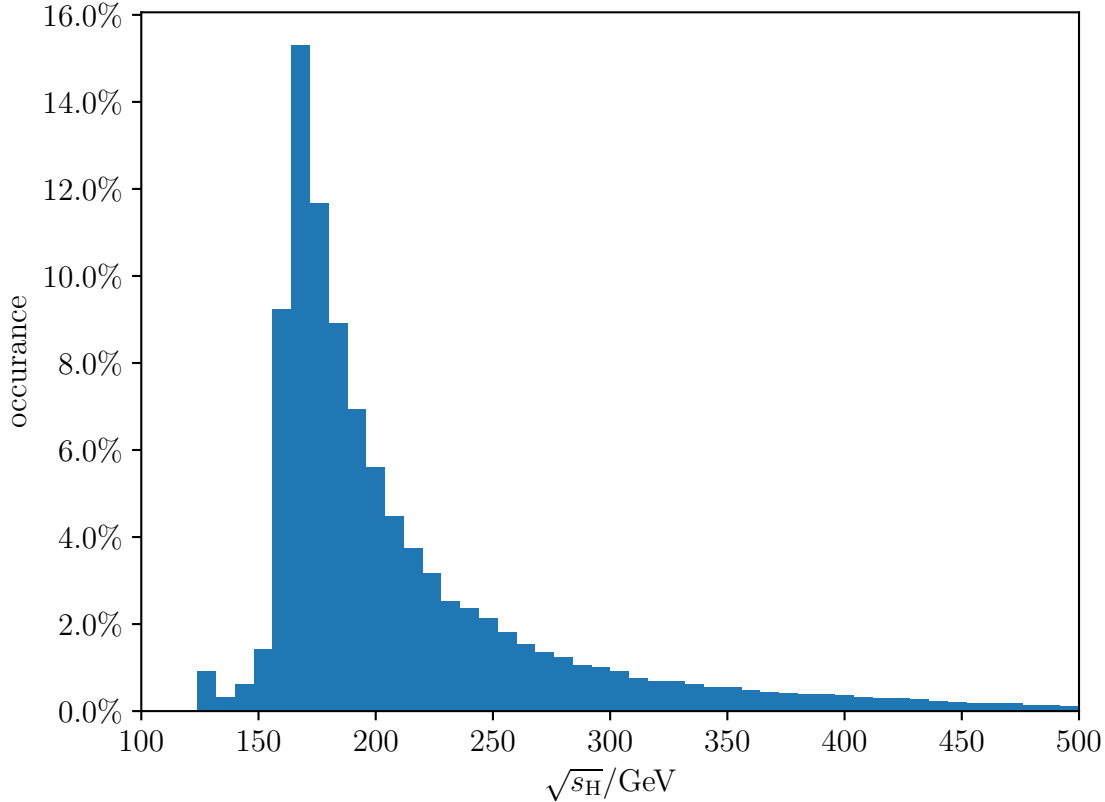
Figure 3.14: Distribution of $\sqrt{s_\mathrm{H}}$ for 10^6 generated events in the integration channel shown in Figure 3.13 (a) for $ud \rightarrow 4\ell ud$. Note that the probability of generating momenta accidentally hitting the Higgs-boson resonance for $\sqrt{s_{4\ell}}$ might be larger in other integration channels *without* resonant Higgs boson by chance.

For the other case, consider the 3VP diagram from Figure 3.13 (b) again. This type of diagram becomes problematic only if the total centre-of-mass energy is too small to put all three W (or one Z and two W) bosons onto their resonance peaks. The fixed order of determining the invariants then leads to an asymmetry in the momenta of the decay products since, in all of these events, only the W boson with the highest priority (or the two highest priorities) is mapped correctly. For our cut setup, this situation is excluded. Suppose the partonic centre-of-mass energy is just above the threshold to be accepted by our cuts. In that case, the event is most likely cut away independent of the priority of the propagators since either there is not enough energy left for the jets (see also footnote 22) or the invariant mass of the two jets is mapped to the W or Z resonance way lower than the required $\sqrt{s}$-value for the event selection.

Although the second issue is only of theoretical interest, we resolved both of the problems at once by introducing new integration channels into Bɴᴍᴄ. Our goal was to construct a method which guarantees that every propagator can become resonant and that subsequent possibly resonant propagators are addressed with identical probability. In very generality, to naively cover all eventualities, we would have to ensure that every ordering of *s*-channel propagators has its own integration channel: only then can we guarantee that there is at least one channel for all combinations of resonance mappings. Having between two and four (five) independent *s*-channel invariants for our (N)LO process would introduce between $2! = 2$ and $5! = 120$ channels, where formerly we had only one. The number of integration channels directly affects computation time

when calculating each event weight, and most of the channels would be redundant. If physical constraints forbid particles to become resonant, these particles could have become resonant anyhow, or a smaller set of new integration channels would have been already sufficient. The latter is always the case for more than 3 resonances by simple combinatoric considerations. Each propagator can become either resonant or not resonant. For each Feynman diagram, there are, thus, at most 2^n cases to cover and to address by a particular integration channel. For $n > 3$, the inequality $n! > 2^n$ holds. Since $n!$ grows much faster than 2^n, the inclusion of all possible integration channels results in a large number of redundant integration channels for more complicated processes.

Our first observation is that massless propagators can be put aside from the procedure. Massless particles never become resonant, and therefore, there is no necessity to permute them to the front. Since it is of much more importance to map the resonances of massive propagators correctly, we can, in fact, give the least priority to all massless particles. The improved algorithm thus differentiates between massive and massless propagators and calculates the massive invariants always before the massless ones in the new integration channels. Considering only the ordering of the massless propagators, it is identical to the default Bbmc ordering.

In the case of W^+W^- scattering, there are up to 5 massive independent s-channel propagators and a plethora of different types of Feynman diagrams. To discuss and invent a general – not only working for W^+W^- scattering – and at the same time minimal procedure exceeds the scope of this thesis. We chose a procedure, which is sufficient to produce stable integration results for our process and our targeted precision of integration. Especially, the need for integration channels, when the total energy inside the process is not sufficient to put all possible particles onto their resonances, was considered to be unimportant since our phase-space cuts guarantee a minimum centre-of-mass energy to be sufficient for all intermediate particles to become resonant. The method of choice was taking only *cyclic permutations* of the order, in which massive s-channel invariants are calculated, into account. With at most 5 massive propagators, this leads to a maximum factor of 5 times the original number of integration channels instead of up to 120 times. Of course, this method is neither general nor minimal. Nevertheless, we show that the resonances are mapped sufficiently correctly with our method.

Since we impose a veto on external bottom quarks and assume a diagonal CKM matrix, there are no massive fermions to take care of. Only bosonic propagators can become resonant. It turns out that there are only very few classes of LO Feynman diagrams left with three or more bosonic s-channel propagators for W^+W^- scattering (the case of two or less massive propagators is trivial since the cyclic permutations are already all possible permutations). With 8 external particles, there are, neglecting 4-particle vertices, 5 propagators. Let us assume all external particles are fermions. This neglects the case of LO photon-photon-induced contributions and NLO quark-photon-induced contributions with quark radiation, as well as gluon-induced contributions.[23]

For having 3 s-channel propagators, we must have 2 t- or u-channel propagators (for simplicity we only call them t-channel propagators). This then splits into three cases:

1. Both t-channel propagators are bosonic. This means the two quark lines flow from the initial to the final state, and there is a bosonic s-channel propagator attached to both of the t-channel propagators. Since we need two more massive s-channel propagators with 5 propagators in total, they also have to be directly connected to the s-channel propagator we already have. This case is depicted in Figure 3.15 (a).

2. One of the t-channel propagators is fermionic, and one is bosonic. In this case, one of the quarks must emit a massive vector boson, which decays into two bosons before they decay into fermions. Figure 3.15 (b) shows this case.

---

[23]In case of W^+W^- scattering, gluon-induced LO contributions appear at $\mathcal{O}\left(\alpha_s\alpha^5\right)$ only in combination with photons in the initial-state or at $\mathcal{O}\left(\alpha_s^2\alpha^4\right)$. In the latter case, there are at most two massive EW bosons appearing in the process.

3. Both t-channel propagators are fermionic. This means both initial-state quarks are on the same fermion line, and we have to attach three bosonic s-channel propagators to that line, leading to the diagram shown in Figure 3.15 (c).

There are also three cases with four s-channel propagators, of which three or four are massive:

4. There is one bosonic t-channel propagator. One of the quarks emits a massive boson after its interaction with the other quark, in contrast to case 2, where the emission happened before the interaction. Compared to that case, we traded the t-channel fermion propagator for a massless s-channel one. Figure 3.15 (d) is a depiction of that case.

5. There is one fermionic t-channel propagator connecting the two initial-state quarks. Two massive bosons are emitted from this line, of which both decay into fermions. Then one of these fermion lines emits an additional massive boson (see Figure 3.15 (e)).

6. There is one fermionic t-channel propagator, like in case 5, but only one of the bosons decays into fermions. The other splits into two massive bosons, leading to four massive propagators. This case is shown in Figure 3.15 (f).

At last, there are the s-channel-induced integration channels, in which an initial-state quark-antiquark pair annihilates into a boson X. These channels have five s-channel propagators. Out of these five propagators, however, only four are independent since the s-value of the first propagator X is fixed by the total centre-of-mass energy. There are either three or four bosonic s-channel propagators:

7. The boson X can split into two fermions. One of the fermion lines emits a massive boson, which then splits into two massive bosons. This is depicted in Figure 3.15 (g).

8. The boson X splits into two massive bosons. Like in case 5, both of them decay into fermions, and one fermion line emits another massive boson. The corresponding diagram is given in Figure 3.15 (h)

9. The last case is similar to cases 6 and 8: The initial boson split into two bosons, of which one decays fermionically and the other one into two massive bosons. This is shown in Figure 3.15 (i).

Surely, it can happen in cases 6 and 9 that only three of the four bosons are massive, but if the algorithm can handle massive propagators, replacing one of them with a massless one does not do harm.

In cases 1, 2, 4 and 7 (Figure 3.15 (a,b,d,g)), all massive bosons are attached to the same vertex. The BBMC standard mapping procedure determines the s-values of both daughter bosons first ($D_1 D_2 M$). One cyclic permutation leads to the determination of the mother boson and one of the daughters ($D_2 M D_1$) and the last one to the other daughter and the mother ($M D_1 D_2$), covering all processes, in which only two of the three bosons could become resonant. Case 6 (Figure 3.15 (f)) is analogous since the additional decay chain does not affect the three bosons. In principle, it would have been sufficient to permute only the propagators attached to the triple gauge boson vertex and determine the additional propagator always at last. Case 9 (Figure 3.15 (i)) is also related. Since we do not have to care about the first s-channel propagator in the decay chain, the subsystems A and $M D_1 D_2$ are independent.

In cases 5 and 8 (Figure 3.15 (e,h)), we have to distinguish two subcases: either $M_C < M_B$ or $M_C > M_B$. In the first case, everything is fine: Neither boson B nor C becoming resonant hinders the other one from also becoming resonant, and their order does not matter. In the second case, the order of B and C matters since one of the bosons becoming resonant hinders the other one. Because of the permutation, some channels can map A and B first, and other channels can map A and C first. Case 3 (Figure 3.15 (c)) is trivially covered since there are no
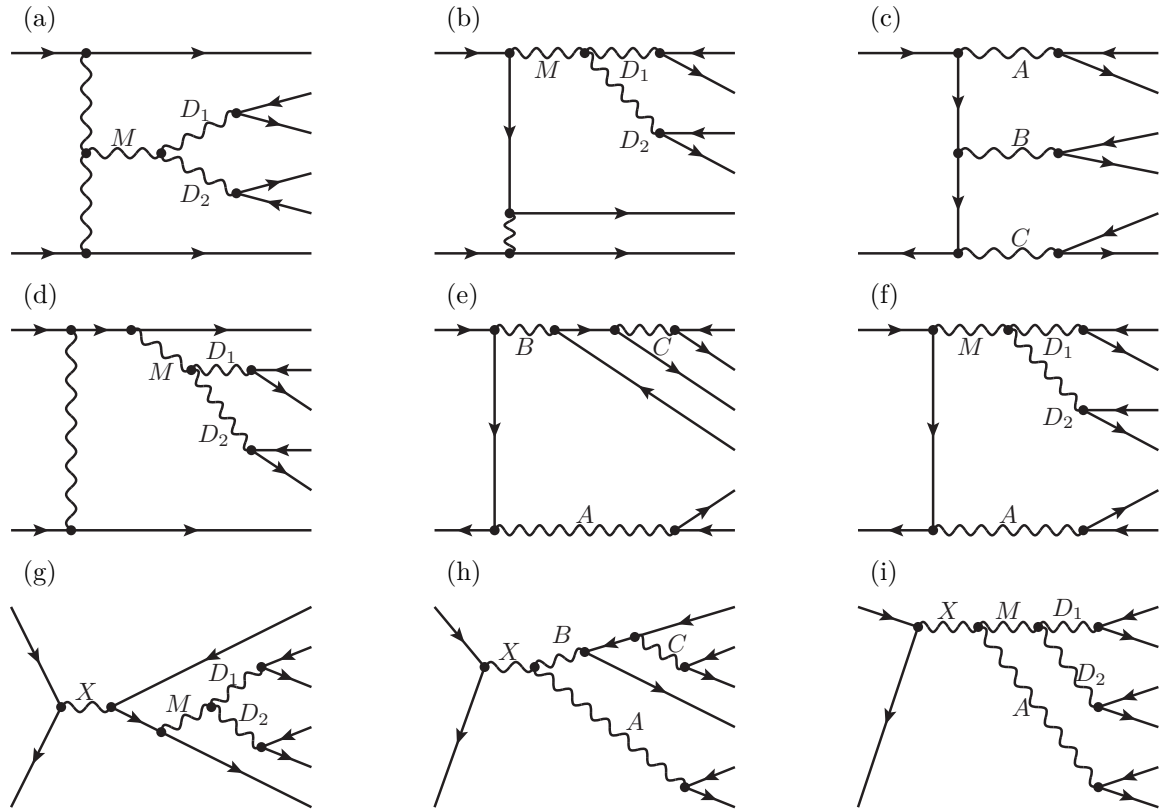
Figure 3.15: Types of generic Feynman diagrams with at least three massive s-channel propagators for W^+W^- scattering at $\mathcal{O}\left(\alpha^6\right)$. Note that we did not distinguish between vector and scalar bosons in our discussion, and the wavy lines M in subdiagrams (a) and (i) might also represent a scalar Higgs boson.

physical constraints on resonances of different decay chains, and only insufficient energy causes problems.

Hence, we showed that our method of cyclic permutations is able to cover all LO Feynman diagrams for W^+W^- scattering with only external fermions. For NLO processes, we note that attaching an external photon to a massive propagator (cutting it thereby into two propagators) does not affect the ability of either of these propagators to become resonant since the external photon momentum is determined at last and can become arbitrarily small. It is, hence, unimportant in which order the s-values of these two propagators are determined. If the "ancestor" is the first to be determined, the minimum s-value of its "heir" is not affected. Its maximum s-value is identical to the s-value of the "ancestor", whose maximum s-value, on the other hand, is only affected by other decay chains or even further predecessors in the same decay chain and identical to the one of the "heir", if it would have been determined first. If the "heir" is determined first, the analogue is true vice-versa: The maximum s-value of the "ancestor" does not depend on the s-value of the "heir" and the minimum s-value of "heir" and "ancestor" are identical. It can happen by chance that the first propagator to be determined does not become resonant by receiving a too large or too small s-value and therefore forbids the second one to become resonant as well, but this is a physical constraint in a single phase-space point. The other boson then tends to have an identical s-value (leaning most likely to its resonance peak), which results in the emission of a very soft photon, no matter whether the "ancestor" or the "heir" was determined first. Such events are unavoidable in a Monte Carlo procedure, and their influence will eventually smooth out, averaging over a large number of generated phase-space points. There is, however, a

small caveat concerning case 7, which does not notably affect the stability of the integration.[24] We can conclude that our method is capable to handle all classes of diagrams that are obtained by attaching a photon to an already existing LO diagram. This generalises to gluon emission, since the gluon never couples to a massive propagator in our case. Thus, our method works for the large class of $qq \to 4\ell qq\gamma$ and $qq \to 4\ell qq$g NLO partonic processes.

We did not investigate resonance permutations in depth for photon-induced processes. At LO, they turn out to be negligible (see Section 4.3.1); at NLO, they have some influence, but the integration procedure seems to be stable enough. The latter part is also true for gluon-induced processes, especially since there is no sharp Higgs boson resonance peak for LO gluon-induced processes of $\mathcal{O}\left(\alpha_\mathrm{s}\alpha^5\right)$ and $\mathcal{O}\left(\alpha_\mathrm{s}^2\alpha^4\right)$.

The possibility of permuting the integration channels slightly changes the assignment of minimal and maximal s-values for the individual propagators: Since it can happen that the invariant mass of an ancestor is fixed before the s-values of all of its heirs are determined, equation (248) is not universally applicable any more. The maximal s-value in such a case depends only on the s-values of the ancestor and its other heirs, and not on the s-value of other particles in the process or the partonic centre-of-mass energy. However, the form of the equation remains unchanged, if we identify $\hat{s}$ with the invariant mass of the ancestor squared and sum only over propagators k with the same ancestor. Vice versa, the minimal invariant mass of a propagator now depends only on its direct daughter propagators, if they are already determined before.

> We again fill this discussion with life by reconsidering our example of the last section and use the permuted channel of Figure 3.13 (a) with the Higgs boson propagator determined first and equally permuted random numbers $\vec{x} = \begin{pmatrix} x_1 & 0.4 & 0.7 & 0.6 & 0.9 & 0.1 & \ldots \end{pmatrix}$. The results are
>
> $$x_4 = 0.6, \quad \sqrt{s_{60,\mathrm{min}}} = 0\,\mathrm{TeV}, \quad \sqrt{s_{60,\mathrm{max}}} = 6.9\,\mathrm{TeV} \quad \Rightarrow \quad \sqrt{s_{60}} = 125.0\,\mathrm{GeV}; \quad (256)$$
>
> $$x_5 = 0.9, \quad \sqrt{s_{12,\mathrm{min}}} = 0\,\mathrm{GeV}, \quad \sqrt{s_{12,\mathrm{max}}} = 125.0\,\mathrm{GeV} \quad \Rightarrow \quad \sqrt{s_{12}} = 83.4\,\mathrm{GeV}; \quad (257)$$
>
> $$x_6 = 0.1, \quad \sqrt{s_{48,\mathrm{min}}} = 0\,\mathrm{GeV}, \quad \sqrt{s_{48,\mathrm{max}}} = 41.6\,\mathrm{GeV} \quad \Rightarrow \quad \sqrt{s_{48}} = 15.1\,\mathrm{GeV}, \quad (258)$$
>
> pushing the Higgs boson towards its resonance peak and pulling one of the W bosons away from its resonance peak compared to the unpermuted results.

In Figure 3.16, we demonstrate the influence of the new integration channels. We generated momenta for the partonic process ud $\to 4\ell$ud at $\mathcal{O}\left(\alpha^6\right)$ until the third channel weight optimisation and threw away those until the first one to remove the bias from the equal a priori channel weights. The statistics in the graph include 81600 events without and 127200 events with the new channels. In contrast to Figure 3.14, we used all integration channels for this plot and applied the event selection cuts for the VBS setup (see Section 4.2.1), i. e. this is actual data from our calculation. Formerly, the momenta were most likely mapped towards two resonant W bosons and only in less than 0.5% of the cases towards the Higgs-boson resonance. With the new integration channels, the picture changes dramatically: Events revolving around the Higgs-boson resonance occur in almost 20% of all generated momenta. This corresponds to large weights of integration channels, in which the Higgs boson can be mapped towards the resonance. In fact, the probability of picking one of the two integration channels of Figure 3.13 (a) with the Higgs boson permuted to the first or second place is 28.5% after the third optimisation (the probability of the two channels of the corresponding ZZ $\to$ WW diagram is another 5%), whilst the a priori weight sum of four channels was only below 1%.

We did not produce explicit NLO data for testing purposes, but to stress the importance of the new channels, we quote from a posteriori data. Including the permuted channels, there are 4438 integration channels for ud $\to 4\ell$ud $+ \gamma$ at $\mathcal{O}\left(\alpha^7\right)$. After our complete analysis, including

---

[24]Consider case 7 and attach a photon to the first propagator, which was formerly completely determined by the total centre-of-mass energy. We then concluded that the decay chains A and MDD' were independent. If we insert the photon, the "ancestor" is still fixed, but the "heir" becomes free. The order of determining the s-values of the "heir" and the other propagator certainly has an influence on the subsystems A and MDD'. We did not investigate this case further, since the invariant-mass cut on the two jets already forces the minimum s-value of the "heir" much above the resonance. If the integrator picks this class of diagrams, the resulting phase-space point is cut anyway.
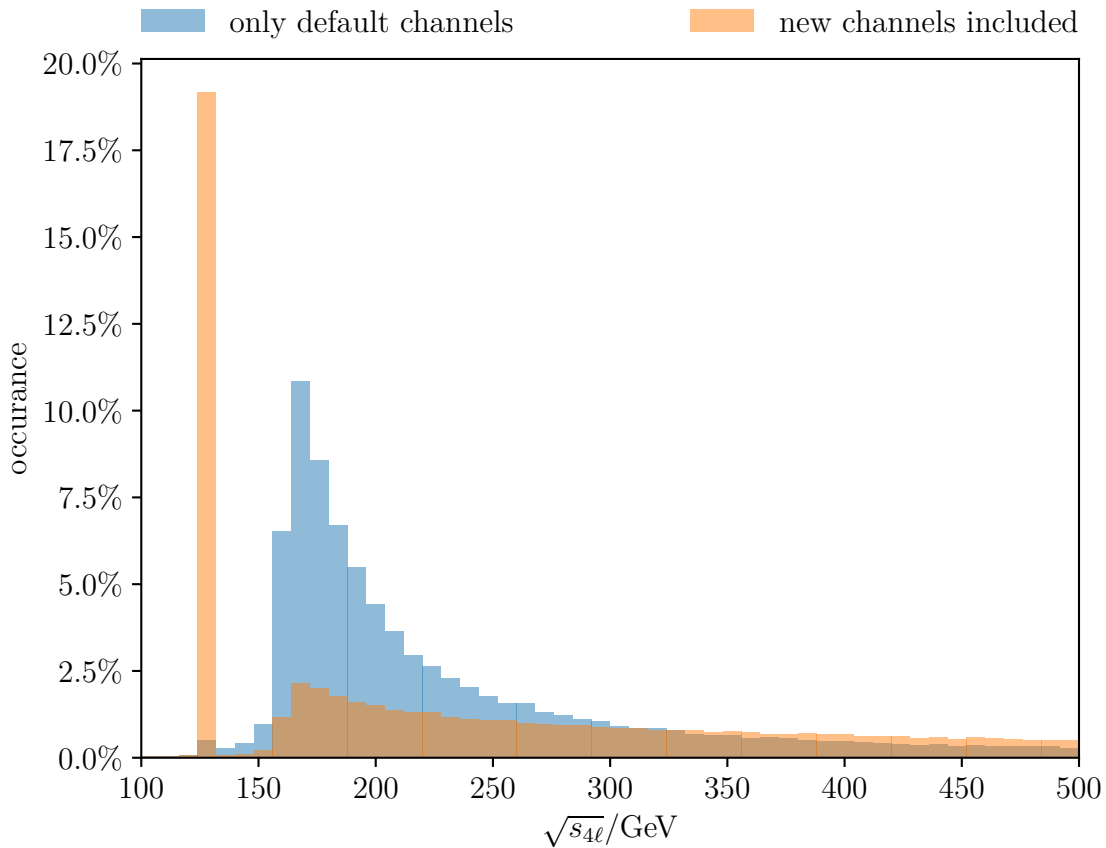
Figure 3.16: Distribution of $\sqrt{s_{4\ell}}$ between the first and third weight optimisation for the partonic channel ud $\rightarrow 4\ell$ud at $\mathcal{O}\left(\alpha^6\right)$ in the VBS setup (see Section 4.2.1). The default Bʙᴍᴄ momentum generation routine without resonance permutation is shown in blue, and the Bʙᴍᴄ momentum generation routine including resonance permutation in orange.

several millions of accepted events, the last weight optimisation gave a cumulated channel weight of $62,8\%$ to a number of only four integration channels. All of these included the Higgs-boson resonance and were permuted channels.

3.2.3   The Catani–Seymour algorithm revisited: resonances

For our calculations, we make use of the CS algorithm. In Section 2.2.5, we saw that this formalism can be used to subtract divergences which emerge from the emission of a real photon. In general, it is an advantage that all external momenta of the $(n+1)$-particle phase space are mapped on-shell onto the reduced n-particle phase space: The reduced matrix element is then a physically valid quantity. However, in the course of W⁺W⁻ scattering and any other process with sharp resonance peaks, there is a negative by-product.

In a very unfortunate momentum constellation of emitter, emissus and spectator, the CS algorithm may take a phase-space point, which does not necessarily need to be near a singularity and which has thus a small event weight, i. e. without subtraction procedure would be completely innocuous, and send the subtraction term directly onto a resonance. In these cases, the subtraction term has a much higher weight than the original phase-space point. This is fine when carrying out the integration analytically. However, it is a catastrophe for Monte Carlo integration: Those events completely spoil the numerical stability of the integration and manifest themselves as sharp edges when plotting the cross section over the number of generated events.

After introducing the new integration channels, this problem was partially solved, because more events were sent towards the resonance peak. A further refinement is not applying the

CS dipole formalism to every phase-space point far away from dangerous phase-space regions, in which the emitted photons cause divergences. This is done by introducing the so-called α parameter (not to be confused with the channel weight α), which was proposed by Nagy and Trócsányi [114]. In the original CS formalism, the dipoles are defined over the complete phase space. The α parameter ($0 < \alpha \leq 1$) restricts the phase-space volume to the more singular regions. While $\alpha = 1$ corresponds to the application of the subtraction dipoles to the full phase space, $\alpha < 1$ introduces a cut-off for the subtraction terms and correspondingly an α dependence of the integrated dipole terms. The modified α-dependent formulae for subtraction terms and integrated dipoles we used can be found in [115]. We also refer to the references therein.

The advantage of taking an $\alpha < 1$ is, at first, a gain in computation time since fewer dipoles have to be computed. On the other hand, if α is chosen too small, the faster integration is spoiled by large numerical cancellations between the real-subtracted and the integrated dipole processes. In the past, we have had positive experiences with $\alpha = 10^{-2}$ as optimum. In our case, we benefit in another way from smaller α parameters: If there are fewer events in which subtraction terms have to be evaluated, there are automatically fewer events in which bad subtraction behaviour can occur. A small value of α also results in a smaller change of the momenta because the phase space is restricted to the singular regions. We hence tried to lower α to a value of 10^{-4} for W^+W^- scattering at $\mathcal{O}\left(\alpha^7\right)$. Although the cancellations between the real emission process and the integrated dipole terms became larger, we still benefitted from the effect of fewer bad subtraction points. Together with the resonance permutation, we could achieve a stable integration for processes with photon radiation from leptons. In the other orders of coupling constants, in which this problem does not occur, we stuck to our usual value of $\alpha = 10^{-2}$.

3.2.4 Photon-to-jet conversion and photon fragmentation

In the context of real emission, there are two subtleties for W^+W^- scattering and similar processes. The photon-to-jet conversion function appears mainly at $\mathcal{O}\left(\alpha_\mathrm{s}\alpha^6\right)$ (and at $\mathcal{O}\left(\alpha^7\right)$ only for photon-induced contributions); the photon fragmentation function mainly at $\mathcal{O}\left(\alpha_\mathrm{s}^2\alpha^5\right)$ (and at $\mathcal{O}\left(\alpha_\mathrm{s}\alpha^6\right)$ also only for photon-induced contributions).

The photon-to-jet conversion function is needed for final-state photon splittings into a quark-antiquark pair. There is an IR divergence connected to this kind of process if the pair is collinear. The underlying types of Born processes for the CS algorithm are hence $\gamma q \to 4\ell q\gamma$, $gq \to 4\ell q\gamma$ or $qq \to 4\ell g\gamma$, and the divergences are cancelled by interfering Born processes of these types with their corresponding virtual processes. The arising problem is that they are not part of our signal final state since it has to contain exactly two jets at the Born level. In the original framework of Bbmc, these final-state photon splitting dipoles are not found by the dipole algorithm, and even if they were, we would miss the corresponding virtual contribution.
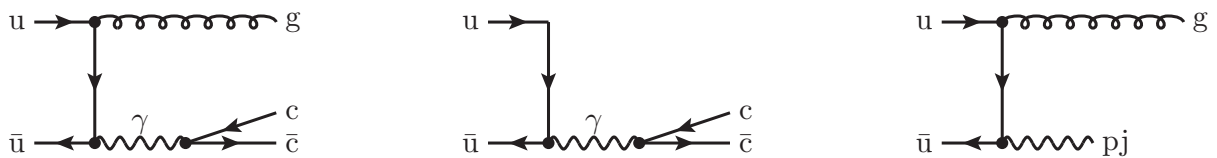
Figure 3.17: Implementation of photon-to-jet conversion. $u\bar{u} \to 4\ell c\bar{c}g$ (left; we omit the leptonic part for clarity) is categorised as gluon-radiation process at $\mathcal{O}\left(\alpha_\mathrm{s}\alpha^6\right)$. The underlying Born, when the internal quark propagator goes on-shell with a QCD singularity, is $u\bar{u} \to 4\ell c\bar{c}$ (middle). If the final-state quark-antiquark pair becomes collinear, then there is a QED singularity associated with the Born process $u\bar{u} \to 4\ell g\gamma$, which does not pass our event selection criteria, unless the photon γ is treated as photojet pj (right).

The first step was making the program recognise that it had to find those contributions. We therefore introduced for internal bookkeeping an auxiliary particle, the photojet pj, and an additional auxiliary coupling $g_\mathrm{pj} = 1$. As the name suggests, the photojet has the same properties

as an ordinary photon (especially it couples to the same particles) but is treated as a jet by our algorithm and couples with a strength of gg_{pj}. Since $g_{\mathrm{pj}} = 1$, this variable is only used for internal bookkeeping. By default, all processes are of $\mathcal{O}\left(g_{\mathrm{pj}}^0\right)$. Only if a quark-antiquark pair is present in the final state of a real emission contribution, the process is defined to be of $\mathcal{O}\left(g_{\mathrm{pj}}^1\right)$. When searching for possible underlying Born contributions, the algorithm also includes photojets in the construction of integration channels. Since internal photojets would immediately lead to expressions of $\mathcal{O}\left(g_{\mathrm{pj}}^2\right)$, such integration channels are dismissed right away and do not lead to double counting of integration channels. In channels without quark–antiquark pairs in the real emission process, no final-state photojets are allowed in the underlying Born contribution, and if such a pair is present, exactly one photojet has to be in the final state to match the required $\mathcal{O}\left(g_{\mathrm{pj}}^1\right)$. A second final-state photojet would also lead to a process of $\mathcal{O}\left(g_{\mathrm{pj}}^2\right)$. With this procedure, we thus assure that we get at most one pj particle in the final state if the ordinary Feynman rules for a photon allow it. We mention that this approach is general for all possible NLO processes, even if there are other photons in the signal LO final-state particle content that must not be identified as jets. The singularity in the real emission matrix element with two collinear quarks is then taken care of by the usual $\gamma^* \to f\bar{f}$ CS dipole. After Bᴮᴍᴄ passes the process to Rᴇᴄᴏʟᴀ for the calculation of the reduced matrix element, the photojet is treated as an ordinary photon by Rᴇᴄᴏʟᴀ again. We give a pictorial description of the problem in Figure 3.17.

The second step is taking account of the virtual singularities connected to this process. Therefore, we added the photon-to-jet conversion function to the usual $\gamma^* \to f\bar{f}$ integrated CS dipole if a configuration with a photojet in the reduced matrix element appears. The photon-to-jet conversion function $D_{\gamma \to \mathrm{j}}$ is related to the hadronic vacuum polarisation $\Delta\alpha_{\mathrm{had}}^{(5)}$ [116]. It is defined as

$$D_{\gamma \to \mathrm{j}}(z, \mu_{\mathrm{F}}) = \Delta\alpha_{\mathrm{had}}^{(5)}(M_{\mathrm{Z}}^2) + \sum_q N_c \frac{Q_q^2 \alpha}{2\pi} \left[\ln\left(\frac{\mu_{\mathrm{F}}^2}{M_{\mathrm{Z}}^2}\right) + \frac{5}{3} \right] P_{f\gamma}(z), \qquad (259)$$

in which $\Delta\alpha_{\mathrm{had}}^{(5)}(M_{\mathrm{Z}}^2) = 276.11 \times 10^{-4}$ is an experimentally determined constant [117], $N_c = 3$ is the number of colours, Q_q the charge of the quarks the photon splits into, μ_{F} is the factorisation scale and $P_{f\gamma}(z)$ the Altarelli–Parisi splitting function evaluated the integration variable z. We refer to [116] for detailed information. Since we calculate each partonic channel separately, we distributed $\Delta\alpha_{\mathrm{had}}^{(5)}(M_{\mathrm{Z}}^2)$ equally over the four active flavours, pulling it under the summation as

$$D_{\gamma \to \mathrm{j}}(z, \mu_{\mathrm{F}}) = \sum_{q=\mathrm{u,d,c,s}} \left\{ \frac{\Delta\alpha_{\mathrm{had}}^{(5)}(M_{\mathrm{Z}}^2)}{4} + N_c \frac{Q_q^2 \alpha}{2\pi} \left[\ln\left(\frac{\mu_{\mathrm{F}}^2}{M_{\mathrm{Z}}^2}\right) + \frac{5}{3} \right] P_{f\gamma}(z) \right\}. \qquad (260)$$

The photon fragmentation function appears when the final state consists of both photons and gluons. This happens in W⁺W⁻ scattering at $\mathcal{O}\left(\alpha_{\mathrm{s}}\alpha^6\right)$ and $\mathcal{O}\left(\alpha_{\mathrm{s}}^2\alpha^5\right)$ when Born processes with final-state gluons emit real photons. Like in the case of the photon-to-jet conversion function, the problem is connected to a misidentification of the underlying singularity and the Born process. The critical real emission processes are $q\gamma \to 4\ell qg\gamma$, $qg \to 4\ell qg\gamma$ or $q\bar{q} \to 4\ell gg\gamma$, when a hard photon and a soft gluon collinear to each other are recombined into a single hard jet. Together with another hard jet, the event may pass the selection criteria (whilst an event with only one hard jet, as well as a soft gluon and a hard photon that are not collinear to each other would not). The soft gluon leads to a QCD singularity with an underlying Born of type $q\gamma \to 4\ell q\gamma$, $qg \to 4\ell q\gamma$ or $q\bar{q} \to 4\ell g\gamma$, which are not part of the signal final state. Apart from other dipole types that stem from a different singularity, the Bᴮᴍᴄ dipole algorithm only finds Born processes with the gluon in the final state ($q\gamma \to 4\ell qg$ et cetera) and their corresponding QED photon emission dipole $q^* \to q\gamma$. In the relevant configurations, Bᴮᴍᴄ thus falsely assumes that there are only QED singularities from photon emission (which are indeed present if the photon is soft and the gluon is hard) and no QCD singularities from soft gluon emission. We show this graphically

in Figure 3.18. In the case of final-state gluon-to-quark-antiquark or photon-to-quark-antiquark splitting, we do not face these soft singularities. If the QCD partons become collinear, the event never passes the selection criteria since we see only one jet in the final state.
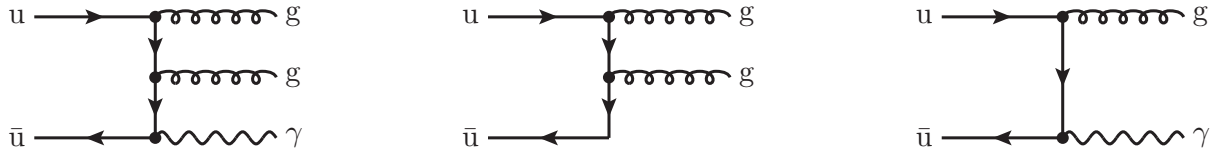

Figure 3.18: Hidden QCD singularity at photon emission.
$u\bar{u} \to 4\ell gg\gamma$ (left; we omit the leptonic part for clarity) is a process at $\mathcal{O}\left(\alpha_s^2\alpha^5\right)$. BBMC assumes the presence of QED dipoles for soft and/or collinear photons with an underlying Born of $u\bar{u} \to 4\ell gg$ (middle). However, one of the gluons can become soft *and* collinear to the photon, recombining into a single jet and leading to a QCD singularity. The underlying Born $u\bar{u} \to 4\ell g\gamma$ (right) is not part of our signal final state. In contrast to the photon-to-jet conversion, the photon must not be identified as jet in this case since it is present as a real particle at NLO.

The solution to the problem of soft gluons recombining with hard photons is to veto configurations in which jets are dominated by photon energies. It had been shown to be convenient in previous works of our group [36, 38, 118] to restrict the energy fraction of photons inside a jet,

$$z_\gamma = \frac{E_\gamma}{E_\gamma + E_a}, \tag{261}$$

where in a given jet E_γ is the energy of the photon and E_a the energy of the QCD particle, to values of $z_\gamma \leq z_{\gamma,\text{cut}} = 0.7$. This cut destroys the IR safety of our calculation, which can be restored by including the fragmentation of quarks into photons [118–122]. Referring back to equation (206), we write

$$d\sigma_{\text{NLO}} = \int_{n+1} \Theta(z_{\gamma,\text{cut}} - z_\gamma)[d\sigma_{\text{real}} - d\sigma_{\text{dip}}] \tag{262}$$

$$+ \int_n \left[d\sigma_{\text{virt}} + \int_1 \left(d\sigma_{\text{dip}} - d\sigma_{\text{dip}}^{\gamma\,\text{coll}}(z_{\gamma,\text{cut}}) \right) - d\sigma_{\text{frag}}(z_{\gamma,\text{cut}}) \right] \tag{263}$$

with the additional term of $d\sigma_{\text{frag}}(z_{\gamma,\text{cut}})$ absorbing the singularities from the imperfect cancellation between virtual and real contribution and

$$d\sigma_{\text{dip}}^{\gamma\,\text{coll}}(z_{\gamma,\text{cut}}) = \Theta(z_\gamma - z_{\gamma,\text{cut}})d\sigma_{\text{dip}} \tag{264}$$

The fragmentation contribution $d\sigma_{\text{frag}}$ is defined via

$$d\sigma_{\text{frag}} = \sum_i d\sigma_{\text{born}} \int_{z_{\gamma,\text{cut}}}^1 dz_\gamma D_{q_i\to\gamma}(z_\gamma), \tag{265}$$

where the sum runs over all quarks and $D_{q_i\to\gamma}$ is the photon fragmentation function. We refer to Appendix A of [118] for appropriate definitions of the modified dipoles and the fragmentation function. As therein, we use for the appearing fit parameters

$$\mu_0 = 0.14\,\text{GeV} \qquad C = -13.26 \tag{266}$$

as measured by ALEPH [123].

BBMC does not combine the two dipole terms to integrate them numerically simultaneously. Instead, the expression $\int d\sigma_{\text{dip}}^{\gamma\,\text{coll}} + d\sigma_{\text{frag}}$ can be integrated analytically and be subtracted from the "standard" dipole contribution.

The newly implemented photon-to-jet conversion function and photon fragmentation function, as well as types of dipoles that were not yet implemented in BBMC for other scattering processes

before calculating W^+W^- scattering, were verified against their implementation in the program MoCaNLO. MoCaNLO is a multichannel integrator used by our group that is independent of Bbmc and can be used as a cross-check. The check was performed in the course of our work on ZZ scattering [37, 38] and is valid in case of W^+W^- scattering since the dipoles, conversion and fragmentation function are universal quantities and all of them that are used for W^+W^- scattering are also required for ZZ scattering and vice versa. The verification was carried out both on the phase-space point level and on the level of integrated cross sections. On the phase-space point level, we took phase-space points generated by MoCaNLO, fed Bbmc with the specific momentum configuration and compared the resulting matrix elements and dipole contributions. We found no deviations between MoCaNLO and Bbmc. In case of the integrated cross sections, we calculated a selection of partonic channels at all appearing orders of the coupling constants. We also found no deviations within a range of 3σ of the integration error.

3.2.5   Integrable singularities and technical cuts

The CS algorithm allows us to compute real and virtual contributions separately and guarantees *integrability*, which means we can carry out the integration $\int d\Gamma$. However, it does not guarantee the finiteness of the integrand since integrable singularities may remain in the phase space. Although hitting such a singular phase-space point by the Monte Carlo integration would not spoil the correctness of the result after generating infinitely many phase-space points, it might destroy the numerical stability of the integration when we generate only a finite number.

As we already discussed, singularities in the case of real emission on the integrand level appear when an emitted massless particle becomes either soft or collinear to its emitter. Formerly, Bbmc used a technical cut on all squared invariant masses s_{ij} of all pairs of final-state particles i and j to exclude such events. These dismissed configurations did not necessarily lead to a singularity because s_{ij} could belong to a particle pair that was never able to emerge from a single propagator (e. g. a gluon and an electron). Fortunately, with the dipole finding algorithm, we already had a tool at hand to refine the technical cuts: The dipole finder checks whether a certain splitting of a propagator to a pair i, j can appear in the process. We, hence, only have to apply the technical cut on such pairs of i and j, for which a possible dipole can be found.
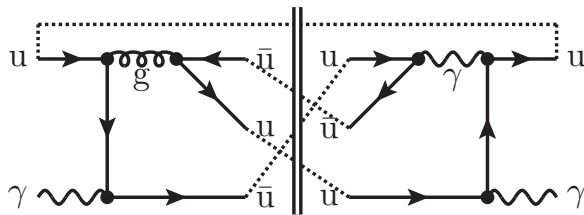
Figure 3.19: Integrable singularity at $\mathcal{O}\left(\alpha_s\alpha^6\right)$:
The process $u\gamma \to 4\ell u u\bar{u}$ appears at $\mathcal{O}\left(\alpha_s\alpha^6\right)$ as interference process with an s-channel gluon or photon (we omit the leptonic part for clarity). If one of the $u\bar{u}$-pairs becomes collinear, there is an integrable singularity from the gluon or photon propagator.

We explicitly state that this dipole does not have to appear in the final calculation of the real process. This is the case for interference processes: If there is no underlying squared Born, then there is no dipole contribution, but the integrable singularity is still present. We show an example in Figure 3.19. However, although the dipole is finally rejected, we may apply the cut on its particle configuration. The value of our technical cut is

$$\frac{s_{ij}}{\hat{s}} < 10^{-10}, \tag{267}$$

where $\hat{s}$ denotes the partonic squared centre-of-mass energy. The phase-space region that is cut away leads to a negligible contribution in the cross section.

4 Numerical results

In this section, we present the numerical results that we obtained for the calculation of the cross section of W^+W^- scattering by using the methods that we described throughout the last sections. We produced LO and NLO differential cross sections for several physical (and one unphysical) observables as well as the integrated cross sections in two different experimental setups.

4.1 Input parameters

The input parameters for physical parameters are identical in both setups and follow the previous setups of our group investigating VBS processes. We simulate an LHC run at a centre-of-mass energy of 13 TeV. As parton distribution functions we use the NLO NNPDF3.1luxQED set with $\alpha_s(M_Z) = 0.118$ in the $n_F = 5$ fixed-flavour scheme [124, 125] as provided by the LHAPDF library [126] throughout. Singularities from initial-state collinear radiation are treated in the $\overline{\text{MS}}$ redefinition of the PDFs.

The central renormalisation and factorisation scales $\mu_{\text{ren}}^{\text{central}}$, $\mu_{\text{fac}}^{\text{central}}$, introduced in Section 2.2.2 and Section 2.2.4, are the geometric average of the transverse momenta of the two hardest jets, called tagging jets,

$$\mu_{\text{ren}}^{\text{central}} = \mu_{\text{fac}}^{\text{central}} = \sqrt{p_{\text{T},\text{j}_1} p_{\text{T},\text{j}_2}}. \tag{268}$$

The discriminating criterion of being "hardest" follows an ordering of identical objects according to their transverse momentum. To check the scale dependence of our calculations, we perform a 7-point scale variation around the central scales, i. e. we use the seven scale pairs

$$(\mu_{\text{ren}}/\mu_{\text{ren}}^{\text{central}}, \mu_{\text{fac}}/\mu_{\text{fac}}^{\text{central}}) = (0.5, 0.5),\ (0.5, 1),\ (1, 0.5),\ (1, 1),\ (1, 2),\ (2, 1),\ (2, 2) \tag{269}$$

for the calculation of the cross sections and use the envelope for an estimation of the perturbative uncertainty.

The EW coupling constant α is fixed within the G_μ scheme [127], where we use the Fermi constant

$$G_\mu = 1.16638 \times 10^{-5}\,\text{GeV}^{-2} \tag{270}$$

as input parameter and calculate the coupling constant via

$$\alpha = \frac{\sqrt{2}}{\pi} G_\mu M_W^2 \left(1 - \frac{M_W^2}{M_Z^2}\right). \tag{271}$$

The (on-shell) masses and widths of the massive gauge bosons are taken from the PDG review 2020 [106],

$$M_Z^{\text{OS}} = 91.1876\,\text{GeV}, \qquad\qquad \Gamma_Z^{\text{OS}} = 2.4952\,\text{GeV}, \tag{272}$$

$$M_W^{\text{OS}} = 80.379\,\text{GeV}, \qquad\qquad \Gamma_W^{\text{OS}} = 2.085\,\text{GeV}, \tag{273}$$

$$\tag{274}$$

and the conversion between on-shell and pole masses and widths, which we use in our calculations, is obtained via [128]

$$M_V = \frac{M_V^{\text{OS}}}{\sqrt{1 + (\Gamma_V^{\text{OS}}/M_V^{\text{OS}})^2}}, \qquad \Gamma_V = \frac{\Gamma_V^{\text{OS}}}{\sqrt{1 + (\Gamma_V^{\text{OS}}/M_V^{\text{OS}})^2}}, \tag{275}$$

where V stands for the W and Z boson, respectively. Since we treat the bottom quark as massless, the only other massive particles in our setup are the Higgs boson and the top quark. Whilst their masses can also be read off the aforementioned PDG review, we can set the top-quark width to

zero because we neglect external bottom quarks and use a diagonal CKM matrix. Therefore, top and bottom quarks can only appear in closed fermion loops and never become resonant particles.[25] The Higgs decay width is taken from [129].

$$m_\text{t} = 173.0\,\text{GeV}, \qquad\qquad \Gamma_\text{t} = 0\,\text{GeV}, \tag{276}$$

$$M_\text{H} = 125.0\,\text{GeV}, \qquad\qquad \Gamma_\text{H} = 4.07 \times 10^{-3}\,\text{GeV}. \tag{277}$$

Propagators of unstable particles are treated in the complex-mass scheme [130–133].

4.2   Event selection

Experimentally, different final states of opposite-sign W scattering have been probed, including either a pair of opposite-charged leptons of the same generation (e^+e^- or $\mu^+\mu^-$) or of different generations ($e^+\mu^-$ or $e^-\mu^+$). As already discussed in Section 3.1, we restrict ourselves in this analysis to a final state with different lepton generations. Especially, we only use the $e^+\mu^-$ state. Since we assume lepton universality and zero lepton masses, the inclusion of the charge-conjugate state would only lead to an overall factor of two in the integrated cross section and differential cross sections with observables containing a single charged lepton would have to be symmetrised with the corresponding observable containing the lepton of opposite charge.

We simulate two different experimental setups, the VBS and the Higgs setup. The selection criteria that are dictated by the construction of the detector are identical in both setups: QCD partons are clustered into jets, and real photons are recombined with jets into jets or with leptons into dressed leptons by the use of the anti-k_T algorithm [134] and a resolution parameter of $R = 0.4$. Only partons with rapidity $|y| < 5$ are considered for recombination, while particles with larger rapidity are assumed to be lost in the beam pipe. The rapidity and the transverse momentum of a particle are defined as

$$y = \frac{1}{2}\ln\frac{E + p_z}{E - p_z}, \qquad p_\text{T} = \sqrt{p_x^2 + p_y^2}, \tag{278}$$

where E is the energy of the particle, p_z is the component of its momentum along the beam axis and p_x, p_y are the components perpendicular to the axis. The other selection criteria differ according to the setup.

4.2.1   VBS setup

We call the first setup "VBS setup" since it is inspired by the previous work on VBS of our group [34–39] and the CMS [135] and ATLAS measurements [136] of opposite-sign W-boson pair production, appropriately modified to the different final-state particle content. Recently, CMS used a similar setup for the observation of W^+W^- scattering [26–28].

Each of the charged leptons has to fulfil

$$p_{\text{T},\ell} > 25\,\text{GeV}, \qquad |y_\ell| < 2.4 \tag{279}$$

and together, they must satisfy

$$p_{\text{T},\ell^+\ell^-} > 30\,\text{GeV}, \qquad M_{\ell^+\ell^-} > 20\,\text{GeV}, \tag{280}$$

where $p_{\text{T},\ell^+\ell^-}$ is the vectorial sum of the transverse momenta (i. e. summing the momenta and extracting the transverse part, *not* taking the sum of the transverse momenta) of both charged leptons and $M_{\ell^+\ell^-}$ is their invariant mass. The missing transverse momentum, which is the transverse part of the sum of the neutrino momenta, is required to fulfil

$$p_{\text{T,miss}} > 40\,\text{GeV}. \tag{281}$$

---

[25]In a cross-check calculation concerning the effect of initial-state bottom quark pairs, they can also appear only as t-channel particles, and we may neglect their decay widths.

After jet clustering, jets that fulfil the conditions

$$p_{\mathrm{T,j}} > 30\,\mathrm{GeV}, \qquad |y_{\mathrm{j}}| < 4.5, \qquad \Delta R_{\mathrm{j}\ell} > 0.4 \tag{282}$$

are called identified jets. The distance ΔR_{ij} is defined as

$$\Delta R_{ij} = \sqrt{(\Delta\phi_{ij})^2 + (\Delta y_{ij})^2} \tag{283}$$

with the azimuthal angle difference $\Delta\phi_{ij} = \min(|\phi_i - \phi_j|, 2\pi - |\phi_i - \phi_j|)$ and the rapidity difference $\Delta y_{ij} = y_i - y_j$. The two identified jets with the highest transverse momenta, called hardest, leading or tagging jets, must obey

$$M_{\mathrm{j_1 j_2}} > 500\,\mathrm{GeV}, \qquad |\Delta y_{\mathrm{j_1 j_2}}| > 2.5. \tag{284}$$

4.2.2   Higgs setup

Our second setup dubbed "Higgs setup" inspired by the CMS measurements of EW Higgs-boson production and decay into a $\mathrm{W}^+\mathrm{W}^-$ pair [137]. This subprocess is, as can be especially inferred from the discussion in Section 3.2.2, an important building block of $\mathrm{W}^+\mathrm{W}^-$ scattering.

In this setup, the charged leptons have to fulfil

$$p_{\mathrm{T},\ell_1} > 25\,\mathrm{GeV}, \qquad p_{\mathrm{T},\ell_2} > 10\,\mathrm{GeV}, \qquad |y_\ell| < 2.4 \tag{285}$$

individually. As in the case of the jets, the leptons are ordered according to their transverse momentum, and we call the harder lepton leading, the softer lepton trailing lepton. The properties of the charged lepton pair are

$$M_{\ell^+\ell^-} > 12\,\mathrm{GeV}, \qquad p_{\mathrm{T},\ell^+\ell^-} > 30\,\mathrm{GeV} \tag{286}$$

and in addition to the VBS setup, there is a minimum distance between the charged leptons with

$$\Delta R_{\ell^+\ell^-} > 0.5. \tag{287}$$

The missing transverse momentum must exceed

$$p_{\mathrm{T,miss}} > 20\,\mathrm{GeV}. \tag{288}$$

Additionally, we require the transverse mass of the four-lepton system $M_{\mathrm{T},4\ell}$ to be within a range below the Higgs mass,

$$60\,\mathrm{GeV} < M_{\mathrm{T},4\ell} < 125\,\mathrm{GeV}, \tag{289}$$

where $M_{\mathrm{T},4\ell}$ is defined as

$$M_{\mathrm{T},4\ell} = \sqrt{2 p_{\mathrm{T},\ell^+\ell^-} p_{\mathrm{T,miss}} \left[1 - \cos\Delta\phi(\ell^+\ell^-, \nu\bar{\nu})\right]}, \tag{290}$$

in which $\Delta\phi(\ell^+\ell^-, \nu\bar{\nu})$ is the azimuthal angle between the sum of the charged-lepton momenta and the sum of the neutrino momenta. We explicitly mention that this is a measurable quantity since the neutrino momenta do not enter this formula individually.

The tagging jets in this setup are required to fulfil

$$p_{\mathrm{T,j_{1,2}}} > 30\,\mathrm{GeV}, \qquad |y_{\mathrm{j_{1,2}}}| < 4.7, \qquad \Delta R_{\mathrm{j_{1,2}}\ell} > 0.4 \tag{291}$$

and the typical VBS topology cuts

$$|\Delta y_{\mathrm{j_1 j_2}}| > 3.5, \qquad M_{\mathrm{j_1 j_2}} > 400\,\mathrm{GeV}. \tag{292}$$

Contribution	$\mathcal{O}\left(\alpha^6\right)$	$\mathcal{O}\left(\alpha_{\mathrm{s}}\alpha^5\right)$	$\mathcal{O}\left(\alpha_{\mathrm{s}}^2\alpha^4\right)$	sum
VBS setup				
$\sigma(4q,\mathrm{VBS})[\,\mathrm{fb}]$	2.6988(3)	0.05439(2)	2.2315(3)	4.9846(4)
$\sigma(4q,\mathrm{non\text{-}VBS})[\,\mathrm{fb}]$	$1.4734(9)\times10^{-4}$	–	0.008641(3)	0.008788(3)
$\sigma(\gamma/\mathrm{g})[\,\mathrm{fb}]$	$6.832(2)\times10^{-6}$	0.010605(2)	4.6714(8)	4.6820(8)
$\sigma(\mathrm{total})[\,\mathrm{fb}]$	2.6988(3)	0.06500(2)	6.9115(9)	9.6752(9)
fraction [%]	27.9	0.7	71.4	100
Higgs setup				
$\sigma(4q,\mathrm{VBS})[\,\mathrm{fb}]$	1.5322(2)	0.007490(5)	0.39866(7)	1.9384(2)
$\sigma(4q,\mathrm{non\text{-}VBS})[\,\mathrm{fb}]$	$1.850(2)\times10^{-5}$	–	0.0012729(6)	0.00129138(6)
$\sigma(\gamma/\mathrm{g})[\,\mathrm{fb}]$	$7.764(4)\times10^{-7}$	0.0015062(4)	1.2923(3)	1.2938(3)
$\sigma(\mathrm{total})[\,\mathrm{fb}]$	1.5322(2)	0.008996(5)	1.6923(3)	3.2335(3)
fraction [%]	47.4	0.3	52.3	100

Table 4.1: Division of LO cross sections into contributions of partonic channels with specific subprocesses. No contributions with external bottom quarks are included. Each contribution is given in fb and as a fraction relative to the sum of the four contributions in per cent. The digits in parentheses indicate integration errors. Note that no non-VBS processes containing two quarks in both the initial and final state contribute at order $\mathcal{O}\left(\alpha_{\mathrm{s}}\alpha^5\right)$.

Additionally, there is a jet veto for any third jet that is produced in NLO real emissions. After clustering, an event with three jets is only kept if the third (softest) jet obeys

$$p_{\mathrm{T},\mathrm{j}_3} < 30\,\mathrm{GeV}. \tag{293}$$

Furthermore, the rapidities of the charged leptons are bounded by the rapidity of the two tagging jets, for which we use the quantity of centrality, also called the Zeppenfeld variable $z_{\ell\mathrm{j}_1\mathrm{j}_2}$. It is defined as

$$z_{\ell\mathrm{j}_1\mathrm{j}_2} = \frac{y_\ell - \frac{y_{\mathrm{j}_1}+y_{\mathrm{j}_2}}{2}}{\Delta y_{\mathrm{j}_1\mathrm{j}_2}} \tag{294}$$

and required to fulfil

$$-0.5 < z_{\ell\mathrm{j}_1\mathrm{j}_2} < 0.5. \tag{295}$$

4.3   Integrated cross sections

4.3.1   Leading order

In this section, we present our LO numerical results. A general overview of both setups at the central scale is given in Table 4.1.

In the VBS setup, which is most comparable to other setups that our group used for the investigation of other VBS processes, the EW process of $\mathcal{O}\left(\alpha^6\right)$ contributes with 2.7 fb to the total cross section. The interference of $\mathcal{O}\left(\alpha_{\mathrm{s}}\alpha^5\right)$ is almost negligible with 0.065 fb and the QCD background of $\mathcal{O}\left(\alpha_{\mathrm{s}}^2\alpha^4\right)$ with 6.9 fb is very large. The total LO cross section amounts to 9.68 fb, to which the EW process contributes 27.9%, the QCD background 71.4% and the interference contribution does not exceed the negligible amount of 0.7%. We can relate this to other VBS processes, of which we give an overview of the relevant orders in Table 4.2.

When we compare the EW contributions among the different processes, W$^+$W$^-$ scattering has the highest cross section of this order and W$^+$W$^+$ scattering comes second. The difference between these processes is the amount of QCD background, and comparing the ratios of EW and QCD-induced cross sections, W$^+$W$^-$ scattering mostly relates to ZZ scattering. This is

Order	W$^+$W$^+$ [35]	W$^+$Z [36]	ZZ [38] (VBS setup)	W$^+$W$^-$ (VBS setup)
$\sigma_{\mathrm{LO}}^{\alpha^6}$[fb]	1.4178(2)	0.25511(1)	0.073676(3)	2.6988(3)
$\sigma_{\mathrm{LO}}^{\alpha_{\mathrm{s}}^2\alpha^4}$[fb]	0.17229(5)	1.0973(1)	0.13614(2)	6.9115(9)
$\sigma_{\mathrm{LO}}^{\mathrm{tot}}$[fb]	1.6383(2)	1.3592(1)	0.2288(3)	9.6752(9)

Table 4.2: LO cross sections of different VBS processes at the central scale for relevant orders with comparable selection criteria, adjusted to the final-state leptonic particle content: $\mathrm{e}^+\nu_{\mathrm{e}}\mu^+\nu_{\mu}$ for W$^+$W$^+$, $\mathrm{e}^+\nu_{\mathrm{e}}\mu^+\mu^-$ for W$^+$Z, $\mathrm{e}^+\mathrm{e}^-\mu^+\mu^-$ for ZZ and $\mathrm{e}^+\nu_{\mathrm{e}}\mu^-\bar{\nu}_{\mu}$ for W$^+$W$^-$. For details, we refer to the given references.

understandable since both processes consist of a neutral final state in the leptonic sector, so there is a plethora of combinations of initial- and final-state partons leading to a physically valid partonic process. All partonic channels that contribute to W$^+$W$^-$ scattering appear in ZZ scattering and vice versa. The processes are thus closely related. The presence of partonic processes with external gluons leads to the large QCD background in particular. This background is not present in W$^+$W$^+$ scattering since we need two positively charged quarks ($\sum q_{q,\mathrm{in}} = 4/3$) in the initial state that flip their weak isospins ($\sum q_{q,\mathrm{out}} = -2/3$) for charge conservation reasons. Similarly, there is one initial/final-state quark pair in W$^+$Z scattering with a weak isospin flip, leading already to an enhanced background, which is, however, still smaller than in the case of a neutral initial state.

In our second setup, the Higgs setup, the EW contribution amounts to 1.5 fb and is smaller than in the VBS setup due to generally stricter cuts. We checked that the most dominant and efficient cut for this setup compared to the VBS setup is the transverse mass cut on the four-lepton system, whose influence superimposes all looser cuts on the trailing lepton, the missing transverse momenta and the jets. The interference contribution is also negligible in this setup with 0.009 fb. The QCD background is drastically reduced to 1.7 fb, which leads to a relative contribution of 47.4% of the EW and of 52.3% of the QCD-induced process.

In the substructure of Table 4.1, we compare the cross sections of partonic channels which contain VBS as subprocess at $\mathcal{O}\left(\alpha^6\right)$ (denoted as $4q$, VBS) with background processes, which are quark-induced channels that feature only 3VP at $\mathcal{O}\left(\alpha^6\right)$ ($4q$, non-VBS) and LO processes with external photons or gluons at all orders (γ/g). We recognise that the VBS contribution at $\mathcal{O}\left(\alpha^6\right)$ is dominant for both setups, whilst non-VBS and photon-induced contributions are completely negligible at this order. At the interference level, the photon–gluon-induced contributions are also smaller than the quark-induced contributions. For the QCD-induced processes, the cross section of non-VBS partonic channels with four external quarks is still much smaller than the one of VBS channels. As already discussed in Section 3.1, calling an $\mathcal{O}\left(\alpha_{\mathrm{s}}^2\alpha^4\right)$ process "VBS" or "non-VBS" is a simplification. In this table it should be rather seen as an abbreviation for "the contribution of those channels at $\mathcal{O}\left(\alpha_{\mathrm{s}}^2\alpha^4\right)$, that have the same external particles as channels, which are featured by VBS subprocesses at $\mathcal{O}\left(\alpha^6\right)$". It is, however, not futile to do this discrimination at $\mathcal{O}\left(\alpha_{\mathrm{s}}^2\alpha^4\right)$ at least once: It allows us to estimate the influence of the PDFs and combinatorical factors to the corresponding cross section of $\mathcal{O}\left(\alpha^6\right)$. At $\mathcal{O}\left(\alpha_{\mathrm{s}}^2\alpha^4\right)$, the different size cannot be explained by the lack of VBS subprocesses. For the QCD-induced process, it is rather an effect of the much smaller PDF share of the parton combinations that appear in non-VBS processes. Additionally, fewer partonic channels are contributing to non-VBS processes. All processes with two valence quarks in the initial state are categorised as VBS processes. However, the ratio between non-VBS and VBS processes at $\mathcal{O}\left(\alpha_{\mathrm{s}}^2\alpha^4\right)$ is in both setups between 3 and 4%, whereas the ratio at $\mathcal{O}\left(\alpha^6\right)$ is of $\mathcal{O}\left(10^{-5}\right)$. We therefore conclude that the non-VBS channels are dominated by the VBS channels at $\mathcal{O}\left(\alpha^6\right)$ even if we take the influence of the PDFs and their numerical inferiority into account. This conclusion is further backed up when we investigate a modified version of our setups in Section 4.3.5.

Order	$\mathcal{O}\left(\alpha_{\mathrm{s}}^2 \alpha^6\right)$	$\mathcal{O}\left(\alpha_{\mathrm{s}}^3 \alpha^5\right)$	$\mathcal{O}\left(\alpha_{\mathrm{s}}^4 \alpha^4\right)$	Sum
VBS setup				
σ_{loop}[fb]	$5.2(6) \times 10^{-8}$	$2.2(1) \times 10^{-4}$	$0.1952(8)$	$0.1954(8)$
fraction [%]	3×10^{-5}	0.1	99.9	100
Higgs setup				
σ_{loop}[fb]	$9(1) \times 10^{-9}$	$8(2) \times 10^{-5}$	$0.1057(7)$	$0.1057(7)$
fraction [%]	9×10^{-6}	0.1	99.9	100

Table 4.3: Loop-induced cross sections at the central scale.

The channels with external gluons dominate in both setups the QCD-induced cross section. On a global comparison of all values in Table 4.1, the Higgs-setup cuts are very efficient to curtail the QCD-induced background by a factor of 4, whereas the EW cross section shrinks only by roughly a factor of 2. Especially the quark-induced content of $\mathcal{O}\left(\alpha_{\mathrm{s}}^2 \alpha^4\right)$ is drastically reduced.

4.3.2   Loop-induced contributions

The loop-induced contributions are, as expected, clearly dominated by the gluon–gluon-induced process of $\mathcal{O}\left(\alpha_{\mathrm{s}}^4 \alpha^4\right)$. They have a value of 0.20 fb in the VBS and a value of 0.11 fb in the Higgs setup. The gluon–photon-induced process of $\mathcal{O}\left(\alpha_{\mathrm{s}}^3 \alpha^5\right)$ and the photon-photon-induced process of $\mathcal{O}\left(\alpha_{\mathrm{s}}^2 \alpha^6\right)$ are completely negligible. We present the results for completeness in Table 4.3. Compared to the summed LO cross sections, they amount to a relative percentage of 2.0% in the VBS and 3.3% in the Higgs setup.

4.3.3   Next-to-leading order

We already stated the impossibility to distinguish between QCD and EW corrections at some orders in the context of the process description with Figure 3.9. However, since the interference contribution is almost negligible in both setups compared to the EW and to the QCD-induced process, we ignore it in our discussion of NLO effects. This means, we pretend in our discussion that there were no corrections to the interference (while, of course, taking them into account in our calculations). So we denote the corrections of $\mathcal{O}\left(\alpha_{\mathrm{s}} \alpha^6\right)$ as QCD corrections to the LO processes of $\mathcal{O}\left(\alpha^6\right)$ and the corrections of $\mathcal{O}\left(\alpha_{\mathrm{s}}^2 \alpha^5\right)$ as EW corrections to the LO processes of $\mathcal{O}\left(\alpha_{\mathrm{s}}^2 \alpha^4\right)$. This is a necessary simplification to unambiguously define relative corrections since it allows us to compare the corrections of $\mathcal{O}\left(\alpha^7\right)$ and $\mathcal{O}\left(\alpha_{\mathrm{s}} \alpha^6\right)$ with $\mathcal{O}\left(\alpha^6\right)$ as well as the comparison of the corrections of $\mathcal{O}\left(\alpha_{\mathrm{s}}^2 \alpha^5\right)$ and $\mathcal{O}\left(\alpha_{\mathrm{s}}^3 \alpha^4\right)$ with $\mathcal{O}\left(\alpha_{\mathrm{s}}^2 \alpha^4\right)$. It is physically impossible to distribute NLO corrections between the different LO bases quantitatively. We nevertheless expect that corrections to the already small interference only lead to effects at the sub-percent level anyway.

Corrections to the electroweak process   We start with the discussion of the corrections to the EW process, which we present in Table 4.4. In this table, we divided the partonic channels further, according to our characterisation in Section 3.1: partonic channels with VBS and without 3VP, partonic channels with VBS and 3VP, further divided in WWZ and WWW production, channels with only 3VP, and the photon-photon- and photon-gluon-induced channels. As we also already stated in Section 3.1.4, NLO partonic channels of the kind $q\bar{q} \to q\bar{q}$g are always treated as gluon-radiation corrections to the $qq \to qq$ LO partonic channel, not as quark-radiation to $q\gamma \to q$g; and NLO partonic channels of the kind $qg/q\gamma \to qq\bar{q}$ are treated as corrections to the photon/gluon-induced process.

Contribution	$\sigma_{\mathrm{LO}}^{\alpha^6}[\,\mathrm{fb}]$	$\Delta\sigma_{\mathrm{NLO}}^{\alpha^7}[\,\mathrm{fb}]$	$\delta^{\alpha^7}[\%]$	$\Delta\sigma_{\mathrm{NLO}}^{\alpha_{\mathrm{s}}\alpha^6}[\,\mathrm{fb}]$	$\delta^{\alpha_{\mathrm{s}}\alpha^6}[\%]$
VBS setup					
VBS only	2.1695(3)	$-0.2812(8)$	-13.0	$-0.149(2)$	-6.8
VBS + WWW	0.13783(3)	$-0.0164(2)$	-11.9	0.0071(4)	5.2
VBS + WWZ	0.39140(6)	$-0.0427(3)$	-10.9	$-0.0135(9)$	-3.5
WWW only	$5.319(8) \times 10^{-5}$	$-1.49(5) \times 10^{-5}$	-28.0	0.01169(1)	2×10^4
WWZ only	$9.415(3) \times 10^{-5}$	$-2.72(3) \times 10^{-5}$	-28.8	0.003907(2)	4×10^3
$\gamma\gamma/\gamma\mathrm{g}$	$6.832(2) \times 10^{-6}$	0.03292(1)	5×10^5	$-2(6) \times 10^{-4}$	-3×10^3
total	2.6988(3)	$-0.3074(9)$	-11.4	$-0.140(2)$	-5.2
Higgs setup					
VBS only	1.1958(2)	$-0.091(1)$	-7.6	$-0.241(1)$	-20.2
VBS + WWW	0.06603(1)	$-0.0052(2)$	-7.8	$-0.0092(2)$	-14.0
VBS + WWZ	0.27030(4)	$-0.0160(5)$	-5.9	$-0.0459(6)$	-17.0
WWW only	$6.28(2) \times 10^{-6}$	$-1.8(1) \times 10^{-6}$	-28.9	0.002509(5)	4.0×10^4
WWZ only	$1.223(2) \times 10^{-5}$	$-3.30(8) \times 10^{-6}$	-27.0	$6.769(6) \times 10^{-4}$	6×10^3
$\gamma\gamma/\gamma\mathrm{g}$	$7.764(4) \times 10^{-7}$	0.00916(2)	1×10^6	$-0.0590(7)$	-7×10^5
total	1.5322(2)	$-0.1033(13)$	-6.7	$-0.352(1)$	-23.0

Table 4.4: NLO corrections at $\mathcal{O}\left(\alpha^7\right)$ and $\mathcal{O}\left(\alpha_{\mathrm{s}}\alpha^6\right)$ in relation to their LO counterparts of $\mathcal{O}\left(\alpha^6\right)$, classified after appearing subprocesses, and corresponding relative corrections $\delta^{\alpha^7} = \Delta\sigma_{\mathrm{NLO}}^{\alpha^7}/\sigma_{\mathrm{LO}}^{\alpha^6}$ and $\delta^{\alpha_{\mathrm{s}}\alpha^6} = \Delta\sigma_{\mathrm{NLO}}^{\alpha_{\mathrm{s}}\alpha^6}/\sigma_{\mathrm{LO}}^{\alpha^6}$.

Electroweak corrections, $\mathcal{O}\left(\alpha^7\right)$ As we have already seen in the discussion of our LO results, the dominant contribution arises from partonic channels with VBS subprocesses. Quantitatively, this does not change at NLO since the bulk of the absolute EW corrections also emerges from VBS channels. Channels with VBS processes even dominate the channels with combinations of VBS and 3VP, but this is also a PDF effect. In terms of relative EW corrections, they are quite similar, ranging roughly between -11% and -13% in the VBS and -6% and -8% in the Higgs setup. The two pure 3VP categories also do not differ sizeably within the setups concerning the EW corrections, which are between -28% and -29% in the VBS and -27% and -29% in the Higgs setup. The corrections to the photon-induced processes have the enormous size of $\mathcal{O}\left(+10^6\%\right)$ in both setups. Due to the small absolute size of the LO contributions, neither the corrections to the photon-induced nor those to the pure 3VP contributions have a large influence on the overall relative corrections, which are aligned with the corrections of the VBS processes with -11.4% in the VBS and -6.7% in the Higgs setup.

Compared to the other VBS processes, which we briefly recapitulate in Table 4.5, the relative size of the total corrections is *relatively* small. In other VBS processes, the EW corrections range between -15% and -18%. However, we have to state that an EW correction of -11% or even -7% should not *generally* be considered as "small" because the naively expected size of a relative EW correction is around $\alpha \approx 1/137 \approx 1\%$. The large EW corrections in other VBS processes emerge from the presence of Sudakov logarithms. We recall that the Sudakov logarithms are terms proportional to $\ln M_{\mathrm{W}}^2/Q^2$ and $\ln^2 M_{\mathrm{W}}^2/Q^2$ which survive the Bloch–Nordsieck cancellation. In our case, Q^2 is the four-lepton invariant mass squared $M_{4\ell}^2 \equiv s_{4\ell}$ as the energy scale of the EW subprocess. Studies from our group with other VBS processes have shown that this quantity is particularly large in VBS processes giving rise to large Sudakov logarithms and the Sudakov approximation [138] is a viable method to estimate the NLO cross section [34, 36, 37].

The leading contribution for $\mathrm{W}^+\mathrm{W}^-$ scattering is

$$\sigma_{\mathrm{LL}} = \sigma_{\mathrm{LO}} \left[1 - \frac{\alpha}{4\pi} 4 C_W^{\mathrm{EW}} \ln^2 \frac{s}{M_{\mathrm{W}}^2} + \frac{\alpha}{4\pi} 2 b_W^{\mathrm{EW}} \ln \frac{s}{M_{\mathrm{W}}^2} \right] \qquad (296)$$

	W$^+$W$^+$ [35]	W$^+$Z [36]	ZZ [38] (VBS setup)	W$^+$W$^-$ (VBS setup)	W$^+$W$^-$ (Higgs setup)
$\sigma_{\mathrm{LO}}^{\alpha^6}$[fb]	1.4178(2)	0.25511(1)	0.073676(3)	2.6988(3)	1.5322(2)
$\Delta\sigma_{\mathrm{NLO}}^{\alpha^7}$[fb]	$-0.2169(3)$	$-0.0409^\dagger$	$-0.01299(5)$	$-0.3074(9)$	$-0.1033(13)$
δ^{α^7}[%]	-15.3	-16.0	-17.6	-11.4	-6.7

Table 4.5: NLO EW corrections for different VBS processes at the central scale.
†This is a value not given explicitly in the cited paper reconstructed from $\sigma_{\mathrm{LO}}^{\alpha^6}$ and $\sigma_{\mathrm{NLO}}^{\alpha^6+\alpha^7}$, thus lacking the specification of an integration error.

with the EW Casimir operator $C_W^{\mathrm{EW}} = 2/\sin^2\theta_{\mathrm{w}}$ and the beta function coefficient $b_W^{\mathrm{EW}} = 19/(6\sin^2\theta_{\mathrm{w}})$. This correction factor is universal to $VV \to VV$ processes and does not depend on particular kinematic variables except the centre-of-mass energy of the four-lepton system. This means, in contrast to the subleading terms, we can perform a global approximation and do not have to evaluate it event-by-event. We applied the Sudakov approximation to our differential cross section with respect to the four-lepton invariant mass, calculating $(\mathrm{d}\sigma/\mathrm{d}M_{4\ell})_{\mathrm{LL}}$ with a bin width of 100 GeV, and integrated it. We give further information on this topic in Appendix A. The results of our setups are

$$\delta_{\mathrm{LL,VBS}}^{\alpha^7} = -11.9\%, \qquad \delta_{\mathrm{LL,Higgs}}^{\alpha^7} = -5.6\% \tag{297}$$

with the definition $\delta_{\mathrm{LL}}^{\alpha^7} = \sigma_{\mathrm{LL}}/\sigma_{\mathrm{LO}} - 1$. We remark that the approximation fits very well with the VBS result and underestimates the corrections for the Higgs result. Nevertheless, we have to be careful in our process since the Sudakov approximation is only valid if $s_{4\ell} \gg M_{\mathrm{W}}^2$. In our case, however, the sharp Higgs-boson resonance peak at $M_{\mathrm{H}} \approx 1.5 M_{\mathrm{W}}$ is a crucial contribution, which drags the cross section towards small values of $M_{4\ell}$. This becomes especially clear when we calculate the mean value for the invariant mass $\langle M_{4\ell} \rangle$ from of the binned distribution,[26] which is

$$\langle M_{4\ell} \rangle_{\mathrm{VBS}} \approx 333\,\mathrm{GeV}, \qquad \langle M_{4\ell} \rangle_{\mathrm{Higgs}} \approx 221\,\mathrm{GeV}. \tag{298}$$

We may compare this value with the literature result for W$^+$W$^+$ scattering of $\langle M_{4\ell} \rangle_{\mathrm{W^+W^+}} \approx 390\,\mathrm{GeV}$ [34]. The mean value for the VBS setup is already smaller, and, as expected, the cuts for the Higgs setup are designed such that even lower values of $M_{4\ell}$ are favoured.

We did not put special effort into explaining the large EW corrections in channels with only 3VP because of their small absolute size, which makes them completely negligible. For our fiducial phase space concerning VBS, we are in far-off corners of the fiducial phase space for a sensible investigation of 3VP. In fact, the applied invariant mass and rapidity difference cuts on the two jets are almost complementary (see e. g. [139]), since 3VP cuts focus on s-channel jets, whereas VBS cuts try to avoid them.

In contrast, the absurdly large relative corrections to the photon-induced processes at $\mathcal{O}(\alpha^7)$ are easily explicable. All of these channels are doubly PDF-suppressed at LO because of the $\gamma\gamma$ initial state, whereas some of them with a $q\gamma$ initial state are only singly suppressed at NLO. Additionally, in some photon–quark-induced processes at $\mathcal{O}(\alpha^7)$ the possibility of VBS-subprocesses opens up (c. f. Figure 3.12 (a)), allowing the particular partonic process to pass our cuts more likely. These two features do not only combine to an extreme relative correction due to the small LO normalisation base but also to a sizeable absolute NLO correction of $\mathcal{O}(1\%)$ if we normalise the photon-induced corrections to the total LO cross section of $\mathcal{O}(\alpha^6)$.

QCD corrections, $\mathcal{O}(\alpha_{\mathrm{s}}\alpha^6)$ The QCD corrections of $\mathcal{O}(\alpha_{\mathrm{s}}\alpha^6)$ show a qualitatively different behaviour between the VBS and the Higgs setup. While the total EW corrections are

---

[26]We remark that $\langle M_{4\ell} \rangle \neq \sqrt{\langle s \rangle}$. $\langle M_{4\ell} \rangle$ is used as comparison with the literature, $\langle s \rangle$ for our proper calculations, see Appendix A.

smaller in the Higgs setup, the QCD corrections are much larger and amount to -23% in the Higgs compared to -5% in the VBS setup. As for the EW corrections, there is a quantitative difference in the size of relative corrections between the channels including VBS and those including only 3VP processes.

In the VBS channels, the QCD correction in the VBS setup ranges between -7% and $+5\%$, whereas the Higgs setup shows corrections of -14% to -20%. This large difference between the two setups emerges from the jet veto, which suppresses the (positive) contributions from real gluon emissions whilst leaving the (negative) contributions from virtual corrections unaffected. The experimental cut on $p_{\mathrm{T,j_3}} \leq 30\,\mathrm{GeV}$ is very strict and delivers an example for incomplete Kinoshita–Lee–Nauenberg cancellations (c. f. Section 2.2). The jet veto leads to terms proportional to $\alpha_{\mathrm{s}} \ln p_{\mathrm{T,j\ cut}}^2/Q^2$, instead of α_{s} in the perturbation series expansion, where Q is a typical energy scale within the hard process [140, 141]. When we take $Q^2 = \langle s_{4\ell,\mathrm{LO}\ \alpha^6} \rangle = 268.3^2\,\mathrm{GeV}^2$ (see Appendix A) as typical scale in the Higgs setup, we obtain $\ln p_{\mathrm{T,j\ cut}}^2/Q^2 \approx -4.4$ and we effectively expand in $4.4\alpha_{\mathrm{s}}$ instead of α_{s}. This larger (absolute) value of the expansion factor in the perturbation series spoils its convergence rate. It is still an open question whether including a jet resummation procedure is crucial for reliable predictions of the cross section with recent studies coming to different results for different processes [141].

The 3VP channels show very large positive corrections of $\mathcal{O}\left(+10^4\%\right)$ in both setups. We can explain this effect as follows: In these channels, the two quarks forming the two jets in the final state have to emerge from an s-channel vector boson (c. f. Figure 3.2 (c) and (d)) at LO. This resonance is extremely suppressed by our cut on the invariant mass of the two jets. However, the emission of a gluon at NLO changes the situation since the two hard jets may consist of the gluon and one of the quarks (c. f. Figure 3.10 (b) and similar diagrams). This new configuration is much more likely to pass the VBS cuts, leading to a strong enhancement of the 3VP contributions at NLO. This effect evidently outshines the effect of the jet veto because the two jets that emerge from the s-channel boson are most likely low-energetic and have a small transverse momentum that naturally allows them to pass the jet veto. As a result, these corrections are the only positive QCD corrections in the Higgs setup. The extreme values of the relative corrections in both setups are also due to the small reference value at LO. In absolute values, the channels are still irrelevant compared to the VBS channels.

The other extremely large relative corrections in the last column of Table 4.4 come from the photon/gluon-induced channels. Several effects we already discussed come together in this case: less PDF-suppressed initial states, new channels including VBS, a small LO reference value and, in the case of the Higgs setup, additionally, the jet veto. In the VBS setup, the large relative corrections might also only be an artefact when we look at the small size of the absolute value and its corresponding integration error. We thus cannot definitely state their origins.

Corrections to the QCD-induced process Next, we present the results for $\mathcal{O}\left(\alpha_{\mathrm{s}}^2\alpha^5\right)$ and $\mathcal{O}\left(\alpha_{\mathrm{s}}^3\alpha^4\right)$. As already discussed, the latter are unambiguously the QCD corrections to the QCD-induced process. In contrast, the first ones consist of both QCD corrections to the interference as well as EW corrections to the QCD-induced contributions. By simple power-counting arguments and the size of the coupling constants α and α_{s}, it is generally expected that relative QCD corrections are about 10 times larger than EW ones. However, the QCD-induced LO contribution itself is 100–200 times larger than the interference contribution in our two setups. We therefore expect that the EW corrections to $\mathcal{O}\left(\alpha_{\mathrm{s}}^2\alpha^4\right)$ are the main part of $\mathcal{O}\left(\alpha_{\mathrm{s}}^2\alpha^5\right)$ and define this order conventionally as EW corrections. The "error" we obtain with this convention is – presumably[27] – larger than in the case of $\mathcal{O}\left(\alpha\alpha^6\right)$, where we neglected the influence of EW corrections to a small quantity. However, we have to decide on a nomenclature and normalisation. The inclusion of the interference contribution to the normalisation of $\mathcal{O}\left(\alpha_{\mathrm{s}}^2\alpha^5\right)$ and the labelling as combined correction would only result in a minor difference. As already stated in the process description, we divide the process into categories according to appearing Mandelstam variables. In addition

---

[27]It is still physically impossible to quantify the specific amounts, and we rely on power-counting estimations.

Contribution	$\sigma_{\mathrm{LO}}^{\alpha_{\mathrm{s}}^2\alpha^4}\,[\mathrm{fb}]$	$\Delta\sigma_{\mathrm{NLO}}^{\alpha_{\mathrm{s}}^2\alpha^5}\,[\mathrm{fb}]$	$\delta^{\alpha_{\mathrm{s}}^2\alpha^5}\,[\%]$	$\Delta\sigma_{\mathrm{NLO}}^{\alpha_{\mathrm{s}}^3\alpha^4}\,[\mathrm{fb}]$	$\delta^{\alpha_{\mathrm{s}}^3\alpha^4}\,[\%]$
VBS setup					
$4q$, s-channel	$0.008641(2)$	$-0.001994(6)$	-23.1	$-0.02488(8)$	-288
$4q$, t-channel	$0.46532(5)$	$-0.0400(2)$	-8.6	$-0.1765(7)$	-37.9
$4q$, s- & t-channel	$0.46617(7)$	$-0.048(2)$	-10.4	$-0.1987(7)$	-42.6
$4q$, t- & u-channel	$1.3000(3)$	$-0.096(2)$	-7.4	$-0.681(3)$	-52.4
$qq \to \mathrm{gg}$	$0.4334(1)$	$-0.0381(4)$	-8.8	$-0.112(1)$	-25.9
$\gamma\mathrm{g}/\mathrm{gg}/q\mathrm{g}$	$4.2380(8)$	$-0.350(1)$	-8.3	$-0.899(4)$	-21.2
total	$6.9115(9)$	$-0.574(3)$	-8.3	$-2.098(6)$	-30.3
Higgs setup					
$4q$, s-channel	$0.001273(1)$	$-3.38(2)\times10^{-4}$	-26.6	$-0.01471(6)$	-1155
$4q$, t-channel	$0.09375(2)$	$-0.0057(2)$	-6.1	$-0.0970(2)$	-104
$4q$, s- & t-channel	$0.09048(2)$	$-0.00683(7)$	-7.5	$-0.1077(3)$	-119
$4q$, t- & u-channel	$0.2144(1)$	$-0.0120(3)$	-5.6	$-0.2518(5)$	-117
$qq \to \mathrm{gg}$	$0.15914(8)$	$-0.0078(3)$	-4.9	$-0.0607(5)$	-38.1
$\gamma\mathrm{g}/\mathrm{gg}/q\mathrm{g}$	$1.1332(3)$	$-0.0570(5)$	-5.0	$-0.781(2)$	-68.9
total	$1.6920(3)$	$-0.0897(6)$	-5.3	$-1.312(2)$	-77.6

Table 4.6: NLO corrections at $\mathcal{O}\left(\alpha_{\mathrm{s}}^2\alpha^5\right)$ and $\mathcal{O}\left(\alpha_{\mathrm{s}}^3\alpha^4\right)$ in relation to their LO counterparts of $\mathcal{O}\left(\alpha_{\mathrm{s}}^2\alpha^4\right)$, classified after appearing subprocesses, and corresponding relative corrections $\delta^{\alpha_{\mathrm{s}}^2\alpha^5} = \Delta\sigma_{\mathrm{NLO}}^{\alpha_{\mathrm{s}}^2\alpha^5}/\sigma_{\mathrm{LO}}^{\alpha_{\mathrm{s}}^2\alpha^4}$ and $\delta^{\alpha_{\mathrm{s}}^3\alpha^4} = \Delta\sigma_{\mathrm{NLO}}^{\alpha_{\mathrm{s}}^3\alpha^4}/\sigma_{\mathrm{LO}}^{\alpha_{\mathrm{s}}^2\alpha^4}$.

to channels with four external quarks, there are channels with external (final-state and/or initial-state) gluons already at LO. Like in the case of the EW process, we use the convention that NLO partonic channels of $qq \to qq\mathrm{g}$ and $qq \to qq\gamma$ are corrections to the corresponding $qq \to qq$ LO partonic channel and all other partonic channels count as corrections to the photon- and/or gluon-induced processes or processes with two gluons in the final state. The results are summarised in Table 4.6.

Electroweak corrections, $\mathcal{O}\left(\alpha_{\mathrm{s}}^2\alpha^5\right)$ The corrections of $\mathcal{O}\left(\alpha_{\mathrm{s}}^2\alpha^5\right)$ amount in total to -8% in the VBS and -5% in the Higgs setup. This overall behaviour verifies our assumption that the corrections are mainly EW and not QCD corrections: Real QCD corrections are accompanied by the emergence of an additional jet, which would trigger the harsh jet veto in the Higgs setup, as we already saw at $\mathcal{O}\left(\alpha_{\mathrm{s}}\alpha^6\right)$ and which we also see later at $\mathcal{O}\left(\alpha_{\mathrm{s}}^3\alpha^4\right)$. In the absence of these large corrections at $\mathcal{O}\left(\alpha_{\mathrm{s}}^2\alpha^5\right)$, the corrections in the Higgs setup are smaller than in the VBS setup, giving evidence of our claim. However, this picture changes when looking at individual contributions. We recognise that the corrections in the VBS setup are larger than in the Higgs setup except for the channels with only s-channel gluon exchange, where -23% in the VBS setup compare to -27% in the Higgs setup. This particular relative correction is also much larger than the average. This contribution is also special because of its very small LO base. We explain this as follows: The small contribution resembles the fact that jets emerging from s-channel vector bosons are strongly suppressed, as we already saw in the case of the EW 3VP channels. However, there is the same effect at $\mathcal{O}\left(\alpha_{\mathrm{s}}^2\alpha^5\right)$ as at $\mathcal{O}\left(\alpha_{\mathrm{s}}\alpha^6\right)$ (and also at $\mathcal{O}\left(\alpha_{\mathrm{s}}^3\alpha^4\right)$), when we interpret it as QCD correction to the interference process: the additional radiated gluon is able to form a third jet which is then able to pass the VBS cuts. Especially, this opens up additional t-channel diagrams at NLO. We hence conclude that the corrections to the s-channel contributions at $\mathcal{O}\left(\alpha_{\mathrm{s}}^2\alpha^5\right)$ are *not* mainly EW corrections – the emission of an additional photon does not lead to additional jets with t-channel vector bosons and subsequently not to an enhancement of the process –, but in fact a manifestation of QCD corrections to the interference. To a much less dominant extent, this effect is also seen in partonic channels with s- and t-channel diagrams with

a relative correction larger than the average with -10% in the VBS and -8% in the Higgs setup. The other contributions do not show very distinct behaviour with relative corrections between -7% and -9% in the VBS and -5% and -6% in the Higgs setup.

QCD corrections, $\mathcal{O}\left(\alpha_s^3\alpha^4\right)$ At $\mathcal{O}\left(\alpha_s^3\alpha^4\right)$, we see large negative corrections for both setups. While the overall corrections for the VBS setup have a reasonable size of -30%, the size of the corrections for the Higgs setup reaches -78%. In general, we see that channels with four external quarks show larger corrections than channels with external gluons in both setups. All of these partonic channels show QCD corrections of more than -100% in the Higgs setup, which is clearly an unphysical result. Also for the sum of all partonic contributions, the differential cross section becomes negative, as we will see in a moment. We thus expect large higher-order corrections, which can be estimated by investigating the scale dependence. We address this topic in the following section. The only very distinct individual cross section that we want to mention are the $4q$, s-channel contributions. As in the case of $\mathcal{O}\left(\alpha_s\alpha^6\right)$ and $\mathcal{O}\left(\alpha_s^2\alpha^5\right)$, they receive their enormous size due to the third jet at NLO that is produced via t-channel.

4.3.4   Scale dependence

In this section, we present our results for the seven-point scale variation. Factorisation and renormalisation scales are not physical parameters but are artificially introduced for calculations in perturbation theory. We introduced the renormalisation scale in Section 2.2.1 for dimensional regularisation and briefly talked about it in the context of renormalisation. The factorisation scale was introduced in Section 2.2.4. The choice of a specific scale value in a fixed-order perturbation-theory calculation is arbitrary and its effects are cancelled when taking all orders of perturbation theory into account. Investigating the scale dependence of a cross section is, hence, an estimation for higher-order effects. Therefore, one has to carefully balance between a good position in the region near the optimum, where

$$\frac{\mathrm{d}\sigma_{\mathrm{NLO}}}{\mathrm{d}\mu_{\mathrm{R}}} \approx 0, \qquad \frac{\mathrm{d}\sigma_{\mathrm{NLO}}}{\mathrm{d}\mu_{\mathrm{F}}} \approx 0, \tag{299}$$

to obtain a solid fixed-order result on the one hand and not underestimate higher-order effects on the cross section by exactly placing oneself on the optimum. At LO, the results generally become smaller at higher scales due to the running of α_s. NLO results show a maximum of the cross section with a steep rising left and a moderately falling right flank (for diagrammatic examples see also Figure 5.1 and Figure 5.2). A good central scale choice is said to be placed somewhere on the right of the maximum in a region with moderate NLO corrections.

For our process, we first have a look at the LO results in Table 4.7. Since we work in the G_μ scheme with a fixed electromagnetic coupling constant α, altering the renormalisation scale does not influence the cross section of $\mathcal{O}\left(\alpha^6\right)$. The EW cross section depends only very little on the factorisation scale, which enters through the PDFs for these processes. As soon as our process includes the strong coupling constant α_s, the scale dependence becomes stronger because of the running of α_s. We see at LO the typical behaviour of the interference, QCD-induced and loop-induced cross sections becoming smaller with higher scales. At LO, the cross sections in the two setups have a scale uncertainty of

$$\sigma_{\mathrm{LO,VBS}}^{\mathrm{total}} = 9.6753(9)^{+29.2\%}_{-20.1\%}\,\mathrm{fb}, \qquad \sigma_{\mathrm{LO,Higgs}}^{\mathrm{total}} = 3.2335(4)^{+22.7\%}_{-16.0\%}\,\mathrm{fb}. \tag{300}$$

In absolute values, this translates to a variation between $12.449\,\mathrm{fb}$ and $7.7354\,\mathrm{fb}$ in the VBS setup and between $3.9672\,\mathrm{fb}$ and $2.7175\,\mathrm{fb}$ in the Higgs setup. We note that the lesser scale dependence in the Higgs setup at LO is a result of the smaller QCD-induced background.

Next, we look at the NLO cross sections of $\mathcal{O}\left(\alpha^7\right)$ and $\mathcal{O}\left(\alpha_s\alpha^6\right)$. As before, we treat them as corrections to the EW process of $\mathcal{O}\left(\alpha^6\right)$ and normalise them accordingly. The full results are shown in Table 4.8. Like the LO EW process, the NLO EW corrections do not depend on

Scale $(\mu_{\mathrm{F}}, \mu_{\mathrm{R}})$	$\sigma_{\mathrm{LO}}^{\alpha^6}[\,\mathrm{fb}]$	$\sigma_{\mathrm{LO}}^{\alpha_{\mathrm{s}}\alpha^5}[\,\mathrm{fb}]$	$\sigma_{\mathrm{LO}}^{\alpha_{\mathrm{s}}^2\alpha^4}[\,\mathrm{fb}]$	$\sigma_{\mathrm{LO}}^{\mathrm{total}}[\,\mathrm{fb}]$	$\sigma_{\mathrm{loop}}[\,\mathrm{fb}]$
VBS setup					
$(1/2, 1/2)$	2.9187(3)	0.07639(3)	9.504(1)	12.499(1)	0.375(2)
$(1/2, 1)$	2.6988(3)	0.07191(2)	8.588(1)	11.358(1)	0.314(1)
. $(1, 1/2)$	2.9187(3)	0.06907(2)	7.650(1)	10.637(1)	0.2331(9)
$(1, 1)$	2.6988(3)	0.06500(2)	6.9115(9)	9.6753(9)	0.1954(8)
$(1, 2)$	2.5069(3)	0.06144(2)	6.2853(8)	8.8537(9)	0.1661(7)
$(2, 1)$	2.6988(3)	0.05932(2)	5.6882(7)	8.4463(8)	0.1282(5)
$(2, 2)$	2.5069(3)	0.05607(2)	5.1726(7)	7.7354(7)	0.1089(4)
Higgs setup					
$(1/2, 1/2)$	1.6324(2)	0.010598(6)	2.3242(4)	3.9672(5)	0.201(1)
$(1/2, 1)$	1.5322(2)	0.010009(5)	2.1319(4)	3.6741(4)	0.172(1)
$(1, 1/2)$	1.6324(2)	0.009529(5)	1.8453(3)	3.4872(4)	0.1235(9)
$(1, 1)$	1.5322(2)	0.008996(5)	1.6923(3)	3.2335(4)	0.1057(7)
$(1, 2)$	1.4418(1)	0.008533(5)	1.5580(3)	3.0084(3)	0.0915(7)
$(2, 1)$	1.5322(2)	0.008173(4)	1.3774(3)	2.9177(3)	0.0686(5)
$(2, 2)$	1.4418(1)	0.007751(4)	1.2679(2)	2.7175(3)	0.0593(4)

Table 4.7: Seven-point scale variations at LO $\mathcal{O}\left(\alpha^6\right), \mathcal{O}\left(\alpha_{\mathrm{s}}\alpha^5\right), \mathcal{O}\left(\alpha_{\mathrm{s}}^2\alpha^4\right)$ and the total LO cross section as well as the total loop-induced cross section. The scales are given in multiples of $\mu_{\mathrm{F}}^{\mathrm{centralsc}}$ and $\mu_{\mathrm{F}}^{\mathrm{centralsc}}$ defined in equation (268).

the renormalisation scale and show only a flat dependence on the factorisation scale due to the PDFs. The QCD corrections are also quite flat. Especially in the VBS setup, we seem to be very close to the peak, where $\mathrm{d}\sigma_{\mathrm{NLO}}/\mathrm{d}\mu \approx 0$. In the Higgs setup, we are clearly on the left of the maximum since our largest $(2, 2)$-scale provides higher cross sections than any other scale choice. For the total NLO corrections to the EW process, the scale uncertainty ranges between

$$\sigma_{\mathrm{NLO,VBS}}^{\alpha^6+\alpha^7+\alpha_{\mathrm{s}}\alpha^6} = 2.253(3)_{-2.5\%}^{+1.3\%}, \qquad \sigma_{\mathrm{NLO,Higgs}}^{\alpha^6+\alpha^7+\alpha_{\mathrm{s}}\alpha^6} = 1.077(2)_{-7.8\%}^{+5.3\%} \tag{301}$$

or in absolute values between 2.196 fb and 2.283 fb in the VBS setup, and between 0.993 fb and 1.134 fb in the Higgs setup.

We now focus our attention on the QCD-induced process of $\mathcal{O}\left(\alpha_{\mathrm{s}}^2\alpha^4\right)$ and its corrections of $\mathcal{O}\left(\alpha_{\mathrm{s}}^2\alpha^5\right)$ and $\mathcal{O}\left(\alpha_{\mathrm{s}}^3\alpha^4\right)$ which we present in Table 4.9. We note that the NLO cross sections at $\mathcal{O}\left(\alpha_{\mathrm{s}}^2\alpha^4\right) + \mathcal{O}\left(\alpha_{\mathrm{s}}^2\alpha^5\right)$ are still dominated by the falling behaviour of the LO cross section and follow them almost exactly. This justifies again our nomenclature as EW corrections since EW corrections always mimic the LO behaviour due to their lack of introducing an own scale dependence. The QCD corrections for the QCD-induced contribution show the exact opposite behaviour and increase with higher scales in both setups. As for the QCD corrections to the EW contribution, we are on the steep rising flank of the scale dependence. We particularly point out that the results for the NLO cross section become unphysical, negative, for a downscaling of the factorisation scale by a factor of $1/2$. Subsequently, the scale uncertainty of

$$\sigma_{\mathrm{NLO,VBS}}^{\alpha_{\mathrm{s}}^2\alpha^4+\alpha_{\mathrm{s}}^2\alpha^5+\alpha_{\mathrm{s}}^3\alpha^4} = 4.176(5)_{-43.0\%}^{+11.4\%} \qquad \sigma_{\mathrm{NLO,Higgs}}^{\alpha_{\mathrm{s}}^2\alpha^4+\alpha_{\mathrm{s}}^2\alpha^5+\alpha_{\mathrm{s}}^3\alpha^4} = 0.328(3)_{-250.6\%}^{+104.9\%} \tag{302}$$

is very large for an NLO cross section and exceeds even the LO scale dependence. This points to a bad scale choice. The absolute values for the NLO QCD-induced cross section range between 2.382 fb and 4.651 fb in the VBS setup and between -0.494 fb and 0.672 fb in the Higgs setup.

Given our results, it is necessary to argue in defence of our scale that it has been proven to be a good scale for other VBS processes like ZZ scattering. We believe that it is still a viable option for the EW contribution but is obviously too low for the QCD-induced contribution of

Scale $(\mu_{\mathrm{F}}, \mu_{\mathrm{R}})$	$\sigma_{\mathrm{LO}}^{\alpha^6}[\,\mathrm{fb}]$	$\sigma_{\mathrm{NLO}}^{\alpha^6+\alpha^7}[\,\mathrm{fb}]$	$\sigma_{\mathrm{NLO}}^{\alpha^6+\alpha_{\mathrm{s}}\alpha^6}[\,\mathrm{fb}]$	$\sigma_{\mathrm{NLO}}^{\alpha^6+\alpha^7+\alpha_{\mathrm{s}}\alpha^6}[\,\mathrm{fb}]$
VBS setup				
$(1/2, 1/2)$	2.9187(3)	2.573(1)	2.542(3)	2.196(3)
$(1/2, 1)$	2.6988(3)	2.3914(9)	2.546(3)	2.238(3)
$(1, 1/2)$	2.9187(3)	2.573(1)	2.579(3)	2.233(3)
$(1, 1)$	2.6988(3)	2.9314(9)	2.560(2)	2.253(3)
$(1, 2)$	2.5069(3)	2.2318(9)	2.558(2)	2.283(2)
$(2, 1)$	2.6988(3)	2.3914(9)	2.572(2)	2.265(2)
$(2, 2)$	2.5069(3)	2.2318(9)	2.553(2)	2.278(2)
Higgs setup				
$(1/2, 1/2)$	1.6324(2)	1.517(1)	1.109(2)	0.993(2)
$(1/2, 1)$	1.5322(2)	1.429(1)	1.140(2)	1.036(2)
$(1, 1/2)$	1.6324(2)	1.517(1)	1.164(2)	1.048(2)
$(1, 1)$	1.5322(2)	1.429(1)	1.180(2)	1.077(2)
$(1, 2)$	1.4418(1)	1.349(1)	1.204(1)	1.111(2)
$(2, 1)$	1.5322(2)	1.429(1)	1.213(1)	1.110(2)
$(2, 2)$	1.4418(1)	1.349(1)	1.226(1)	1.134(2)

Table 4.8: Seven-point scale variations at LO $\mathcal{O}\left(\alpha^6\right)$ and NLO with corrections of $\mathcal{O}\left(\alpha^7\right)$ and $\mathcal{O}\left(\alpha_{\mathrm{s}}\alpha^6\right)$.

Scale $(\mu_{\mathrm{F}}, \mu_{\mathrm{R}})$	$\sigma_{\mathrm{LO}}^{\alpha_{\mathrm{s}}^2\alpha^4}[\,\mathrm{fb}]$	$\sigma_{\mathrm{NLO}}^{\alpha_{\mathrm{s}}^2\alpha^4+\alpha_{\mathrm{s}}^2\alpha^5}[\,\mathrm{fb}]$	$\sigma_{\mathrm{NLO}}^{\alpha_{\mathrm{s}}^2\alpha^4+\alpha_{\mathrm{s}}^3\alpha^4}[\,\mathrm{fb}]$	$\sigma_{\mathrm{NLO}}^{\alpha_{\mathrm{s}}^2\alpha^4+\alpha_{\mathrm{s}}^2\alpha^5+\alpha_{\mathrm{s}}^3\alpha^4}[\,\mathrm{fb}]$
VBS setup				
$(1/2, 1/2)$	9.504(1)	8.702(2)	3.184(7)	2.382(7)
$(1/2, 1)$	8.588(1)	7.881(2)	3.708(6)	3.001(6)
$(1, 1/2)$	7.650(1)	7.002(2)	4.586(5)	3.939(5)
$(1, 1)$	6.9115(9)	6.341(2)	4.746(4)	4.176(5)
$(1, 2)$	6.2853(8)	5.781(2)	4.911(4)	4.407(4)
$(2, 1)$	5.6882(7)	5.218(1)	5.082(3)	4.612(4)
$(2, 2)$	5.1724(7)	4.756(1)	5.067(3)	4.651(3)
Higgs setup				
$(1/2, 1/2)$	2.3242(4)	2.1976(9)	$-0.367(4)$	$-0.494(4)$
$(1/2, 1)$	2.1319(4)	2.0195(8)	$-0.148(4)$	$-0.260(4)$
$(1, 1/2)$	1.8453(3)	1.7442(7)	0.308(3)	0.206(3)
$(1, 1)$	1.6923(3)	1.6025(7)	0.417(2)	0.328(3)
$(1, 2)$	1.5580(3)	1.4780(6)	0.523(2)	0.443(2)
$(2, 1)$	1.3774(3)	1.3040(5)	0.690(2)	0.617(2)
$(2, 2)$	1.2679(2)	1.2026(5)	0.738(2)	0.672(2)

Table 4.9: Seven-point scale variations at LO $\mathcal{O}\left(\alpha_{\mathrm{s}}^2\alpha^4\right)$ and NLO with corrections of $\mathcal{O}\left(\alpha_{\mathrm{s}}^2\alpha^5\right)$ and $\mathcal{O}\left(\alpha_{\mathrm{s}}^3\alpha^4\right)$.

our calculations of W^+W^- scattering. We seem to severely underestimate the NLO cross section, especially in the Higgs setup. We come back to this problem in our final Section 5, where we briefly discuss another possible scale choice.

4.3.5   The influence of the Higgs-boson resonance

As we stated in the discussion of the results, many differences between opposite-sign WW scattering and other VBS processes stem from the presence of the Higgs-boson resonance in the fiducial phase space. While typical other VBS events take place at high $s_{4\ell}$, a large fraction of the events in opposite-sign WW scattering is taken over by on-shell Higgs production and decay, in contrast to the on-shell production and decay of two vector bosons.[28] As an overstatement, we could say that Higgs production and decay is an additional background process, which we cannot get rid of by physical cuts, which is present in all partonic channels with VBS subprocesses and which, therefore, overlaps our signal. Furthermore, we stated that the small EW corrections are an effect of the dominating Higgs contribution.

We investigate this effect quantitatively by introducing two modified VBS and Higgs setups, which differ from the original setups by an unphysical invariant-mass cut on the four-lepton system, where we require

$$|M_{4\ell(+\gamma)} - M_{\mathrm{H}}| > N\Gamma_{\mathrm{H}}. \tag{303}$$

This means we cut out a small region of our fiducial phase space around the Higgs mass with a width of $2N$ times the Higgs decay width Γ_{H}. This cut is unphysical because we are not able to measure the neutrino momenta; however, in the course of a Monte Carlo simulation, we can impose such a cut. In contrast to diagram-removal techniques, which were proposed in [142, 143], this method has the advantage of being manifestly gauge-invariant, and it does not spoil the important role of the Higgs boson for unitarity preservation, which we discussed in Section 2.1.7. In fact, if we *were* able to measure the neutrino momenta, this would be a totally standard method to remove an undesired background. If we assume a Breit–Wigner distribution of the cross section in the area around the resonance peak, which sits on top of the non-resonant background, we cut away a fraction of

$$\frac{\sigma^{\mathrm{cut}}}{\sigma^{\mathrm{BW}}} \approx \frac{2}{\pi} \arctan(2N) \tag{304}$$

for $N\Gamma_{\mathrm{H}} \ll M_{\mathrm{H}}$, where σ^{cut} is the removed part of the Breit-Wigner cross section σ^{BW}. For our analysis, we have chosen

$$N = 20, \tag{305}$$

which results in a removal of 98.4% of the resonance. While removing most of the resonance contribution, the slice in the fiducial phase space is tiny compared to the range of $M_{4\ell}$ over hundreds of GeV: $20\Gamma_{\mathrm{H}} \approx 80\,\mathrm{MeV}$. Since the cut slice is very small, we do not expect the cut to influence the cross section of non-resonant processes significantly. Nevertheless, we have to state that, at NLO, we also cut away events in which a hard photon is not emitted from the decay products of the Higgs boson, and the momentum constellation of the four leptons, and the photon is accidentally within our cut region. We rely on the smallness of the region and that such events are, hence, very seldom and negligible.

In Table 4.10, we show our numerical results for the modified setups. There are two main observations: In all channels with VBS, and thus the Higgs resonance, the EW corrections are more negative, and QCD corrections tend to be more positive than in the original setups. We recognise that the EW corrections for the modified VBS setup range between -12.5% and -14.8% in channels with VBS. In total, we get an EW correction of -13.2% in the VBS setup. When we take only the channels with VBS subprocesses into account, the EW corrections amount to -14.5% in the VBS setup, which is almost at the order of EW corrections for other VBS processes, especially since photon-induced corrections to other VBS processes have been neglected so far. The modified Higgs setup still has relatively small EW corrections between -9.0% and -10.7%

---

[28]To relate this statement to our investigations of ZZ scattering [38], we imposed a two-lepton invariant mass $M_{\ell^+\ell^-}$ cut of $60\,\mathrm{GeV} < M_{\ell^+\ell^-} < 120\,\mathrm{GeV}$, which is roughly a $30\,\mathrm{GeV}$, or $12\Gamma_{\mathrm{Z}}$, range around M_{Z}.

Contribution	$\sigma_{\mathrm{LO}}^{\alpha^6}$[fb]	$\Delta\sigma_{\mathrm{NLO}}^{\alpha^7}$[fb]	δ^{α^7}[%]	$\Delta\sigma_{\mathrm{NLO}}^{\alpha_{\mathrm{s}}\alpha^6}$[fb]	$\delta^{\alpha_{\mathrm{s}}\alpha^6}$[%]
VBS setup with Higgs-resonance cut					
VBS only	$1.6117(2)$	$-0.239(2)$	-14.8	$-0.043(3)$	-2.7
VBS + WWW	$0.11398(2)$	$-0.0143(2)$	-12.5	$0.0080(5)$	7.1
VBS + WWZ	$0.24916(4)$	$-0.0324(3)$	-13.0	$0.002(1)$	0.1
WWW only	$5.303(2)\times10^{-5}$	$-1.43(2)\times10^{-5}$	-27.0	$0.01110(2)$	2×10^4
WWZ only	$9.415(2)\times10^{-5}$	$-2.80(2)\times10^{-5}$	-29.7	$0.004021(3)$	4×10^3
$\gamma\gamma/\gamma\mathrm{g}$	$6.832(4)\times10^{-6}$	$0.02575(3)$	4×10^5	$0.0108(2)$	2×10^5
total	$1.9750(2)$	$-0.260(2)$	-13.2	$-0.007(3)$	-0.4
Higgs setup with Higgs-resonance cut					
VBS only	$0.4841(1)$	$-0.0513(6)$	-10.6	$-0.050(3)$	-10.3
VBS + WWW	$0.03654(1)$	$-3.30(9)\times10^{-3}$	-9.0	$-0.0037(3)$	-10.1
VBS + WWZ	$0.07925(2)$	$-7.4(2)\times10^{-3}$	-9.3	$-0.0109(6)$	-13.8
WWW only	$6.220(7)\times10^{-6}$	$-1.63(8)\times10^{-6}$	-26.2	$2.25(1)\times10^{-3}$	4×10^5
WWZ only	$1.2170(9)\times10^{-5}$	$-3.2(1)\times10^{-6}$	-26.0	$5.70(2)\times10^{-4}$	5×10^3
$\gamma\gamma/\gamma\mathrm{g}$	$7.767(3)\times10^{-7}$	$2.754(3)\times10^{-3}$	4×10^5	$-0.0161(1)$	-2×10^6
total	$0.5999(1)$	$-0.0592(7)$	-9.9	$-0.078(3)$	-12.9

Table 4.10: LO cross section of $\mathcal{O}\left(\alpha^6\right)$ and NLO cross section of $\mathcal{O}\left(\alpha^7\right)$ and $\mathcal{O}\left(\alpha_{\mathrm{s}}\alpha^6\right)$ in fb and relative corrections in per cent with an unphysical invariant-mass cut on the Higgs-boson resonance in both setups, classified after appearing subprocesses and corresponding relative corrections $\delta^{\alpha^7} = \Delta\sigma_{\mathrm{NLO}}^{\alpha^7}/\sigma_{\mathrm{LO}}^{\alpha^6}$ and $\delta^{\alpha_{\mathrm{s}}\alpha^6} = \Delta\sigma_{\mathrm{NLO}}^{\alpha_{\mathrm{s}}\alpha^6}/\sigma_{\mathrm{LO}}^{\alpha^6}$.

in channels with VBS. Combining the three categories with VBS subprocesses, the relative corrections are -10.4%, and in total, the EW corrections amount to -9.9%. The comparison between the physical VBS setup and the modified VBS setup shows that the presence of the Higgs boson resonance is the main reason for the small corrections in the VBS setup. However, even with the unphysical cut, they are sizeably smaller in the modified Higgs setup than in the modified VBS setup. We explain this as follows: The event selection in the Higgs setup is tailored to Higgs production and specifically built such that a small four-lepton invariant mass is favoured. We see this explicitly in the differential distribution of the two-lepton and the four-lepton invariant masses in Figure 4.6. From an experimentalist standpoint, it seems dubious to construct such a setup in the first place and then to cut out the main ingredient. Cutting away the Higgs boson resonance at small $M_{4\ell}$ does not reinstate the events at large $M_{4\ell}$, that are cut away by the other selection criteria and which are the reason for the large EW corrections in other VBS processes and the modified VBS setup.

The mean values for the four-lepton invariant mass are

$$\langle M_{4\ell}\rangle_{\text{VBS modified}} \approx 400\,\mathrm{GeV}, \qquad \langle M_{4\ell}\rangle_{\text{Higgs modified}} \approx 333\,\mathrm{GeV}. \tag{306}$$

In comparison to the original setups, both values are larger. However, the value in the modified Higgs setup is still much smaller than the corresponding value in the modified VBS setup. This reflects the fact that the Higgs-setup cuts are designed such that the tails of the four-lepton invariant-mass distribution are suppressed, leading to a smaller EW correction than in the VBS setup. We can also apply the Sudakov approximation differentially to the modified setups, and we obtain

$$\delta_{\mathrm{LL,VBS\ modified}}^{\alpha^7} = -15.8\%, \qquad \delta_{\mathrm{LL,Higgs\ modified}}^{\alpha^7} = -12.1\%. \tag{307}$$

These results overestimate the corrections in both setups, also in the case when only channels with VBS subprocesses are taken into account. Since the approximation in the VBS setup becomes

Contribution	$\sigma_{\text{LO}}^{\alpha^6}$[fb]	fraction[%]	$\Delta\sigma_{\text{NLO}}^{\alpha^7}$[fb]	δ^{α^7}[%]	$\Delta\sigma_{\text{NLO}}^{\alpha_{\text{s}}\alpha^6}$[fb]
VBS setup, Higgs-resonance contribution					
VBS only	0.5577(4)	25.7	$-0.042(2)$	-7.5	$-0.10(1)$
VBS + WWW	0.02385(4)	17.3	$-2.3(3) \times 10^{-3}$	-9.5	$-1(1) \times 10^{-3}$
VBS + WWZ	0.14224(7)	36.3	$-0.0103(4)$	-7.2	$-0.015(3)$
WWW only	$1.6(9) \times 10^{-7}$		$-6(5) \times 10^{-7}$		$5.9(3) \times 10^{-4}$
WWZ only	$3(37) \times 10^{-9}$		$8(4) \times 10^{-7}$		$-1.15(3) \times 10^{-4}$
$\gamma\gamma/\gamma$g	$-5(25) \times 10^{-10}$		$7.17(3) \times 10^{-3}$		$-0.0109(9)$
total	0.7238(4)	26.8	$-0.047(2)$	-6.5	$-0.13(1)$
Higgs setup, Higgs-resonance contribution					
VBS only	0.7118(2)	59.5	$-0.040(1)$	-5.6	$-0.191(4)$
VBS + WWW	0.02950(2)	44.7	$-1.9(2) \times 10^{-3}$	-6.3	$-5.5(4) \times 10^{-3}$
VBS + WWZ	0.19105(4)	70.7	$-8.6(5) \times 10^{-3}$	-4.5	$-0.0349(8)$
WWW only	$6(2) \times 10^{-8}$		$-1.8(16) \times 10^{-7}$		$2.6(1) \times 10^{-4}$
WWZ only	$6(2) \times 10^{-8}$		$-1.3(14) \times 10^{-7}$		$1.07(2) \times 10^{-4}$
$\gamma\gamma/\gamma$g	$-2(5) \times 10^{-10}$		$6.41(2) \times 10^{-3}$		$-0.043(1)$
total	0.9323(2)	60.8	$-0.044(1)$	-4.7	$-0.274(4)$

Table 4.11: LO cross section at $\mathcal{O}\left(\alpha^6\right)$ and NLO corrections at $\mathcal{O}\left(\alpha^7\right)$ and $\mathcal{O}\left(\alpha_{\text{s}}\alpha^6\right)$ in fb and relative corrections in per cent, classified after appearing subprocesses, for the contribution of the Higgs resonance to the cross section $\sigma_{\text{resonance}} = \sigma_{\text{original setup}} - \sigma_{\text{modified setup}}$ and the fraction of the Higgs-resonance contribution to the fiducial cross section $\sigma_{\text{resonance}}/\sigma_{\text{original setup}}$ at LO.

worse when cutting out the resonance contribution, we conclude that the approximation does not lead to the almost perfect match despite the presence of the low-energy resonance peak, but coincidentally because of it dragging the cross section into a region, in which the approximation is not applicable. However, even if we cut out the resonance, the leading logarithmic approximation is not much worse than in the case of the other VBS processes, being off by only a few percentage points.

Next, we analyse the complement of our cut, i. e. we subtract the modified setups from our original setups to obtain the contribution of the Higgs resonance. The results are shown in Table 4.11. We remark that these results suffer from extreme cancellation in those instances, in which the cut is not effective and only slightly affects the cross section, since we then subtract two almost identical numbers. As a result, we obtain large relative integration errors in those cases. This affects the non-VBS channels at LO in particular. An alternative would have been to calculate the results directly with the complementary cuts. Because of the small slice as fiducial phase space and hence many events not passing the cuts, this approach would be very computation-time intensive. We did not believe this method to be resource-efficient, especially since we already had collected the other data. For the channels that are affected by the cut, we get a satisfying integration error, and the other channels are negligible.

In this depiction, we see our assumption confirmed that the cut affects only partonic channels with a present Higgs resonance. At LO, these are mainly the channels with VBS subprocesses. All other channels at LO are compatible with zero within a 3σ integration error, except WWZ production in the Higgs setup with 3.2σ (in WWW production, it is just under the 3σ limit with 2.8σ). We believe this to be a statistical fluctuation in light of the small cross sections, although we have to admit that there are some Feynman diagrams with Higgs-boson resonances also in 3VP already at LO (c. f. Figure 3.10 (c) without the final-state gluon). However, these contributions are extremely suppressed by our event selection criteria. The cross sections of the photon-induced channels being negative at LO is also an artefact of the Monte-Carlo integration since, physically, they have to be positive. The Higgs resonance contribution in the VBS setup

amounts to 26.8% ranging between 17% and 36% in the individual subdivisions. The Higgs setup actually enhances the fraction of Higgs-production events over VBS events with 60.8% of the total cross section emerging from the Higgs-boson resonance. The contributions in the different subdivisions range between 45% and 71%. We did not include the values for only 3VP and the photon-induced channels at LO since the absolute values are already compatible with zero, and we cannot infer any information from them. We note the interesting fact that not only the relative but also the absolute cross section at $\mathcal{O}\left(\alpha^6\right)$ that stems from the Higgs resonance contribution is larger in the Higgs than in the VBS setup. However, the overall cross section in the (unmodified) Higgs setup is smaller than in the (unmodified) VBS setup.

The EW corrections are small in both setups and resemble more the corrections in Higgs-production processes than in VBS processes [144, 145], as we expect near the Higgs resonance. The average correction is -6.5% in the VBS setup and -4.8% in the Higgs setup, which repeats the general pattern of EW corrections being smaller in the Higgs setup than in the VBS setup. The 3VP channels are still compatible with zero at $\mathcal{O}\left(\alpha^7\right)$ in both setups, but the cut on $M_{4\ell}$ affects the EW corrections of the photon-induced partonic channels because of the newly opened VBS subprocesses in mixed $q\gamma$-induced channels at $\mathcal{O}\left(\alpha^7\right)$. We see similar effects for the QCD corrections for the photon/gluon-induced channels. The additional non-zero effect concerning the 3VP channels can be explained as follows: Considering Figure 3.10 (c) again, the additional gluon allows the passing of the VBS cuts when it becomes a tagging jet, as we already discussed for the original setups. This means that in these situations the cut on the Higgs-boson resonance can become relevant. This effect is absent in the case of EW corrections, where an emitted photon does not lead to the required jet, and so the cut does not affect the corrections of $\mathcal{O}\left(\alpha^7\right)$ to these channels.

We did not extend the analysis of the modified setups to contributions of the other orders. Since the Higgs boson is not present in any Feynman diagram of $\mathcal{O}\left(g_{\mathrm{s}}^2 g^4\right)$, the QCD-induced process of $\mathcal{O}\left(\alpha_{\mathrm{s}}^2 \alpha^4\right)$ is expected to be almost completely unaffected by this cut, like the 3VP processes of $\mathcal{O}\left(\alpha^6\right)$ are unaffected. Additionally, we also do not expect the cut to have an influence on the corrections of $\mathcal{O}\left(\alpha_{\mathrm{s}}^3 \alpha^4\right)$. For the interference process, we performed a summary calculation in the VBS setup at LO, where we found $\sigma_{\mathrm{LO,VBS\ modified}}^{\alpha_{\mathrm{s}}\alpha^5} = 0.06500(2)\,\mathrm{fb}$, which is the same value as for the physical VBS setup given in Table 4.1 within the limits of the numerical integration error. Thus, we do also not expect a significant influence on $\mathcal{O}\left(\alpha_{\mathrm{s}}^2 \alpha^5\right)$ via NLO QCD corrections. However, the Higgs boson resonance cut affects the loop-induced contributions: The closed fermion loop might be a top quark, to which a Higgs boson couples, and the Higgs boson subsequently decays into the four-lepton system.
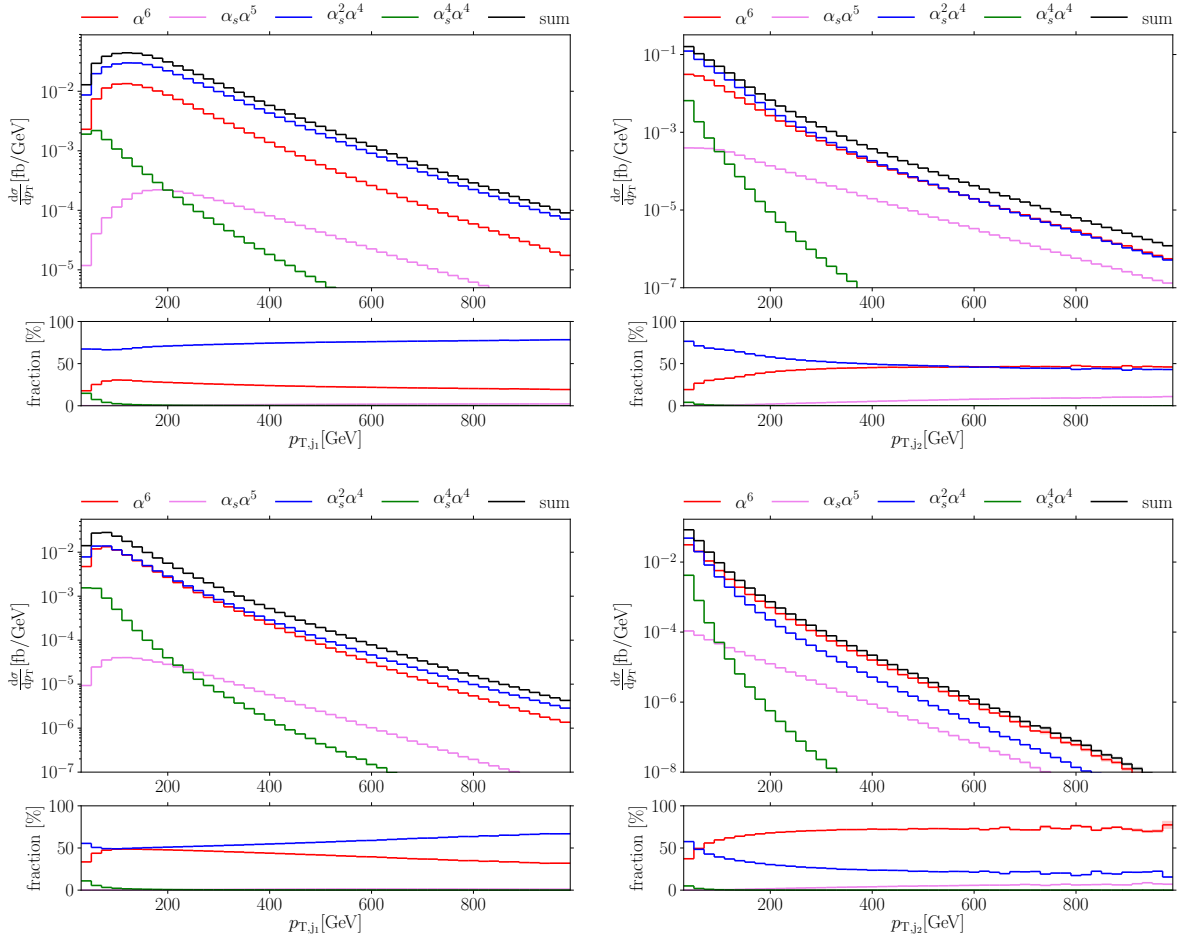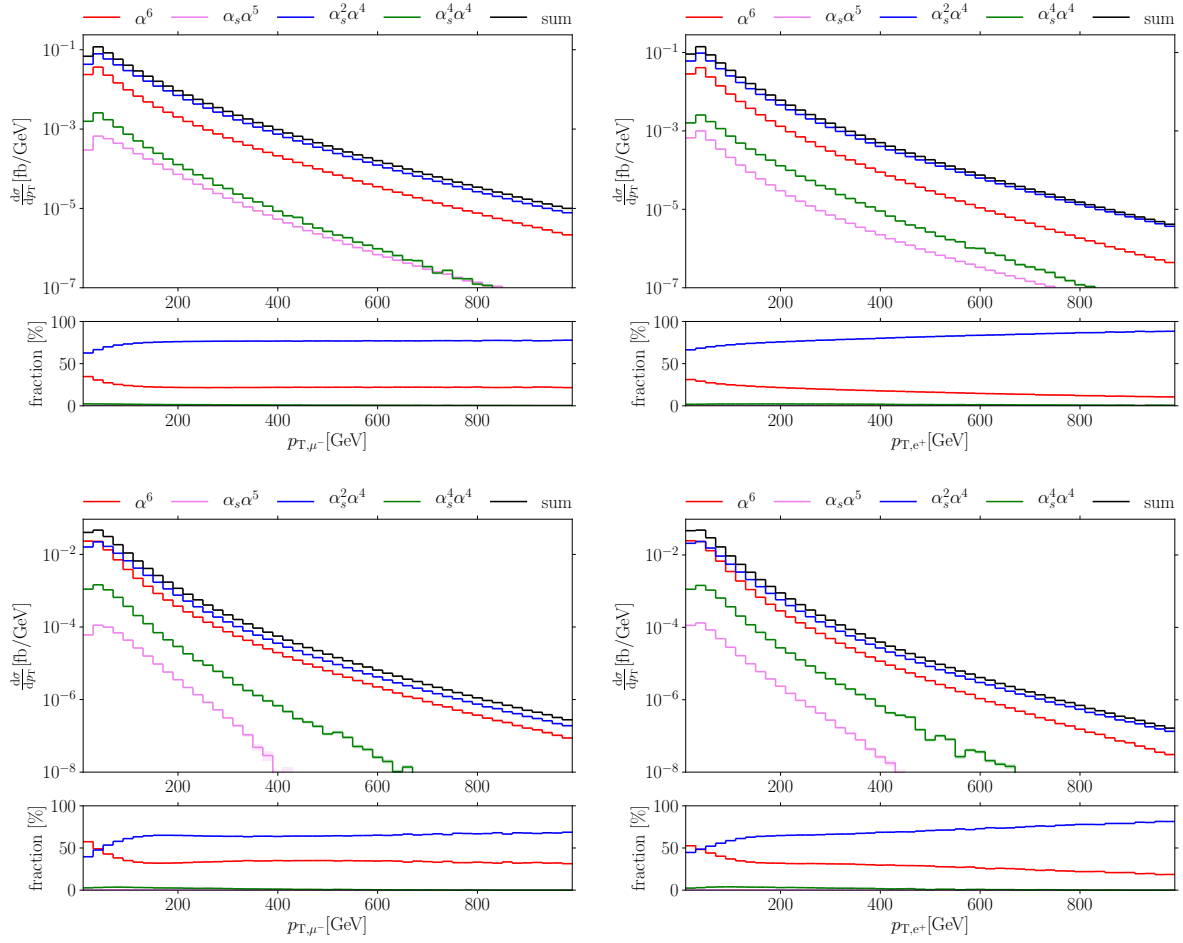
Figure 4.1: Differential distributions at LO in the transverse momentum of the hardest (left) and the second-hardest jet (right) in the VBS (top) and the Higgs setup (bottom). The upper panels show the absolute EW contribution at $\mathcal{O}\left(\alpha^6\right)$, the interference at $\mathcal{O}\left(\alpha_\mathrm{s}\alpha^5\right)$, the QCD contribution at $\mathcal{O}\left(\alpha_\mathrm{s}^2\alpha^4\right)$, the loop-induced contribution at $\mathcal{O}\left(\alpha_\mathrm{s}^4\alpha^4\right)$, and the sum of all contributions. The lower panels show the relative contributions normalised to the sum of all contributions. Shaded bands indicate integration errors.

4.4 Differential distributions

4.4.1 Leading order

In this section, we graphically present differential distributions for both VBS and Higgs setup at the leading orders $\mathcal{O}\left(\alpha^6\right), \mathcal{O}\left(\alpha_\mathrm{s}\alpha^5\right), \mathcal{O}\left(\alpha_\mathrm{s}^2\alpha^4\right)$ and $\mathcal{O}\left(\alpha_\mathrm{s}^4\alpha^4\right)$ as well as the sum of all LO cross sections. The figures are generally built up as follows: Each figure is a 2×2 grid of four subfigures. The rows of the grid correspond to the two different physical setups, and in the two columns, we present two observables per figure. Each of the subfigures is again divided into two panels, of which the upper panel shows the absolute contributions and the lower one presents the relative contributions normalised to the sum of the LO differential cross sections.

We begin with the transverse momentum of the leading jet in the left and the subleading jet in the right panels of Figure 4.1. There is a maximum in the sum of the differential cross sections with respect to the hardest jet at $p_{\mathrm{T},\mathrm{j}_1} \approx 100\,\mathrm{GeV}$. The differential cross section with respect to the second-hardest jet decreases from the first bin on in both setups. The subleading jet shows a sharper falling flank than the leading one. These statements for the sum of the differential cross sections are also valid for the individual contributions of different orders. This observation is easily explicable since the hardest jet must have more transverse momentum than any other jet by

definition. A specific value of $p_{\mathrm{T,j_2}}$ imposes no constraint on $p_{\mathrm{T,j_1}}$. Thus, $\mathrm{d}\sigma/\mathrm{d}p_{\mathrm{T,j_2}}$ at small $p_{\mathrm{T,j_2}}$ can acquire contributions from regions of the phase space with large $p_{\mathrm{T,j_1}}$, whereas the reverse statement, replacing $1 \leftrightarrow 2$, is false. The inequality $\int_0^P \mathrm{d}p_{\mathrm{T,j_1}}\,(\mathrm{d}\sigma/\mathrm{d}p_{\mathrm{T,j_1}}) \leq \int_0^P \mathrm{d}p_{\mathrm{T,j_2}}\,(\mathrm{d}\sigma/\mathrm{d}p_{\mathrm{T,j_2}})$ has to hold for any P. The shape of the loop-induced contribution for the hardest jet in the Higgs setup is slightly different. Its maximum is also in the lowest bin. This phenomenon is explicable because the PDF of the gluon peaks at small parton energies, also leading towards small transverse momenta that can be distributed among the system. In fact, the falling flank of the loop-induced contribution is the sharpest of all and the loop-induced process becomes very soon negligible with higher transverse momenta. For the leading jet, the QCD-induced process is dominant over the EW-induced process, clearly seen in the VBS setup, whereas, in the Higgs setup, both contributions become almost equal at low transverse momentum. We observe that there is a peak of the EW-induced process in the relative contribution at $p_{\mathrm{T,j_1}} \approx 100\,\mathrm{GeV}$, near the absolute peak of the summed differential cross section in both setups. The interference contribution is negligible over the complete range of transverse momentum concerning the hardest jet. In the differential distribution in the second-hardest jet, the QCD-induced contribution dominates the EW contribution only at low transverse momentum. In the VBS setup, both contributions become equally large at about $p_{\mathrm{T,j_2}} \approx 500\,\mathrm{GeV}$ and the relative share between them does not change sizeably at higher values. In the Higgs setup, on the other hand, the EW contribution starts to exceed the QCD-induced contribution already at $p_{\mathrm{T,j_2}} > 50\,\mathrm{GeV}$ with a rising tendency towards higher values of $p_{\mathrm{T,j_2}}$. An interesting fact is the behaviour of the interference contribution for the subleading jet, whose relative size starts to grow with higher transverse momenta.

We present the transverse momentum sums of the two hardest jets and the transverse momentum sum of the four-lepton system in Figure 4.2. Since these two groups of particles are complementary and form the complete final-state content at LO, and the total transverse momentum must sum up to zero, the differential distributions are completely identical at LO. However, they become different at NLO and we already include both variables at LO as a placeholder for the future NLO discussion and to explicitly demonstrate the identicalness. We recognise a peak in the EW and QCD-induced contributions around $p_{\mathrm{T,j_1j_2}} \approx 100\,\mathrm{GeV}$ in the VBS and around $p_{\mathrm{T,j_1j_2}} \approx 80\,\mathrm{GeV}$ in the Higgs setup. In both setups, the ratios between the relative EW and QCD-induced contributions are quite constant until $p_{\mathrm{T,j_1j_2}} \approx 160\,\mathrm{GeV}$, after which the relative EW contribution starts slowly falling. After $p_{\mathrm{T,j_1j_2}} > 800\,\mathrm{GeV}$, the ratio becomes almost constant again in the VBS setup, whilst the decay continues linearly in the Higgs setup up to $p_{\mathrm{T,j_1j_2}} = 1000\,\mathrm{GeV}$.

The next two observables that we discuss are the transverse momenta of the charged leptons, the muon and the positron. We show differential distributions of the cross section with respect to their transverse momenta in Figure 4.3. There is no striking difference in the shapes of the distributions according to the different electric charges of the leptons, which could have happened because the process in a proton–proton collider is not invariant under charge conjugation. The relative contributions of the processes remain constant over a large range of transverse momentum above $p_{\mathrm{T},\mu^-} > 200\,\mathrm{GeV}$ in the VBS setup for the negative-charged muon after a relative increase of the QCD-induced contribution over the first $200\,\mathrm{GeV}$. In contrast, the relative contribution of the QCD-induced process keeps rising until $p_{\mathrm{T,e^+}} = 1000\,\mathrm{GeV}$ in case of the positive-charged electron, where the depicted range ends. The behaviour of the cross sections in the Higgs setup almost mimics the VBS setup with the difference that the ratio between QCD- and EW-induced process is smaller than in the VBS setup for the integrated cross section and hence also in the differential cross sections.

The differential cross section with respect to the two charged leptons and the differential cross section with respect to the missing transverse momentum are shown in Figure 4.4. For the transverse momentum sum of the two charged leptons, the maximum of all contributions for both setups is around $p_{\mathrm{T,e^+\mu^-}} \approx 20\,\mathrm{GeV}$. At this value, the relative EW contribution also shows a slight maximum. Like in the case of the transverse momentum sum of the two hardest jets, the relative
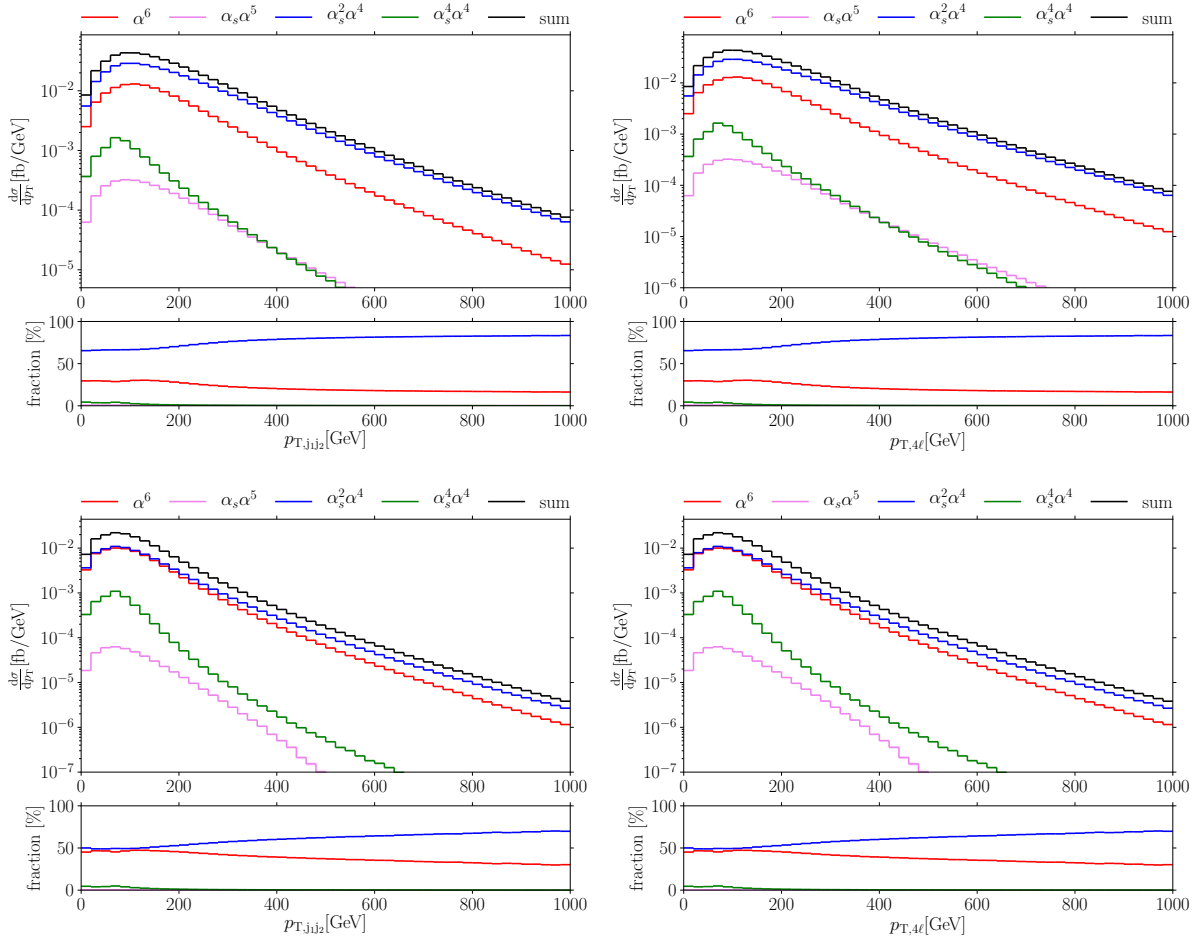
Figure 4.2: Differential distributions at LO in the (vectorial) transverse momentum sum of the two hardest jets (left) and the four-lepton system (right) in the VBS (top) and the Higgs setup (bottom).

EW contribution becomes smaller for large $p_{\mathrm{T},\mathrm{e}^+\mu^-}$. In the VBS setup, the ratio between the EW and the QCD-induced contribution is almost constant and very slowly linearly decaying for $400\,\mathrm{GeV} < p_{\mathrm{T},\mathrm{e}^+\mu^-} < 1000\,\mathrm{GeV}$, while it decays linearly between $300\,\mathrm{GeV} < p_{\mathrm{T},\mathrm{e}^+\mu^-} < 1000\,\mathrm{GeV}$ in the Higgs setup. The only significant difference between Higgs and VBS setup in both of these observables is the ratio between the negligibly small interference and the loop-induced contribution; in the VBS setup, the interference contribution starts to exceed the loop-induced contribution at some point, while in the Higgs setup, it does not. Concerning the missing transverse momentum, the maximum for all contributions in both setups is at low missing transverse momentum of $p_{\mathrm{T},\mathrm{mis}} \approx 40\,\mathrm{GeV}$. We see that the EW contribution falls faster than the QCD-induced one. Furthermore, we notice a difference between VBS and Higgs setup in the behaviour of the loop-induced and interference contributions. In the Higgs setup, both of these contributions are strongly suppressed for high missing transverse momentum.

We turn our attention to the invariant mass of the total visible system, i. e. all final-state objects excluding the neutrinos, and the invariant mass of the two hardest jets in Figure 4.5. For the total visible invariant mass, we see an absolute maximum in all contributions at $M_{\mathrm{vis}} \approx 900\,\mathrm{GeV}$ in the VBS and at $M_{\mathrm{vis}} \approx 700\,\mathrm{GeV}$ in the Higgs setup. In both setups, the relative contribution of the QCD-induced process has a single maximum at an invariant mass slightly lower than the value where the absolute maximum occurs, and the EW process has a corresponding minimum. The EW process is more important at small and large invariant masses. In the VBS setup, the EW process dominates the QCD-induced process at invariant masses
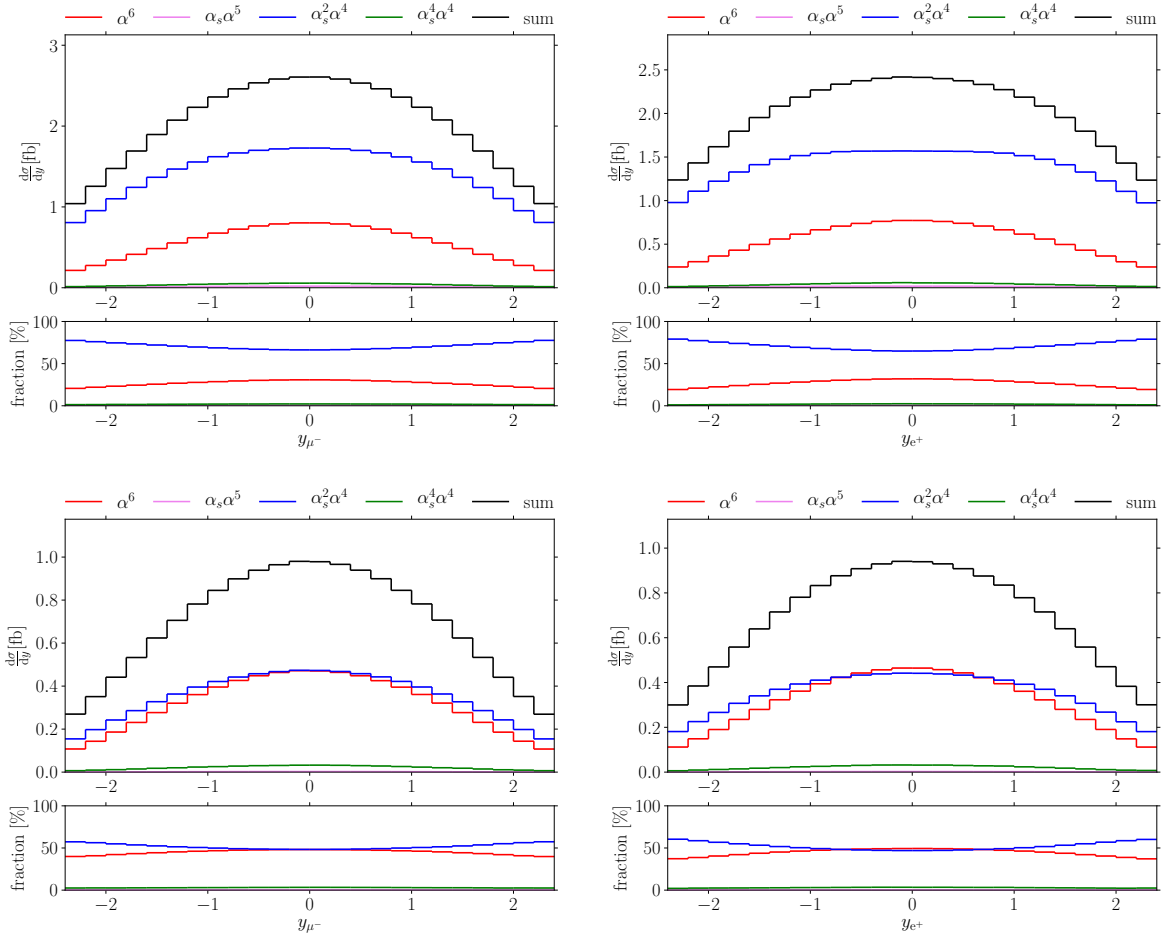
Figure 4.3: Differential distributions at LO in the transverse momentum of the muon (left) and the positron (right) in the VBS (top) and the Higgs setup (bottom).

higher than $M_{\text{vis}} > 2500\,\text{GeV}$ and in the Higgs setup at invariant masses above $M_{\text{vis}} > 1300\,\text{GeV}$. Whilst the EW contribution is slightly smaller than the QCD-induced one at low invariant masses in the VBS setup, it also dominates that differential cross section below $M_{\text{vis}} < 440\,\text{GeV}$ in the Higgs setup. We note that this region is not within the fiducial phase space for the VBS setup. The absolute cross section in this region in the Higgs setup is extremely small (around $10^{-7}\,\text{fb/GeV}$), which even the best particle accelerators are unable to measure in these days. The dominance of the EW contribution at high invariant masses is typical for VBS processes and resembles the dominance of the EW contribution at high invariant masses of the jets. The relatively large EW contribution at small invariant masses is special for W^+W^- scattering. It is likely due to the presence of the Higgs resonance and the enhancement of the EW cross section at small four-lepton invariant masses. As we already stated in the discussion of the transverse momenta of the jets, the slope of the loop-induced contribution falls steepest. It leads to a sizeable contribution only below $M_{\text{vis}} < 1500\,\text{GeV}$ in the VBS and $M_{\text{vis}} < 2000\,\text{GeV}$ in the Higgs setup with a maximal relative contribution of around 5%, before the graph of the relative contribution becomes non-visible behind the axis. The interference contribution is negligible over the complete phase space. The differential cross section with respect to the invariant mass of the two jets shows at large invariant masses the same behaviour as the invariant mass of the complete visible system. However, there is no EW enhancement at low invariant masses. This provides evidence that the effect at low total visible invariant masses emerges from the leptonic part of the process. The distribution of the invariant mass of the two jets is typical for VBS processes. The QCD-induced contribution is only dominant at small invariant masses, and the
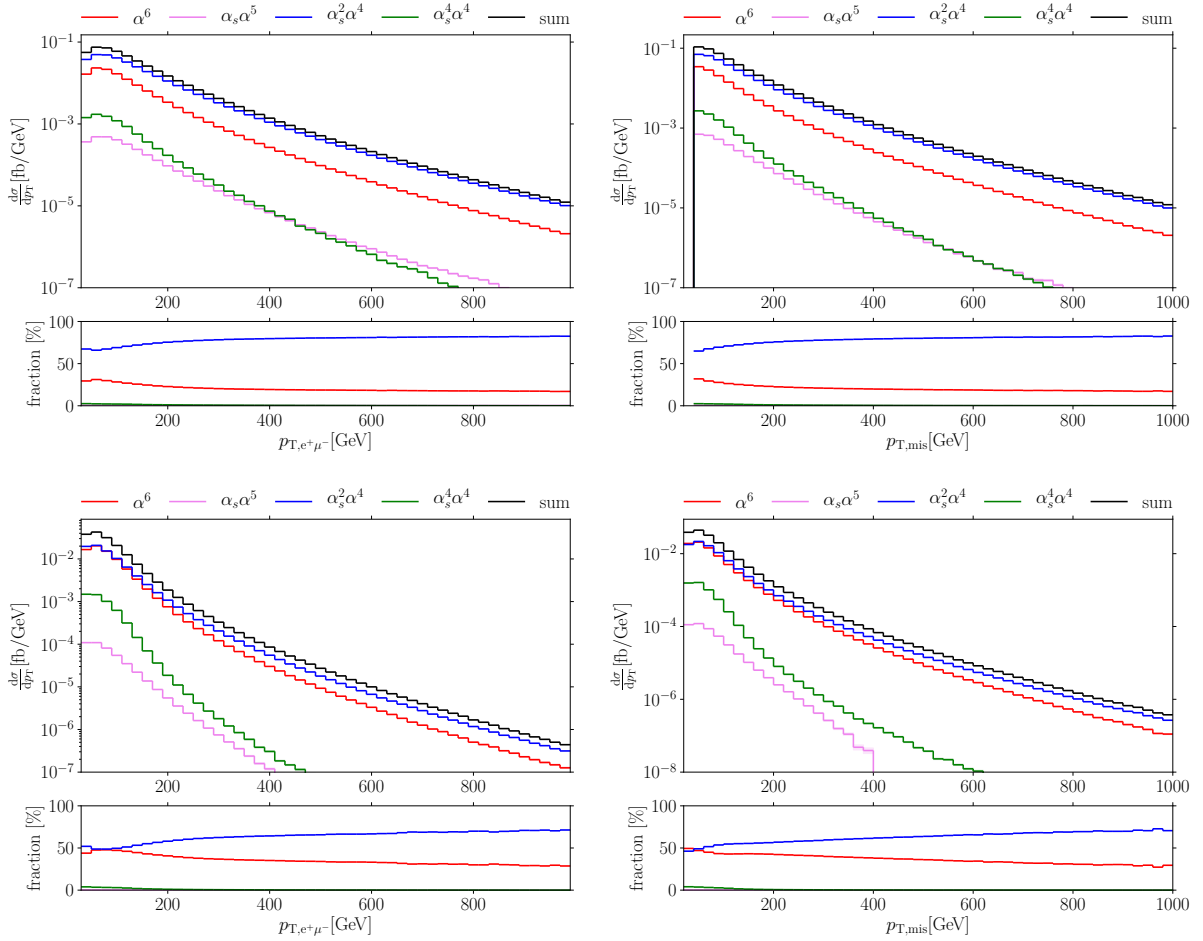
Figure 4.4: Differential distributions at LO in the transverse momentum of the two charged leptons (left) and the missing transverse momentum (right) in the VBS (top) and the Higgs setup (bottom).

EW contribution takes over above $M_{\mathrm{j_1j_2}} > 1500\,\mathrm{GeV}$ in the VBS and $M_{\mathrm{j_1j_2}} > 1000\,\mathrm{GeV}$ in the Higgs setup. The loop-induced contribution is only relevant for small invariant masses, and the interference contribution is negligible. The invariant-mass cuts in equations (284) and (292), respectively, are thus a well-suited tool to enhance the EW contribution.

The next observables are the invariant mass of the two charged leptons and the invariant mass of the four-lepton system in Figure 4.6. We emphasise that only the invariant mass of the two leptons is a physical observable, and the invariant mass of the four-lepton system serves only to illustration purposes. In the VBS setup, the absolute maximum of the differential cross section with respect to the invariant mass of the two-lepton system appears around $M_{\mathrm{e^+\mu^-}} \approx 80\,\mathrm{GeV}$ for all contributions. In the relative contributions, we observe a maximum for the EW process at very small invariant masses, at such below $M_{\mathrm{e^+\mu^-}} < 40\,\mathrm{GeV}$ it is of comparable size as the QCD-induced one, which decays to a minimum at invariant masses around $M_{\mathrm{e^+\mu^-}} \approx 100\,\mathrm{GeV}$, followed by a smooth increase until the ratio between EW and QCD-induced contribution becomes constant above $M_{\mathrm{e^+\mu^-}} > 600\,\mathrm{GeV}$. Interference and loop-induced contributions are both negligible over the complete phase space. In the Higgs setup, we observe the same overall behaviour with the exception that the maximum of the EW differential cross section appears at low two-lepton invariant masses below $M_{\mathrm{e^+\mu^-}} < 40\,\mathrm{GeV}$. In this bin, it even exceeds the QCD-induced contribution before being compatible in size between $40\,\mathrm{GeV} < M_{\mathrm{e^+\mu^-}} < 80\,\mathrm{GeV}$. We also observe the constant ratio between QCD-induced and EW contribution above $M_{\mathrm{e^+\mu^-}} > 600\,\mathrm{GeV}$. The loop-induced contribution shows a very flat maximum around $M_{\mathrm{e^+\mu^-}} \approx 500\,\mathrm{GeV}$, but its relative
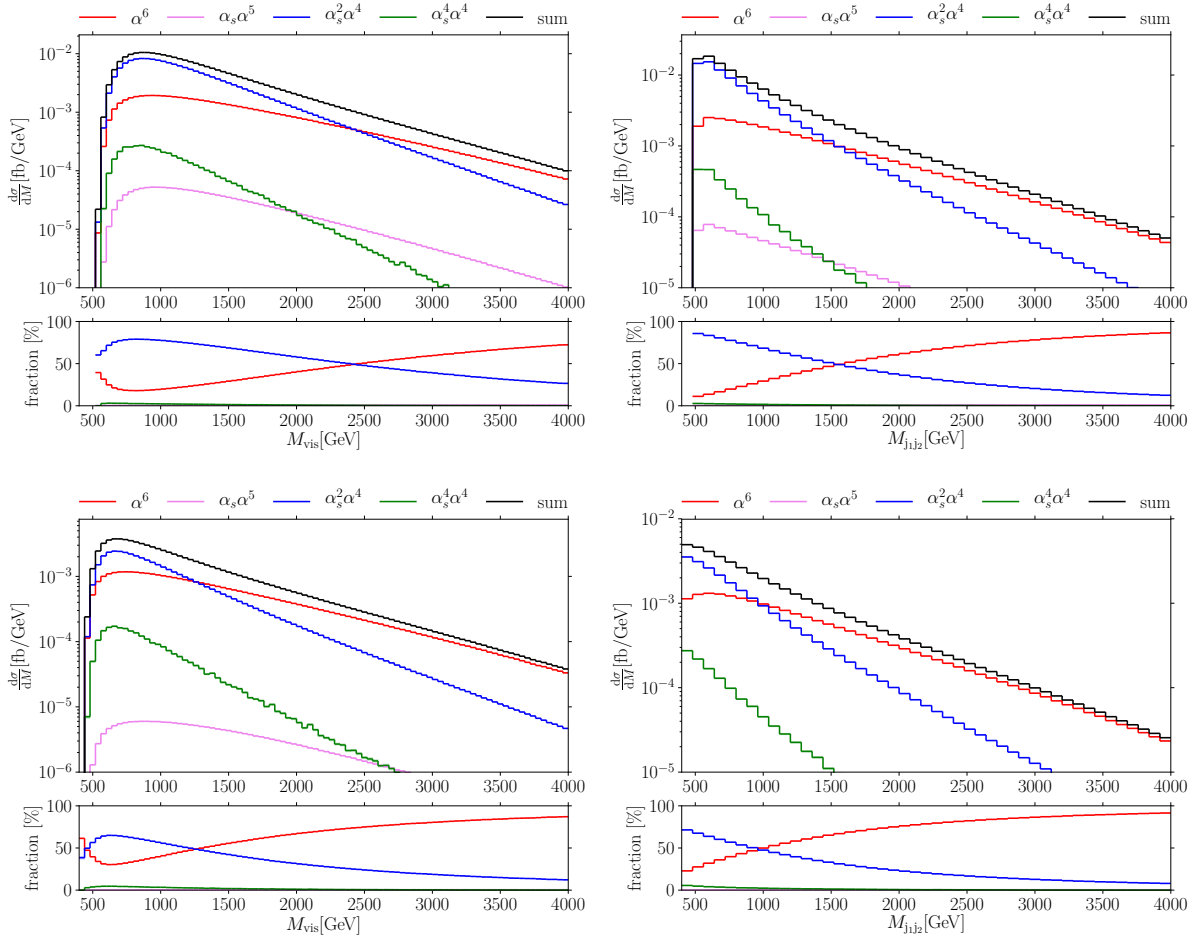
Figure 4.5: Differential distributions at LO in the invariant mass of all visible particles (left) and the two hardest jets (right) in the VBS (top) and the Higgs setup (bottom).

contribution remains below 5%. As already stated, the large EW contribution at low invariant masses of the two charged leptons emerges from the presence of the Higgs-boson resonance. To emphasise this, we included the non-observable differential cross section with respect to the invariant mass of the four-lepton system. In this graph, we only mention both the absolute and relative maximum of the EW contribution in the bin between $120\,\mathrm{GeV} < M_{4\ell} < 240\,\mathrm{GeV}$ – the bin, in which the Higgs-boson resonance sits at $125\,\mathrm{GeV}$. The relative EW contribution reaches almost 50% in the VBS and almost 70% in the Higgs setup as a clear outlier compared to its surrounding bins with a very smooth envelope of both EW and QCD-induced contributions.

The differential cross section with respect to the rapidities of the hardest and second-hardest jets are shown in Figure 4.7. As expected, all of these graphs are symmetric around zero, so we use "large" and "small" rapidities as abbreviations for large and small values of the absolute value of the rapidity. In both setups, both distributions show a maximum of the sum of the differential cross sections at medium rapidities. The absolute maximum of the QCD-induced contribution is at a smaller rapidity than the absolute maximum of the EW contribution. For the leading jet, the QCD-induced absolute maximum occurs at a rapidity of $y_{\mathrm{j_1}} \approx 1.5$ and the EW one at $y_{\mathrm{j_1}} \approx 2.1$ in the VBS setup, in the Higgs setup they occur at $y_{\mathrm{j_1}} \approx 2.2$ and $y_{\mathrm{j_1}} \approx 2.5$ respectively. The relative maxima of the EW contribution are placed at even larger rapidities of the hardest jet for both setups, at about $y_{\mathrm{j_1}} \approx 4$ for the VBS setup and at the edge of the fiducial phase space at $y_{\mathrm{j_1}} \approx 4.5$ for the Higgs setup. We recognise that the QCD-induced contribution has a much steeper shape in the Higgs setup compared to the VBS setup, both for values below and above the maximum. Comparing the rapidities of the hardest and the second-hardest jet, the
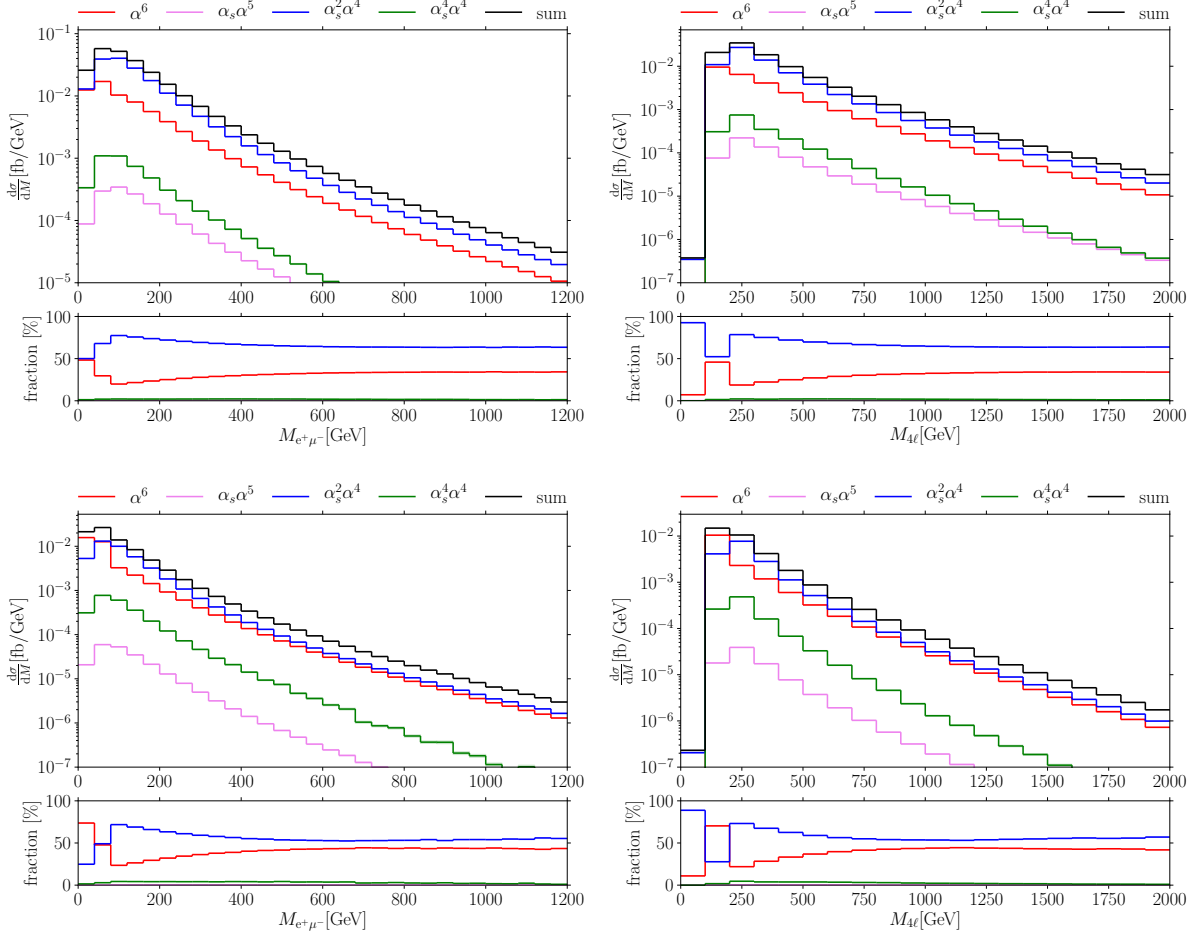
Figure 4.6: Differential distributions at LO in the invariant mass of the two charged leptons (left) and the four-lepton system (right) in the VBS (top) and the Higgs setup (bottom).

hardest jet tends towards small rapidities and the softer one to large rapidities for both setups. This is easily explicable if we assume that the energy and transverse momentum of a jet are not strongly correlated. Then, the momentum of a jet with smaller transverse momentum points in the forward or backward direction, leading to a higher rapidity. The relative contributions of the EW and the QCD-induced process are flatter in the case of the second-hardest jet compared to the hardest jet in the VBS case, where the relative EW contribution shows a minimum at zero rapidity and barely a maximum at $y_{j_2} \approx 3.7$. The absolute maximum of the EW and the QCD-induced contribution are both at $y_{j_2} \approx 2.7$. For the Higgs setup, we recognise a similar pattern in the absolute differential cross sections of the second-hardest jet as for the VBS setup with an absolute maximum of the EW contribution at 2.9 and for the QCD-induced contribution at $y_{j_2} \approx 2.5$. The relative differential distributions, however, differ between the setups since there is a second maximum of the relative EW cross section at small rapidities. This maximum emerges through the strong suppression of the QCD-induced process, especially at small rapidities. The responsible cut that leads to this suppression is the cut on the Zeppenfeld variable z: If both leptons have rapidity with opposite signs, then this cut forces any tagging jet to have larger rapidity than the lepton with the smallest rapidity.

We now discuss the differential cross sections with respect to the lepton rapidities in Figure 4.8 briefly. We see, as in the case of the transverse momenta, a slight asymmetry between the distributions of muon and positron rapidities for both setups. This asymmetry is stronger in the QCD-induced process, where the differential cross section with respect to the rapidity of the positron forms a much larger flat plateau than in the case of the muon. Nevertheless, the
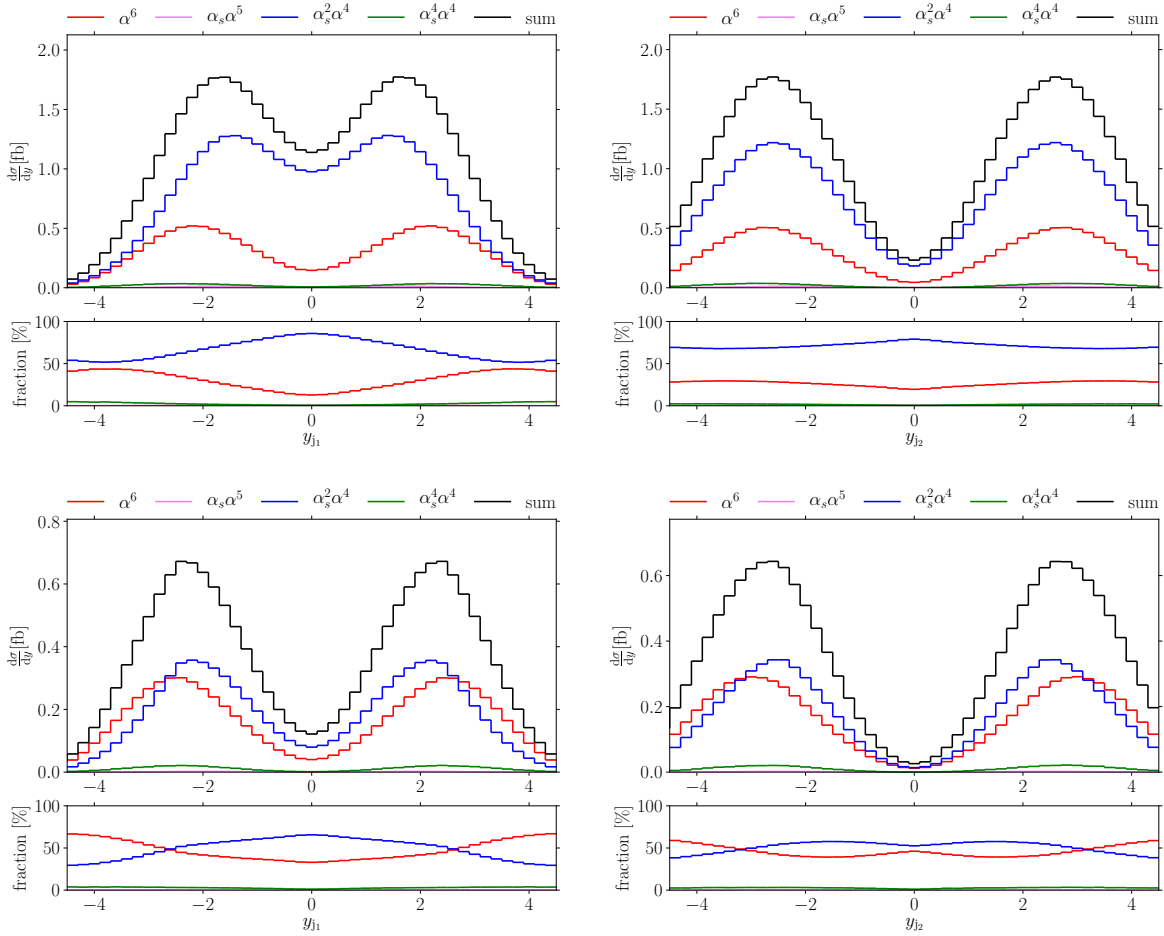
Figure 4.7: Differential distributions at LO in the rapidity of the hardest (left) and the second-hardest jet (right) in the VBS (top) and the Higgs setup (bottom).

general shape of the absolute differential cross sections for all contributions in both setups and both charges of the leptons is similar, with an absolute maximum at zero rapidity. The relative contributions are also always of the same shape with a maximum of the EW contribution at zero rapidities.

The differential cross sections with respect to the rapidity difference of the two jets and the differential cross section with respect to the rapidity difference of the two charged leptons are shown in Figure 4.9. Since all rapidity distributions are symmetric around zero and uncorrelated, the distributions in rapidity difference are also symmetric and we show only the absolute values, especially since we imposed a cut on the rapidity difference of the two hardest jets. This cut explains the small value of all contributions in the first non-empty bin of the absolute differential cross sections in both setups regarding the jets since half of the bin is actually cut away. Apart from this artefact, we see smooth curves with an absolute maximum of the EW contribution around $|\Delta y_{j_1 j_2}| \approx 4.4$ in the VBS and $|\Delta y_{j_1 j_2}| \approx 4.8$ in the Higgs setup. The maximum of the QCD-induced contribution is at $|\Delta y_{j_1 j_2}| \approx 3.6$ in the VBS and at $|\Delta y_{j_1 j_2}| \approx 3.8$ in the Higgs setup. Looking at the relative contributions, we recognise the typical VBS pattern, where the EW contribution dominates at high rapidity separation when both jets are back-to-back. In the VBS setup, the EW dominance begins at $|\Delta y_{j_1 j_2}| \approx 6.0$ and in the Higgs setup at $|\Delta y_{j_1 j_2}| \approx 5.2$. Like the invariant-mass distribution, this behaviour confirms the use of the phase-space cuts of equations (284) and (292). The absolute differential cross section with respect to the rapidity difference of the charged leptons does not show fundamental differences in its shape when we compare VBS and Higgs setup. It has a maximum for all contributions at a very small rapidity

Figure 4.8: Differential distributions at LO in the rapidity of the muon (left) and the positron (right) in the VBS (top) and the Higgs setup (bottom).

difference apart from zero in both setups, i. e. most of the time, both leptons are emitted into the same direction projected to the beam axis. The relative contributions show an interesting shape: At small rapidity differences, the relative contributions of EW and QCD-induced processes oscillate. This effect is due to the Higgs boson resonance. We discuss it in more detail in the context of Figure 4.22 with the NLO corrections. The minimum of the relative EW contribution is at $\Delta y_{e^+\mu^-} \approx 1.0$ in the VBS and $\Delta y_{e^+\mu^-} \approx 2.0$ in the Higgs setup, and the EW contribution rises from thereon. The dominance of the QCD-induced process at small jet rapidity differences for both setups, combined with the fact that the charged leptons are mostly central with low rapidity difference, confirms our statement about the different shapes of the differential cross section with respect to the rapidity of a single jet for VBS and Higgs setup: QCD-driven events tend to small rapidity difference *and* most likely both leptons are central.

We present the differential cross sections with respect to the azimuthal angular separation of the two hardest jets and with respect to the azimuthal angular separation of the two charged leptons in Figure 4.10. Beginning with the jets, we see for both setups a similar pattern, where the differential cross section is increasing for both EW and QCD-induced processes with larger angular separation. In terms of relative contributions, the EW process becomes slightly more important at large angular separation, although the ratio is almost constant in both setups. We note that the EW process takes over at an azimuthal angular separation of $\Delta\phi_{j_1j_2} = 2.5$ in the Higgs setup. We explicitly mention the otherwise subordinate loop-induced contribution, whose absolute differential cross section shows the different behaviour of staying almost constant. For the angular separation of the leptons, there are more differences between the VBS and the Higgs
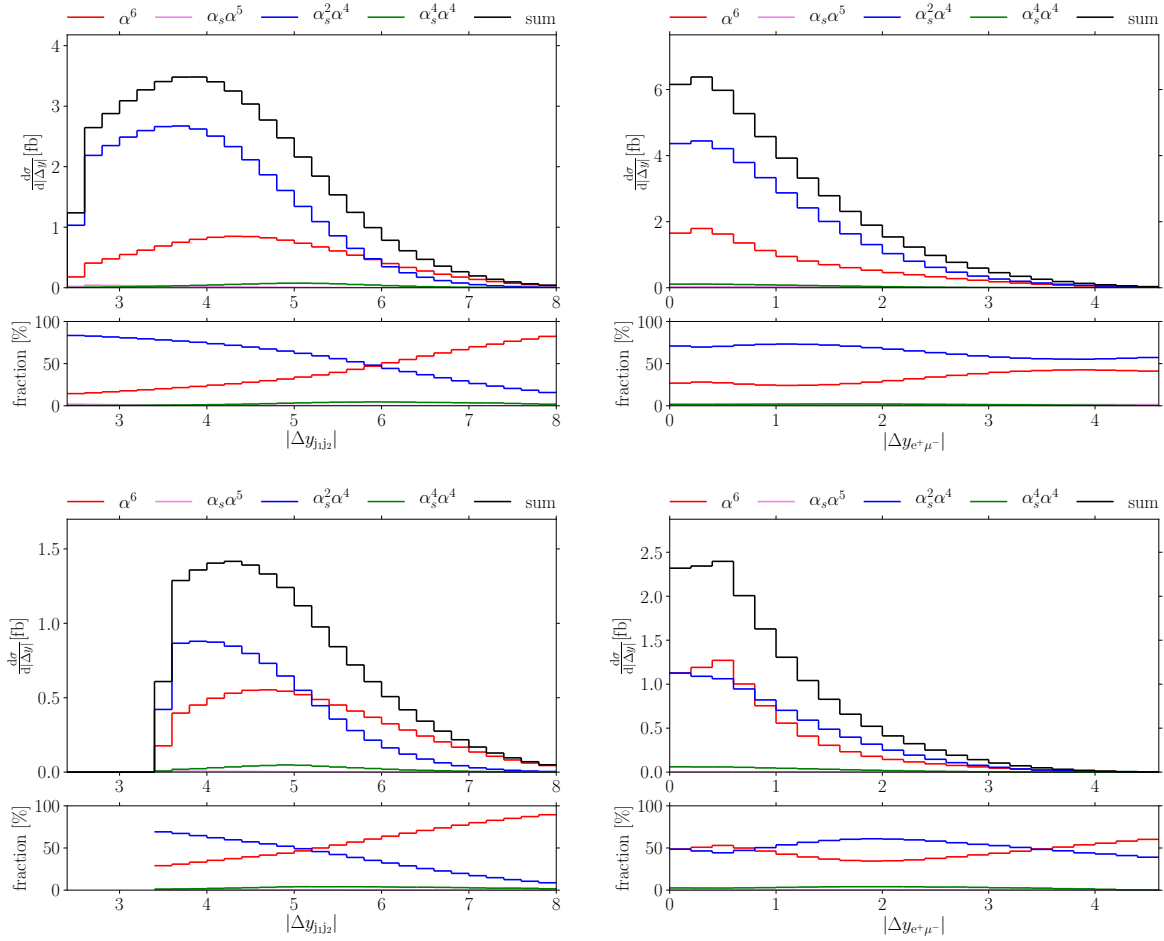
Figure 4.9: Differential distributions at LO in the absolute value of the rapidity difference of the two hardest jets (left) and the two charged leptons (right) in the VBS (top) and the Higgs setup (bottom).

setup than in any other distribution we presented so far. In the VBS setup, there is a maximum for both EW and QCD-induced contributions at $\Delta\phi_{\mathrm{e}^+\mu^-} \approx 0.4$. The EW contribution falls until it reaches a minimum at $\Delta\phi_{\mathrm{e}^+\mu^-} \approx \pi/2$ and rises to a second, lower maximum at $\Delta\phi_{\mathrm{e}^+\mu^-} = \pi$. The QCD-induced contribution remains almost constant after its first maximum and shows its absolute maximum at $\Delta\phi_{\mathrm{e}^+\mu^-} = \pi$. No substructure is seen for the loop-induced contribution with a maximum at $\Delta\phi_{\mathrm{e}^+\mu^-} = \pi$. The sum of all differential cross sections subsequently shows its maxima at the same positions as each contribution, and its minimum is slightly below $\pi/2$. The relative contributions of the EW and QCD-induced process are almost constant until their first maximum and in the interval $\pi/2 < \Delta\phi_{\mathrm{e}^+\mu^-} < \pi$. Although there is still a maximum for the EW contribution at $\Delta\phi_{\mathrm{e}^+\mu^-} \approx 0.4$ in the Higgs setup, it does not show a second maximum at π, but instead it falls off until it reaches the absolute *minimum* there. The QCD-induced contribution has no maximum at $\Delta\phi_{\mathrm{e}^+\mu^-} \approx 0.4$, since it rises until $\Delta\phi_{\mathrm{e}^+\mu^-} \approx 2.2$, but it shows a step at this value. We also mention the loop-induced contribution, which also shows a maximum near $\Delta\phi_{\mathrm{e}^+\mu^-} \approx 2.2$ before falling again. Thus, the maximum of the sum of all differential cross sections is around $\Delta\phi_{\mathrm{e}^+\mu^-} \approx 0.4$, but the rising slope of the QCD-induced contribution does not compensate for the falling one of the EW contribution at large $\Delta\phi_{\mathrm{e}^+\mu^-}$, so the sum of the differential cross sections also has its absolute minimum at $\Delta\phi_{\mathrm{e}^+\mu^-} = \pi$. The EW process dominates for small azimuthal angular separations. Like in the case of the VBS setup, the relative contributions are almost constant until the maximum is reached. Afterwards, the relative EW
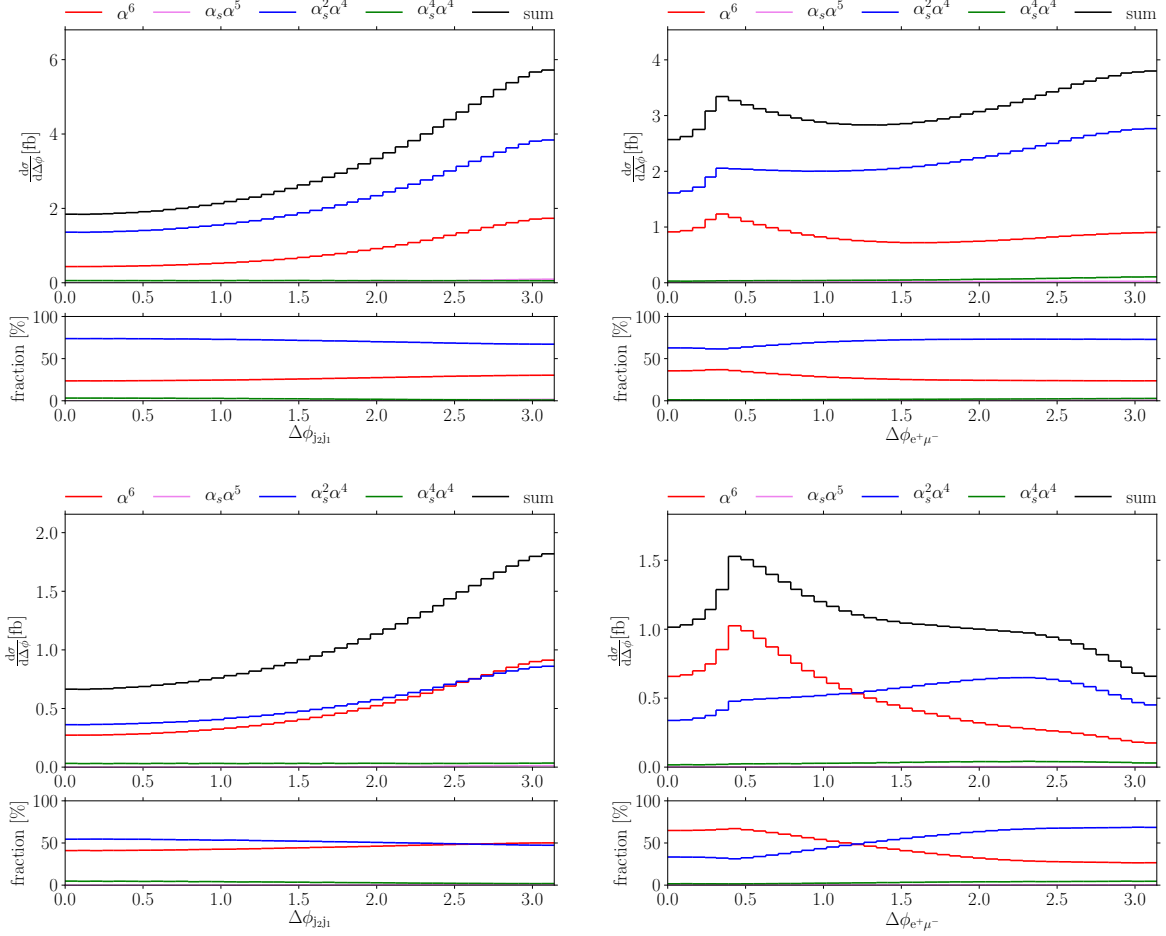
Figure 4.10: Differential distributions at LO in the azimuthal angular separation of the two hardest jets (left) and the two charged leptons (right) in the VBS (top) and the Higgs setup (bottom).

contribution drops and at $\Delta\phi_{\mathrm{e}^+\mu^-} \approx 1.3$ the QCD-induced process becomes dominant. Around $\Delta\phi_{\mathrm{e}^+\mu^-} \approx 2.5$ the relative contributions become constant again.

Figure 4.11 shows the differential cross section with respect to the R separation between the two hardest jets and with respect to the separation between the two charged leptons. For the differential distribution in the R separation of the two hardest jets, both setups show almost identical behaviour. There is a maximum for the absolute QCD-induced contribution at $\Delta R_{\mathrm{j}_1\mathrm{j}_2} \approx 4.0$ and $\Delta R_{\mathrm{j}_1\mathrm{j}_2} \approx 4.6$ in the Higgs setup and a maximum for the absolute EW contribution at $\Delta R_{\mathrm{j}_1\mathrm{j}_2} \approx 4.8$ for the VBS and $\Delta R_{\mathrm{j}_1\mathrm{j}_2} \approx 5.0$ for the Higgs setup. As usual in VBS processes, the EW contribution is dominant for high jet R separations, e. g. when the jets are back-to-back. In the VBS setup, the EW contribution exceeds the QCD-induced contribution for $\Delta R_{\mathrm{j}_1\mathrm{j}_2} > 6.2$ and in the Higgs setup for $\Delta R_{\mathrm{j}_1\mathrm{j}_2} > 5.6$. We mention that the range of this observable is determined by cuts on the rapidity separation of the jets, the maximum rapidity of a single jet and the domain of definition of the azimuthal angular separation to explain the shape of the relative contributions for large $\Delta R_{\mathrm{j}_1\mathrm{j}_2}$ in the VBS and small ones in the Higgs setup. Next, we discuss the differential distribution of the R separation between the two charged leptons. We recognise in both setups a large dip after $\Delta R_{\mathrm{e}^+\mu^-} = \pi$, which is due to the numerical domain of definition of the azimuthal angular separation: R separations below this value can be achieved by any rapidity difference if the azimuthal angular separation is large enough; R separations above this value require a minimum rapidity difference. In this observable, we realise some similarities and differences between the VBS and the Higgs setup. The shape of the QCD-induced contribution
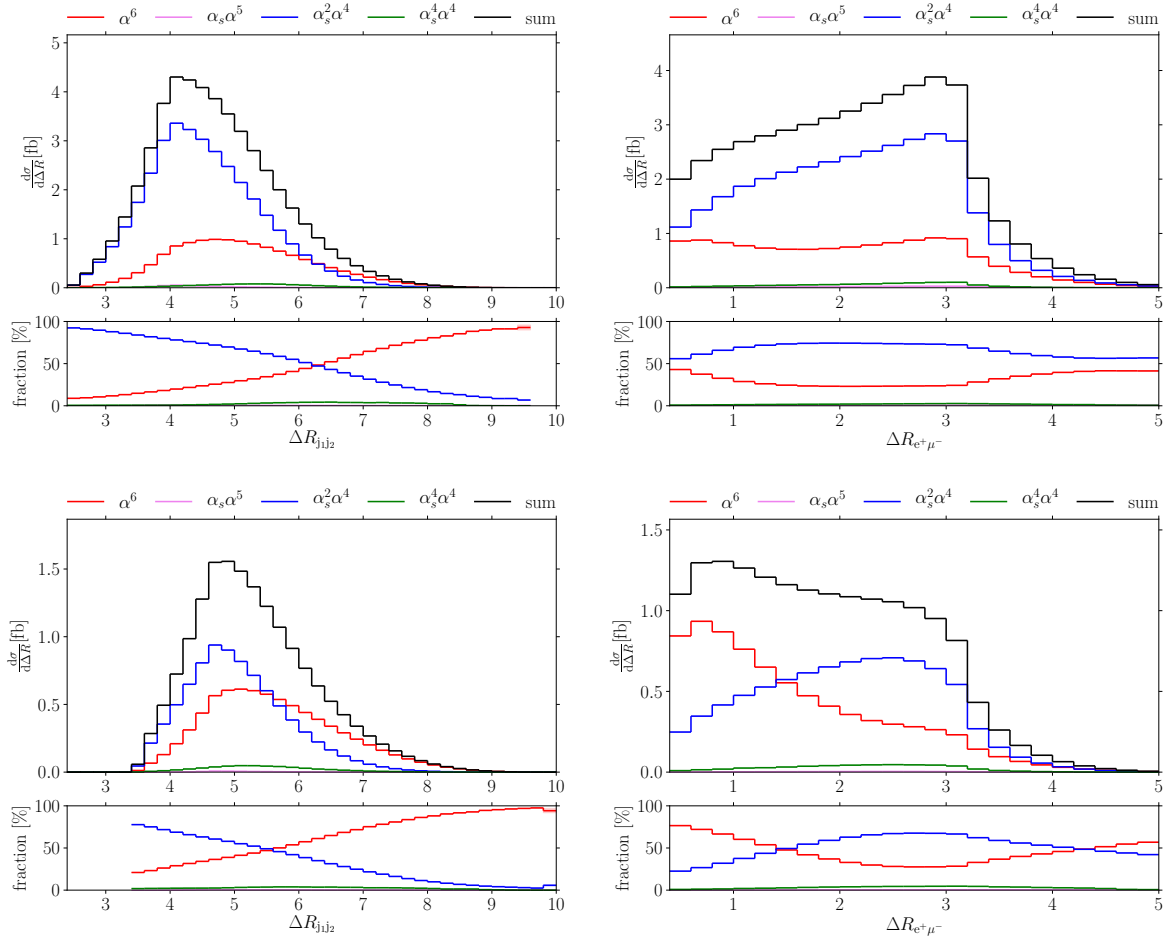
Figure 4.11: Differential distributions at LO in the R separation of the two hardest jets (left) and the two charged leptons (right) in the VBS (top) and the Higgs setup (bottom).

is quite similar since it raises until a separation of $\Delta R_{e^+\mu^-} \approx 3$ in the VBS and $\Delta R_{e^+\mu^-} \approx 2.5$ in the Higgs setup, after which it starts falling and has the aforementioned dip at π. A slight difference between both setups is the smoother curve in the case of the Higgs setup. The EW contributions are shaped differently in the two setups. In the VBS setup, there are two flat maxima, one around $\Delta R_{e^+\mu^-} \approx 0.4$ and the other at $\Delta R_{e^+\mu^-} \approx 3$ with a minimum in between at $\Delta R_{e^+\mu^-} \approx 1.5$. In the Higgs setup, the maximum appears at small $\Delta R_{e^+\mu^-}$ with an afterwards monotonously falling behaviour, although the curve is quite flat around $\Delta R_{e^+\mu^-} \approx 3$. We already mentioned in the discussion of Figure 4.9 that the differential distribution in the rapidity difference between the charged leptons is similar in the two setups. However, the differential distribution in the azimuthal angular separation, discussed in Figure 4.10, is different. With the different differential distribution in the azimuthal angular separation, we can also explain the differences in this observable: While the differential distribution in the azimuthal angular separation for the EW process is very flat in the VBS setup, it shows a clear tendency towards small values in the Higgs setup, so we also see this tendency in the total separation. We also mention the sum of the LO differential cross sections, which therefore also has different shapes comparing both setups: In the VBS setup, it is growing to a maximum at $\Delta R_{e^+\mu^-} \approx 3$, in the Higgs setup it has its maximum already at $\Delta R_{e^+\mu^-} \approx 1$ and sinks afterwards. While its shape in the VBS setup resembles the shape of the QCD-induced contribution due to the flat EW contribution, the raising QCD-induced and the falling EW contribution lead to a smoothly falling curve in the Higgs setup. The relative contributions show more similarity than the absolute ones. In the VBS setup, they are almost equal at low separation, and the relative EW contribution falls
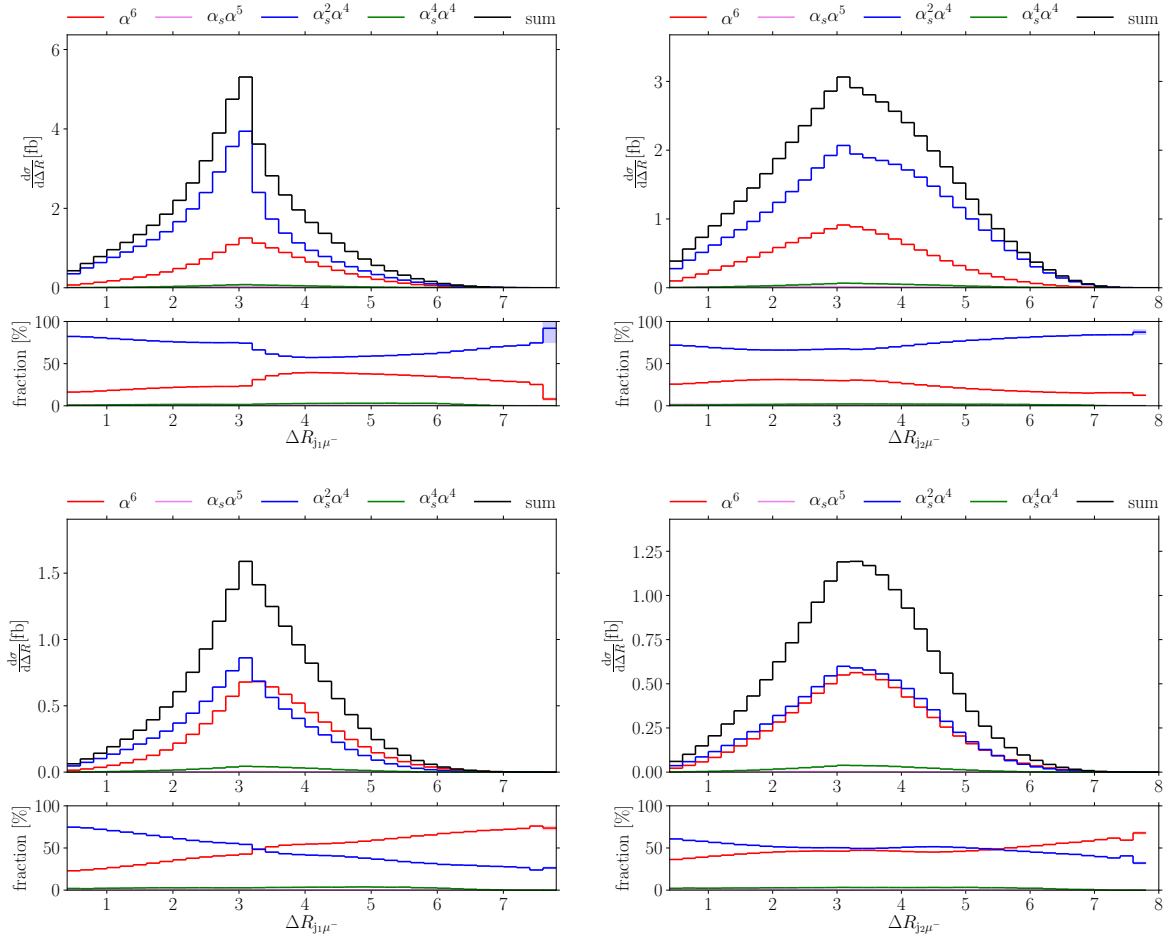
Figure 4.12: Differential distributions at LO in the R separation of the hardest jet and the muon (left) and the second hardest one and the muon (right) in the VBS (top) and the Higgs setup (bottom).

to a very flat minimum between $2 < \Delta R_{e^+\mu^-} < 3$, where the ratio between both contributions is almost constant. Afterwards, the relative EW contribution rises again and for $\Delta R_{e^+\mu^-} > 4.5$, the ratio becomes constant again. In the Higgs setup, the EW contribution dominates for small separations and falls and also reaches a plateau with constant ratios between $2.4 < \Delta R_{e^+\mu^-} < 3$. In contrast to the VBS setup, there is no second plateau within the depicted range of the variable, but it grows constantly.

We discuss the differential cross section with respect to the R separation of the hardest jet and the muon and with respect to the separation of the second-hardest jet and the muon depicted in Figure 4.12. The differential distributions concerning the R separation of a jet and the positron are almost identical and are not discussed separately. Concerning the separation between the hardest jet and the muon, the shape of the absolute EW contribution is very similar with a maximum at $\Delta R_{j_1\mu^-} \approx 3$. The shape of the QCD-induced contribution is, however, different. In both setups, we recognise the drop around $\Delta R_{j_1\mu^-} = \pi$ after the maximum at $\Delta R_{j_1\mu^-} \approx 3$, which is almost absent in the EW contribution, but in the VBS setup it is much more pronounced. The relative contributions also behave differently in the two setups. We recognise the drop in the shapes at $\Delta R_{j_1\mu^-} = \pi$, until which, in both setups, the relative EW contribution is almost linearly growing. In the Higgs setup, after the break, we have the same linear behaviour as before and the EW contribution exceeds the QCD-induced one at $\Delta R_{j_1\mu^-} \approx 3.4$, but in the VBS setup, the EW contribution has a flat maximum at $\Delta R_{j_1\mu^-} \approx 4$ and becomes less important for large separations. We can compare this with the separation of the second-hardest jet and the
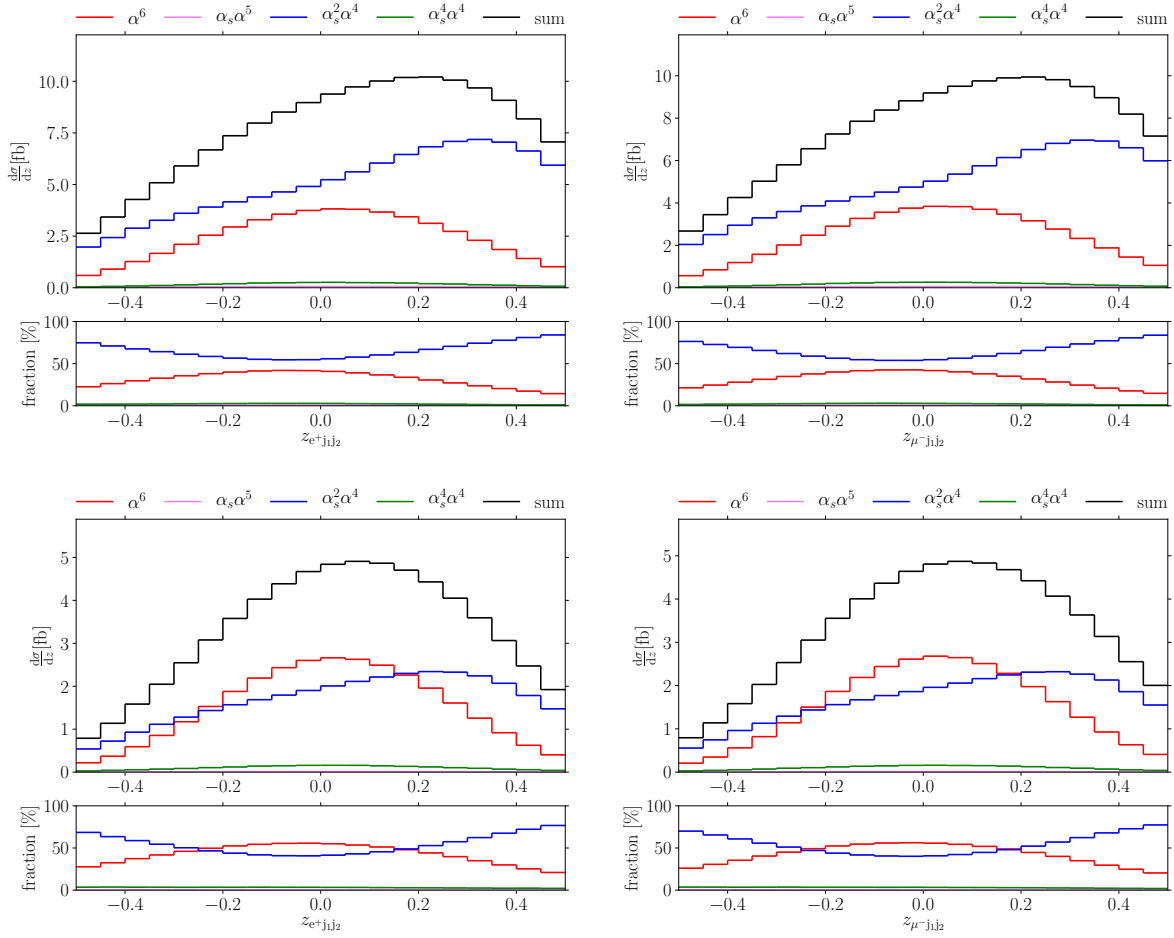
Figure 4.13: Differential distributions at LO in the centrality of the electron (left) and the muon with respect to the two hardest jets (right) in the VBS (top) and the Higgs setup (bottom).

muon. In both setups, the maximum of the QCD-induced contribution is at $\Delta R_{j_2\mu^-} \approx 3$, while the maximum of the EW contribution is at $\Delta R_{j_2\mu^-} \approx 3$ in the VBS and $\Delta R_{j_2\mu^-} \approx 3.2$ in the Higgs setup. We do not see a recognisable dip at $\Delta R_{j_2\mu^-} = \pi$ in any contribution; especially for the EW contribution in the Higgs setup, the maximum is at larger separations. Both EW and the QCD-induced relative contributions in the VBS setup are very flat. The EW relative contribution has two very slight maxima at $\Delta R_{j_2\mu^-} \approx 2.2$ and $\Delta R_{j_2\mu^-} \approx 3.2$, after which it drops until becoming almost constant at $\Delta R_{j_2\mu^-} > 6$. For the Higgs setup, we also have a very flat behaviour of the relative contributions with a maximum of the EW relative contribution at $\Delta R_{j_2\mu^-} \approx 3.4$. After a minimum at $\Delta R_{j_2\mu^-} \approx 4.4$, the relative EW contribution grows in contrast to the VBS setup. As we have seen in Figure 4.8, leptons are mostly central in both setups and in Figure 4.7, we investigated the rapidities of the jets in both setups. There, we saw that the second-hardest jet tends to have larger rapidity than the hardest one. This explains the broader shape in the differential distribution in the separation of the second-hardest jet and lepton compared to the separation of the hardest jet and lepton.

At last, we discuss the differential cross section with respect to the centralities of the two charged leptons compared to the two hardest jets (Zeppenfeld variables) in Figure 4.13. We do not recognise remarkable differences between the electron and the muon. Comparing both setups, the shapes of the distributions are also quite similar. The absolute and relative EW contribution peaks at $z_{\ell,j_1j_2} = 0$, which means, in both setups the leptons are mostly placed around the average of the jet rapidities in the EW processes. In the QCD process, however, the Zeppenfeld variable has a maximum at $z_{\mu^-,j_1j_2} \approx 0.3$ in both setups. We explicitly mention that
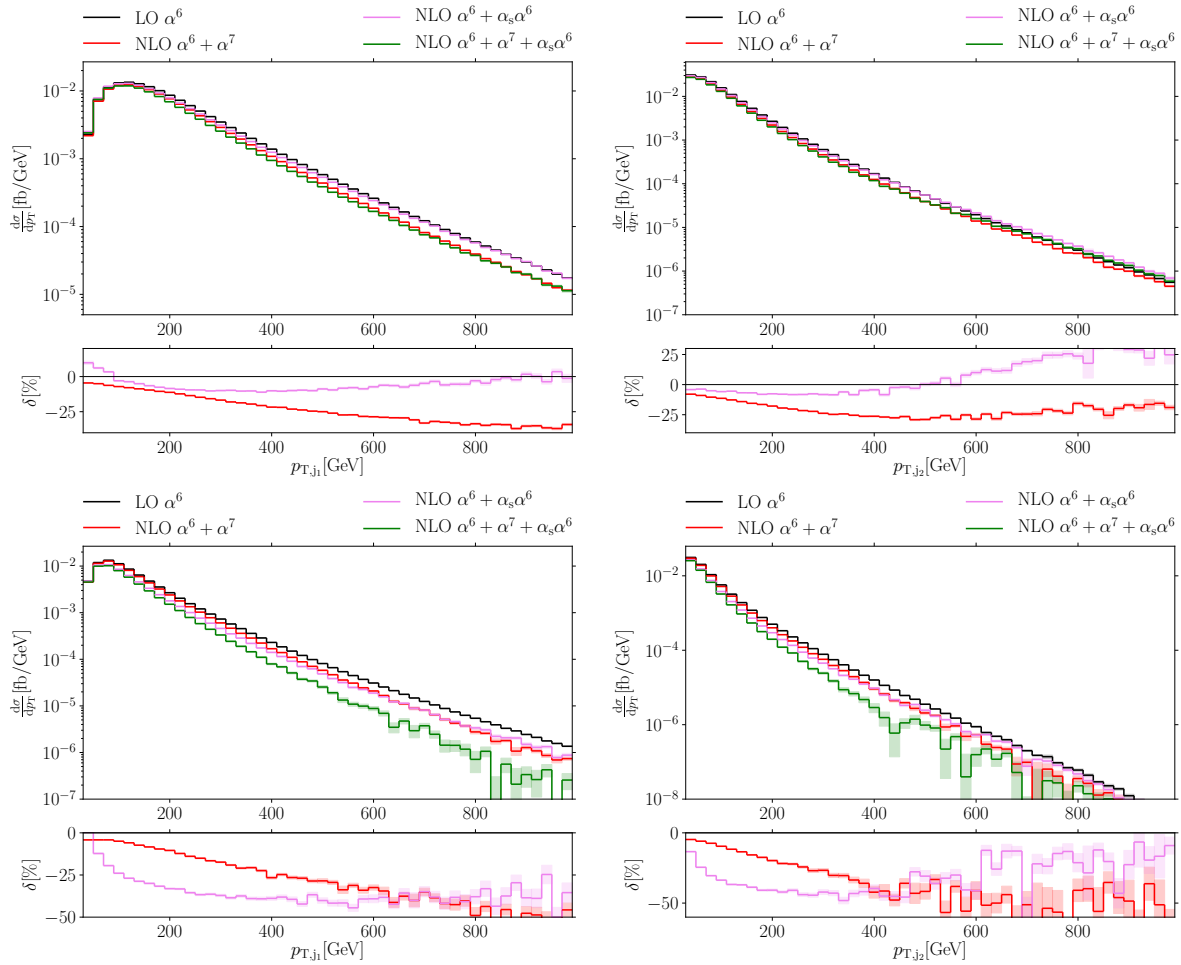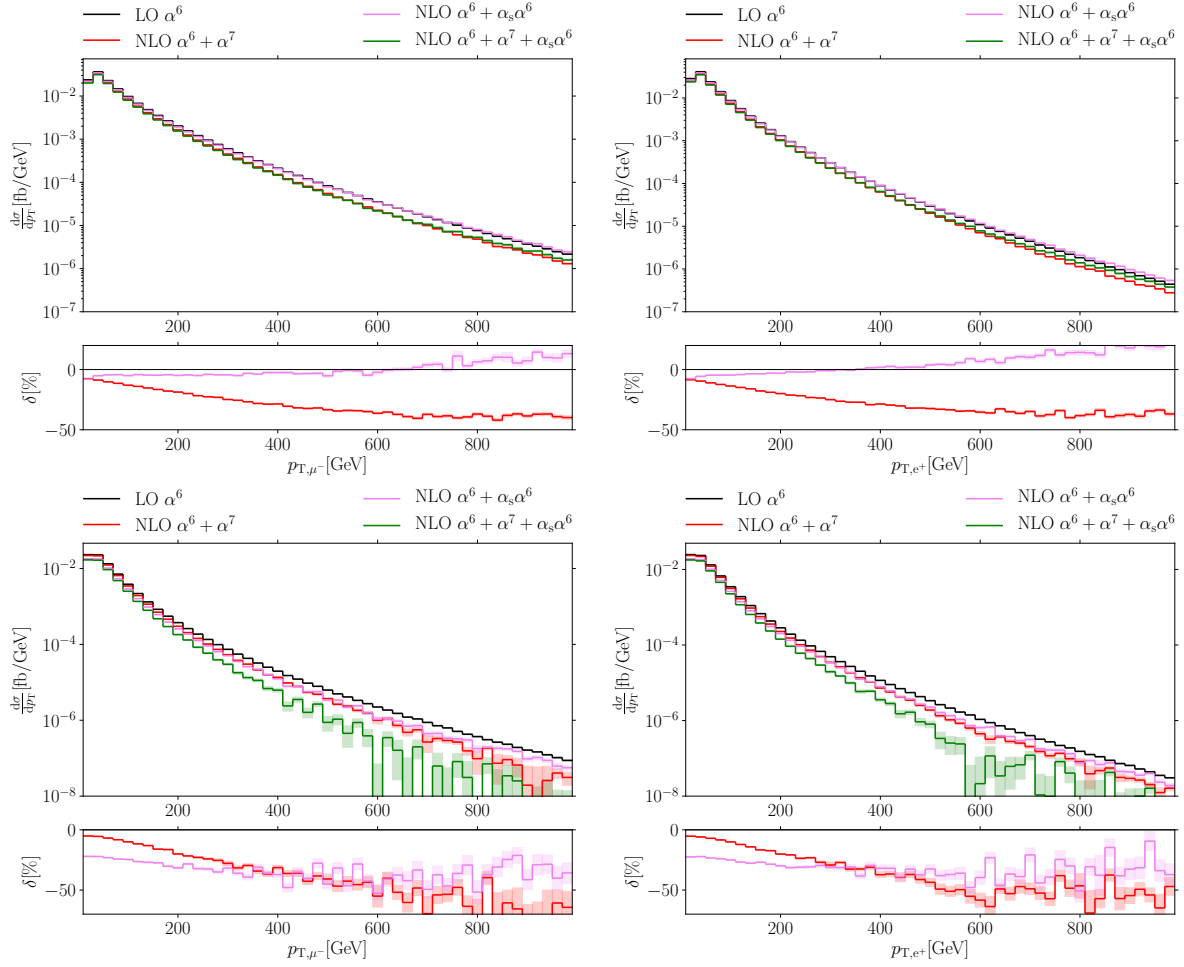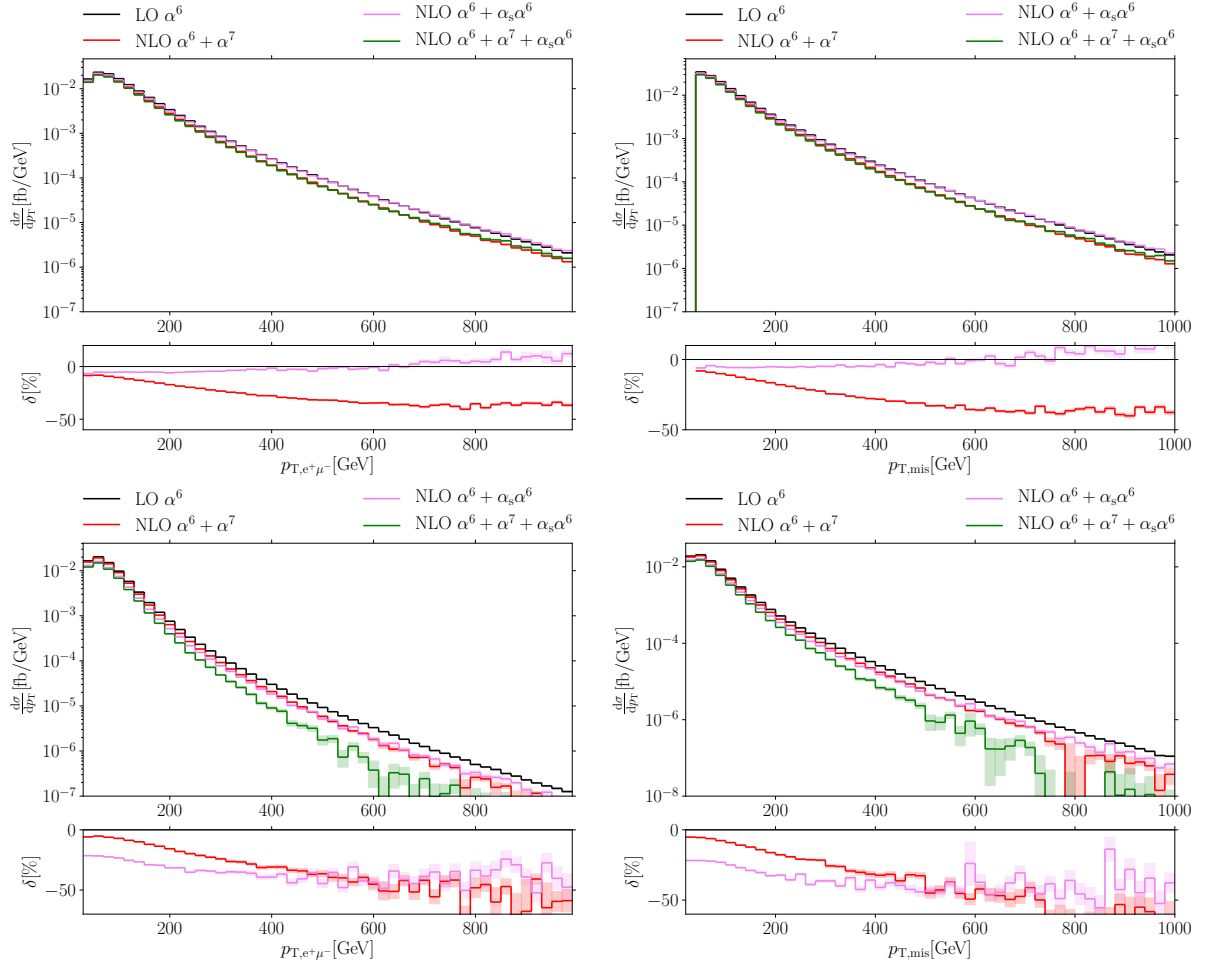
Figure 4.14: Differential distributions for the NLO corrections to the EW contribution in the transverse momentum of the hardest (left) and the second-hardest jet (right) in the VBS (top) and the Higgs setup (bottom). The upper panels show the absolute LO EW contribution at $\mathcal{O}\left(\alpha^6\right)$, the NLO cross sections including the EW corrections $(\mathcal{O}\left(\alpha^6\right) + \mathcal{O}\left(\alpha^7\right))$, the QCD corrections $(\mathcal{O}\left(\alpha^6\right) + \mathcal{O}\left(\alpha_s\alpha^6\right))$ and the complete NLO cross sections $(\mathcal{O}\left(\alpha^6\right) + \mathcal{O}\left(\alpha^7\right) + \mathcal{O}\left(\alpha_s\alpha^6\right))$. The lower panels show the relative NLO contributions normalised to the LO EW contribution. Shaded bands indicate integration errors.

the depicted range of the differential distribution was designed to cover the fiducial phase space in the Higgs setup, and about 30% of the QCD-induced cross section lies outside the depicted range of the histogram in the VBS setup, while only about 10% of the EW cross section does so, which matches our previous observation of both jets in QCD-induced processes being more likely central than EW jets.

4.4.2   NLO corrections to the EW contribution

In this section, we discuss the NLO corrections to the EW contribution for both VBS and Higgs setup. As usual, we talk about the contributions of $\mathcal{O}\left(\alpha_s\alpha^6\right)$ as QCD corrections to the EW cross section and ignore the fact that they also include EW corrections to the interference process. We thus depict in our plots the LO contribution of $\mathcal{O}\left(\alpha^6\right)$ and the combined NLO contributions $\mathcal{O}\left(\alpha^6\right) + \mathcal{O}\left(\alpha^7\right)$ and $\mathcal{O}\left(\alpha^6\right) + \mathcal{O}\left(\alpha_s\alpha^6\right)$ in the upper panels and the relative corrections of both $\mathcal{O}\left(\alpha^7\right)$ and $\mathcal{O}\left(\alpha_s\alpha^6\right)$ normalised to the LO contribution of $\mathcal{O}\left(\alpha^6\right)$ in the lower panels. The general design of our figures is the same as in the previous section with the VBS setup depicted in the upper, the Higgs setup depicted in the lower row and two different observables in the two columns.

We begin with the transverse momentum of the leading and subleading jet in Figure 4.14. We recognise that the behaviour of the EW corrections is similar in both setups for both distributions. For the hardest jet, the EW corrections are always negative and become larger with higher $p_{\mathrm{T},\mathrm{j}_1}$, although the relative corrections start fluctuating due to the integration error in the Higgs setup. These corrections reach -35% in the VBS and -50% in the Higgs setup for $p_{\mathrm{T},\mathrm{j}_1} > 800\,\mathrm{GeV}$. The behaviour of the relative EW corrections for the differential distribution of the second-hardest jet is similar, but there is a maximum in the VBS setup around $p_{\mathrm{T},\mathrm{j}_2} \approx 500\,\mathrm{GeV}$ with a relative correction of -30%. For the Higgs setup, we can only suspect such a maximum between $600\,\mathrm{GeV} < p_{\mathrm{T},\mathrm{j}_2} < 800\,\mathrm{GeV}$ since this is, unfortunately, the region with large integration errors due to the smallness of both LO and NLO cross section. In all cases, the results are not unexpected. Large EW corrections with higher transverse momenta, i. e. with higher energy in the system, are already well known due to the influence of large Sudakov logarithms. The behaviour of the QCD corrections differs between the setups as we could already infer from the integrated cross section. In the VBS setup, the QCD corrections for the hardest jet start positive and show a very flat minimum around $p_{\mathrm{T},\mathrm{j}_1} \approx 400\,\mathrm{GeV}$ with a relative value around -10%. At about $p_{\mathrm{T},\mathrm{j}_1} \approx 900\,\mathrm{GeV}$, the QCD corrections become zero. This behaviour is mirrored by the QCD corrections regarding the second-hardest jet. They are negative for small values of $p_{\mathrm{T},\mathrm{j}_2}$ and peak at $p_{\mathrm{T},\mathrm{j}_2} \approx 300\,\mathrm{GeV}$ with a value of -10%, before they become positive for large transverse momentum, crossing the zero-line around $p_{\mathrm{T},\mathrm{j}_2} \approx 500\,\mathrm{GeV}$ and amounting to even $+25\%$ for $p_{\mathrm{T},\mathrm{j}_2} > 800\,\mathrm{GeV}$. This is in contrast to their behaviour in the Higgs setup. Although the QCD corrections for the hardest jet are only slightly positive in the first bin, they start similarly, and after a first rapid negative growth, the corrections flatten in the region at $p_{\mathrm{T},\mathrm{j}_1} > 400\,\mathrm{GeV}$. The amount of relative contributions is with -40% much larger than in the VBS setup in this region, and in contrast to the VBS setup, they do not tend to zero afterwards but stay almost constant. The QCD corrections for the second-hardest jet are very flat in a region between $100\,\mathrm{GeV} < p_{\mathrm{T},\mathrm{j}_2} < 450\,\mathrm{GeV}$, also with a value of -40%, and start to tend to zero for very large transverse momenta again. The large negative corrections for the leading jet with large and the subleading jet with medium transverse momenta are explicable by the jet veto: If already the leading jet is soft, then the second- and third-hardest jet must also be very soft and the third jet passes the cut criteria. The same is true if only the subleading jet is soft. Hence, we do not get those large negative corrections for small values of $p_{\mathrm{T},\mathrm{j}_1}$ or $p_{\mathrm{T},\mathrm{j}_2}$. As soon as both tagging jets exceed a certain amount of transverse momentum, the cut for the third jet can become efficient, and we recognise the immense drop in the corrections.

We turn to the transverse momentum sum of the two hardest jets on the left-hand side of Figure 4.15. The EW corrections in both setups are negative and become larger with growing transverse momentum. This resembles the behaviour of the corrections in the transverse momenta of a single jet. We note that in the region of a large absolute cross section, the relative EW corrections in the Higgs setup are smaller than in the VBS setup, whereas the relative corrections are larger for high $p_{\mathrm{T},\mathrm{j}_1\mathrm{j}_2}$. The QCD corrections also resemble the corrections in the transverse momentum of a single jet. In the VBS setup they are positive at both borders of the spectrum and negative between $80\,\mathrm{GeV} < p_{\mathrm{T},\mathrm{j}_1\mathrm{j}_2} < 900\,\mathrm{GeV}$ with a negative maximum around $p_{\mathrm{T},\mathrm{j}_1\mathrm{j}_2} \approx 350\,\mathrm{GeV}$, where they reach about -10%. The QCD corrections in the Higgs setup start already off negative at -15% and reach -40% at $p_{\mathrm{T},\mathrm{j}_1\mathrm{j}_2} \approx 600\,\mathrm{GeV}$, before they start to fluctuate. The different behaviour compared to the VBS setup and the negative value of the correction from the start on is also a consequence of the jet veto: If the sum of the transverse momentum of the two hardest jets is about zero, then the system would like to have a third hard jet to carry away transverse momentum that is acquired from the leptonic system. Until $p_{\mathrm{T},\mathrm{j}_1\mathrm{j}_2} \approx 80\,\mathrm{GeV}$, the corrections for both VBS and Higgs setup are almost constant; afterwards the Higgs setup QCD corrections massively drop before they become constant again around $p_{\mathrm{T},\mathrm{j}_1\mathrm{j}_2} \approx 300\,\mathrm{GeV}$. The correlated observable of the transverse momentum of the four leptons does not differ significantly for the EW corrections in both setups. However, the QCD corrections in the VBS setup are largest at $p_{\mathrm{T},4\ell} = 0$ tend almost linearly to zero at $p_{\mathrm{T},4\ell} \approx 1000\,\mathrm{GeV}$. In the Higgs setup, the QCD
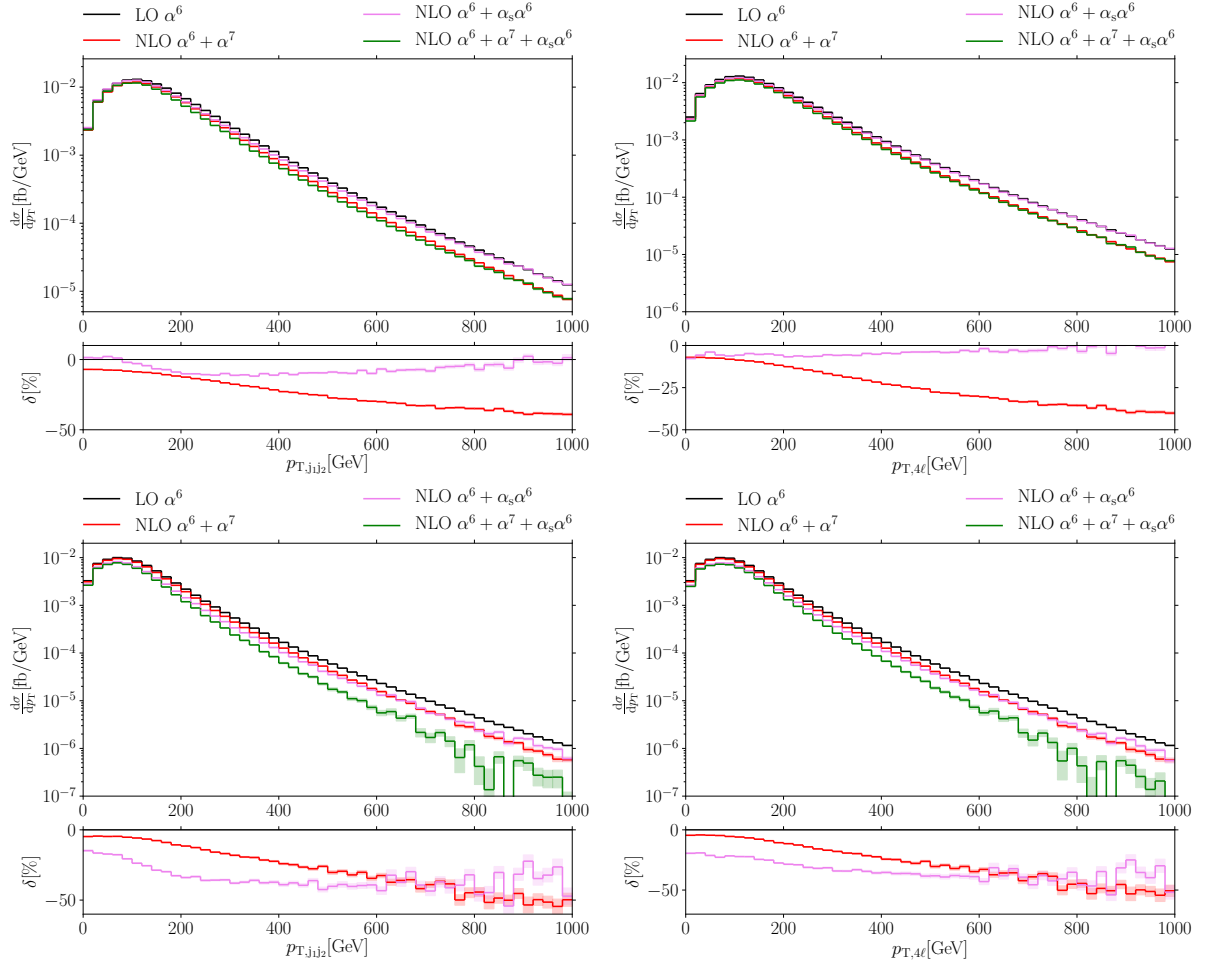
Figure 4.15: Differential distributions for the NLO corrections to the EW contribution in the (vectorial) transverse momentum sum of the two hardest jets (left) and the four-lepton system (right) in the VBS (top) and the Higgs setup (bottom).

corrections are always negative and grow with larger $p_{\mathrm{T},4\ell}$, but they have a more linear shape than in case of $p_{\mathrm{T},\mathrm{j}_1\mathrm{j}_2}$.

The next distributions that we discuss are the corrections to the differential cross sections with respect to the muon and the electron transverse momentum in Figure 4.16. As we have seen for LO, both of these distributions are almost identical. The EW corrections behave as expected and grow larger with larger transverse momentum for both setups and particles. We recognise again that the relative corrections are smaller in the Higgs setup than in the VBS setup for small transverse momenta and larger for large transverse momenta. In the VBS setup, they amount up to -45% in the depicted range; in the Higgs setup, they are up to -50% in the region with reliable integration errors. The QCD corrections in both setups behave oppositely in the two setups. In the VBS setup, they start negative and become almost linearly positive with larger transverse momentum, where we see the zero point at $p_{\mathrm{T},\mu^-} \approx 600\,\mathrm{GeV}$ for the muon and at $p_{\mathrm{T},\mathrm{e}^+} \approx 400\,\mathrm{GeV}$ for the positron. In the Higgs setup, they tend to have more negative values with growing transverse momentum, which is again a direct consequence of the jet veto. After $p_{\mathrm{T}} \approx 200\,\mathrm{GeV}$, the QCD corrections become, disregarding statistical fluctuations in the tails, almost constant.

The differential cross section with respect to the transverse momentum sum of the two charged leptons and the differential cross section with respect to the missing transverse momentum are shown in Figure 4.17. Both EW and QCD corrections behave similiarly in these two observables. We see again the enormous EW corrections at high transverse momenta of the system in both
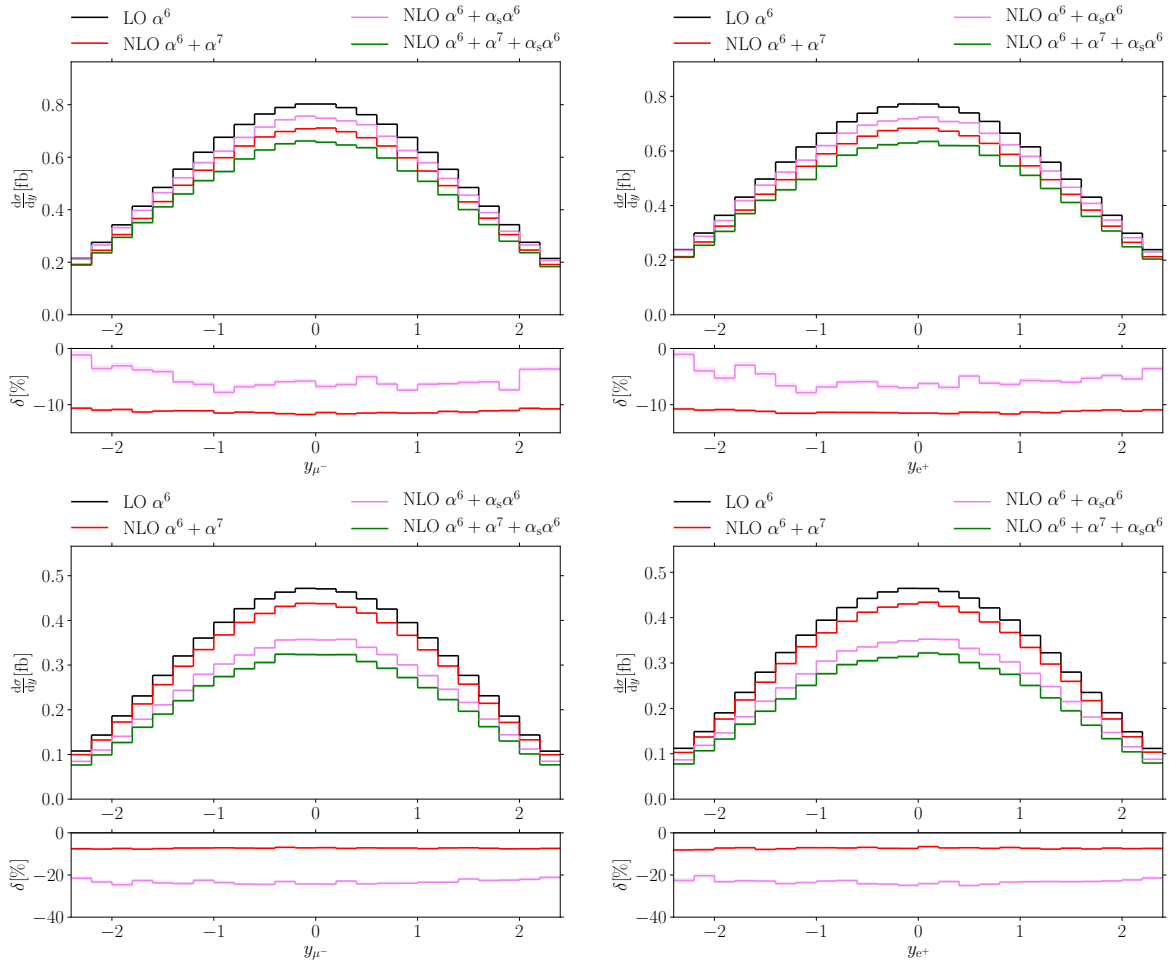
Figure 4.16: Differential distributions for the NLO corrections to the EW contribution in the transverse momentum of the muon (left) and the positron (right) in the VBS (top) and the Higgs setup (bottom).

setups. As for other distributions, the EW corrections are in the Higgs setup smaller than in the VBS setup for small transverse momenta and larger for large transverse momenta. In the VBS setup, they reach a maximum at -45%, whereas they tend to values below -50% in the Higgs setup. In the peak region of the absolute cross section, the EW corrections in the Higgs setup are smaller than in the VBS setup. The QCD corrections behave as we already know from other distributions in transverse momentum: While they are moderate and tending almost linearly from -10% at zero to $+10\%$ at $p_{\mathrm{T}} = 1000\,\mathrm{GeV}$ in the VBS setup, with a zero $p_{\mathrm{T}} \approx 600\,\mathrm{GeV}$, they become more negative in the Higgs setup with growing p_{T}, beginning at -25% at zero transverse momentum and also reaching values of approximately -50% at $p_{\mathrm{T},\mathrm{e}^+\mu^-} \approx 600\,\mathrm{GeV}$.

We now discuss the corrections to the differential cross section with respect to the invariant mass of the visible system and to the invariant mass of the two hardest jets in Figure 4.18. For both of these distributions in both setups, the EW corrections behave as expected and become larger with larger invariant masses. We see the repeating pattern that the EW corrections in the Higgs setup are smaller than the ones in the VBS setup for small energies and – in these cases – equally large for high energies. They amount up to -20% both at large M_{vis} and $M_{\mathrm{j_1j_2}}$ in both setups. We emphasise that the EW corrections grow slower at large energies and become almost constant, except for M_{vis} in the Higgs setup. The QCD corrections to the differential distribution in the visible system are also almost constant over the complete depicted range and have a small tendency to slightly positive values for large M_{vis} in the VBS setup. In the Higgs setup, the QCD corrections are also almost constant over the complete depicted range and hence

Figure 4.17: Differential distributions for the NLO corrections to the EW contribution in the transverse momentum sum of the two charged leptons (left) and the missing transverse momentum (right) in the VBS (top) and the Higgs setup (bottom).

show a different behaviour than in the case of transverse momenta. The QCD corrections for the invariant-mass distribution of the two hardest jets in the VBS setup are almost zero for small invariant masses, after which we see a drop around $M_{j_1 j_2} \approx 600\,\mathrm{GeV}$ to a relative value of about -5%. After a second phase of being almost constant until around $M_{j_1 j_2} \approx 2500\,\mathrm{GeV}$, the QCD corrections tend back to zero for larger values of $M_{j_1 j_2}$. We see a qualitatively identical behaviour for the QCD corrections in the Higgs setup. Although the corrections are larger than in the VBS setup, the curve is only shifted towards more negative values, and we also see the phase of almost constant corrections between $1000\,\mathrm{GeV} < M_{j_1 j_2} < 3200\,\mathrm{GeV}$, before the curve tends back to smaller values. In contrast to the transverse momentum distributions of the two jets, the shape of the relative QCD corrections in both setups is similar. We can therefore deduce that the transverse momentum cut on the jets does not affect specific values of invariant masses; i. e. transverse momentum and invariant mass of the jet pair are largely uncorrelated. This also confirms our considerations in the last chapter, when we discussed the connection between energies, rapidities and transverse momenta in the LO distributions.

We turn our attention to the leptonic system and present the NLO corrections to the invariant-mass distribution in the two charged leptons and the four-lepton system in Figure 4.19. We again emphasise that the four-lepton invariant mass is not a physical observable. The behaviour of the EW corrections is identical in both setups for both observables, and we get large negative corrections at high invariant masses. In the VBS setup, they reach -30% for both $M_{e^+\mu^-} = 1200\,\mathrm{GeV}$ and $M_{4\ell} = 2000\,\mathrm{GeV}$, while they reach -40% in the Higgs setup for
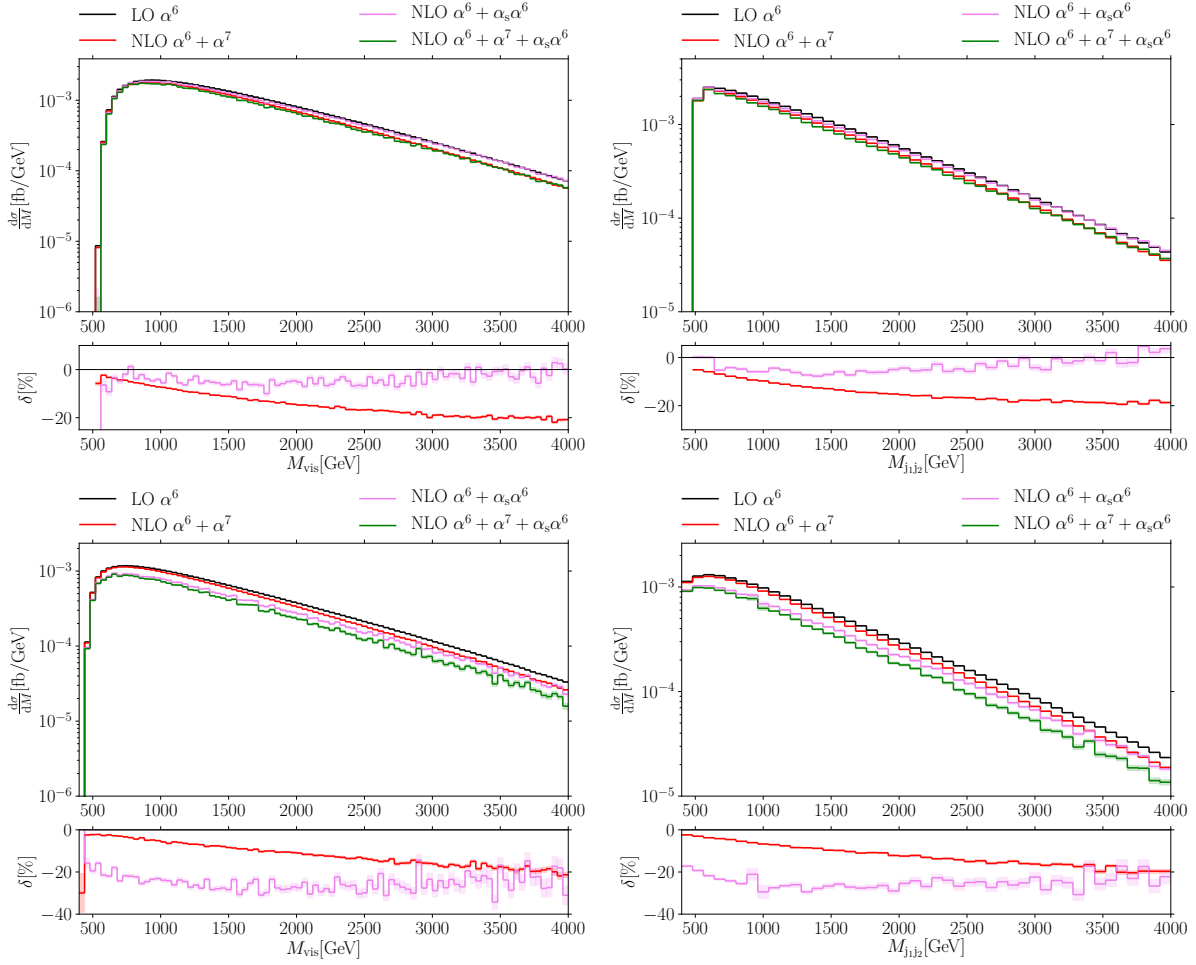
Figure 4.18: Differential distributions for the NLO corrections to the EW contribution in the invariant mass of the total visible system (left) and the two hardest jets (right) in the VBS (top) and the Higgs setup (bottom).

these values and the pattern of larger EW corrections at high energies in the Higgs setup than in the VBS setup also repeats. At low invariant masses, the EW corrections are smaller in the Higgs setup. The QCD corrections for both observables are almost constant over the complete depicted range for both setups. In the VBS setup, the QCD corrections are quite large for very small two-lepton invariant masses before they reach a plateau, and we observe a slight tendency towards positive values at large $M_{e^+\mu^-}$. In the Higgs setup, the effect at low two-lepton invariant masses is absent. The same effect can be seen in the four-lepton invariant mass, where the QCD corrections are constant in both setups except for the first two bins. In the bin, in which the Higgs-boson resonance resides, between $100\,\text{GeV} < M_{4\ell} < 200\,\text{GeV}$, there is a dip in the QCD corrections for the VBS setup, which is absent for the Higgs setup. A second effect that can be seen in the distribution for the four-lepton invariant mass is the very large relative corrections, both of QCD and EW origin, in the very first bin, at invariant masses below the Higgs-boson resonance. Admittedly, the absolute size of the differential cross section is negligible at LO and remains so at NLO. The four-lepton invariant-mass distribution beautifully demonstrates the threefold nature of W^+W^+ scattering: The first bin below the Higgs boson resonance contains only non-resonant background processes with even positive electroweak corrections. The bin containing the Higgs boson resonance is, in the VBS setup, dominated by large QCD corrections. The typical VBS signature with small QCD corrections and large EW corrections only becomes prominent above the resonance. The last remark on both distributions and their almost constant QCD corrections concerns, as in the case of the invariant masses of the two hardest jets and the
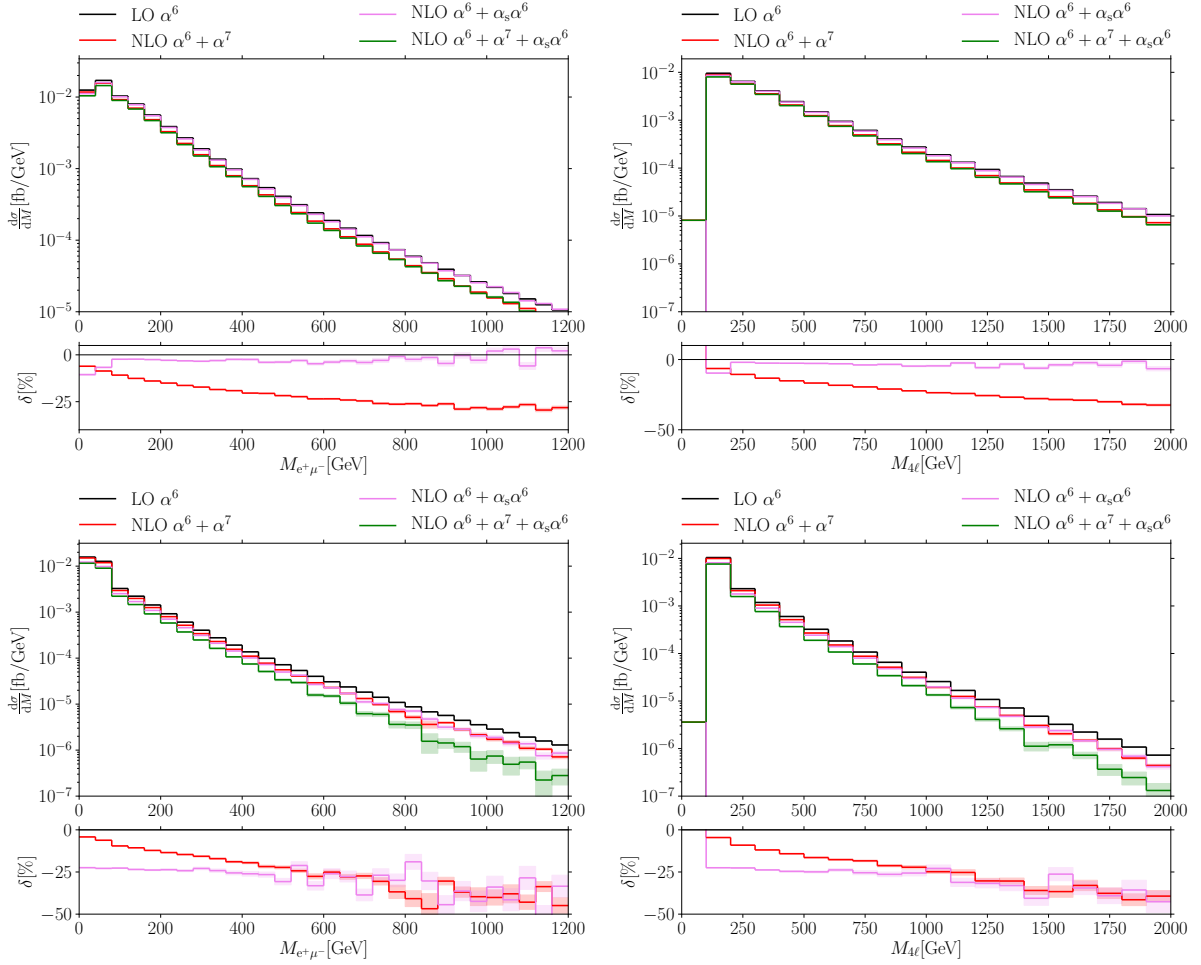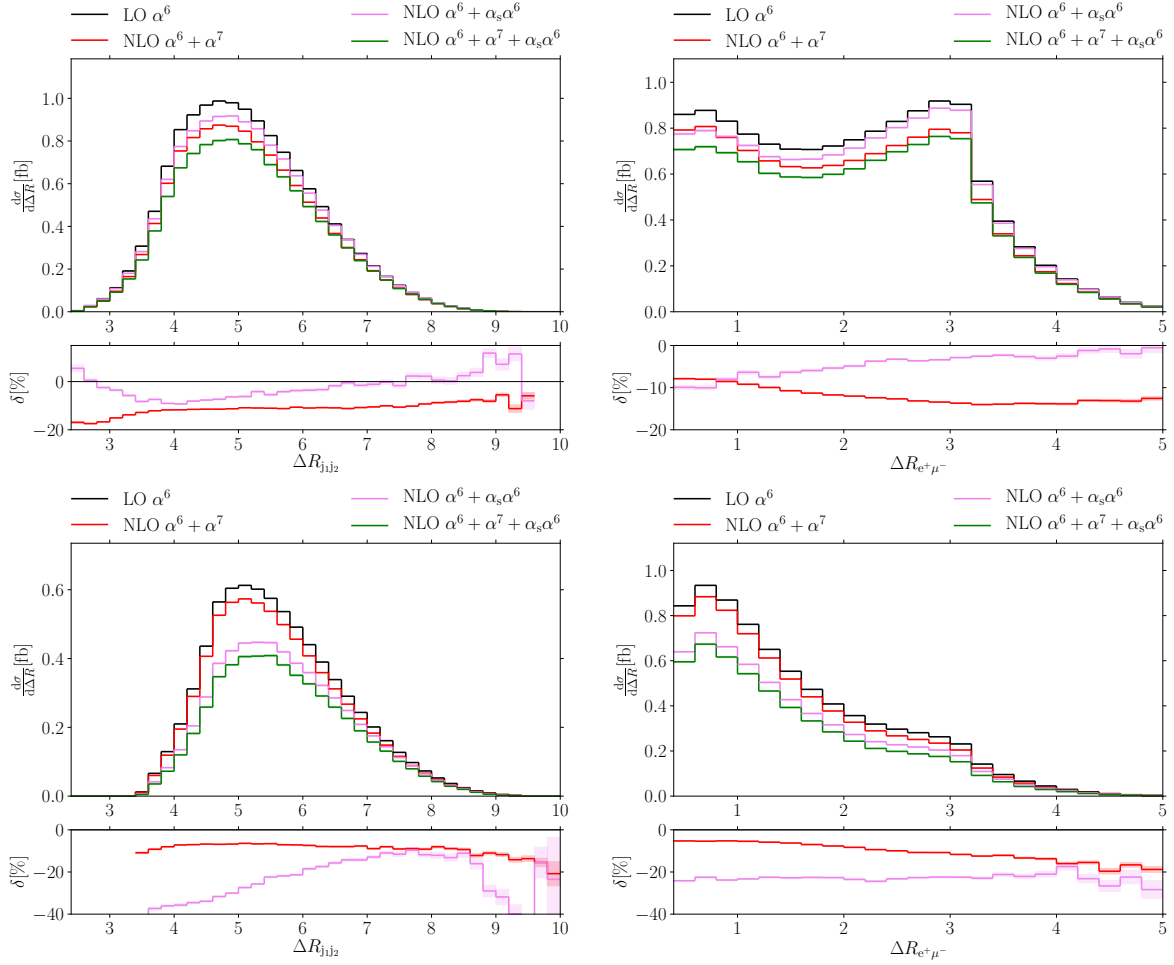
Figure 4.19: Differential distributions for the NLO corrections to the EW contribution in the invariant mass of the two charged leptons (left) and the four-lepton system (right) in the VBS (top) and the Higgs setup (bottom).

total visible system, the fact that the transverse momentum of a jet and invariant mass of the leptons are largely uncorrelated.

The next distributions in Figure 4.20 are the corrections to the differential cross section with respect to the rapidity of the hardest and the second hardest jet. We begin our discussion with the EW corrections in the VBS setup. For both jets, there is a minimum for the absolute value of the relative corrections at zero rapidity and a maximum at medium rapidities. This effect is stronger in the case of the second hardest jet, but the corrections never exceed more than -15% or less than -5%. The Higgs setup shows a similar behaviour, although the shape of the relative corrections is even less pronounced than in the VBS setup, and the corrections never exceed -10%. Since larger EW corrections are a sign of large energies in the system, large energies seem to favour both moderate rapidity and large transverse momentum. The QCD corrections behave differently than the EW ones: For the hardest jet in the VBS setup, the corrections amount to -10% at $y_{j_1} = 0$ and are about $\pm 0\%$ at the borders of the spectrum, although we recognise a tendency towards positive values. On the other hand, the QCD corrections of the second hardest jet show the opposite behaviour with zero relative corrections in the centre and QCD corrections up to -10% at the edges. For the Higgs setup, this picture changes. The overall corrections are more negative than in the VBS setup. However, we also see a negative maximum of the corrections around zero rapidity for both jets at -35%. The QCD corrections at the borders of the spectrum are smaller in the case of the first jet than in the case of the second, with -10% compared to -18%.
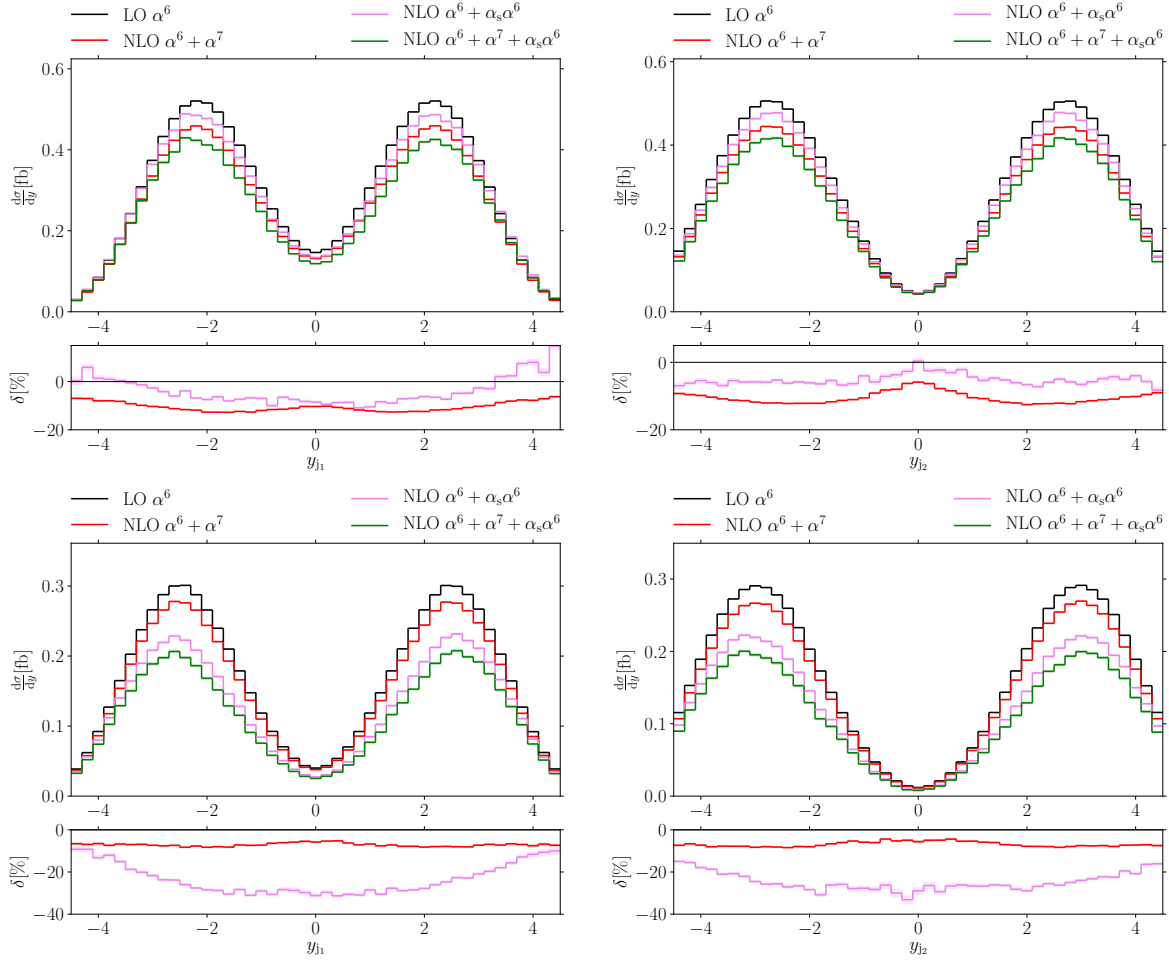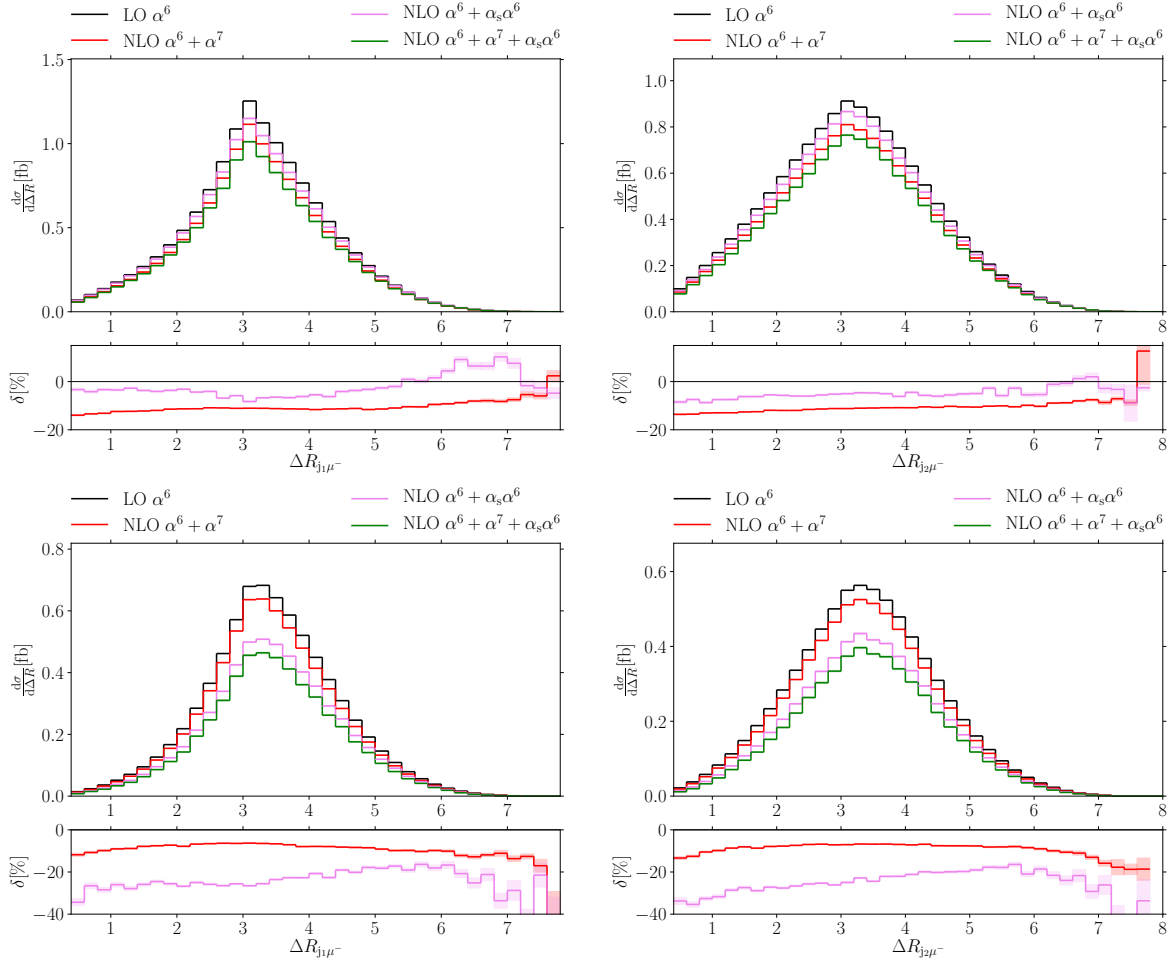
Figure 4.20: Differential distributions for the NLO corrections to the EW contribution in the rapidity of the hardest (left) and the second hardest jet (right) in the VBS (top) and the Higgs setup (bottom).

We discuss very briefly the corrections to the differential cross section with respect to the rapidity of the muon and the electron in Figure 4.21. The EW corrections are constant over the whole depicted range for both setups. The same is true for the QCD corrections in the Higgs setup. We only see a tendency towards smaller QCD corrections at the borders of the phase space for the VBS setup after it remains almost constant between $-1 < y < 2$. These distributions do not deliver new insights, and we can only use them to confirm and repeat our previous statements: The rapidity of the leptons does neither correlate with the energy in the system nor with the transverse momentum of the hadronic system. In consequence, both EW and QCD corrections in the Higgs setup are almost constant and the QCD corrections behave similarly in the two setups.

The corrections to the differential cross sections with respect to the rapidity difference of the two hardest jets and the rapidity difference of the two charged leptons are shown in Figure 4.22. We recognise for both distributions differences in the shapes of the relative corrections between the setups. The EW corrections in the differential cross section with respect to the rapidity difference of the jets are falling (in the sense that they are negative and their absolute value becomes smaller) for large rapidity difference in the VBS and growing in the Higgs setup. It should be annotated that this effect is not very prominent and the relative corrections are in a small band for both setups. The QCD corrections in the distribution in this observable are quite different. In the VBS setup, the relative QCD corrections have a negative maximum around $|\Delta y_{j_1 j_2}| \approx 4$ and tend toward small and positive values at large rapidity differences. In the Higgs
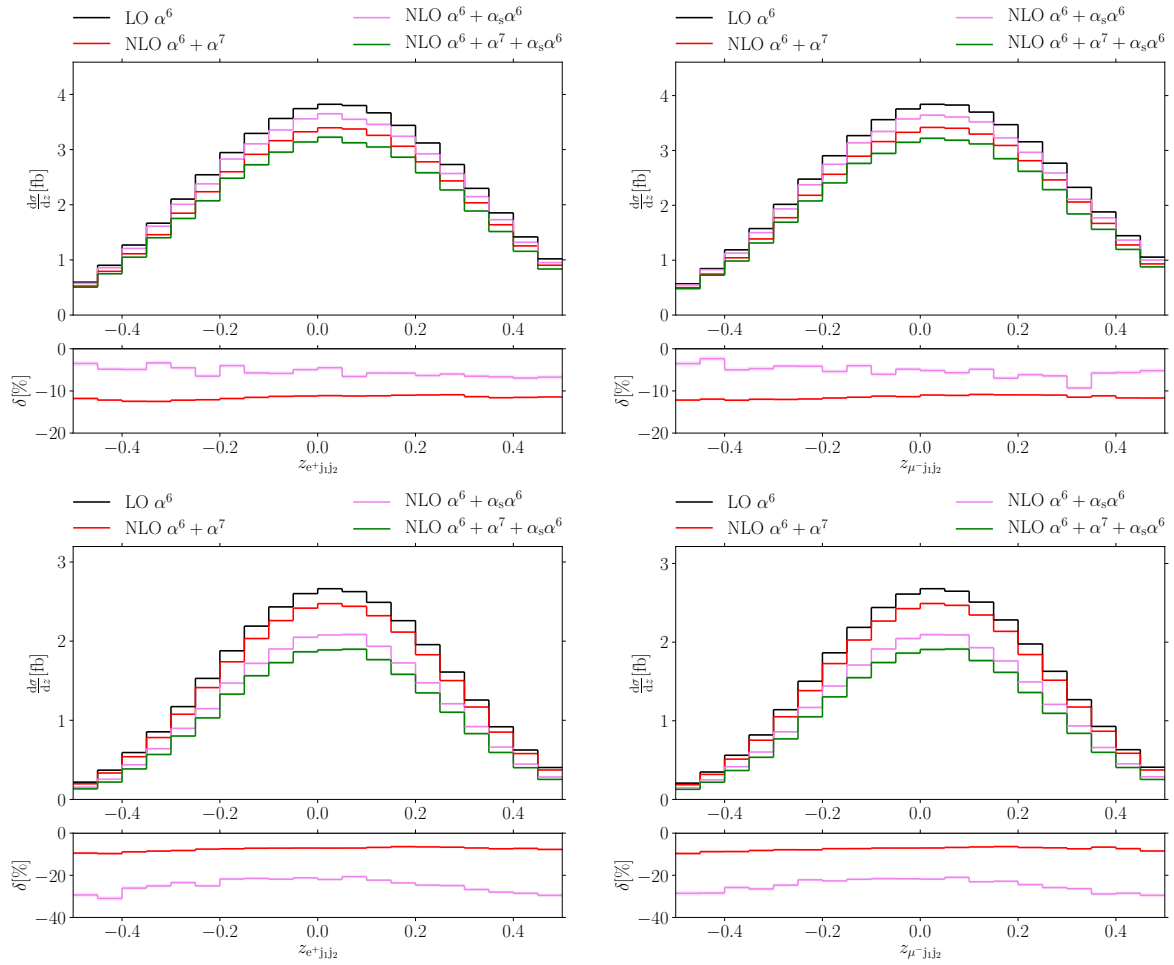
Figure 4.21: Differential distributions for the NLO corrections to the EW contribution in the rapidity of the muon (left) and the positron (right) in the VBS (top) and the Higgs setup (bottom).

setup, almost the opposite is the case. We see large negative QCD corrections both for small and large rapidity difference, -40% for $|\Delta y_{j_1 j_2}| = 3.5$ and even larger for $|\Delta y_{j_1 j_2}| = 9.0$. In contrast, the corrections are moderate with a minimum at intermediate rapidity differences. At a small rapidity difference, one of the two hard jets is likely central. If this is the hardest jet – we know from the distribution of the rapidities of a single jet, *c. f.* Figure 4.7 or Figure 4.20, that the hardest jet is more central than the second hardest – it is also likely that there is large transverse momentum in the hadronic system. The other region with large QCD corrections at large rapidity separation occurs when the differential cross section is already very small. In the differential distribution in the rapidity difference of the two charged leptons, the EW corrections in the VBS setup range between -10% and -15% with a minimum at zero rapidity difference and a maximum for intermediate rapidity differences. In the Higgs setup, there is also a minimum for small $|\Delta y_{e^+\mu^-}|$, but the maximum is at the outer ends of the depicted phase space, and we have a larger range of corrections between -5% and -20%. While the size of the corrections in the VBS setup does not allow further conclusions, the large corrections in the region of large rapidity difference between the charged leptons in the Higgs setup point towards a phase-space region, in which the Higgs-boson resonance is not prominent. We see the larger corrections coming from Sudakov logarithms at high energies. This behaviour is explicable by helicity conservation: The Higgs boson as spin-0 particle forces its daughter W bosons as decay products to have opposite helicity. Since the EW interaction couples only to left-handed fermions, the two oppositely charged leptons emerging from this process are emitted in the same direction. Thus, leptons with
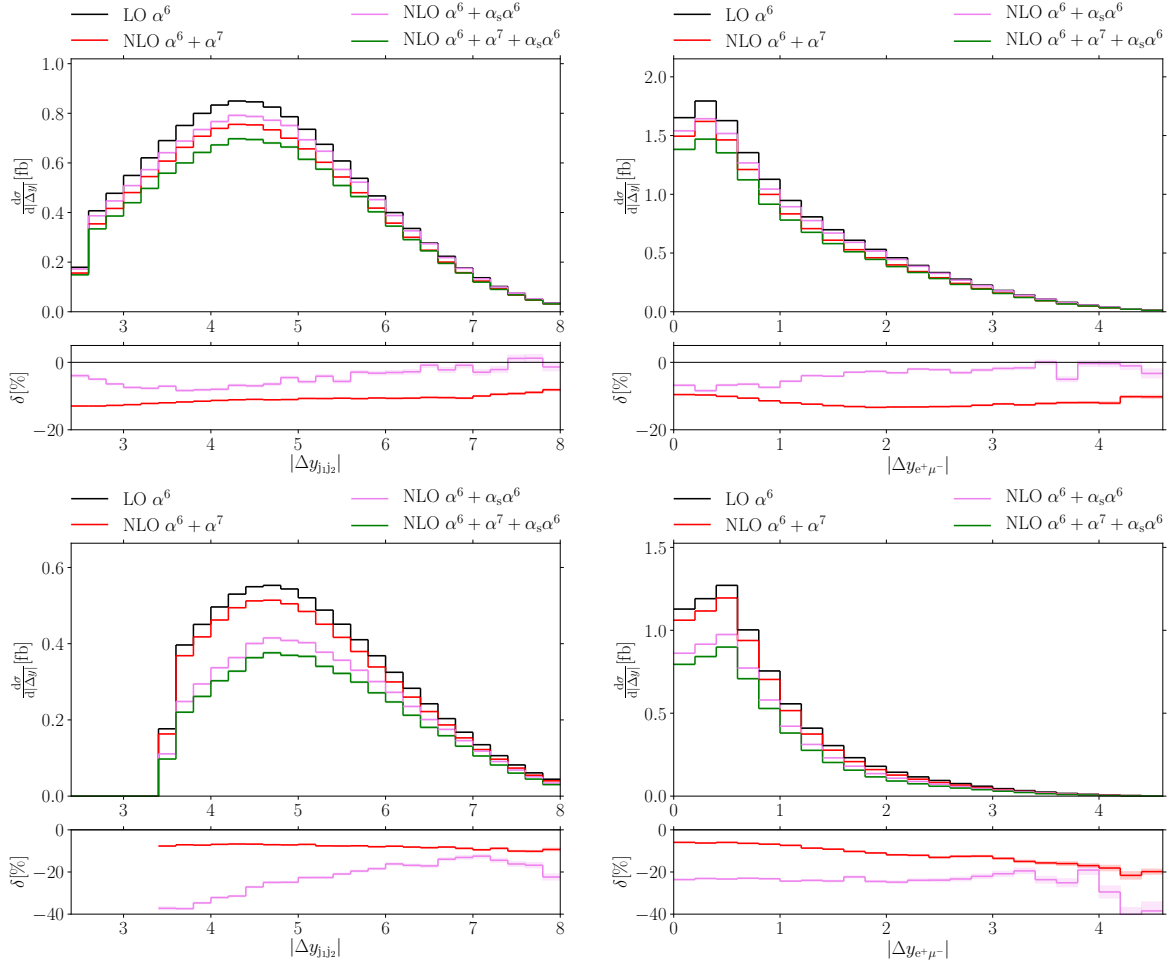
Figure 4.22: Differential distributions for the NLO corrections to the EW contribution in the rapidity separation of the two hardest jets (left) and the two charged leptons (right) in the VBS (top) and the Higgs setup (bottom).

a small rapidity difference are more likely to emerge from the Higgs-production subprocess with small EW corrections, and such with large differences result from the other VBS subprocesses with typical VBS signatures. This consideration is consistent with the fact that the shape of the distribution in the Higgs setup is much narrower than in the VBS setup, since the Higgs-setup cuts enhance the resonant Higgs contribution, as we already saw with the integrated cross section. The QCD corrections are also quite different: In the VBS setup, they are largest for zero rapidity difference and tend towards zero for large $|\Delta y_{e^+\mu^-}|$, whereas they remain almost constant in the Higgs setup.

The next two distributions that we present are the corrections to the differential cross section with respect to the azimuthal angular separation of the two hardest jets and the angular separation of the two charged leptons, depicted in Figure 4.23. For the angular separation of the jets, both EW and QCD corrections are, except for some statistical outliers in the VBS setup, almost constant in both setups. For the angular separation of the charged leptons, the EW corrections in the VBS and the Higgs setup are quite similar and become larger for larger angular separation. However, the range of EW corrections over the complete phase space varies only between -8% and -15% in the VBS setup and -6% and -13% in the Higgs setup. The QCD corrections in the VBS setup vary only moderately between -10% at small and -3% at large angular separation. In the Higgs setup, the QCD corrections are almost constant over the complete phase space.
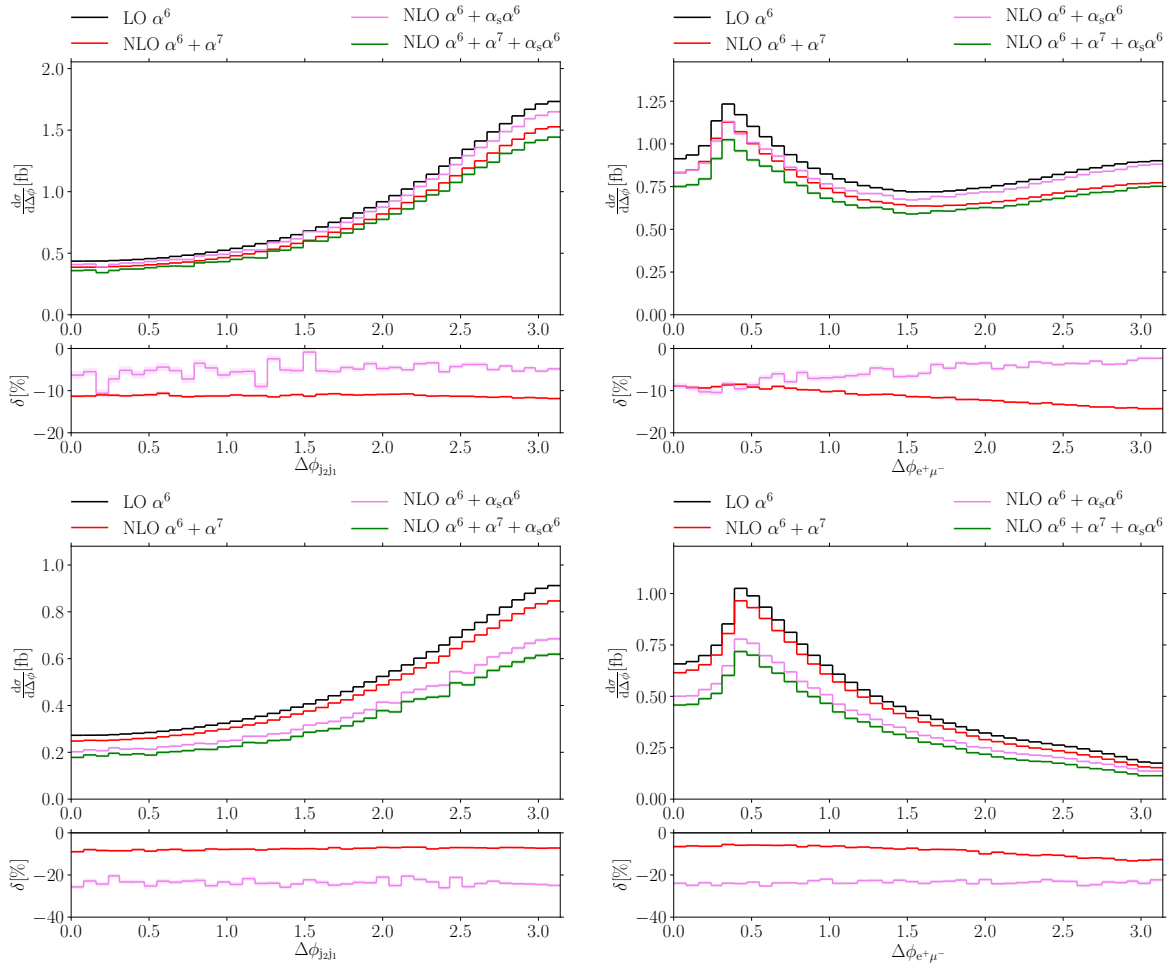
Figure 4.23: Differential distributions for the NLO corrections to the EW contribution in the azimuthal angular separation of the two hardest jets (left) and the two charged leptons (right) in the VBS (top) and the Higgs setup (bottom).

We discuss briefly the corrections to the differential cross section with respect to the R separation of the two hardest jets and the R separation of the two charged leptons, that we show in Figure 4.24. Since both relative EW and QCD corrections for the azimuthal angular separation of the two hardest jets are almost constant, the shape of the relative corrections in the total separation is governed by the shape of the corrections in the rapidity separation and we cannot extract more information than already stated above. For the R separation of the two charged leptons we want to re-emphasise that the different shapes of VBS and Higgs setup are a consequence of the different shapes of the distribution in the azimuthal angular separation and we see this more clearly in the NLO distribution than in the LO one of Figure 4.11 because of a simple rescaling of the axis. The responsible cut is, as mentioned in the LO discussion, the transverse mass cut on the leptons. Both relative corrections are in both setups also an overlay of the behaviour of the corrections in the rapidity and the azimuthal angular separation. Since the EW corrections in the VBS setup are slightly growing for large azimuthal angular separation, and they have a maximum at intermediate rapidity separation, we also see a very slight (negative) maximum at intermediate total separations. The EW corrections in the Higgs setup grow larger for larger azimuthal angular and rapidity separations, and as a consequence they also do for the total separation. The falling QCD corrections in the VBS setup and the constant ones in the Higgs setup for both rapidity and azimuthal angular separation also lead to their respective counterpart in the R separation.
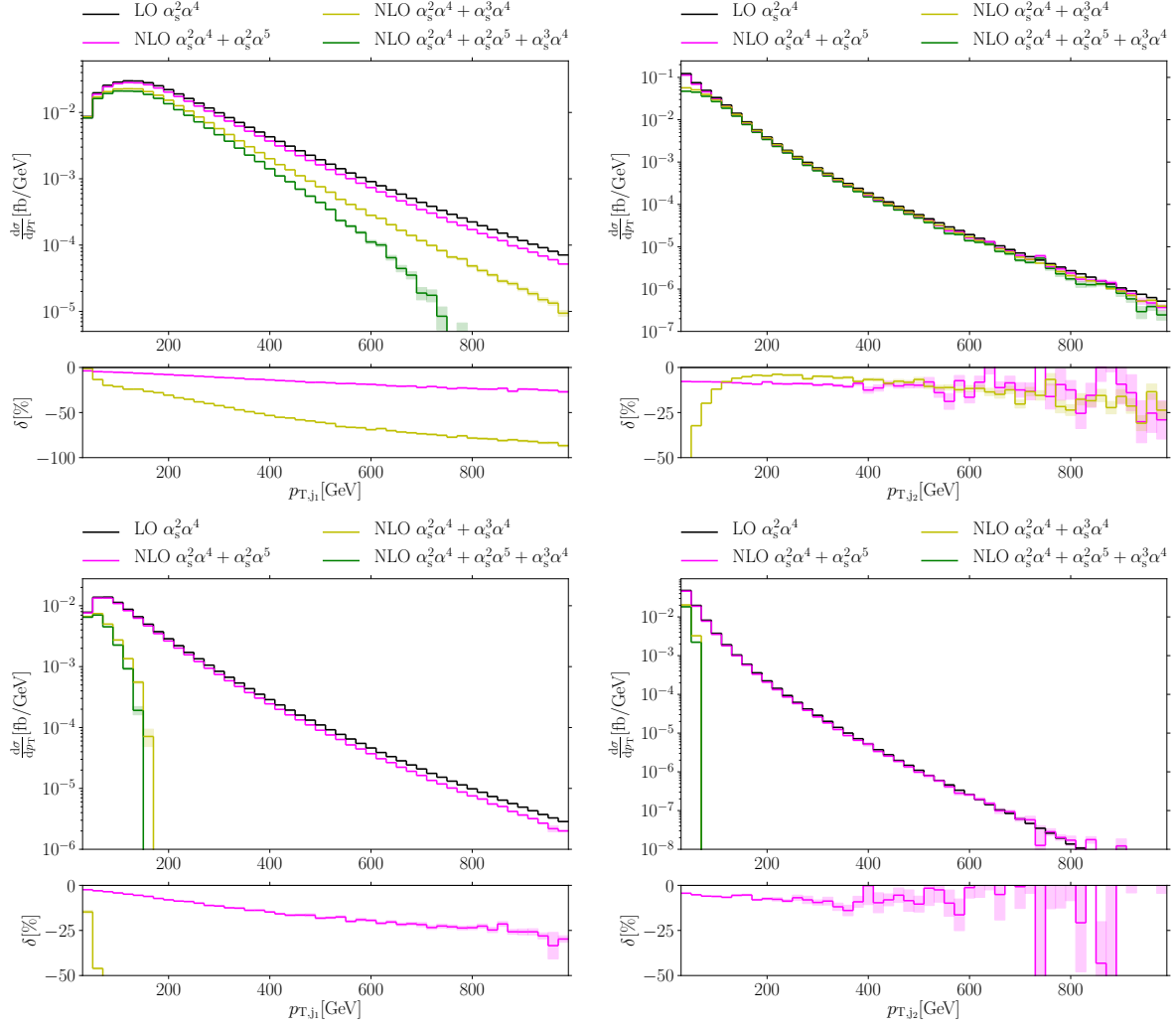
Figure 4.24: Differential distributions for the NLO corrections to the EW contribution in the R separation of the two hardest jets (left) and the two charged leptons (right) in the VBS (top) and the Higgs setup (bottom).

In Figure 4.25, we present the corrections to the differential cross section with respect to the R separation of the muon and the hardest jet as well as the R separation of the muon and the second hardest jet. As in the case of the LO distributions, we mention that the shape of both the LO cross section as well as the NLO corrections of the separation of the electron and the jets is similar to the depicted one. The EW corrections for the separation of the muon and the hardest jet in the VBS setup are almost constant over a long range of the phase space between $0 < \Delta R_{j_1\mu^-} < 5$, varying only between -14% and -10%. Afterwards, they tend linearly to smaller values and the last bin we consider to be a statistical outlier. In the Higgs setup, the behaviour of the EW corrections is slightly different. However, they are still almost constant over the complete depicted range, with only the statistical outlier in the last bin. There is a slight minimum at intermediate values around $\Delta R_{j_1\mu^-} \approx 3$. The QCD corrections in this observable follow a similar shape in the VBS and the Higgs setup, varying only very little for small separation and a tendency towards more positive values for $5 < \Delta R_{j_1\mu^-} < 7$ in case of the VBS setup and smaller values in case of the Higgs setup for $4 < \Delta R_{j_1\mu^-} < 6$. The behaviour of the corrections in the separation of the muon and the second hardest jet is similar to its behaviour for the separation of the muon and the hardest jet: The EW corrections vary very slowly and become smaller with large separation in the VBS setup, whereas they show a minimum at intermediate separations for the Higgs setup. The QCD corrections are also quite constant in the case of the VBS setup with a tendency towards positive values for very large separations. In the Higgs setup, they are also becoming smaller with a larger R separation.

Figure 4.25: Differential distributions for the NLO corrections to the EW contribution in the R separation of the muon and the hardest (left) and the separation of the muon and the second hardest jet (right) in the VBS (top) and the Higgs setup (bottom).

At last, we show the corrections to the differential cross sections with respect to centralities of the electron and the muon compared to the two hardest jets (Zeppenfeld variables) in Figure 4.26. Like in case of the LO distribution, the NLO distributions and the NLO corrections of the two charged leptons are very similar. The EW corrections in the Zeppenfeld variables are almost constant over the depicted range for both setups. The QCD corrections in the VBS setup show slightly larger corrections in case of forward leptons ($z_{\mu^- j_1 j_2} > 0$), but do not vary largely, whereas the QCD corrections in the Higgs setup show a not very prominent minimum around $z_{\mu^- j_1 j_2} = 0$.

Figure 4.26: Differential distributions for the NLO corrections to the EW contribution in the centrality of the electron (left) and the muon compared to the two hardest jets (right) in the VBS (top) and the Higgs setup (bottom).

4.4.3   NLO corrections to the QCD-induced contribution

In this section, we discuss the NLO corrections to the QCD-induced contribution for both VBS and Higgs setup. In our plots we depict the LO contribution of $\mathcal{O}\left(\alpha_s^2\alpha^4\right)$ and the sum of the contributions $\mathcal{O}\left(\alpha_s^2\alpha^4\right) + \mathcal{O}\left(\alpha_s^2\alpha^5\right)$, which are mainly the EW corrections to the QCD-induced contribution, the sum of the contributions $\mathcal{O}\left(\alpha_s^2\alpha^4\right) + \mathcal{O}\left(\alpha_s^3\alpha^4\right)$, which are the QCD corrections to the QCD-induced contribution, and the complete NLO corrections to the QCD-induced contribution $\mathcal{O}\left(\alpha_s^2\alpha^4\right) + \mathcal{O}\left(\alpha_s^2\alpha^5\right) + \mathcal{O}\left(\alpha_s^3\alpha^4\right)$. The absolute values are, as in the previous section, shown in the upper panels, and the relative corrections are shown in the lower ones. In the upper row of our figures, we present two observables in the VBS setup, and in the lower row, the same observables in the Higgs setup.

Before we start with the discussion of the plots, we remind of our remarks from Section 4.3.4, where we already stated that our QCD-induced results should be treated with caution since our chosen scale tends to predict a large LO result with large NLO corrections, leading to a very small or even negative NLO result in a slowly converging perturbation expansion. We will see this throughout, especially in the Higgs setup, in which the effect is larger than in the VBS setup and additionally overlaps with the already large negative corrections because of the jet veto. In fact, many of the differential distributions deliver negative cross sections at some point. We hence decided not to use the $\mathcal{O}\left(\alpha_s^3\alpha^4\right)$ results for the Higgs setup at our particular scale choice as a sensible benchmark, which we could compare with the VBS setup. Since the scale dependence of the integrated cross section in the VBS setup is smaller than in the Higgs setup, we still consider the $\mathcal{O}\left(\alpha_s^3\alpha^4\right)$ absolute cross sections and corrections as valid NLO results with subsequent moderate NNLO corrections in contrast to large expected NNLO corrections in the Higgs setup. In our depicted region, the $\mathcal{O}\left(\alpha_s^3\alpha^4\right)$ results of the VBS setup do not become negative. However, we must admit that the combined $\mathcal{O}\left(\alpha_s^3\alpha^4\right) + \mathcal{O}\left(\alpha_s^2\alpha^5\right)$ corrections exceed -100% on several occasions, especially in distributions that correlate with the centre-of-mass energy inside the process. We checked that the shape of the relative corrections does not change when we perform the 7-point scale variation and show this explicitly in Section 4.5. Since the $\mathcal{O}\left(\alpha_s^2\alpha^5\right)$ results are in both setups mainly the EW corrections and follow the scale dependence of the LO results, the corresponding relative corrections are considered to be valid for both setups.

Our plots in Figure 4.27 depict the differential cross section with respect to the transverse momentum of the hardest and the second hardest jet. The EW corrections are, in both cases for both setups, quite similar. They are always negative and grow with larger transverse momentum and reach values of more than -25% in both setups at the end of our portrayed region at $p_T = 1000\,\mathrm{GeV}$ for both the hardest and second hardest jet. Although not as prominent as for the EW corrections to the EW process, the behaviour of having a tendency of larger corrections in regions of high transverse momentum is typical for the EW NLO corrections. The QCD corrections of the hardest and the second hardest jet in the VBS setup behave differently since they become larger for growing p_{T,j_1}, being almost zero at very small transverse momentum and quickly dropping below -25% around $p_{T,j_1} \approx 100\,\mathrm{GeV}$. They reach almost -100% at the end of our depicted region even in the VBS setup. For the second hardest jet, the QCD corrections in the VBS setup are most negative for small p_{T,j_2}, exceeding more than -50%, and reaching a minimum in absolute values around $p_{T,j_2} \approx 200\,\mathrm{GeV}$. At higher values of p_{T,j_2} the corrections start to grow again and reach around -25% at $p_{T,j_2} = 1000\,\mathrm{GeV}$. Since the second-hardest jet has by definition smaller transverse momentum than the hardest one, and the QCD corrections in the case of the second-hardest jet at low transverse momentum are very large, we can infer that there is a transverse momentum gap for the QCD jets: The relative corrections for the second-hardest jet are largest, where the absolute LO cross section is also largest, which means, there is also a large absolute integrated NLO correction, if we integrate up to some small p_{T,j_2}. To match the absolute corrections in the p_{T,j_1} distributions, it has to be compensated from regions in which either the LO differential cross section with respect to p_{T,j_1} or its relative corrections are large. These are, however, the regions with a signficantly larger p_{T,j_1} than p_{T,j_2}. As a last note
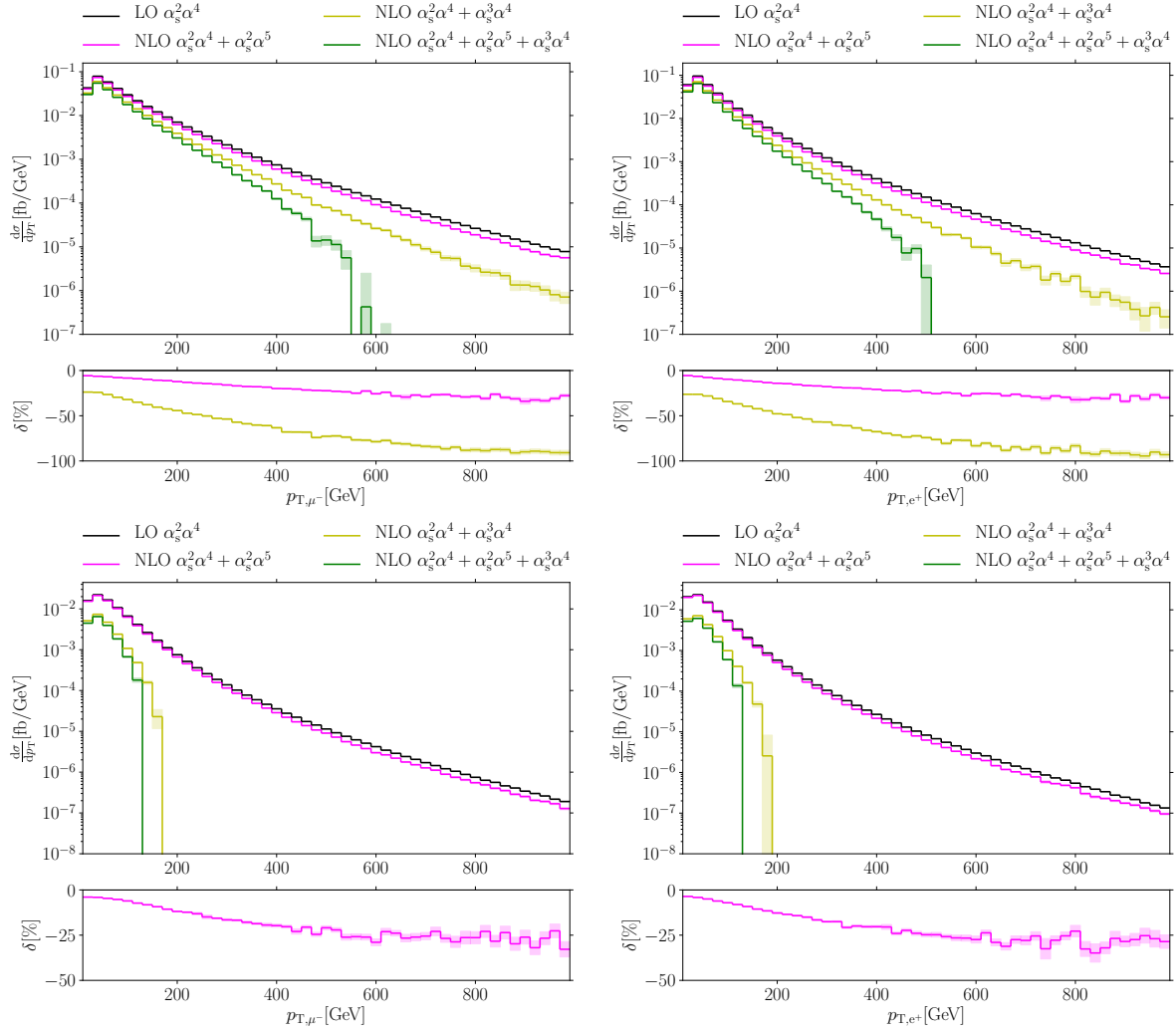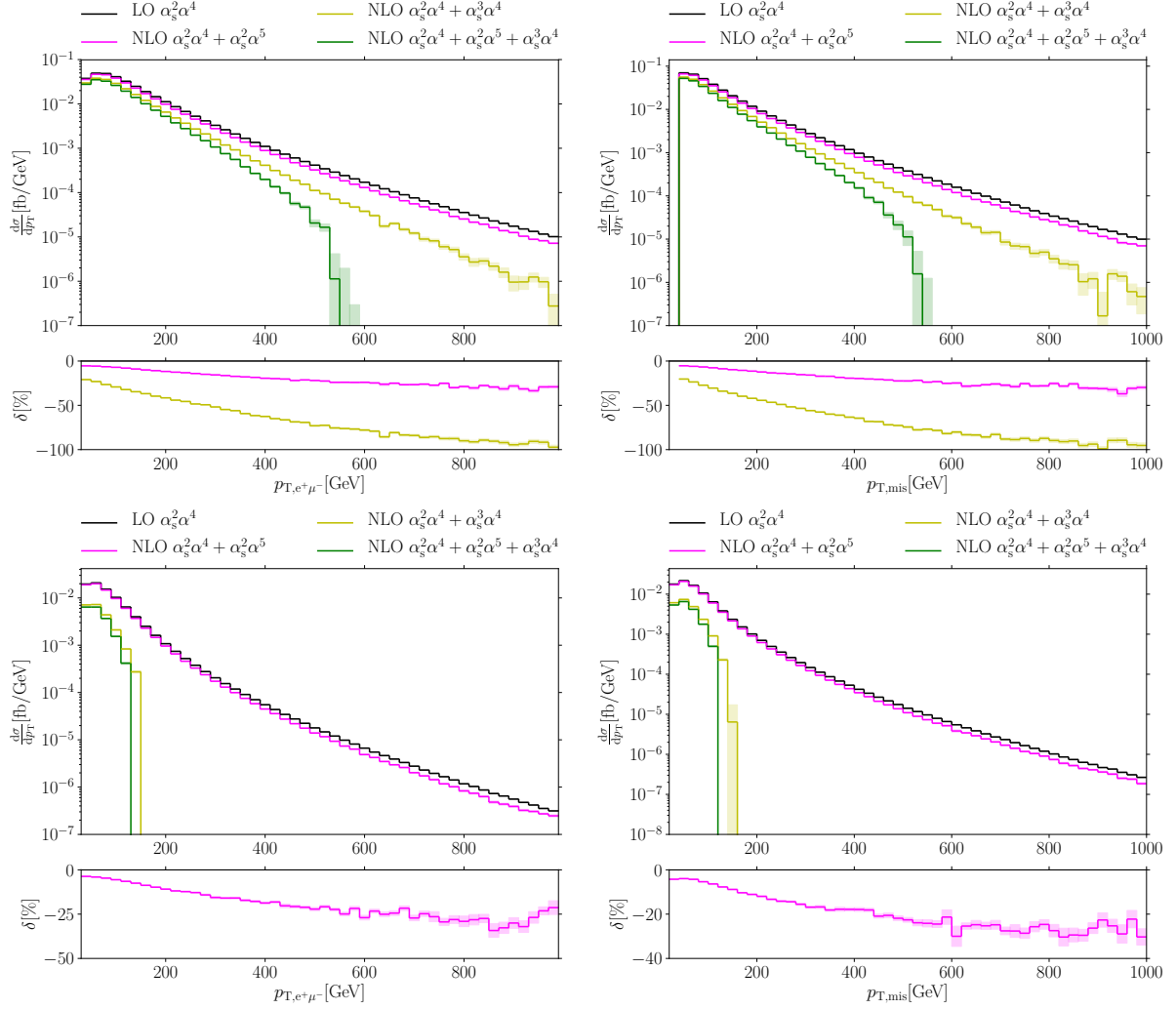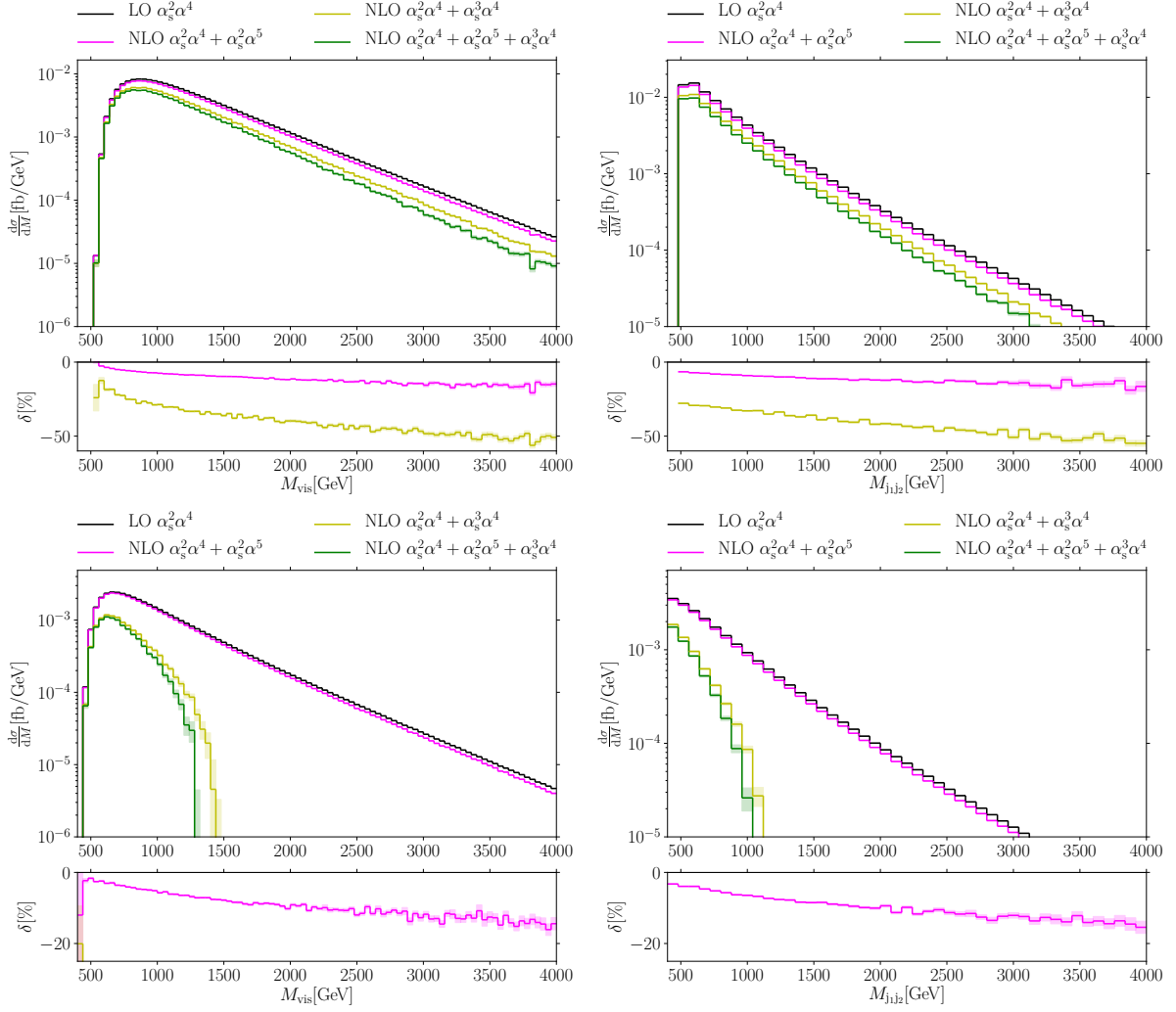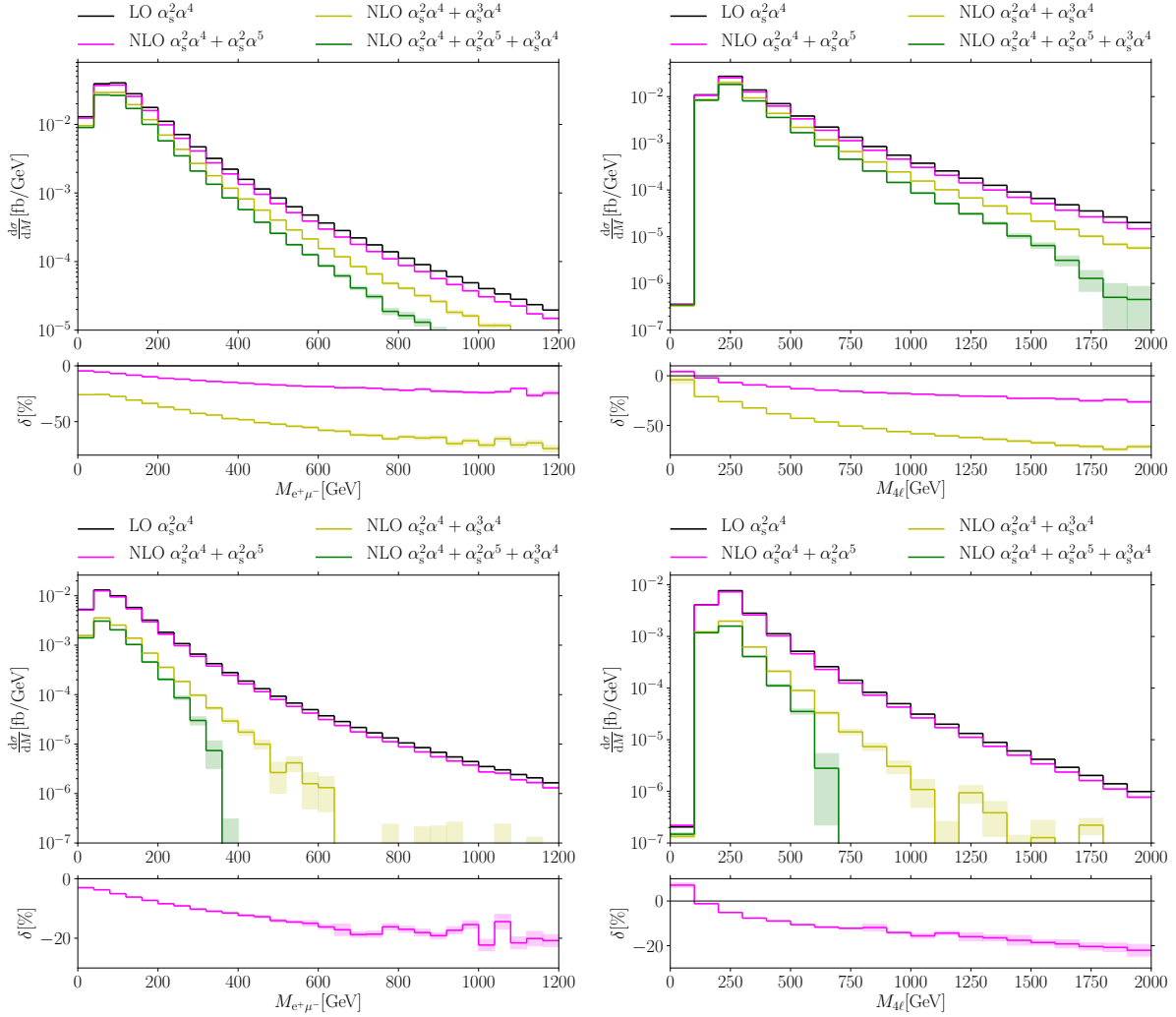
Figure 4.27: Differential distributions for the NLO corrections to the QCD-induced contribution in the transverse momentum of the hardest (left) and the second-hardest jet (right) in the VBS (top) and the Higgs setup (bottom). The upper panels show the absolute LO QCD-induced contribution at $\mathcal{O}\left(\alpha_s^2\alpha^4\right)$, the NLO cross sections including the EW corrections ($\mathcal{O}\left(\alpha_s^2\alpha^4\right) + \mathcal{O}\left(\alpha_s^2\alpha^5\right)$), the QCD corrections ($\mathcal{O}\left(\alpha_s^2\alpha^4\right) + \mathcal{O}\left(\alpha_s^3\alpha^4\right)$) and the complete NLO cross sections ($\mathcal{O}\left(\alpha_s^2\alpha^4\right) + \mathcal{O}\left(\alpha_s^2\alpha^5\right) + \mathcal{O}\left(\alpha_s^3\alpha^4\right)$). The lower panels show the relative NLO contributions normalised to the LO QCD-induced contribution. Shaded bands indicate integration errors.

to the two observables, we mention that the differential cross section with respect to the hardest jet decays, despite the large NLO corrections, still slower than the differential cross section with respect to the second hardest one. This is obvious since for each single event $p_{T,j_2} \leq p_{T,j_1}$.

In Figure 4.28 we present the differential cross sections with respect to the transverse momentum sum of the two jets and differential cross section with respect to the transverse momentum sum of the four leptons. For these observables, the EW corrections also behave similarly in both setups, as they are negative and become larger with growing transverse momentum sum. The relative EW corrections grow up to -30% in the tails around $p_T = 1000\,\mathrm{GeV}$ in the VBS setup. In the Higgs setup, the relative EW corrections amount to about -25% in the tails. The relative QCD corrections in the VBS setup are distinct in the two observables: For the two jets, they are almost zero at $p_{T,j_1j_2} = 0\,\mathrm{GeV}$, and at the other end of the depicted spectrum, the corrections exceed -90%. We note that the shape of the relative corrections in the transverse momentum sum of the two hardest jets follows the shape of the relative corrections with respect to the hardest jet. This confirms our considerations made in the previous discussion. A small
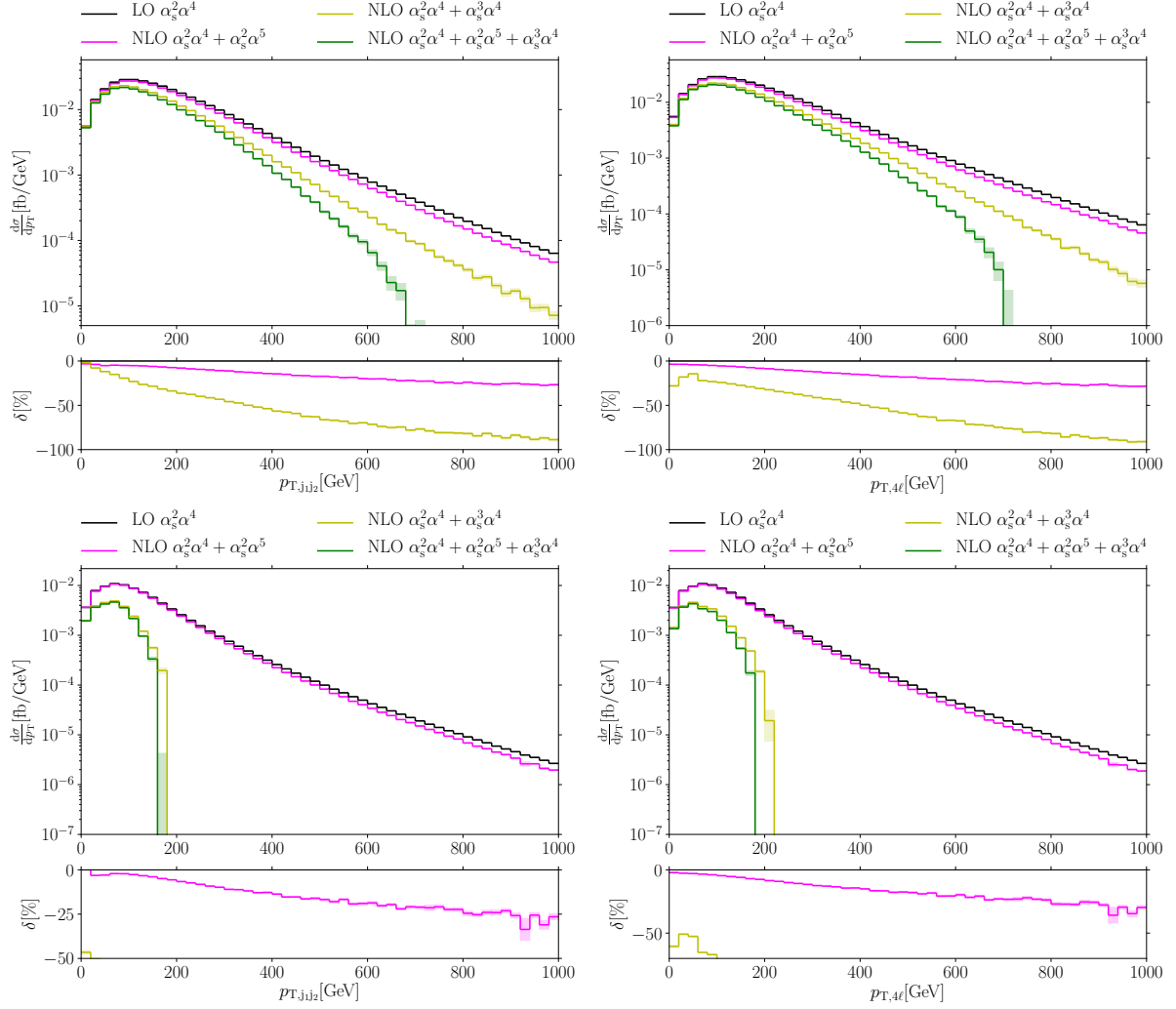
Figure 4.28: Differential distributions for the NLO corrections to the QCD-induced contribution in the transverse momentum sum of the two jets (left) and the four-lepton system (right) in the VBS (top) and the Higgs setup (bottom).

transverse momentum sum implies either small transverse momenta of both jets or jets with a large separation. On the other hand, the QCD corrections to the differential distribution with respect to the transverse momentum sum of the four leptons are already -25% at $p_{\mathrm{T},4\ell} = 0\,\mathrm{GeV}$ and show a minimum around $p_{\mathrm{T},4\ell} \approx 50\,\mathrm{GeV}$. Interestingly, the same minimum appears in the Higgs setup. We cannot explain this effect, especially since we did not expect a QCD correction having a distinct influence on a small phase-space region of a purely leptonic observable without affecting the smooth shape of the complementary jet observable.

We only briefly discuss the corrections to the differential cross section with respect to the transverse momentum of the muon or the electron, respectively, in Figure 4.29. As we expected, both EW and QCD corrections are very similar if we compare the two charged leptons. Concerning the EW correction, the VBS and the Higgs setup behave almost identically. It starts at very small negative corrections and becomes larger with growing transverse momentum. At the end of the depicted spectrum around $p_{\mathrm{T},\ell} = 1000\,\mathrm{GeV}$, the relative EW corrections amount to approximately -40% in the VBS and -30% in the Higgs setup. The QCD corrections are also always negative, become larger with higher transverse momentum, and range between -25% at small $p_{\mathrm{T},\ell}$ and almost -100% at the other end of the shown phase space. We additionally mention that the shape of the relative corrections to the differential cross sections with respect
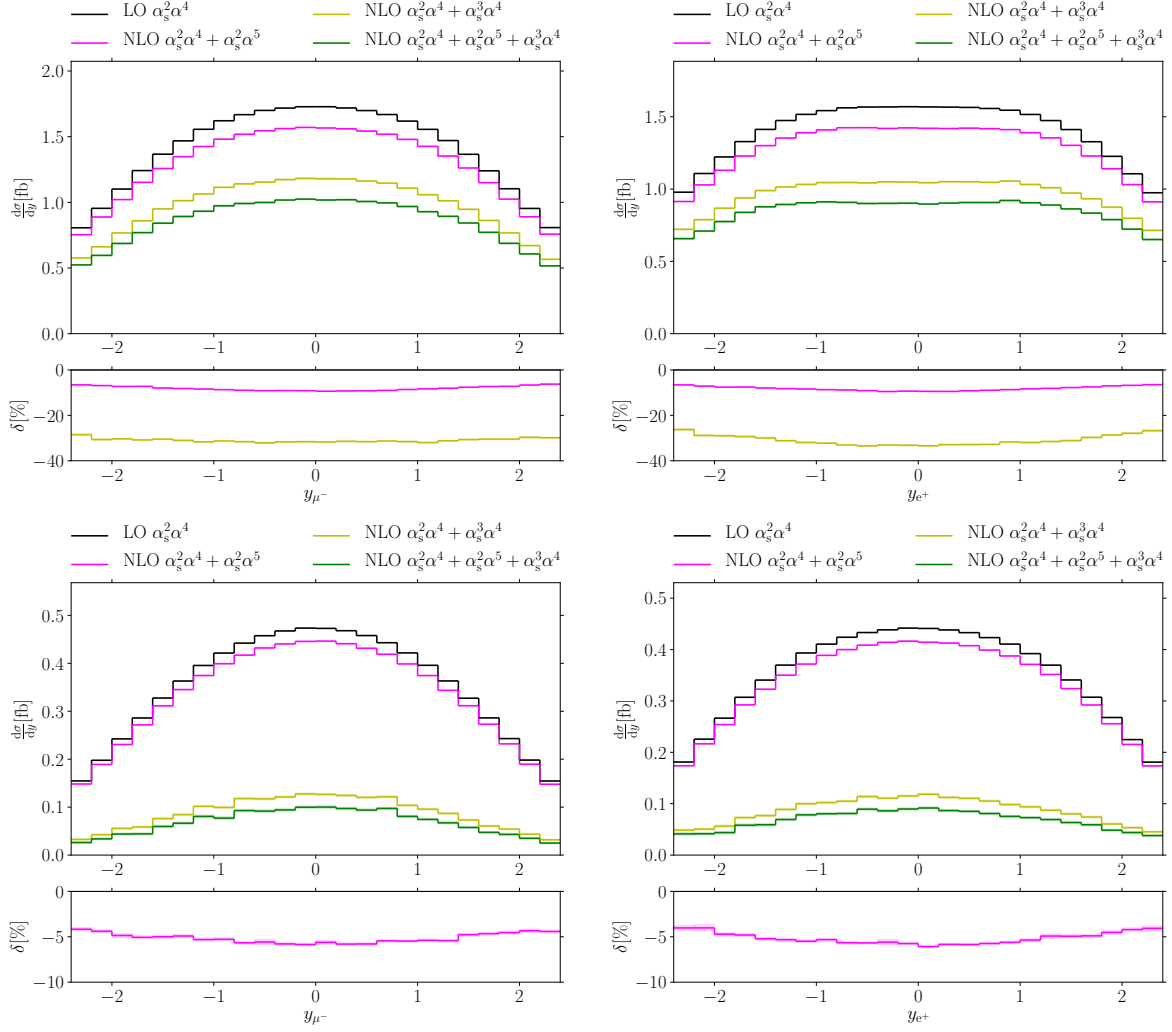
Figure 4.29: Differential distributions for the NLO corrections to the QCD-induced contribution in the transverse momentum of the muon (left) and the positron (right) in the VBS (top) and the Higgs setup (bottom).

to the individual transverse lepton momenta is very similar to the shape of the corrections in the distribution of the transverse lepton momentum sum.

We present the differential cross section with respect to the sum of the transverse momenta of the two charged leptons and the differential cross section with respect to the missing transverse momentum in Figure 4.30. Like in the case of the LO distributions and the corrections to the EW contribution, the two observables behave quite similarly in the QCD-induced contribution and its NLO corrections. We recognise again the typical behaviour of the EW corrections in both setups, where the relative corrections are growing with larger transverse momentum. For both observables, they reach about -40% at $p_T = 1000\,\text{GeV}$ in the VBS setup and between -25% and -30% in the VBS setup. The QCD corrections in the VBS setup follow the typical behaviour in the energy-dependent observables, where the relative corrections correlate with the transverse momentum of the system and reach values of around -100% at $p_T = 1000\,\text{GeV}$.

The corrections to the differential cross section with respect to the invariant mass of the total visible system and the invariant mass of the two hardest jets are shown in Figure 4.31. Both observables are strongly correlated since most of the energy is contained in the jets, and hence, it is not surprising to find an identical behaviour for the corrections. The corrections of $\mathcal{O}\left(\alpha_s^2\alpha^5\right)$ are always negative in both setups and grow with larger invariant mass. The same is true for the QCD corrections. At large invariant masses around $M_{\text{vis}}, M_{j_1 j_2} = 4000\,\text{GeV}$, the

Figure 4.30: Differential distributions for the NLO corrections to the QCD-induced contribution in the transverse momentum sum of the two charged leptons (left) and the missing transverse momentum (right) in the VBS (top) and the Higgs setup (bottom).

EW corrections in the invariant mass of the total visible system reach around -15% in both setups. For the two hardest jets, the relative corrections show more statistical uncertainty, but they also fluctuate around -15 and -20% in both setups. The QCD corrections in the VBS setup reach -50% for both observables. We explicitly mention that the overall behaviour at large invariant masses mimics the behaviour at large transverse momenta. However, the size of the corrections of the differential cross sections is smaller in the tails. At small invariant masses, there is a slight difference in the corrections for the two observables, which is especially seen in the VBS setup. The EW corrections in the invariant mass of the visible system are almost zero, while the corrections in the invariant mass of the two hardest jets take on a finite value. An analogous behaviour can be found in the QCD corrections, which are significantly smaller at low energies. This is reasonable since the leptons play a more significant role in the invariant mass of the total visible system when the invariant mass of the two-jet system is small. We link these findings to the discussion of the next observables, the invariant mass of the two charged leptons and the invariant mass of the four-lepton system.

We present the corrections to the differential cross sections with respect to the invariant mass of the charged lepton pair and the invariant mass of the four-lepton system in Figure 4.32. In general, the EW and the QCD corrections follow the same behaviour as in all previous observables that are connected with the energy contained in the system: Both corrections become more

Figure 4.31: Differential distributions for the NLO corrections to the QCD-induced contribution in the invariant mass of the visible system (left) and the two hardest jets (right) in the VBS (top) and the Higgs setup (bottom).

negative with larger invariant masses. In the case of the invariant mass of the two charged leptons, nothing very noteworthy happens. The EW corrections reach from -5% in the VBS setup and -3% in the Higgs setup at $M_{e^+\mu^-} = 0\,\mathrm{GeV}$ to -25% at $M_{e^+\mu^-} = 1200\,\mathrm{GeV}$ in both setups. The QCD corrections range between -25% and -75% in the VBS setup. For the invariant mass of the four-lepton system, we remark an astonishing detail in both setups: For $M_{4\ell} < 100\,\mathrm{GeV}$, the corrections of $\mathcal{O}\left(\alpha_{\mathrm{s}}^2\alpha^5\right)$ become positive with a relative value of $+10\%$ in both setups. This is the only bin with positive corrections of $\mathcal{O}\left(\alpha_{\mathrm{s}}^2\alpha^5\right)$ in all observables like this was the only bin in all observables with positive corrections of $\mathcal{O}\left(\alpha^7\right)$, seen in Figure 4.19. As in the case of the corrections of $\mathcal{O}\left(\alpha^7\right)$, the absolute value of the differential cross section at LO as well as at NLO is negligible. This effect is smaller for the QCD-induced contribution than for the EW contribution. We verified for the dominant quark-induced channel at $\mathcal{O}\left(\alpha_{\mathrm{s}}^2\alpha^4\right)$ that the positive NLO contribution is present both in the EW correction to the QCD-induced process and the QCD correction to the interference. With this small additional investigation, we can rule out that the effect is connected to remnants of the Higgs resonance in the interference process. Apart from this detail, the corrections behave as expected, and the EW corrections range between 0%, being slightly negative, at $M_{4\ell} \geq 100\,\mathrm{GeV}$ for both setups and -20% in the Higgs and -30% in the VBS setup for $M_{4\ell} = 2000\,\mathrm{GeV}$. The QCD corrections in the VBS setup do not show
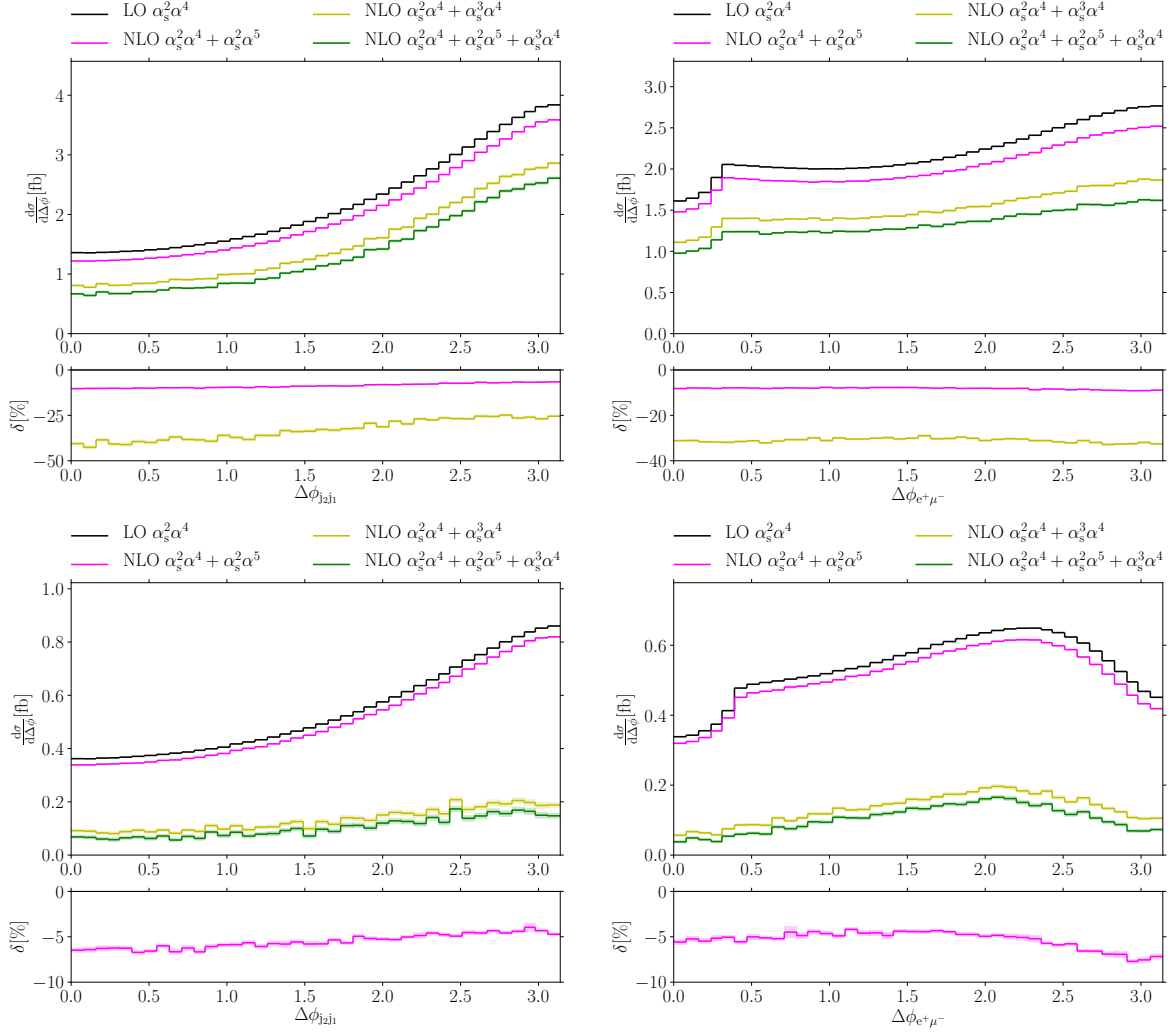
Figure 4.32: Differential distributions for the NLO corrections to the QCD-induced contribution in the invariant mass of the two charged leptons (left) and the four-lepton system (right) in the VBS (top) and the Higgs setup (bottom).

any distinctive features, monotonically decreasing from almost 0% at $M_{4\ell} = 0\,\text{GeV}$ to -75% at $M_{4\ell} = 2000\,\text{GeV}$.

Next, we present in Figure 4.33 the corrections to the differential cross section with respect to the rapidity of the hardest and the rapidity of the second-hardest jet. Since these observables are not correlated with the energy of the system, we observe almost constant EW corrections for both observables in both setups, with a small tendency of larger EW corrections towards more central hardest jets around $|y_{\text{j}_1}| = 0$. For the QCD corrections in the VBS setup, we recognise larger corrections at central hardest jets with a relative value of -35% at $|y_{\text{j}_1}| = 0$ and smaller corrections of -20% at $|y_{\text{j}_1}| = 4.5$. In contrast, the behaviour is exactly the opposite for the second-hardest jet. There we find smallest QCD corrections for $|y_{\text{j}_2}| = 0$ with a value of -15%, while the corrections near $|y_{\text{j}_2}| = 4.5$ reach -50%. For the absolute value of the QCD corrections to the Higgs setup, we remark that they never become negative in the rapidity distributions, equivalent to the relative corrections never hitting -100%, in contrast to all observables that are correlated with transverse momentum and energy.

The corrections to the differential cross section with respect to rapidities of the charged leptons are shown in Figure 4.34. As for the rapidity of the jets, the relative EW corrections are almost constant for both leptons in both setups, with a slight tendency towards larger corrections near zero rapidities. The relative QCD corrections are also very flat in the case of the muon in
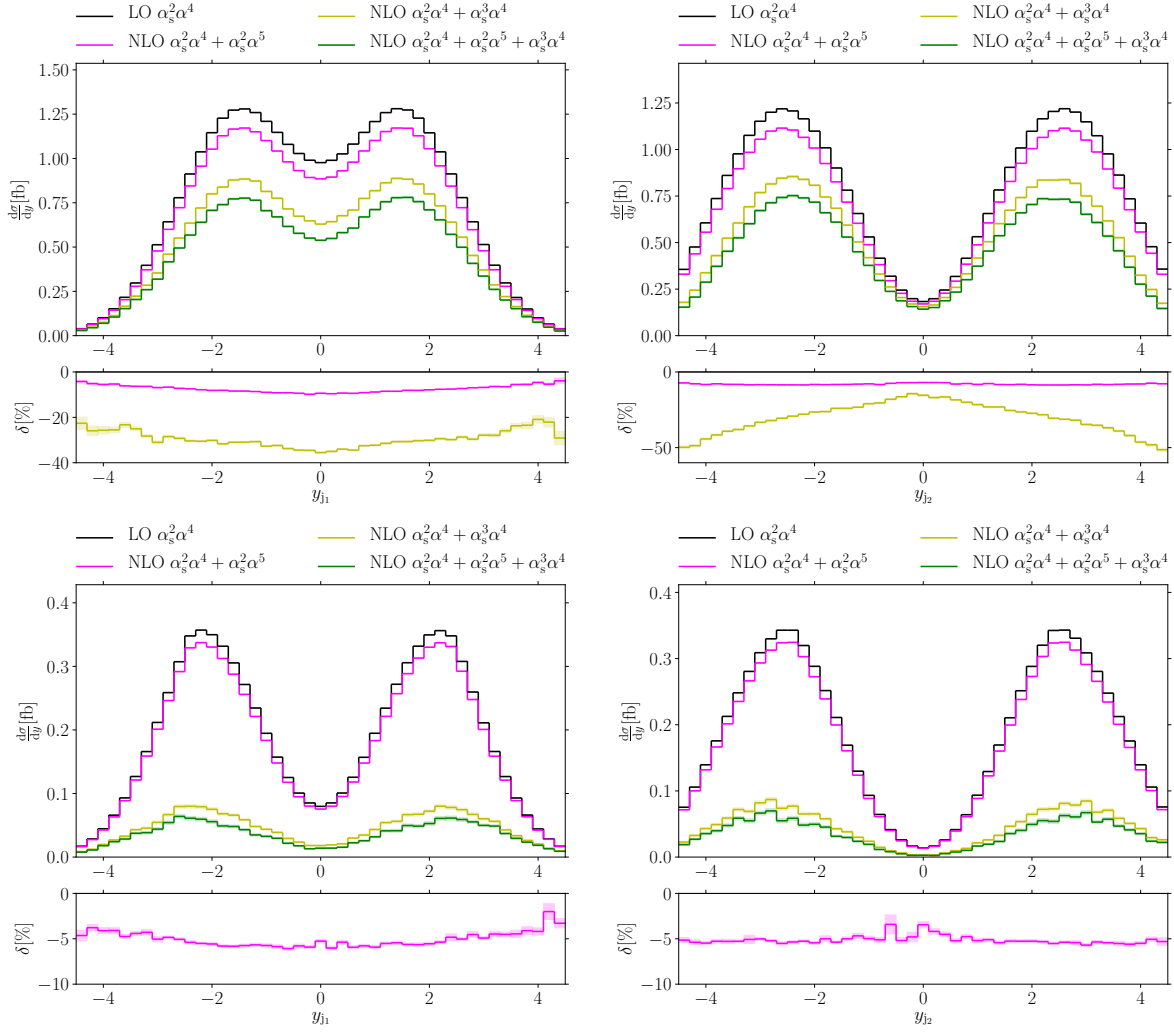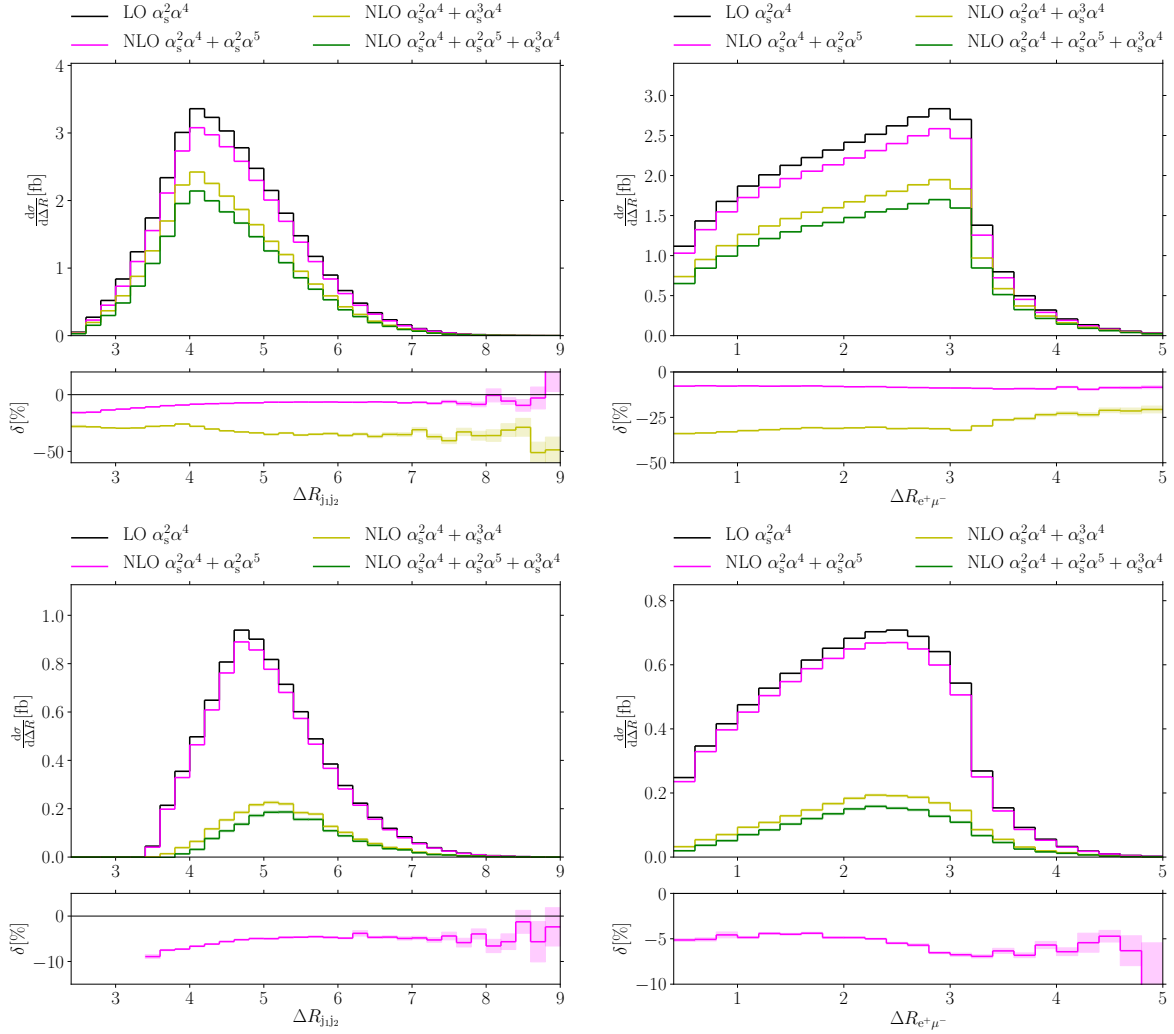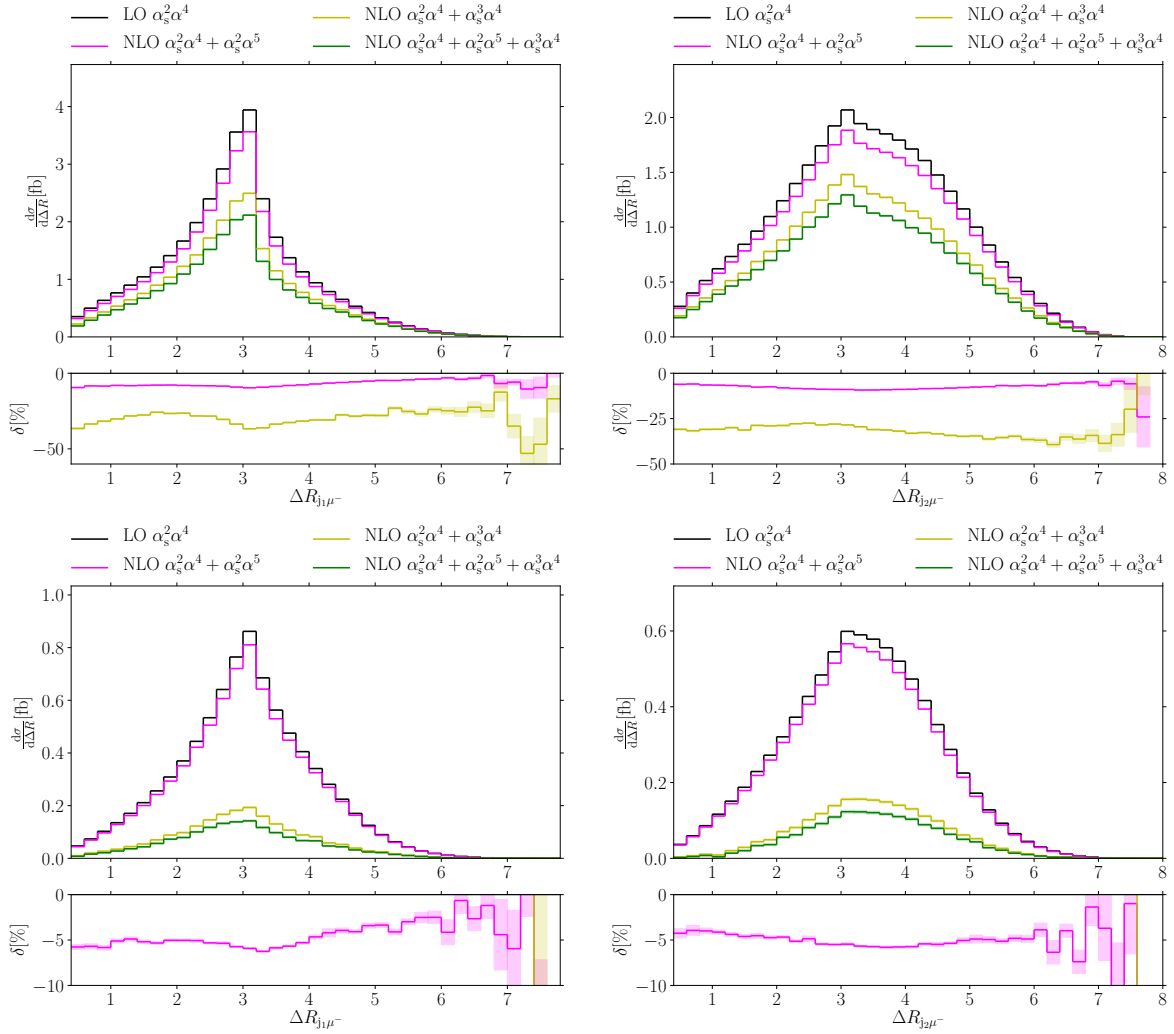
Figure 4.33: Differential distributions for the NLO corrections to the QCD-induced contribution in the rapidity of the hardest jet (left) and the second-hardest jet (right) in the VBS (top) and the Higgs setup (bottom).

the VBS setup but show a more distinctive negative maximum around $y_{\mathrm{e}^+} = 0$. This leads to an even larger plateau of almost constant absolute NLO cross section for the positron than for the muon compared to the LO counterpart.

We present the corrections to the differential cross section with respect to the rapidity separation of the two hardest jets and the rapidity separation of the two charged leptons in Figure 4.35. As before, we remark that the step in the first filled bin in the absolute differential cross sections with respect to the rapidity separation of the jets is due to a mismatch between the (symmetrised) histogram and the cut setup, which cuts exactly half of the first bin. In the relative corrections, we see a smooth transition between the first and the second bin. In both setups the EW corrections show a slight tendency towards larger relative values at small rapidity separation of the two hardest jets with a value of approximately -10% at $|\Delta y_{\mathrm{j}_1\mathrm{j}_2}| = 2.5$ in the VBS setup and -6% at $|\Delta y_{\mathrm{j}_1\mathrm{j}_2}| = 3.5$ in the Higgs setup, albeit they do not vary largely over the complete phase space. The QCD corrections in the VBS setup behave oppositely and are smallest at small jet rapidity separation with a value of -15% at $|\Delta y_{\mathrm{j}_1\mathrm{j}_2}| = 2.5$, dropping to -35% at $|\Delta y_{\mathrm{j}_1\mathrm{j}_2}| = 4.0$ and staying almost constant from thereon. The relative EW corrections in the differential cross section with respect to the lepton rapidity separation are almost constant over the complete phase space in both setups. The relative QCD corrections are largest at small
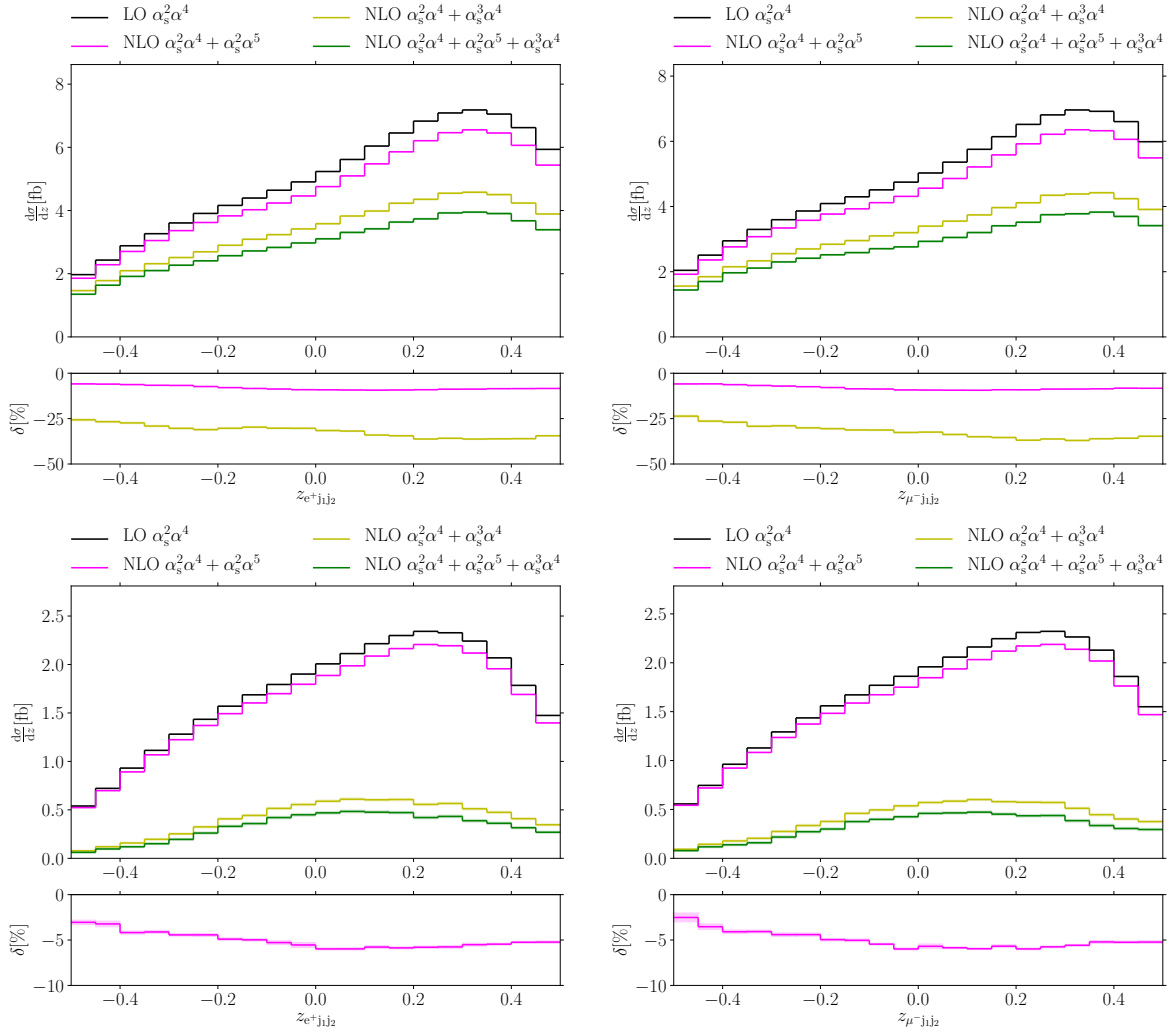
Figure 4.34: Differential distributions for the NLO corrections to the QCD-induced contribution in the rapidity of the muon (left) and the positron (right) in the VBS (top) and the Higgs setup (bottom).

rapidity separation with a value of -35% at $|\Delta y_{e^+\mu^-}| = 0$ in the VBS setup and become sizeably smaller at large separations with only -15% around $|\Delta y_{e^+\mu^-}| = 4$.

The NLO distributions for the differential cross sections with respect to the azimuthal angular separation of the two hardest jets and the azimuthal angular separation of the two charged leptons are depicted in Figure 4.36. Concerning the separation of the two hardest jets, the EW corrections are almost constant, only very slowly decreasing for larger separations in both setups. The QCD corrections are always negative and become smaller for larger $\Delta\phi_{j_2 j_1}$, varying between -40% at $\Delta\phi_{j_2 j_1} = 0$ and -25% at $\Delta\phi_{j_2 j_1} = \pi$ in the VBS setup. The EW corrections in the angular separation of the two charged leptons are almost constant for both setups, with a slight tendency towards larger corrections at very large $\Delta\phi_{e^+\mu^-}$. The QCD corrections in the VBS setup are also almost constant.

In Figure 4.37, we show the corrections to the differential cross section with respect to the R separation of the two hardest jets and the R separation of the two charged leptons. In case of the two jets, the EW corrections in both setups are largest in regions with small separation with approximately -12% in the VBS setup at $\Delta R_{j_1 j_2} \approx 3$ and smallest at medium separations with only -6% at $\Delta R_{j_1 j_2} \approx 6.5$. In the Higgs setup, the corrections amount to -12% at $\Delta R_{j_1 j_2} \approx 3.5$ and only -4% around $\Delta R_{j_1 j_2} \approx 6.2$. The relative QCD corrections in the VBS setup have a slight minimum around $\Delta R_{j_1 j_2} \approx 4$ with also only little variation between -30% at $\Delta R_{j_1 j_2} \approx 3$, -25%
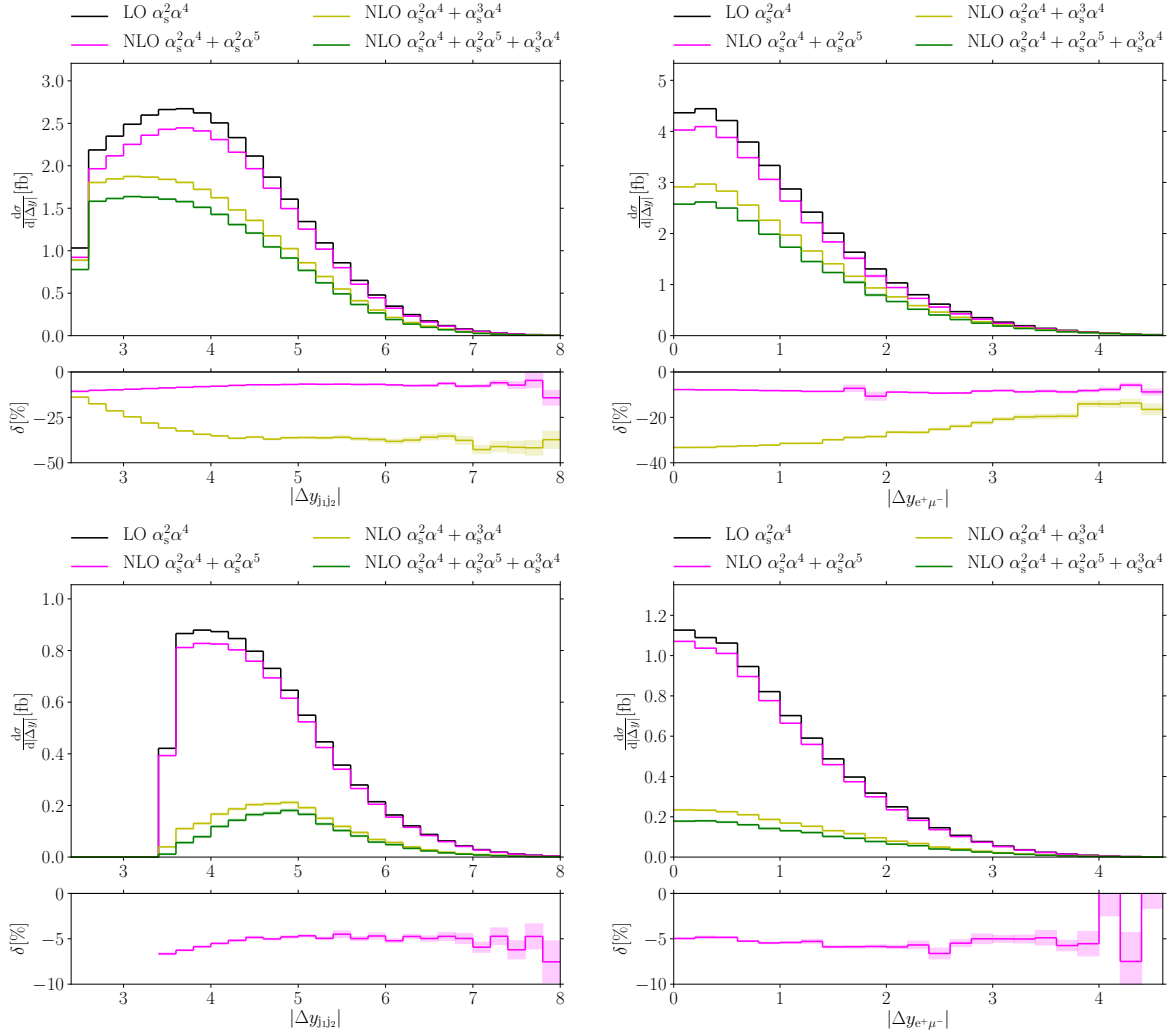
Figure 4.35: Differential distributions for the NLO corrections to the QCD-induced contribution in the rapidity separation of the two hardest jets (left) and the two charged leptons (right) in the VBS (top) and the Higgs setup (bottom).

at the minimum and around -35% between $6 < \Delta R_{j_1j_2} < 7$, before also the QCD corrections start to fluctuate. The behaviour of these very flat relative QCD corrections in the total separation can be seen as a combination of the rising corrections in the rapidity and the falling corrections in the angular separation. For the separation of the two leptons, we get almost constant EW corrections in both setups with a slight tendency towards larger corrections at large separations. We already noted the same tendency in both the rapidity and the angular separation. The QCD corrections in the VBS setup show a significant kink around $\Delta R_{e^+\mu^-} = \pi$. While before only moderately varying between -35% and -30% over the complete span, it falls down to -20% at $\Delta R_{e^+\mu^-} = 5$. This can also be seen as an effect of combining the behaviour in the case of rapidity and angular separation: Total separations larger than π cannot only be achieved by azimuthal angular separation. While the angular corrections were almost flat, the falling behaviour of the corrections in the rapidity separation starts to take over at π, coinciding to the edge in the shape of the absolute cross section both at LO and NLO. Especially, the NLO corrections tend to flatten this edge. Although we do not consider our results in the Higgs setup as trustworthy, we would like to mention that the edge almost disappears in that case.

The corrections to the differential distribution with respect to the R separation of the hardest jet and the muon and the R separation of the second-hardest jet and the muon are given in Figure 4.38. We mention here that we only present the separation of the jets and the muon; the

Figure 4.36: Differential distributions for the NLO corrections to the QCD-induced contribution in the azimuthal angular separation of the two hardest jets (left) and the two charged leptons (right) in the VBS (top) and the Higgs setup (bottom).

distributions of the separation of the jets and the electron are only slightly different concerning some numeric values but show no conceptual differences. We hence only give a qualitative overview of these observables. For the separation of the hardest jet and the muon, both EW and QCD corrections behave identically, although the characteristics can be better seen in the QCD corrections. We can divide the phase space into two regions with the boundary at $\Delta R_{j_1\mu^-} = \pi$. The relative corrections start with a maximum at zero separation and show a first minimum between $0 < \Delta R_{j_1\mu^-} = \pi$ around $\Delta R_{j_1\mu^-} = 1.6$. There is an obvious kink in the corrections at π, where both types of corrections have a maximum, after which both EW and QCD corrections slowly become smaller again. We see the same behaviour also in the Higgs setup. The shape of the absolute cross sections and the relative corrections in the case of the second-hardest jet is completely different than for the hardest one. We do not see a clear fall-off around $\Delta R_{j_2\mu^-} = \pi$. Although the EW corrections have a slight maximum at this point in the VBS setup, and the shapes of the EW correction are similar, this maximum in the Higgs setup lies at $\Delta R_{j_2\mu^-} \approx 4$. The QCD corrections in the VBS setup are also only slowly varying and their minimum is at $\Delta R_{j_2\mu^-} \approx 2.5$. In contrast to $\Delta R_{j_1\mu^-}$, there is nothing special happening at $\Delta R_{j_2\mu^-} = \pi$ and the relative corrections keep growing.

At last, we discuss the corrections to the differential cross section with respect to the centralities of the electron and the muon compared to the two hardest jets in Figure 4.39. As

Figure 4.37: Differential distributions for the NLO corrections to the QCD-induced contribution in the R separation of the two hardest jets (left) and the two charged leptons (right) in the VBS (top) and the Higgs setup (bottom).

in the previous cases concerning these observables, electron and muon do not show significant differences. For both leptons, the EW corrections are almost constant with only a slight tendency towards larger corrections in case of forward leptons. The QCD corrections in the VBS setup also show an asymmetry with larger relative corrections in the forward direction with a maximum around $z_{\ell_{j_1 j_2}} \approx 0.3$, where they reach -35%, while they are slightly below -25% at $z_{\ell_{j_1 j_2}} = -0.5$. We again mention for this diagram that the plot was designed for the Higgs setup and does not depict the complete fiducial phase space in the VBS setup.

Figure 4.38: Differential distributions for the NLO corrections to the QCD-induced contribution in the R separation of the hardest jet and the muon (left) and the second-hardest jet and the muon (right) in the VBS (top) and the Higgs setup (bottom).

Figure 4.39: Differential distributions for the NLO corrections to the QCD-induced contribution in the centrality of the electron (left) and the muon compared to the two hardest jets (right) in the VBS (top) and the Higgs setup (bottom).

4.5   Scale dependence plots

In this section, we give an overview of the scale dependence of some differential distributions both at LO and NLO. As we already stated in the discussion of the integrated cross section, the scale dependence of the pure EW process and its QCD corrections is rather small. In contrast, we get a large scale dependence for the QCD-induced process and especially its QCD corrections. Since the central scale is chosen too small in the QCD-induced process, we can only infer sensible information from higher scales, i. e. the combinations $(2\mu_{\mathrm{F}}^{\mathrm{centralsc}}, \mu_{\mathrm{R}}^{\mathrm{centralsc}})$, $(\mu_{\mathrm{F}}^{\mathrm{centralsc}}, 2\mu_{\mathrm{R}}^{\mathrm{centralsc}})$ and $(2\mu_{\mathrm{F}}^{\mathrm{centralsc}}, 2\mu_{\mathrm{R}}^{\mathrm{centralsc}})$, which all lead to NLO results larger than the central scale in the integrated cross section as well as most bins of the differential cross sections. The scales below the central scale cause unphysical results also in the case of the VBS setup and an even faster breakdown of the QCD corrections for the QCD-induced process in the Higgs setup. For exemplary purposes, they are nevertheless included in the plots below. We also decided not to present all observables of which we have shown the distributions at the central scale before, but only a selection of some energy-correlated and energy-uncorrelated variables. As we saw before, the energy-correlated variables are more likely to become unphysical at the central scale, whereas the uncorrelated observables had positive results also in the Higgs setup.

For our presentation, we decided not to distinguish between EW and QCD corrections and summarised them as NLO corrections to the corresponding LO distribution since the EW corrections do not introduce a distinct dependence on the scale choice – apart from small changes due to the PDFs – compared to their LO counterpart. The figures in this section are hence built up differently than in the previous section. In each figure, we show one observable in both setups. The VBS setup is depicted in the first and the Higgs setup in the second row. Differently from the previous plots, we present in the left column the EW process of $\mathcal{O}\left(\alpha^6\right)$ and the corresponding complete NLO result $(\mathcal{O}\left(\alpha^6\right) + \mathcal{O}\left(\alpha^7\right) + \mathcal{O}\left(\alpha_{\mathrm{s}}\alpha^6\right))$ and on the right the QCD-induced process of $\mathcal{O}\left(\alpha_{\mathrm{s}}^2\alpha^4\right)$ and the corresponding NLO cross section $(\mathcal{O}\left(\alpha_{\mathrm{s}}^2\alpha^4\right) + \mathcal{O}\left(\alpha_{\mathrm{s}}^2\alpha^5\right) + \mathcal{O}\left(\alpha_{\mathrm{s}}^3\alpha^4\right))$. As usual, we neglect the fact that the processes of $\mathcal{O}\left(\alpha_{\mathrm{s}}\alpha^6\right)$ and $\mathcal{O}\left(\alpha_{\mathrm{s}}^2\alpha^5\right)$ also contain interference contributions for our presentation. Each subfigure is split up into three panels. The upper ones depict the absolute differential distributions. The solid line represents the central scale $\mathrm{d}\sigma/\mathrm{d}X(\mu_{\mathrm{F}}^{\mathrm{centralsc}}, \mu_{\mathrm{R}}^{\mathrm{centralsc}})$, the shaded bands in this section indicate the scale variation and cover the area between $\max(\mathrm{d}\sigma/\mathrm{d}X(\mu_{\mathrm{F}}^i, \mu_{\mathrm{R}}^i))$ and $\min(\mathrm{d}\sigma/\mathrm{d}X(\mu_{\mathrm{F}}^i, \mu_{\mathrm{R}}^i))$. The middle panels show the differential NLO and LO cross sections, normalised to the corresponding cross section at the central scale if the cross section at the central scale is larger than zero. We call this ratio δ'. Sub-zero cross sections are considered unphysical, and it is impossible to normalise to a zero or sub-zero value sensibly. The central scale always takes the value of 100% and the shaded area lies between $\max\left(\frac{\mathrm{d}\sigma/\mathrm{d}X(\mu_{\mathrm{F}}^i, \mu_{\mathrm{R}}^i)}{\mathrm{d}\sigma/\mathrm{d}X(\mu_{\mathrm{F}}^{\mathrm{centralsc}}, \mu_{\mathrm{R}}^{\mathrm{centralsc}})}\right)$ and $\min\left(\frac{\mathrm{d}\sigma/\mathrm{d}X(\mu_{\mathrm{F}}^i, \mu_{\mathrm{R}}^i)}{\mathrm{d}\sigma/\mathrm{d}X(\mu_{\mathrm{F}}^{\mathrm{centralsc}}, \mu_{\mathrm{R}}^{\mathrm{centralsc}})}\right)$. We also show the two extreme scale variations, $(\frac{1}{2}\mu_{\mathrm{F}}^{\mathrm{centralsc}}, \frac{1}{2}\mu_{\mathrm{R}}^{\mathrm{centralsc}})$ and $(2\mu_{\mathrm{F}}^{\mathrm{centralsc}}, 2\mu_{\mathrm{R}}^{\mathrm{centralsc}})$, denoted by $-$ and $+$ markers, for the NLO contribution in this panel. We explicitly note that the extrema of the scale variation do not necessarily coincide with the extrema of the differential cross sections at NLO. Furthermore, we included the third, lowest panel, in which we show the relative NLO corrections normalised to the corresponding LO contribution of the same scale. This is the same δ as in the previous sections. The solid line represents the value of $\frac{\mathrm{d}\sigma^{\mathrm{NLO}}/\mathrm{d}X(\mu_{\mathrm{F}}^{\mathrm{centralsc}}, \mu_{\mathrm{R}}^{\mathrm{centralsc}})}{\mathrm{d}\sigma^{\mathrm{LO}}/\mathrm{d}X(\mu_{\mathrm{F}}^{\mathrm{centralsc}}, \mu_{\mathrm{R}}^{\mathrm{centralsc}})}$ and the shaded band covers the area between $\max\left(\frac{\mathrm{d}\sigma^{\mathrm{NLO}}/\mathrm{d}X(\mu_{\mathrm{F}}^i, \mu_{\mathrm{R}}^i)}{\mathrm{d}\sigma^{\mathrm{LO}}/\mathrm{d}X(\mu_{\mathrm{F}}^i, \mu_{\mathrm{R}}^i)}\right)$ and $\min\left(\frac{\mathrm{d}\sigma^{\mathrm{NLO}}/\mathrm{d}X(\mu_{\mathrm{F}}^i, \mu_{\mathrm{R}}^i)}{\mathrm{d}\sigma^{\mathrm{LO}}/\mathrm{d}X(\mu_{\mathrm{F}}^i, \mu_{\mathrm{R}}^i)}\right)$.

We begin our discussion with the transverse momentum of the hardest jet, which is a typical energy-dependent observable of the hadronic system, in Figure 4.40. In the EW process, the relative LO scale uncertainty becomes larger with larger transverse momentum in both setups. At NLO, the scale uncertainty in the VBS setup becomes significantly smaller than at LO for all bins. The relative scale uncertainty at LO is almost symmetrically around the central scale, whereas it is asymmetric at NLO. The scale choice corresponds well to the maximum of the NLO EW cross section. In the graphs, the area of the ratios δ' covers mostly regions below the 100%-line. We point out that the minimal and maximal scale choices cross the 100%-line
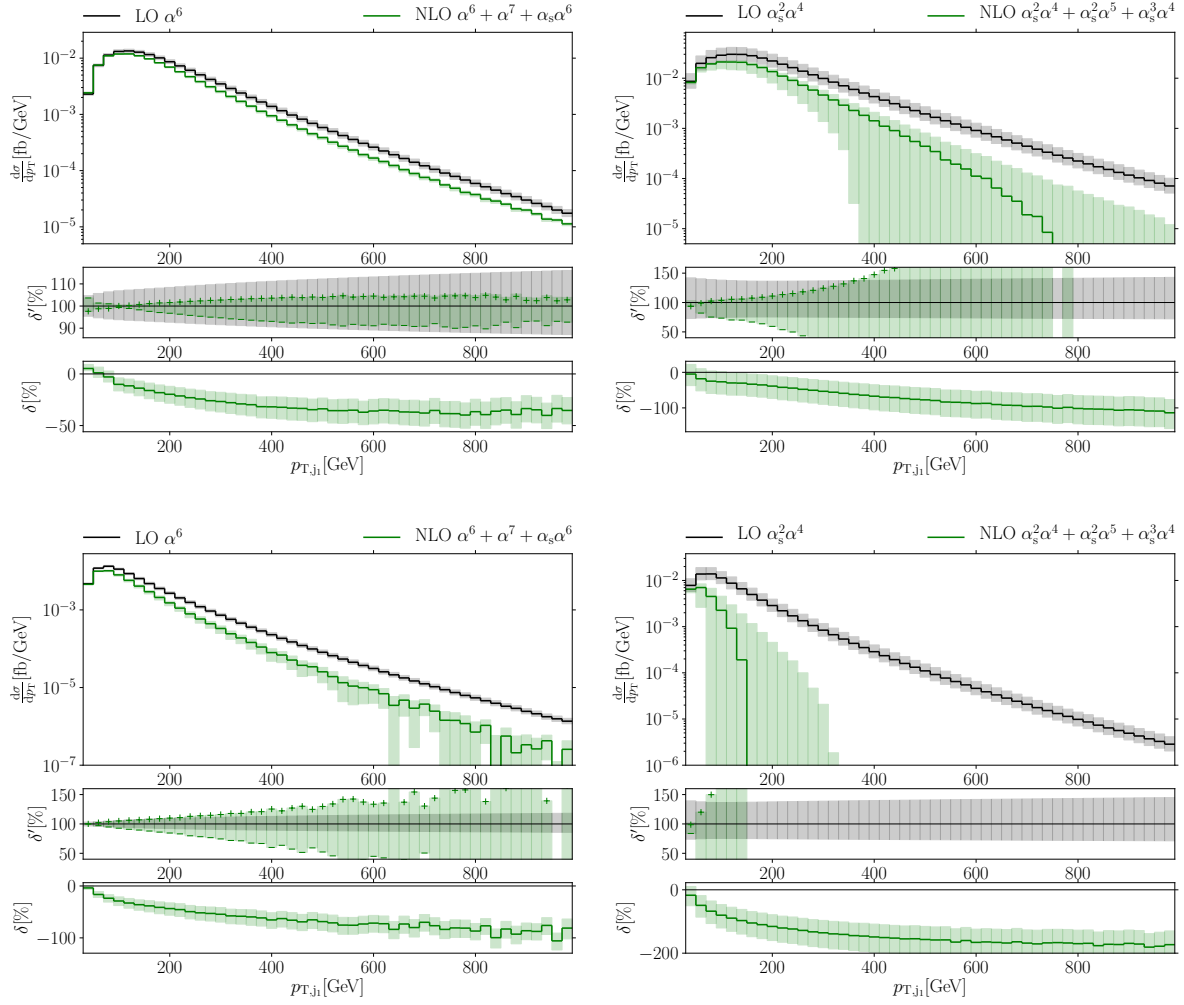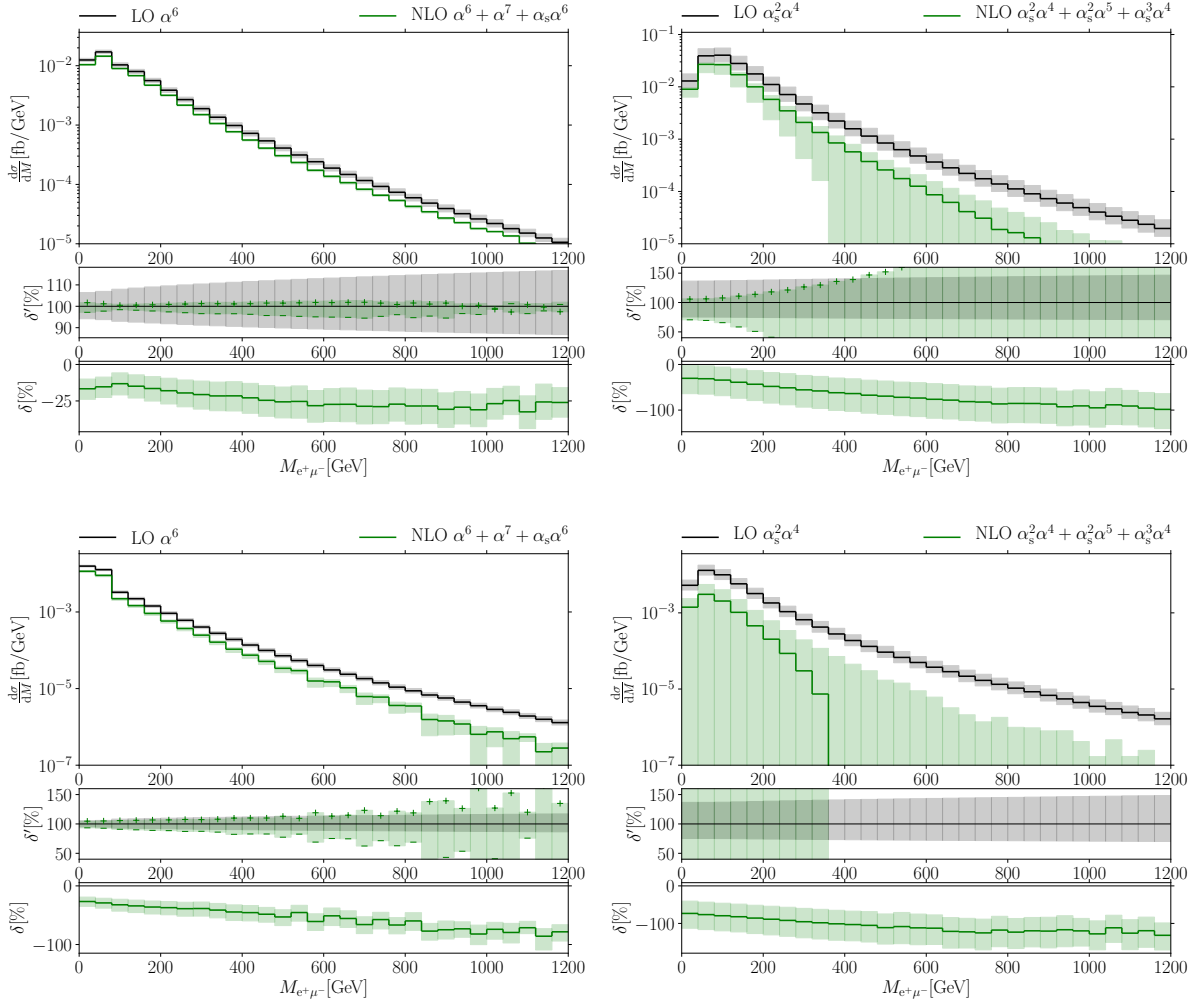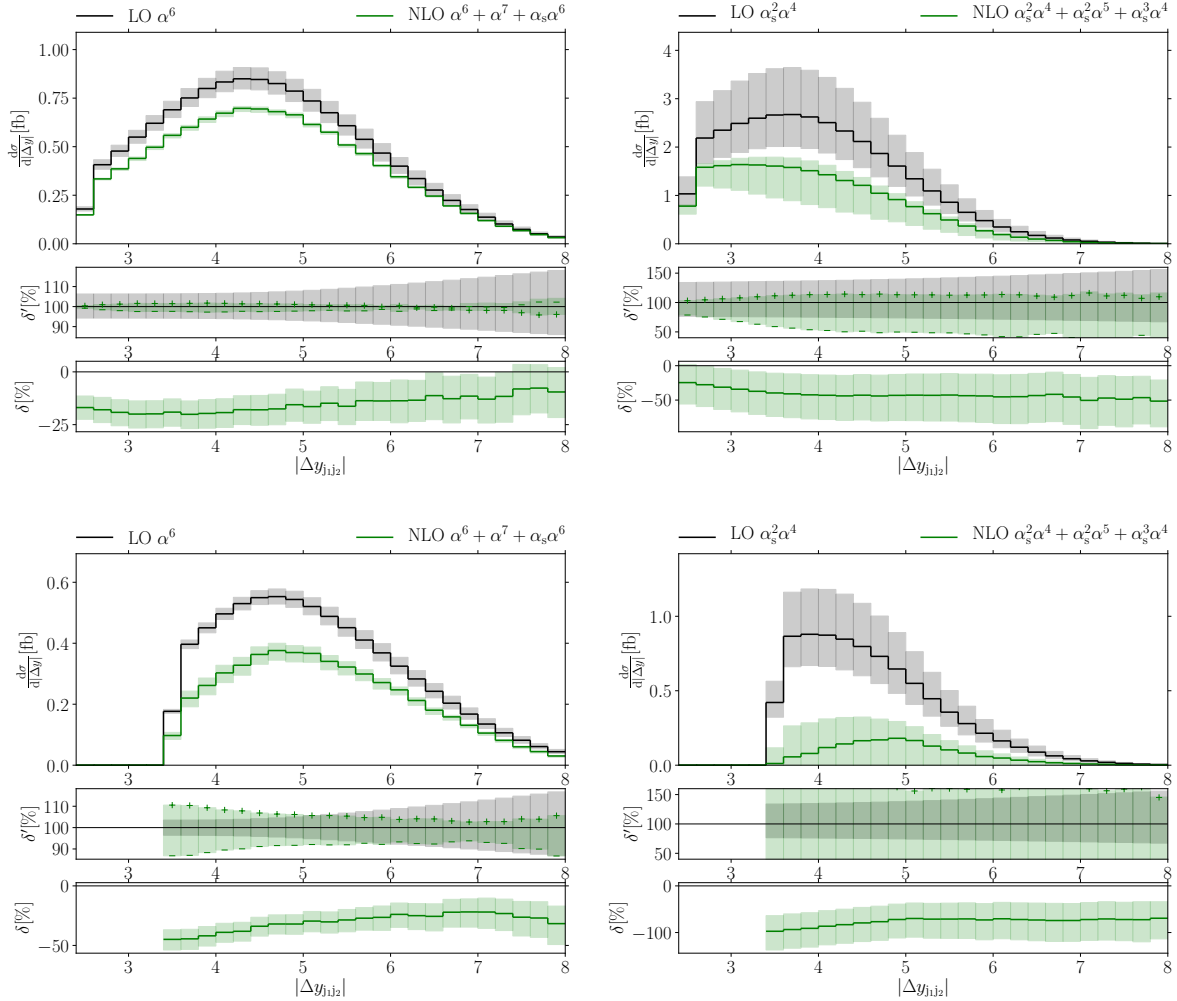
Figure 4.40: Scale variation plot of the transverse momentum of the hardest jet in the VBS (top) and the Higgs setup (bottom) for the EW (left) and the QCD-induced process (right).

around $p_{\mathrm{T,j_1}} \approx 100\,\mathrm{GeV}$ with a smaller scale corresponding to a larger cross section and a larger scale to a smaller one at values below $100\,\mathrm{GeV}$ and vice versa above. In the Higgs setup the scale uncertainty is almost always larger at NLO than at LO. We already noted this effect in the discussion of the integrated cross section. We explained this by the large NLO corrections due to the harsh jet veto since we do not expect these extreme variations for a contribution of $\mathcal{O}\left(\alpha_{\mathrm{s}}\alpha^6\right)$. Especially since we normalise to the NLO cross section, the smallness of the latter almost automatically leads to a large relative uncertainty. When we compare the two setups, the scale uncertainty of the relative corrections does not extremely differ between them since the large relative scale uncertainty in the Higgs setup at NLO results only from a small absolute one. Nonetheless, we are with our central scale choice already in the EW process at the edge of the physical region and we strongly advise against choosing a smaller scale.

For the QCD-induced cross section, the LO scale uncertainty remains almost constant for both setups. At NLO, we recognise in the VBS setup that the scale uncertainties are small for low transverse momentum but become larger than the LO scale variations at high transverse momenta. We remark that the relative scale uncertainty band in the VBS setup shows clearly the asymmetry at NLO also for the QCD-induced process. At large transverse momenta, we get a relative scale uncertainty of more than $\pm50\%$ and very soon unphysical results if we choose a smaller scale than the central one. There are also problems arising in the central scale for $p_{\mathrm{T,j_1}} \approx 800\,\mathrm{GeV}$. However, choosing a scale already twice as large as the central one prevents us
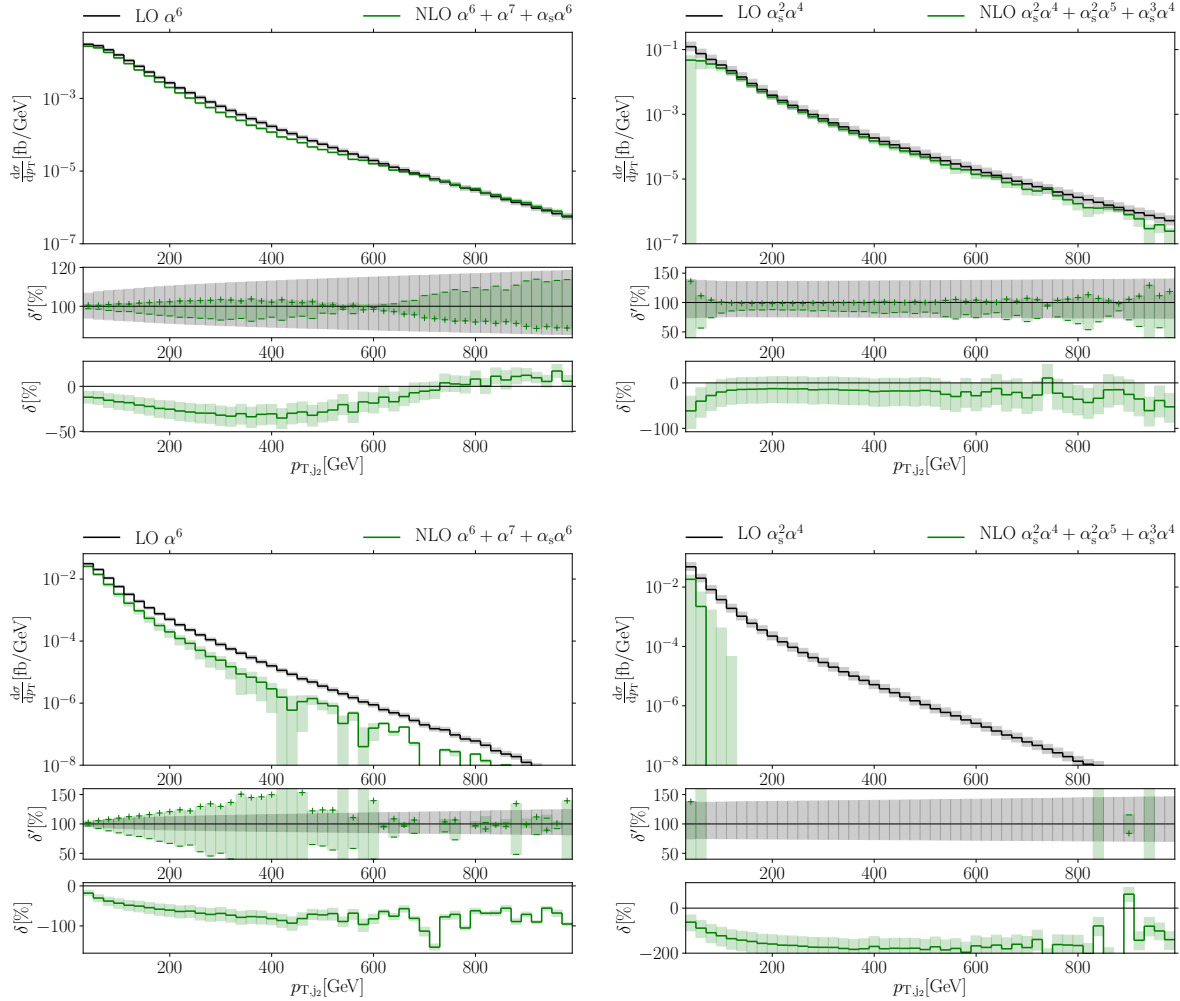
Figure 4.41: Scale variation plot of the transverse momentum of the second-hardest jet in the VBS (top) and the Higgs setup (bottom) for the EW (left) and the QCD-induced process (right).

from these unphysical results. On the other hand, in the Higgs setup, using a slightly higher scale does not prevent the NLO cross section from rapidly decreasing. We may only state that increasing the scales by a factor of 2 leads to a breakdown of the cross section around $p_{T,j_1} \approx 300 \, \mathrm{GeV}$ instead of $150 \, \mathrm{GeV}$.

The next observable that we discuss is the transverse momentum of the second-hardest jet in Figure 4.41. It is of special interest because it is included in the definition of our renormalisation and factorisation scales. Like in the previous observable, the relative scale uncertainty at $\mathcal{O}\left(\alpha^6\right)$ grows with larger transverse momentum in both setups. For the QCD-induced process, the scale uncertainty at LO is almost constant. The shape of the relative scale variation at NLO in the VBS setup features in the VBS setup a minimum at $p_{T,j_2} \approx 600 \, \mathrm{GeV}$ for the EW contribution and around $p_{T,j_2} \approx 200 \, \mathrm{GeV}$ in the QCD-induced contribution. This region of $p_{T,j_2} \approx 600 \, \mathrm{GeV}$ in the EW process in the VBS setup is also an example for the minimal and maximal scale crossing the 100%-line. Especially, this behaviour is contrary to the one in the differential distribution of the hardest jet since the smaller scale corresponds to a larger cross section at *large* transverse momenta of the second-hardest jet. In the QCD-induced contribution of the VBS setup, there is an unexpectedly large relative scale variation at very small transverse momentum. We refer to these two effects in Section 5. In the Higgs setup, the NLO scale variation of the EW contribution is larger than the LO one in the relevant region of the phase space. We cannot infer information

Figure 4.42: Scale variation plot of the invariant mass of the two charged leptons in the VBS (top) and the Higgs setup (bottom) for the EW (left) and the QCD-induced process (right).

from the NLO scale variation in the QCD-induced contribution since it breaks down already in the third bin below $p_{T,j_2} \ll 100\,\text{GeV}$.

The next discussed observable is the invariant mass of the charged lepton pair, depicted in Figure 4.42. Like the previous example, this is an energy-dependent variable, but in the leptonic sector. In the EW process, the uncertainty becomes larger with higher invariant mass in both setups at LO but is drastically reduced at NLO for the VBS setup. In contrast, the scale dependence remains present in the Higgs setup and exceeds the LO uncertainty in almost all bins. However, compared to the transverse momentum of the hardest jet, the scale dependence is relatively moderate in this case. We also recognise the asymmetry in the scale uncertainty for both VBS and Higgs setup. In the QCD-induced process, the uncertainty at LO is again almost constant for both setups. At NLO, large uncertainties remain in both setups, although the scale uncertainty for small invariant masses is smaller than at LO in the VBS setup. We also note that choosing scales twice as large as the central scale already almost always leads to physically sensible results in both setups over the depicted range.

In Figure 4.43, we present an example of an observable that is not correlated to the transverse energy of the system. In the EW process, we recognise at LO larger scale uncertainty at large rapidity differences in both setups. In the VBS setup, the scale uncertainty at NLO behaves as expected and becomes drastically smaller in all regions of the phase space. In the Higgs setup, however, the scale uncertainty at NLO almost reverses its shape with a large error band at small

Figure 4.43: Scale variation plot of the rapidity separation of the two hardest jets in the VBS (top) and the Higgs setup (bottom) for the EW (left) and the QCD-induced process (right).

rapidities and small bands at large rapidities. In fact, above $\Delta y_{j_1 j_2} \approx 5.5$, the relative NLO scale uncertainty is smaller than the LO scale uncertainty. This can be understood with the following reasoning: The scale dependence in the NLO corrections for the EW process emerges mostly from the QCD corrections of $\mathcal{O}\left(\alpha_s \alpha^6\right)$. We saw in Figure 4.14 for the transverse momentum of the hardest jet in the Higgs setup that the QCD corrections mostly affected the cross section at large p_{T}, whereas we saw in Figure 4.22 that the same large corrections affected small jet rapidity differences. In the QCD-induced process, the scale uncertainty at LO becomes larger at high rapidity differences in both setups. At NLO the scale uncertainty in the VBS setup is smaller at low rapidity differences, but also for intermediate ones, the relative NLO scale uncertainty band lies outside of the relative LO uncertainty band, e. g. while the uncertainty at LO is nearly symmetric around 100%, scale variations at NLO show also in this observable everywhere a tendency towards smaller values, which means, the scale choice in the VBS setup is already near the peak value of the NLO cross section. In the Higgs setup, there is a scale uncertainty of more than $\pm 50\%$ for each bin.

The last observable that we present in this section is the azimuthal angular separation of the two charged leptons, depicted in Figure 4.44, which is a leptonic observable not related to energy. We keep the discussion very brief since nothing conceptually changed in comparison to the previous observable, except that the scale variation at NLO in the Higgs setup in the EW process is almost constant over the complete phase space.
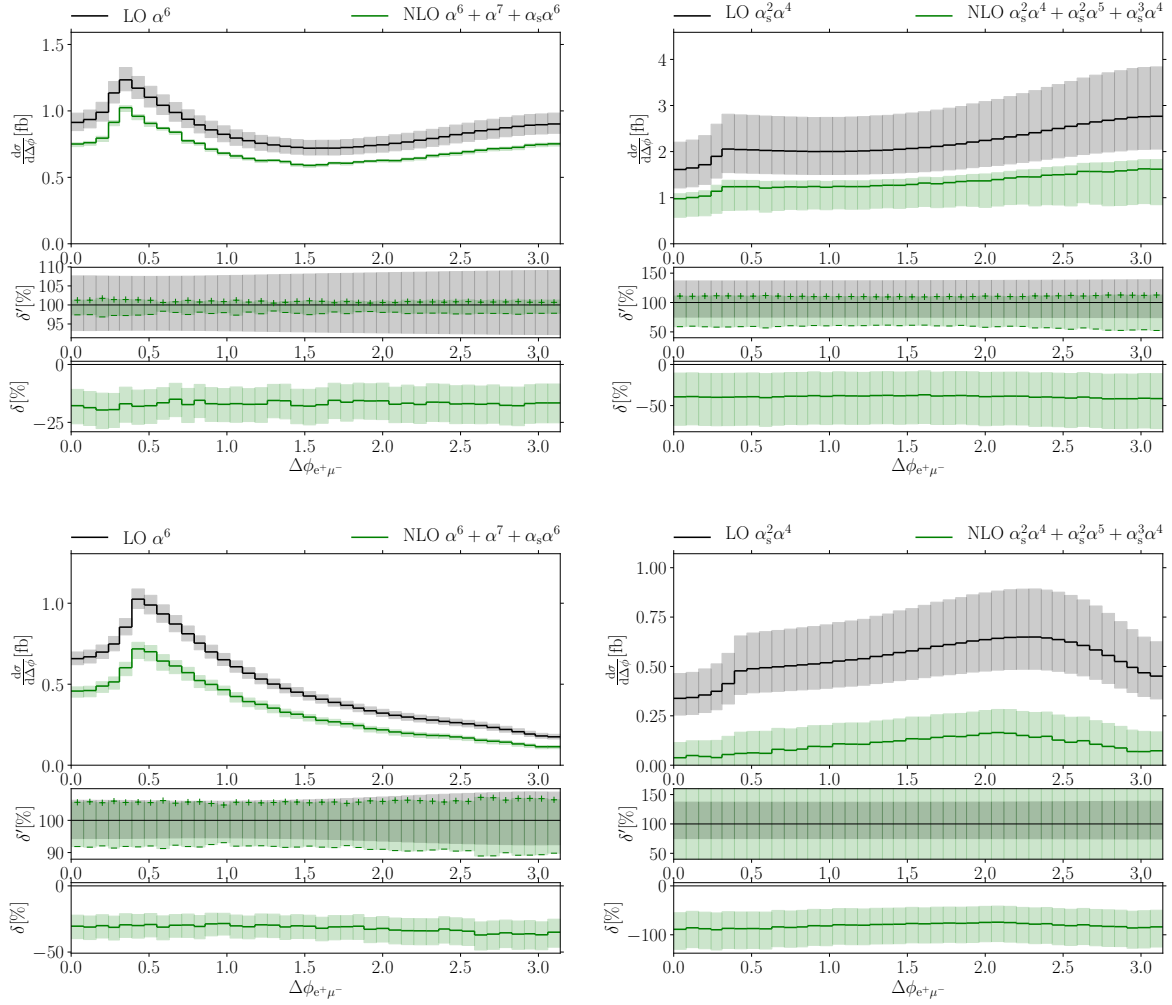
Figure 4.44: Scale variation plot of the azimuthal angular separation of the two charged leptons in the VBS (top) and the Higgs setup (bottom) for the EW (left) and the QCD-induced process (right).

Concluding this section, we state that the choice of our central scale, $\mu_{\mathrm{F}}^{\mathrm{centralsc}} = \mu_{\mathrm{R}}^{\mathrm{centralsc}} = \sqrt{p_{\mathrm{T,j_1}} p_{\mathrm{T,j_2}}}$ is a common scale choice for the investigation of VBS processes and was used in the works of our group successfully before. Only considering the typical VBS setup at $\mathcal{O}\left(\alpha^6\right)$ and its corresponding NLO corrections, the scale choice did not disappoint in mostly reducing the scale dependence at NLO. It is, however, also known that the scale choice is fairly low for the QCD-induced process, and as proven in this study, we must use another scale for sensible results for the QCD-induced background. Especially, we ran into problems with our scale choice when dealing with large transverse momenta. In the Higgs setup, this leads to an additional destructive interplay with the jet veto that already pushes down such events.

4.6 Differential distributions for the unphysical setups

Although we are not able to measure the differential distributions for the modified setups, in which we cut out a region around the Higgs boson resonance, we can infer some information that gives evidence to the remarks that we made in the context of discussing the measurable differential distributions. We admit that the *s*-channel Higgs-boson diagrams as subprocess are an integral part of VBS. Without Higgs boson, the theory would violate the unitarity constraint. However, the Higgs-boson contribution gives rise to a considerable EW background which is not present in other VBS processes or can be cut away by physical cuts, such as in ZZ scattering. It might be interesting to investigate physical cuts for a real experimental setup to enhance further the other VBS contributions over the Higgs-production contribution by exploring the correlations between the not measurable four-lepton invariant mass and other observables. When we talk about the VBS contributions in this section, we explicitly mean those excluding Higgs production.

We thus do not present all observables that were shown in Section 4.4 and do not discuss the plots in full length, but give a selection of those we found the most interesting and present the important details. The figures in this section are built up as follows: As usual, we present two observables per figure in both setups, the VBS setup in the top and the Higgs setup in the bottom column. Each subfigure is divided into three panels: The upper one shows the absolute LO contributions of $\mathcal{O}\left(\alpha^6\right)$, the NLO EW contribution of $\mathcal{O}\left(\alpha^6\right)+\mathcal{O}\left(\alpha^7\right)$ and the complete NLO contribution of $\mathcal{O}\left(\alpha^6\right)+\mathcal{O}\left(\alpha^7\right)+\mathcal{O}\left(\alpha_{\mathrm{s}}\alpha^6\right)$ both for the physical and the modified setup. The middle panel shows the corresponding relative corrections. The additional lower panel compared to the figures from Section 4.4 shows the ratio between the modified setup and the physical setup for all of the three contributions.

We begin with the trivial observation in the left-hand side of Figure 4.45 that the cut is obviously working by showing the differential distributions in the four-lepton invariant mass. Starting at large invariant masses, the ratio between the modified and the physical setups both at LO and NLO is constant at 100%. This verifies our assumption that the effect of the cut on constellations with a photon and the four lepton accidentally having an invariant mass around the Higgs boson mass, while the four leptons are far away from the resonance, is negligible. The situation changes, when we reach the bin between $100\,\mathrm{GeV} < M_{4\ell} < 200\,\mathrm{GeV}$. Both ratios drop significantly, which is the effect of cut-out Higgs-boson resonance, that is the main contribution to the cross section in this phase-space region. Going to even smaller four-lepton invariant masses, the two ratios decouple in both setups: The NLO ratio drops to 0%, the LO ratio goes back to 100%. This effect shows that the tiny contribution in this bin is completely due to the Higgs boson decay products emitting a photon, lowering the four-lepton invariant mass below $100\,\mathrm{GeV}$. The effects of the cut on the unphysical four-lepton invariant mass translates to the physical observable of the two-lepton invariant mass, which we show on the right-hand side: Most of the contribution to the EW cross section in the region of $M_{\mathrm{e}^+\mu^-} < 100\,\mathrm{GeV}$ stems from the Higgs boson resonance. We recognise that the neutrinos carry away a significant amount of energy since the bin between $100\,\mathrm{GeV} < M_{\mathrm{e}^+\mu^-} < 150\,\mathrm{GeV}$ is completely unaffected by the cut. The decoupling of the LO and NLO ratios at small two-lepton invariant masses is not present, because the differential cross section has a non-negligible value in the lowest bin and the effect seen in the four-lepton mass is too tiny to be relevant.

Two other observables that show distinct differences between the VBS signal without the Higgs boson and the Higgs-production contribution are the azimuthal angular difference and the rapidity difference between the two charged leptons, whose distributions we show in Figure 4.46. We recognise that the peak in the differential cross section with respect to the angular separation at $\Delta\phi_{\mathrm{e}^+\mu^-} \approx 0.5$ in both setups is an effect solely due to the Higgs production, and it completely flattens out when cutting away the resonance contribution. The Higgs boson resonance contribution remains dominant for $\Delta\phi_{\mathrm{e}^+\mu^-} < 0.7$ in the VBS and $\Delta\phi_{\mathrm{e}^+\mu^-} < 1.5$ in the Higgs setup. At large azimuthal angular differences, the VBS contribution takes over completely. We also recognise that the cut on the four-lepton invariant mass and the transverse mass cut
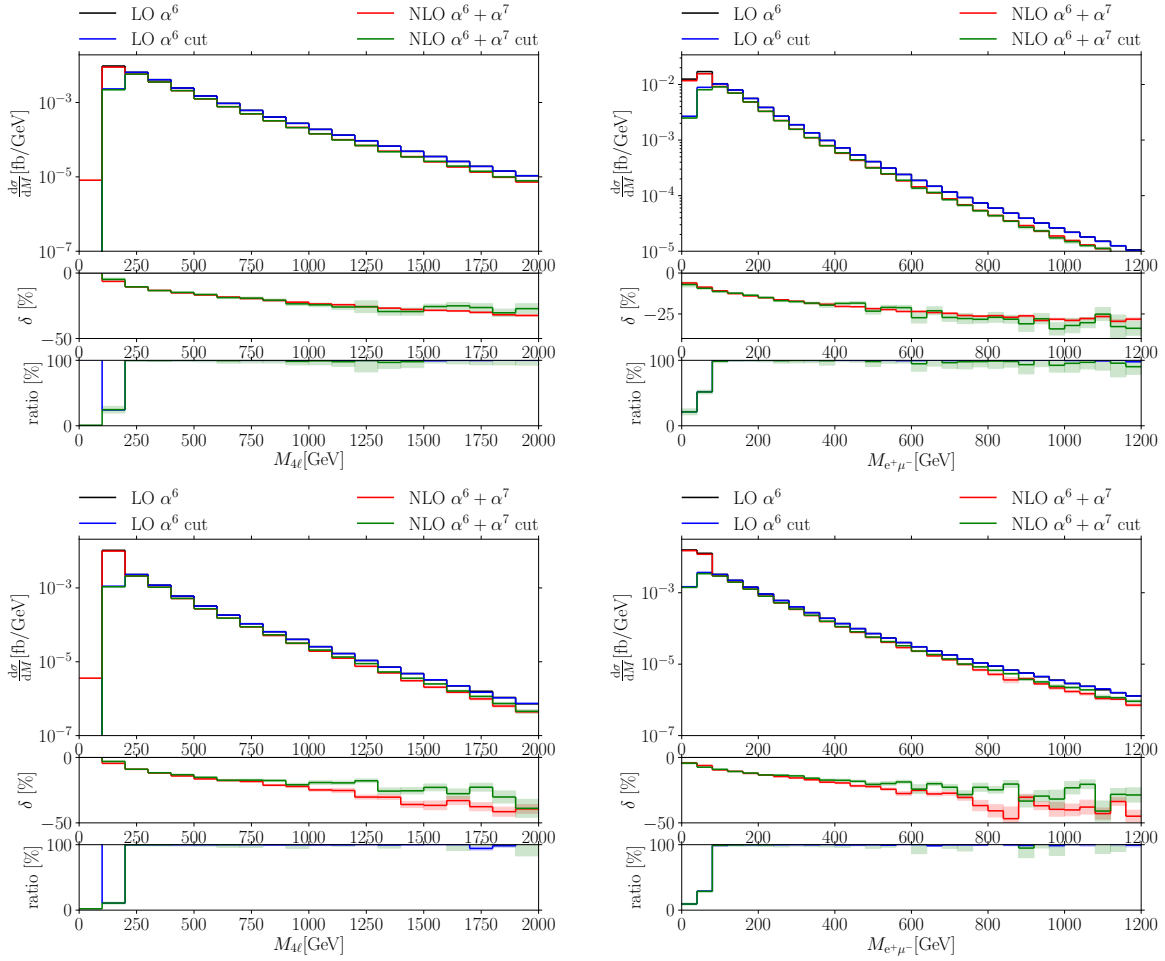
Figure 4.45: Differential cross sections with respect to the four-lepton invariant mass and with respect to the invariant mass of the two charged leptons for the physical VBS (top) and the physical Higgs setup (bottom) compared to the respective modified setups with cut-out Higgs-boson resonance.

(289) are in some sense complementary: We already mentioned that the different shape of this distribution in the two physical setups is due to the cut on the transverse mass, which causes the second maximum at large azimuthal angular separation that we see in the VBS setup to disappear in the Higgs setup. This cut is designed to enhance the Higgs-production contribution, and it does so very efficiently. The related differential distribution with respect to the rapidity difference also flattens out at small values of $\Delta y_{e^+\mu^-}$ in both setups. As we also noted earlier, the distribution in the case of the physical Higgs setup is much narrower than in the case of the physical VBS setup. The difference in shapes completely disappears when cutting away the resonance contribution. This observation is in accordance with our explanation that the Higgs boson as a scalar particle forces its decay products to have opposite helicity, which leads to the two charged leptons being emitted more likely in the same direction: With this contribution cut away this enhancement in the Higgs setup disappears. Angular momentum conservation also explains the strong enhancement of the Higgs-production contribution over the VBS process at small azimuthal angular differences. We do not show this observable explicitly for the unphysical setups. However, it propagates to the R separation of the two charged leptons, which is strongly correlated to the two presented observables. At NLO, we recognise in the two observables that the EW corrections to the EW cross section are significantly smaller in those regions where we cut away the resonance contribution.
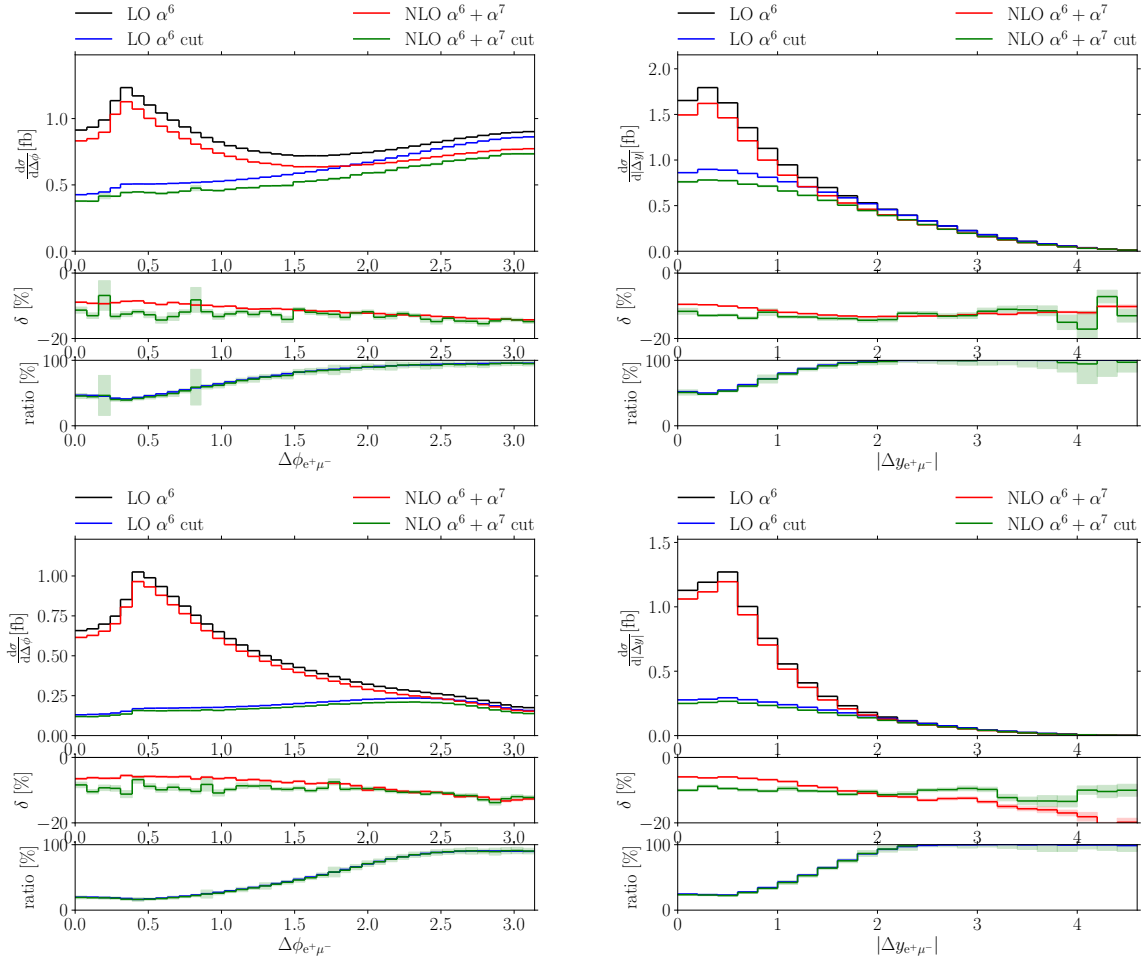
Figure 4.46: Differential cross sections with respect to the azimuthal angular and with respect to the rapidity separation of the two charged leptons for the physical VBS (top) and the physical Higgs setup (bottom) compared to the respective modified setups with cut-out Higgs-boson resonance.

Next, we investigate how the Higgs boson resonance affects the observables on which the typical VBS cuts are applied, the invariant mass of the two jets and their rapidity separation. Their distributions are presented in Figure 4.47. In the invariant-mass distribution, we see only a very small dependence on the additional cut in the VBS setup. However, in the Higgs setup, it becomes clear that the Higgs boson resonance favours small values of $M_{j_1 j_2}$. We see from the rapidity difference that Higgs production takes place at large values of $\Delta y_{j_1 j_2}$.

At last, we present two observables that we did not expect to have a strong dependence on the Higgs boson resonance cut in Figure 4.48: the transverse momenta of the two hardest jets. We clearly see a strong tendency of the VBS subprocesses towards large transverse momenta of both jets. In both setups, they completely dominate the cross section above $p_{T,j_1} > 400\,\mathrm{GeV}$ and $p_{T,j_2} > 200\,\mathrm{GeV}$. This feature of W^+W^- scattering might explain why the choice of our central scale worked for other VBS processes whilst it is already for the EW process of $\mathcal{O}\left(\alpha^6\right)$ too low for W^+W^- scattering, especially in the Higgs setup. The presence of the Higgs boson resonance does not only drag the invariant mass of the four-lepton system towards smaller values compared to the other processes, but also the transverse momenta of the two hardest jets. This effect is even more enhanced in the Higgs setup, explaining the large scale uncertainty of $\mathcal{O}\left(\alpha_s\alpha^6\right)$. However, it does not explain the large scale uncertainty of $\mathcal{O}\left(\alpha_s^3\alpha^4\right)$ in the QCD-induced process since the Higgs boson resonance is not present in that case.
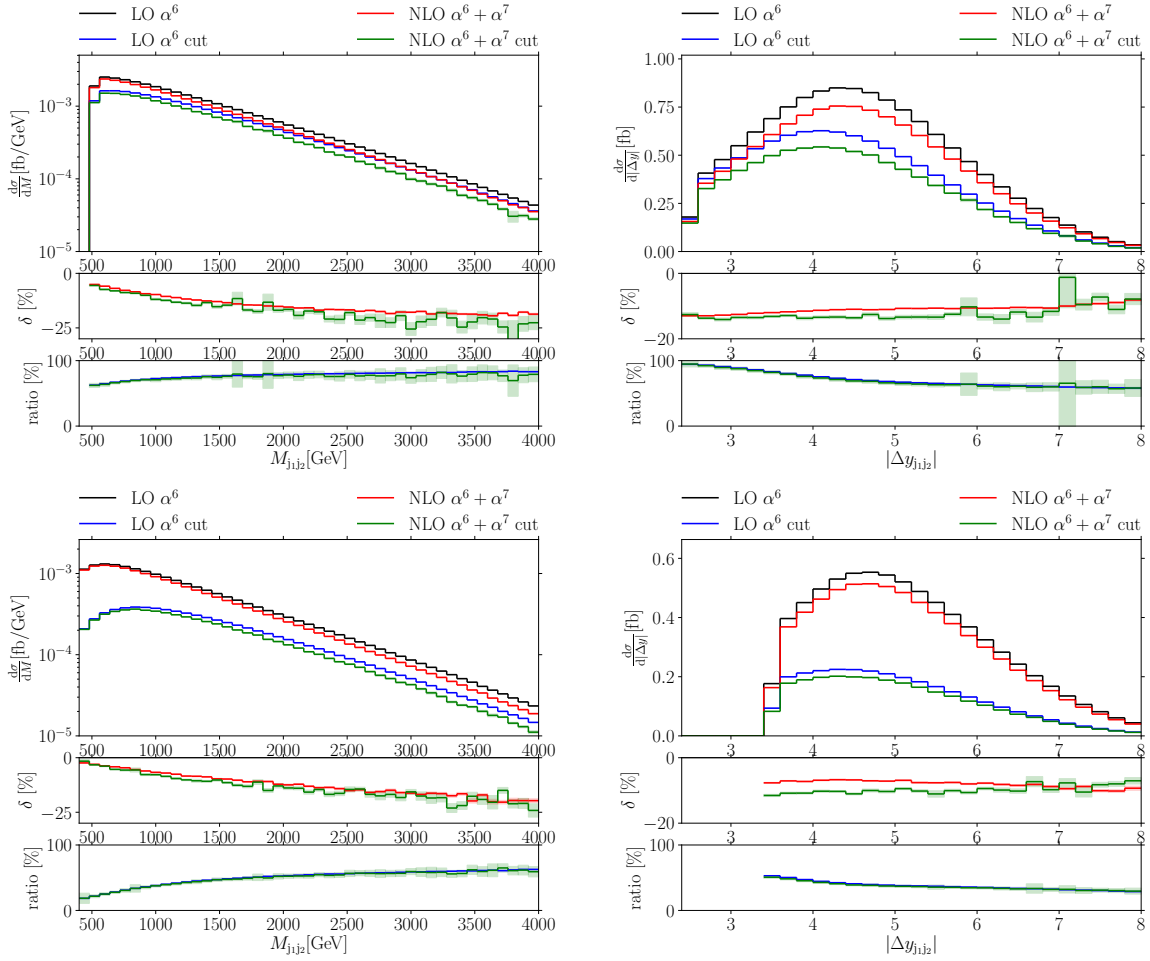
Figure 4.47: Differential cross sections with respect to the invariant mass and with respect to the rapidity separation of the two hardest jets for the physical VBS (top) and the physical Higgs setup (bottom) compared to the respective modified setups with cut-out Higgs-boson resonance.
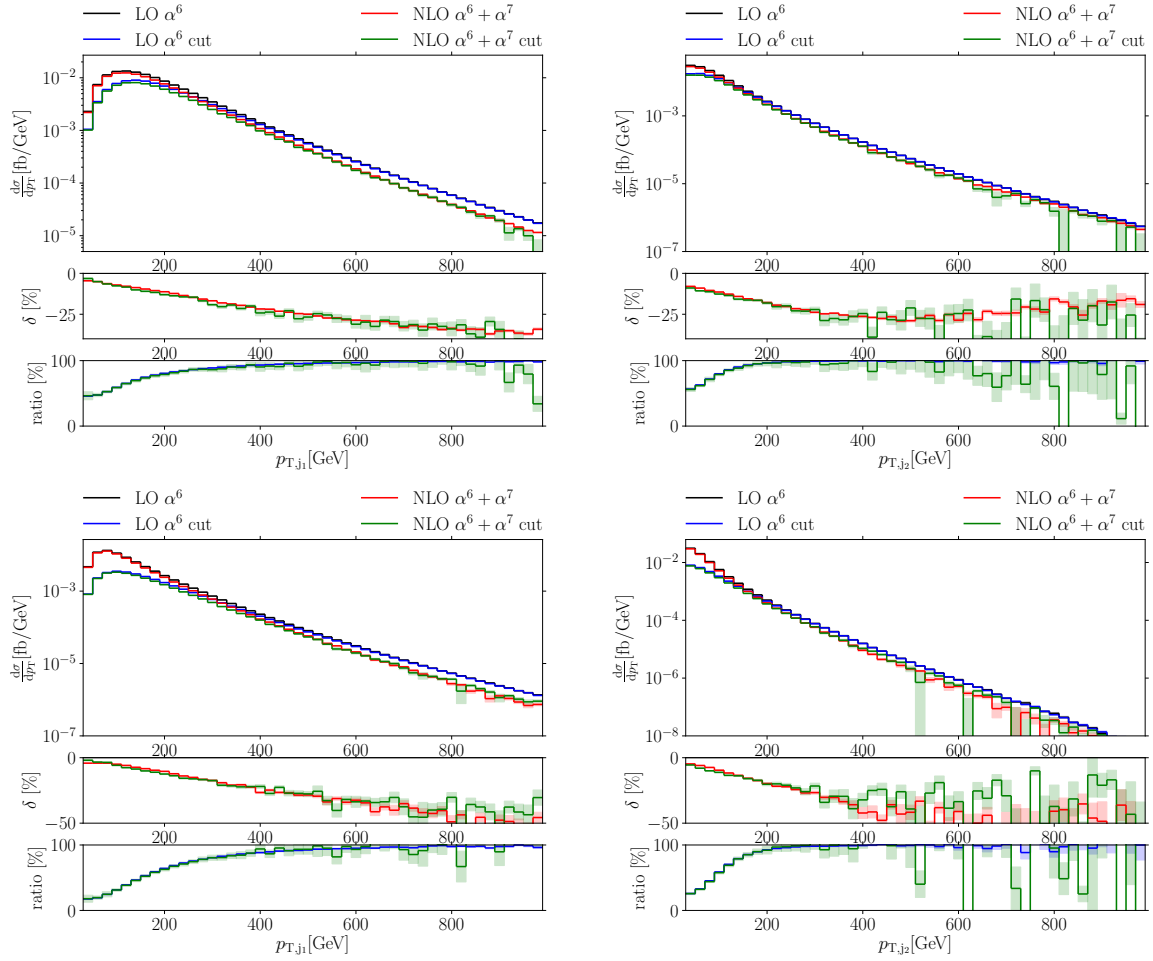
Figure 4.48: Differential cross sections with respect to the invariant mass and with respect to the rapidity separation of the two hardest jets for the physical VBS (top) and the physical Higgs setup (bottom) compared to the respective modified setups with cut-out Higgs-boson resonance.

5 Outlook: Attempts for an improved scale choice

After we ran into problems with our "traditional" scale choice of μ_{F} and μ_{R}, defined in equation (268) as the geometric average of the two hardest jet transverse momenta and henceforth denoted as "geometric scale" μ^{geom}, we chose to briefly investigate another scale for its suitability in the VBS and the Higgs setup for both the VBS signal and the QCD background. Our new try for an appropriate scale choice is

$$\mu_{\mathrm{F}}^{\mathrm{arith}} = \mu_{\mathrm{R}}^{\mathrm{arith}} = \frac{1}{2}\left(p_{\mathrm{T,j_1}} + p_{\mathrm{T,j_2}}\right) + \frac{1}{2}\left(E_{\mathrm{T,W^+}} + E_{\mathrm{T,W^-}}\right), \tag{308}$$

which was proposed in [146] for on-shell WW production associated with two jets. In the context of our off-shell production, the transverse energy of the W bosons $E_{\mathrm{T,W}}$ is calculated from our physical final state via

$$E_{\mathrm{T,W}} = \sqrt{p_{\mathrm{T},\ell\nu}^2 + M_{\mathrm{W}}^2}, \tag{309}$$

in which M_{W} is the W mass, and $p_{\mathrm{T},\ell\nu}$ denotes taking the vectorial sum of the momenta of the lepton and its corresponding neutrino and calculating the transverse part afterwards. Containing the arithmetic mean of the transverse momenta of the two hardest jets, we denote this new scale choice as "arithmetic scale". Since there are two neutrinos in our final state, the two quantities $E_{\mathrm{T,W}}$ are not measurable, but factorisation and renormalisation scales are no physical quantities either. With the arithmetic mean being always larger than the geometric mean and the second term containing the transverse energies of the leptonic sector being always larger than M_{W} (and hence obviously larger than zero), we guarantee that $\mu^{\mathrm{arith}} > \mu^{\mathrm{geom}}$ not only after integrating over the complete phase space, but for each event individually. We explicitly mention that the scale used for the computations in this thesis with its geometric mean leads to relatively small event-wise scales compared to an arithmetic mean, when the difference between the quantities is quite large, i. e. we have a very hard hardest and a very soft second-hardest jet. This effect became especially visible when we investigated the second-hardest jet in Figure 4.41 with its unexpected large scale variation for small transverse momenta. It also explains the opposite behaviour of the distributions of the transverse momenta of the leading and the one of the trailing jet: If the transverse momentum of the leading jet is large and the one of the trailing jet is low, the geometric mean tends to small values; if the transverse momentum of the trailing jet is also large, the difference between the geometric and the arithmetic mean becomes smaller.

In our investigation, we had a closer look at eight partonic channels. Because of technical reasons, BBMC computes a partonic channel together with the partonic channel, in which the generations of the quarks are interchanged, e. g. the channel uu $\rightarrow$ 4ℓuu together with cc $\rightarrow$ 4ℓcc. In our discussion, we abbreviate them with the quarks from the first generation. We calculated the quark-induced channels uu $\rightarrow$ uu $+ 4\ell(+\mathrm{g})$ and ud $\rightarrow$ ud $+ 4\ell(+\mathrm{g})$ at $\mathcal{O}\left(\alpha^6\right)$, $\mathcal{O}\left(\alpha_{\mathrm{s}}\alpha^6\right)$, $\mathcal{O}\left(\alpha_{\mathrm{s}}^2\alpha^4\right)$ and $\mathcal{O}\left(\alpha_{\mathrm{s}}^3\alpha^4\right)$ as well as the gluon-induced channels ug $\rightarrow$ ug $+ 4\ell(+\mathrm{g})$ and dg $\rightarrow$ dg $+ 4\ell(+\mathrm{g})$ at $\mathcal{O}\left(\alpha_{\mathrm{s}}^2\alpha^4\right)$ and $\mathcal{O}\left(\alpha_{\mathrm{s}}^3\alpha^4\right)$. The two quark-induced channels are the largest channels at $\mathcal{O}\left(\alpha^6\right)$, and these two channels alone cumulate to approximately 50% of the integrated EW cross section in both setups. In the QCD-induced process, they are still the largest quark-induced channels and combining them with the two largest gluon-induced partonic channels accounts for approximately 60% of the cross section at $\mathcal{O}\left(\alpha_{\mathrm{s}}^2\alpha^4\right)$. We hence expect that they also play major roles within the arithmetic scale choice and verified this via a low-precision calculation of all LO contributions. We summarise the results in Table 5.1 and justify that an examination of these few channels should suffice for deciding the quality of a particular scale choice.

For the NLO investigation, we only included the QCD corrections since the scale dependence of EW corrections follows the LO results. As stated repeatedly, the assignment of "QCD" and "EW" corrections is ambiguous, and there is no one-to-one correspondence between an LO channel and an NLO one, but we use the convention that adding a gluon to the final state compared to a LO channel is the real QCD correction to this specific channel.

	σ^{α^6} [fb]	$\sigma^{\alpha^6}/\sigma_{\rm tot}^{\alpha^6}$ [%]	$\sigma^{\alpha_{\rm s}^2\alpha^4}$ [fb]	$\sigma^{\alpha_{\rm s}^2\alpha^4}/\sigma_{\rm tot}^{\alpha_{\rm s}^2\alpha^4}$ [%]
VBS setup, geometric scale				
uu → uu	0.4021(2)	14.9	0.5248(2)	7.6
ud → ud	1.0611(3)	39.3	0.6026(2)	8.7
ug → ug	–	–	2.1625(7)	31.3
dg → dg	–	–	1.1412(4)	16.5
total	2.6988(3)	100	6.9115(9)	100
VBS setup, arithmetic scale				
uu → uu	0.36183(9)	15.4	0.36717(7)	8.0
ud → ud	0.9590(4)	40.8	0.4211(1)	10.5
ug → ug	–	–	1.4158(3)	30.8
dg → dg	–	–	0.740(1)	16.1
total	2.348(6)	100	4.601(7)	100
Higgs setup, geometric scale				
uu → uu	0.15475(7)	10.1	0.08332(4)	4.9
ud → ud	0.5995(1)	39.1	0.09907(4)	5.9
ug → ug	–	–	0.5437(3)	32.1
dg → dg	–	–	0.2824(1)	16.7
total	1.5322(2)	100	1.6923(3)	100
Higgs setup, arithmetic scale				
uu → uu	0.136(2)	9.7	0.05759(5)	5.2
ud → ud	0.54(1)	38.5	0.0679(1)	6.1
ug → ug	–	–	0.3511(1)	31.7
dg → dg	–	–	0.181(2)	16.3
total	1.40(2)	100	1.109(5)	100

Table 5.1: Comparison of the absolute and relative contributions of selected major partonic channels at LO in both setups for different scales. We normalise to the sum of all partonic channels for a given order, except the bottom-induced contributions. The geometric scale is defined in equation (268), and the arithmetic scale in equation (308).

In this chapter, we choose both factorisation and renormalisation scales to be equal ($\mu_{\rm F} = \mu_{\rm R} = \mu$) and vary them between $\mu = 2^{-4}\mu^{\rm centralsc}$ and $\mu = 2^4\mu^{\rm centralsc}$ with a step width of 2, i. e. we perform calculations for nine different scale choices. We show the results for the EW process in Figure 5.1 and the results for the QCD-induced process in Figure 5.2. We mention that we merged both quark- and both gluon-induced processes in the case of the QCD-induced process, since the channels uu → 4ℓuu and ud → 4ℓud belong to different subclasses of processes at $\mathcal{O}\left(\alpha^6\right)$ (there is only Z exchange in the first one, but Z and W exchange in the second one), but to the same one at $\mathcal{O}\left(\alpha_{\rm s}^2\alpha^4\right)$ (with both t- and u-channel g exchange). Similarly, the two channels ug → 4ℓug and dg → 4ℓdg are identical from the point of view of Feynman diagrams at $\mathcal{O}\left(\alpha_{\rm s}^2\alpha^4\right)$. Different effects from scale variations are hence only expected from their influence on the PDFs and the minor effect of the QCD couplings being less important in the case of the u quark compared to the d quark because of its larger electric charge.

In Figure 5.1 we can see clearly for the EW process that we are still at the rising flank of the cross section for the main contributions and the geometric scale choice. Although we reach the maximum of the cross section in the VBS setup between $2\mu_{\rm geom}^{\rm centralsc}$ and $4\mu_{\rm geom}^{\rm centralsc}$, we get only a mild dependence on the scale, as we noted earlier in Section 4.3.4. If we choose the arithmetic scale instead, we are almost at the very maximum of the cross section. In the Higgs setup, both
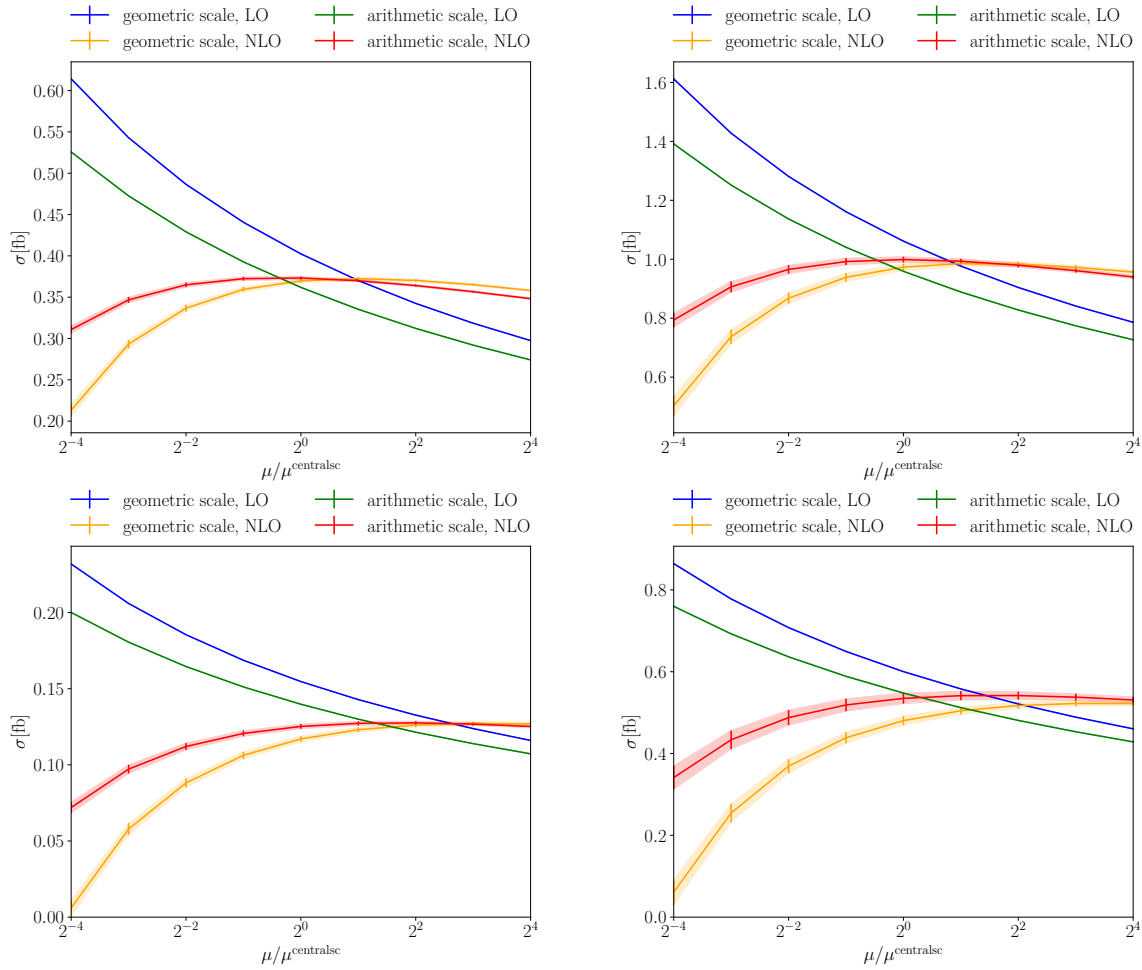
Figure 5.1: Integrated cross sections of the partonic channels uu $\to 4\ell$uu(+g) (left) and ud $\to 4\ell$ud(+g) (right) at $\mathcal{O}\left(\alpha^6\right)$ and $\mathcal{O}\left(\alpha_{\mathrm{s}}\alpha^6\right)$ in the VBS (top) and the Higgs setup (bottom) for different scale choices. The shaded band indicates the integration error.

geometric and arithmetic scale choices are seemingly too low for the main contributions. The scale dependence of the integrated cross section is, as we expected from previous results, larger than in the VBS setup. For the geometric scale choice we reach the maximum at $16\mu_{\mathrm{geom}}^{\mathrm{centralsc}}$. Changing to the arithmetic scale results in a clear reduction of the scale uncertainty. Nevertheless, the dominant partonic channel still favours an even higher scale choice and the optimum lies around $4\mu_{\mathrm{arith}}^{\mathrm{centralsc}}$. In case of the subdominant channel, the optimum is also between $4\mu_{\mathrm{arith}}^{\mathrm{centralsc}}$ and $8\mu_{\mathrm{arith}}^{\mathrm{centralsc}}$.

In Figure 5.2 we can see that the maxima of the NLO cross section are much more pronounced in the case of the QCD-induced contribution than in the case of the EW contribution. We could already infer this fact from the data of our classical seven-point scale variation of the geometric scale. There are also larger differences between VBS and Higgs setup and some different behaviour of the dominant quark- and the dominant gluon-induced channels. The latter effect is also not unexpected, since quark and gluon PDFs behave differently under a change of the factorisation scale. For the VBS setup, the dominant quark-induced contributions are spot-on at the maximum within the central geometric scale. In contrast, the leading gluon-induced contributions are below their peak value. Although the maximum is already reached at $2\mu_{\mathrm{geom}}^{\mathrm{centralsc}}$, the steepness of the curve leads to a large scale uncertainty. In the Higgs setup, the effect is even larger than in the VBS setup. In taking only the dominant contributions into account, the quark-induced part has a negative cross section at NLO already at the central geometric scale. The optimum for the quark-induced contribution within the geometric scale frame is far beyond $16\mu_{\mathrm{geom}}^{\mathrm{centralsc}}$. For
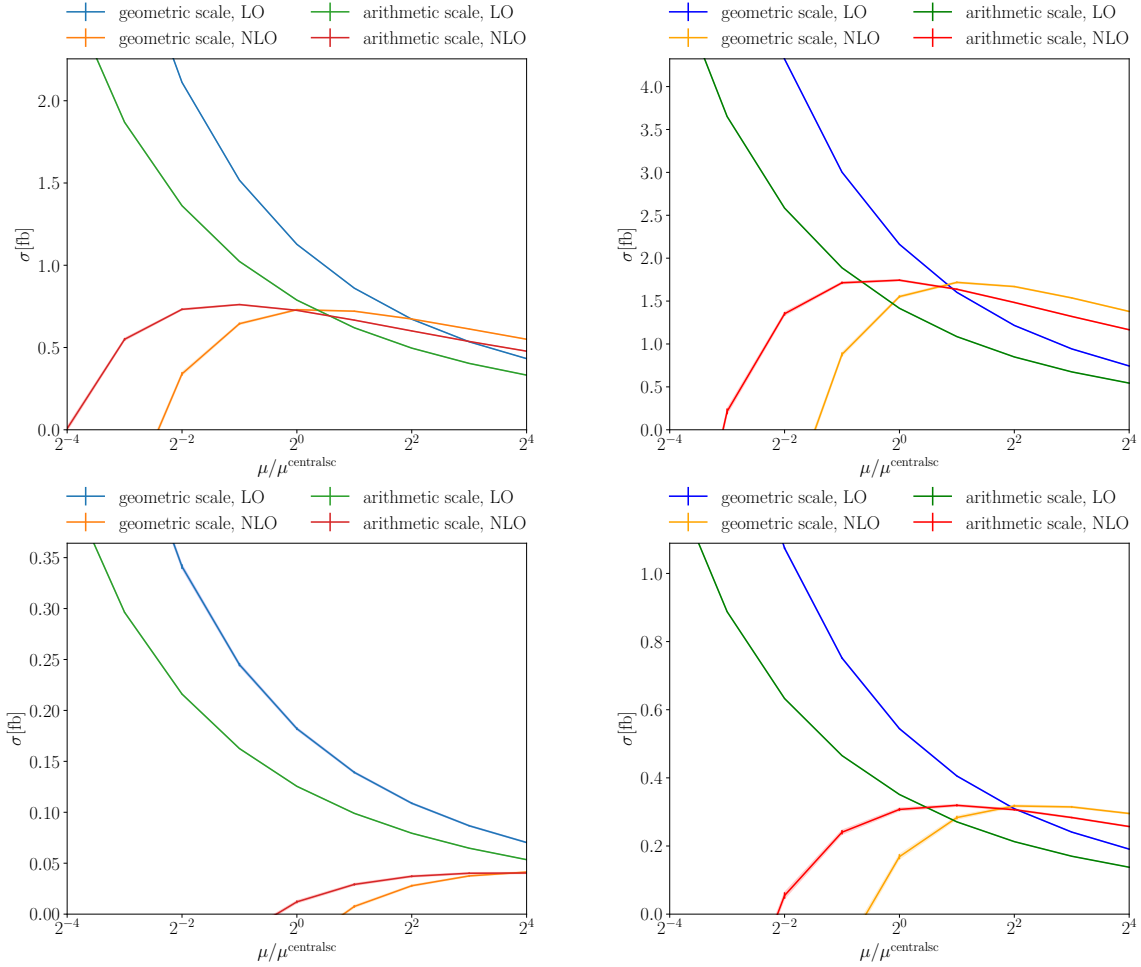
Figure 5.2: Summed integrated cross sections of the two quark-induced partonic channels uu $\rightarrow$ 4ℓuu(+g) and ud $\rightarrow$ 4ℓud(+g) (left) and the two gluon-induced partonic channels ug $\rightarrow$ 4ℓug(+g) and dg $\rightarrow$ 4ℓdg(+g) (right) at $\mathcal{O}\left(\alpha_s^2\alpha^4\right)$ and $\mathcal{O}\left(\alpha_s^3\alpha^4\right)$ in the VBS (top) and the Higgs setup (bottom) for different scale choices.

the dominant gluon-induced channels the optimum would be between $4\mu_{\text{geom}}^{\text{centralsc}}$ and $8\mu_{\text{geom}}^{\text{centralsc}}$, and, as we already saw in Section 4.3.4, already a slight variation of the scale results in a total breakdown of the cross section. Within the arithmetic scale frame, we are past the maximum for the dominant quark-induced contribution and exactly on the maximum for the gluon-induced one for the VBS setup and, hence, in a region of mild scale dependence. Additionally, we are in the region of small relative NLO QCD corrections. For the Higgs setup, the arithmetic scale is passably suited for the gluon-induced contributions with the maximum of the cross section being near $2\mu_{\text{arith}}^{\text{centralsc}}$. We still mention that being on the falling flank of the cross section would result in a much milder scale dependence than being on the rising one. The quark-induced part of the cross section also requires a higher scale. The maximum, however, seems to be much more flat than in the case of the gluon-induced part. We also want to remind that the quark-induced contributions are much smaller than the gluon-induced ones at $\mathcal{O}\left(\alpha_s^2\alpha^4\right)$ in the Higgs setup and, as we can infer from the dominant contributions, this will not change drastically at $\mathcal{O}\left(\alpha_s^3\alpha^4\right)$ also when choosing a much higher scale (up to $16\mu_{\text{arith}}^{\text{centralsc}}$). We believe that optimising the scale for the gluon-induced channels at $\mathcal{O}\left(\alpha_s^3\alpha^4\right)$ is of much more importance in finding a compromise between the two types of processes than choosing an optimum for the quarks.

To summarise, choosing an optimal scale for all types of processes (quark-induced, gluon-induced) for all orders (EW, QCD-induced) and all setups (VBS, Higgs) is impossible. The Higgs setup demands much higher scales than the VBS setup. Especially, none of our investigated

observables seems to be suited for a "natural" distinction between those two setups that could be incorporated into a scale variable that naturally produces much larger scales for the Higgs than for the VBS setup. Nevertheless, the scale that is proposed in this chapter seems to be a very good scale for the VBS setup and pointing in the correct direction for the Higgs setup.

6   Summary and conclusion

In this thesis, we calculated the integrated and differential cross sections of the process $pp \rightarrow e^+\nu_e\mu^-\bar{\nu}_\mu jj + X$, shortly W^+W^- scattering, at LO and NLO using our in-house Monte Carlo integrator BBMC which itself uses the programs RECOLA and COLLIER to calculate scattering amplitudes. For the calculation of NLO corrections, we used the CS dipole formalism and implemented CS dipoles in BBMC that were not necessary yet. We checked these new dipoles both at the level of the integrated cross section, and the level of individual phase-space points against the implementation in the Monte Carlo integrator MOCANLO. Furthermore, we included the method of resonance permutation into the framework of BBMC to be able to handle the Higgs-boson resonance.

Our specific interest was the study of vector boson scattering (VBS) in the process $pp \rightarrow e^+\nu_e\mu^-\bar{\nu}_\mu(+X)$, which is a part of the EW contribution of $\mathcal{O}\left(\alpha^6\right)$, while the main background consists of QCD-induced processes of $\mathcal{O}\left(\alpha_s^2\alpha^4\right)$. Additional background contributions emerge from non-VBS EW processes, the interference at $\mathcal{O}\left(\alpha_s\alpha^5\right)$ and loop-induced contributions of $\mathcal{O}\left(\alpha_s^4\alpha^4\right)$. We considered two different experimental setups. The first one used standard VBS phase-space cuts (VBS setup); in the second one, we used cuts designed for Higgs boson searches (Higgs setup). In both of our setups, we found that the EW non-VBS background and the interference contribution are completely negligible.

We found that the cross section of W^+W^- scattering at $\mathcal{O}\left(\alpha^6\right)$ is the largest cross section of all massive VBS scattering processes, which are of the type $pp \rightarrow \ell\ell\nu\nu jj + X$ when we use a comparable experimental setup. Compared to those other processes, we found many similarities: The LO differential distributions show a clear preference for the signal process of $\mathcal{O}\left(\alpha^6\right)$ towards a large invariant mass and a large rapidity separation of the two final jets. Using these observables to design the experimental setups, we get a relatively large signal-to-background ratio of 0.4 in the standard VBS setup at LO, which is only exceeded by same-sign W^+W^+ scattering. In the Higgs setup the ratio is even 0.9. For all VBS processes and hence also for W^+W^- scattering, there are extremely large EW corrections of up to -50% in the tails of energy-correlated observables such as transverse momenta. In contrast, the EW corrections of energy-uncorrelated observables such as rapidities remained basically constant. As already studied before, the large EW corrections can be traced back to the influence of large Sudakov logarithms.

In contrast to other VBS processes, W^+W^- has some unique features that we also studied in this thesis and whose influences we could see in our results. The main difference to other VBS processes is the presence of the Higgs-boson resonance inside our fiducial phase space. Vector-boson fusion into an s-channel Higgs boson is a fundamental part of W^+W^- scattering in particular: every partonic channel with VBS characteristics includes resonant Higgs production and vice versa. In contrast to ZZ scattering, in which phase-space cuts can remove it, and the other VBS processes, in which it is not present at all, there is no possibility for a physically meaningful cut on this particular subprocess in our process. This led to a hybrid form of our process, in which not only VBS, but also Higgs physics play a role, which manifested itself in considerably smaller EW corrections at $\mathcal{O}\left(\alpha^7\right)$ of only -11.4% for standard VBS cuts and -6.7% for Higgs-search cuts. Partonic channels with VBS and Higgs-boson contributions had significantly smaller NLO corrections than those without. To study the influence of the Higgs-boson resonance further, we introduced an additional cut on the non-measurable four-lepton invariant mass around the Higgs mass and modified our two setups. As expected, the fraction of the Higgs-boson resonance contribution in the Higgs setup is larger than in the VBS setup with 60.8% compared to 26.8%, which explains the smaller EW correction. In our modified setups, the EW corrections of $\mathcal{O}\left(\alpha^7\right)$ amount to -13.2% in the VBS and -9.9% in the Higgs setup.

Apart from the main partonic channels, we also found a sizeable (positive) contribution of photon-induced processes at $\mathcal{O}\left(\alpha^7\right)$, which is not present for same-sign W^+W^+ scattering and which we did not consider when calculating ZZ scattering. Omitting this contribution, the size of the EW corrections in the case of the modified VBS setup is with -14.5% in the same region as for the other VBS processes.

Another difference to our previous investigations of VBS processes was the influence of the renormalisation and factorisation scale. We used the standard scale choice of the geometric average of the transverse momenta of the two hardest jets, that delivered good results in the past and performed a seven-point scale variation. Unfortunately, the scale choice turned out to be too low for W^+W^- scattering, especially in the Higgs setup. This leads to relatively large QCD corrections of $\mathcal{O}\left(\alpha_\mathrm{s}\alpha^6\right)$ in the Higgs setup because of an interplay with the harsh jet veto, which removes most of the (positive) contribution from real gluon emissions. The QCD corrections of $\mathcal{O}\left(\alpha_\mathrm{s}\alpha^6\right)$ have been found to amount to -5.1% in the VBS and -23.0% in the Higgs setup. On the level of partonic channels, we found large QCD corrections to the non-VBS EW background, which emerged from additional emitted gluons that allowed the passing of the invariant-mass cuts but remained irrelevant due to their small absolute size. For future research, we encourage the calculation of the Higgs setup with a p_T resummation of the third jet.

We also calculated the QCD background and its NLO corrections. The main contribution in both setups emerged from gluon-induced processes, whose existence differentiates opposite-sign W^+W^- scattering from same-sign W^+W^+ scattering. We found that the Higgs setup is very efficient in cutting away most of the QCD background already at LO. The corrections of $\mathcal{O}\left(\alpha_\mathrm{s}^2\alpha^5\right)$ are very moderate with -8.2% in the VBS and -5.2% in the Higgs setup, and are, except for the partonic channels with only s-channel gluon exchange, mainly EW corrections to the QCD background. In these types of processes, the additional emission of gluons as QCD corrections to the interference contributions allows, as in the case of $\mathcal{O}\left(\alpha_\mathrm{s}\alpha^6\right)$, the passing of the invariant-mass cuts.

Unfortunately, the corrections of $\mathcal{O}\left(\alpha_\mathrm{s}^3\alpha^4\right)$, i. e. the QCD corrections to the QCD background, turned out to have unphysical properties due to our low scale choice. They amount to -30.3% in the VBS and -77.7% in the Higgs setup. Adding the two corrections of $\mathcal{O}\left(\alpha_\mathrm{s}^2\alpha^5\right)$ and $\mathcal{O}\left(\alpha_\mathrm{s}^3\alpha^4\right)$, we found corrections of more than -100%, and sometimes even more than -200% in several bins of our differential cross sections, especially in observables correlated with transverse momentum. This lead us to a brief investigation of another scale, the arithmetic mean of the transverse momenta of the two hardest jets plus the arithmetic mean of the transverse momenta of the reconstructed W bosons. The arithmetic scale choice produced better results in both setups for a few selected channels, which are capable of most of the cross section, although we found that it is still too small for the Higgs setup. For future research works, we recommend investigating even higher scale choices.

A   A note on the Sudakov approximation

As we stated in Section 4.3.3 and Section 4.3.5, the Sudakov approximation works well for estimating the EW corrections of $\mathcal{O}\left(\alpha^7\right)$ for other VBS processes and gives a reasonable result also for W^+W^- scattering. A main difference between the other processes and this one is, however, as repeatedly mentioned the presence of the Higgs boson resonance which drags the bulk of the cross section towards a region in which the Sudakov approximation is not applicable.

In the other processes, the leading logarithm is off by a few per cent. Compared to these results, the NLO corrections in W^+W^- scattering seem to be very on point with the approximation. In this appendix, we are showing that the extremely good estimate, especially in the VBS setup with $\delta_{\mathrm{LL,VBS}} = -11.9\%$ versus $\delta_{\mathrm{VBS}}^{\alpha^7} = -11.4\%$, is the result of a spurious cancellation. We were pointed to this fact since the Sudakov approximation of the modified setup, in which we cut the region of small centre-of-mass energies, should become more accurate, but actually becomes worse with $\delta_{\mathrm{LL,VBS\ modified}} = -15.8\%$ versus $\delta_{\mathrm{VBS\ modified}}^{\alpha^7} = -13.2\%$.

We recall from equation (296) the leading logarithm corrections:

$$\delta_{\mathrm{LL},i} = -\frac{\alpha}{4\pi} 4C_W^{\mathrm{EW}} \ln^2 \frac{s_i}{M_W^2} + \frac{\alpha}{4\pi} 2b_W^{\mathrm{EW}} \ln \frac{s_i}{M_W^2}. \tag{310}$$

We apply this formula on each bin i of the differential cross section with respect to the four-lepton invariant mass. Due to the bin width, we assume a uniform distribution of $M_{4\ell}$ leading to an estimated value of

$$\langle s \rangle_i = \frac{1}{M_{i\max} - M_{i\min}} \int \mathrm{d}M_{4\ell,i}\, s_i(M_{4\ell,i}) \tag{311}$$

$$= \frac{M_{i\max}^2 + M_{i\max}M_{i\min} + M_{i\min}^2}{3}, \tag{312}$$

where $M_{i\max}$ denotes the upper boundary of bin i and $M_{i\min}$ the lower boundary respectively. We note that $\langle M_{4\ell}\rangle_i$, which we used to compare with the literature, is trivially

$$\langle M_{4\ell}\rangle_i = \frac{M_{i\max} + M_{i\min}}{2}. \tag{313}$$

The variance of s_i is given by

$$\Sigma_{s_i}^2 = \frac{1}{M_{i\max} - M_{i\min}} \int \mathrm{d}M_{4\ell,i}\, s_i^2(M_{4\ell,i}) - \langle s\rangle_i^2 \tag{314}$$

$$= \frac{4M_{i\max}^4 - M_{i\max}^3 M_{i\min} - 6M_{i\max}^2 M_{i\min}^2 - M_{i\max}M_{i\min}^3 + 4M_{i\min}^4}{45}. \tag{315}$$

This variance propagates to an uncertainty of $\delta_{\mathrm{LL},i}$ as

$$\Sigma_{\delta_{\mathrm{LL},i}} = \frac{\delta_{\mathrm{LL},i} - \frac{\alpha}{4\pi} 4C_W^{\mathrm{EW}} \ln^2 \frac{s_i}{M_W^2}}{s_i \ln \frac{s_i}{M_W^2}} \Sigma_{s_i}. \tag{316}$$

With this preparatory work, we can define

$$\langle s \rangle = \frac{1}{\sigma} \sum_i \langle s\rangle_i \left(\frac{\mathrm{d}\sigma}{\mathrm{d}M_{4\ell}}\right)_i (M_{i\max} - M_{i\min}) \tag{317}$$

and

$$\sigma_{\mathrm{LL}} = \sum_i \left(\frac{\mathrm{d}\sigma}{\mathrm{d}M_{4\ell}}\right)_{\mathrm{LO},i} (1 + \delta_{\mathrm{LL},i})(M_{i\max} - M_{i\min}). \tag{318}$$

The leading logarithmic correction factor δ_{LL} is then

$$\delta_{\mathrm{LL}} = \frac{\sigma_{\mathrm{LL}}}{\sigma_{\mathrm{LO}}} - 1. \tag{319}$$

Setup	$\delta^{\alpha^7}[\%]$	$\delta_{\mathrm{LL}}[\%]$	$\langle M_{4\ell}\rangle[\,\mathrm{GeV}]$	$\sqrt{\langle s\rangle}[\,\mathrm{GeV}]$
VBS	-11.4	-11.9	333.0	414.8
Higgs	-6.7	-5.6	221.5	268.3
VBS, modified	-13.2	-15.8	400.0	476.0
Higgs, modified	-9.9	-12.1	332.5	384.2

Table A.1: Overview over NLO EW corrections of $\mathcal{O}\left(\alpha^7\right)$ versus the corrections from the leading-logarithmic Sudakov approximation as well as average centre-of-mass energy and the square root of the average centre-of-mass energy squared in the two investigated setups and their modification according to Section 4.3.5.
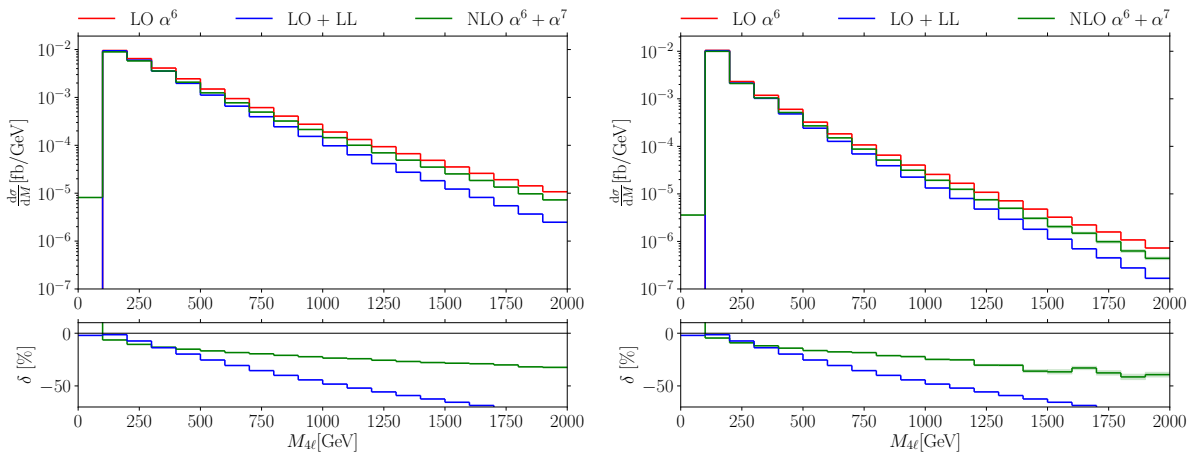
Figure A.1: Differential cross sections in the four-lepton invariant mass for the VBS (left) and the Higgs setup (right) for the LO EW contribution, the NLO EW corrections to the EW contribution and the LL approximation.

An overview of the Sudakov approximation compared with the full NLO results is given in Table A.1.

In Figure A.1, we show the differential distributions in the (not measurable) $M_{4\ell}$. Apart from the first bin with $M_{4\ell} < 100\,\mathrm{GeV}$ with a negligible contribution, we recognise that the Sudakov approximation underestimates the NLO corrections for $M_{4\ell} < 300\,\mathrm{GeV}$ and overestimates them at higher values in both setups. We remark that the region, in which the Sudakov approximation underestimates the corrections, is the part of the phase space in which the approximation is not applicable, but it is also the region of the largest contribution. The very good results of the approximation in the VBS setup of $\mathrm{W^+W^-}$ scattering are just a coincidental result of these two regions cancelling out each other; in the Higgs setup, the region of small four-lepton invariant mass dominates. Cutting away the large contributions around the Higgs boson resonance results, the approximation in the VBS setup becomes worse despite cutting away the non-applicable region.

List of abbreviations

CS   Catani–Seymour

EW   electroweak

GWS   Glashow–Weinberg–Salam

IR   infrared

LO   leading order

NLO   next-to-leading order

QCD   quantum chromodynamics

QED   quantum electrodynamics

UV   ultraviolet

VBS   vector boson scattering

3VP   triple vector boson production

List of Tables

List of Figures

References

[1] M. Planck, *Vom Relativen zum Absoluten*, in *Vorträge Reden Erinnerungen*, H. Roos and A. Hermann, eds., (Berlin, Heidelberg), pp. 103–117, Springer Berlin Heidelberg (2001), DOI.

[2] E. Rutherford and F. Soddy, *LXXXIV. — The radioactivity of thorium compounds. II. The cause and nature of radioactivity*, *J. Chem. Soc., Trans.* **81** (1902) 837.

[3] E. Rutherford, *Bakerian lecture. nuclear constitution of atoms*, *Proceedings of the Royal Society of London. Series A, Containing Papers of a Mathematical and Physical Character* **97** (1920) 374.

[4] G. Jungman, M. Kamionkowski and K. Griest, *Supersymmetric dark matter*, *Phys. Rept.* **267** (1996) 195 [`hep-ph/9506380`].

[5] G. Bertone, D. Hooper and J. Silk, *Particle dark matter: Evidence, candidates and constraints*, *Phys. Rept.* **405** (2005) 279 [`hep-ph/0404175`].

[6] F. Kahlhoefer, *Review of LHC Dark Matter Searches*, *Int. J. Mod. Phys. A* **32** (2017) 1730006 [`1702.02430`].

[7] ATLAS collaboration, *Observation of a new particle in the search for the Standard Model Higgs boson with the ATLAS detector at the LHC*, *Phys. Lett. B* **716** (2012) 1 [`1207.7214`].

[8] CMS collaboration, *Observation of a New Boson at a Mass of 125 GeV with the CMS Experiment at the LHC*, *Phys. Lett. B* **716** (2012) 30 [`1207.7235`].

[9] P.W. Higgs, *Broken Symmetries and the Masses of Gauge Bosons*, *Phys. Rev. Lett.* **13** (1964) 508.

[10] P.W. Higgs, *Spontaneous Symmetry Breakdown without Massless Bosons*, *Phys. Rev.* **145** (1966) 1156.

[11] F. Englert and R. Brout, *Broken Symmetry and the Mass of Gauge Vector Mesons*, *Phys. Rev. Lett.* **13** (1964) 321.

[12] G.S. Guralnik, C.R. Hagen and T.W.B. Kibble, *Global Conservation Laws and Massless Particles*, *Phys. Rev. Lett.* **13** (1964) 585.

[13] T.W.B. Kibble, *Symmetry breaking in nonAbelian gauge theories*, *Phys. Rev.* **155** (1967) 1554.

[14] G.C. Branco, P.M. Ferreira, L. Lavoura, M.N. Rebelo, M. Sher and J.P. Silva, *Theory and phenomenology of two-Higgs-doublet models*, *Phys. Rept.* **516** (2012) 1 [`1106.0034`].

[15] ATLAS collaboration, *Evidence for Electroweak Production of $W^{\pm}W^{\pm}jj$ in pp Collisions at $\sqrt{s} = 8\ TeV$ with the ATLAS Detector*, *Phys. Rev. Lett.* **113** (2014) 141803 [`1405.6241`].

[16] CMS collaboration, *Study of vector boson scattering and search for new physics in events with two same-sign leptons and two jets*, *Phys. Rev. Lett.* **114** (2015) 051801 [`1410.6315`].

[17] ATLAS collaboration, *Measurement of $W^{\pm}W^{\pm}$ vector-boson scattering and limits on anomalous quartic gauge couplings with the ATLAS detector*, *Phys. Rev.* **D96** (2017) 012007 [`1611.02428`].

[18] CMS collaboration, *Observation of electroweak production of same-sign W boson pairs in the two jet and two same-sign lepton final state in proton-proton collisions at $\sqrt{s} = 13\ TeV$*, *Phys. Rev. Lett.* **120** (2018) 081801 [`1709.05822`].

[19] ATLAS collaboration, *Observation of electroweak production of a same-sign W boson pair in association with two jets in pp collisions at $\sqrt{s} = 13$ TeV with the ATLAS detector*, *Phys. Rev. Lett.* **123** (2019) 161801 [`1906.03203`].

[20] ATLAS collaboration, *Observation of electroweak $W^{\pm}Z$ boson pair production in association with two jets in pp collisions at $\sqrt{s} = 13$ TeV with the ATLAS detector*, *Phys. Lett. B* **793** (2019) 469 [`1812.09740`].

[21] CMS collaboration, *Measurement of electroweak WZ boson production and search for new physics in WZ + two jets events in pp collisions at $\sqrt{s} = 13$ TeV*, *Phys. Lett. B* **795** (2019) 281 [`1901.04060`].

[22] CMS collaboration, *Measurements of production cross sections of WZ and same-sign WW boson pairs in association with two jets in proton-proton collisions at $\sqrt{s} = 13$ TeV*, *Phys. Lett. B* **809** (2020) 135710 [`2005.01173`].

[23] CMS collaboration, *Measurement of vector boson scattering and constraints on anomalous quartic couplings from events with four leptons and two jets in proton-proton collisions at $\sqrt{s} = 13$ TeV*, *Phys. Lett.* **B774** (2017) 682 [`1708.02812`].

[24] ATLAS collaboration, *Observation of electroweak production of two jets and a Z-boson pair with the ATLAS detector at the LHC*, `2004.10612` CERN-EP-2020-016, [`2004.10612`].

[25] CMS collaboration, *Evidence for electroweak production of four charged leptons and two jets in proton-proton collisions at $\sqrt{s} = 13$ TeV*, *Phys. Lett.* **B812** (2021) 135992 [`2008.07013`].

[26] CMS collaboration, *First observation of the electroweak production of a leptonically decaying W^+W^- pair in association with two jets in $\sqrt{s} = 13$ TeV pp collisions.*, CMS-PAS-SMP-21-001.

[27] CMS collaboration, *Observation of electroweak W+W− pair production in association with two jets in proton-proton collisions at s=13TeV*, *Phys. Lett. B* **841** (2023) 137495 [`2205.05711`].

[28] F. Cetorelli, *First observation of the electroweak production of a W^+W^- pair in association with two jets in the fully leptonic channel with the CMS detector at the LHC*, Ph.D. thesis, Milan Bicocca U., 2022.

[29] B. Jäger, C. Oleari and D. Zeppenfeld, *Next-to-leading order QCD corrections to W^+W^- production via vector-boson fusion*, *JHEP* **07** (2006) 015 [`hep-ph/0603177`].

[30] T. Melia, K. Melnikov, R. Röntsch and G. Zanderighi, *NLO QCD corrections for W^+W^- pair production in association with two jets at hadron colliders*, *Phys. Rev. D* **83** (2011) 114043 [`1104.2327`].

[31] N. Greiner, G. Heinrich, P. Mastrolia, G. Ossola, T. Reiter and F. Tramontano, *NLO QCD corrections to the production of W^+W^- plus two jets at the LHC*, *Phys. Lett. B* **713** (2012) 277 [`1202.6004`].

[32] B. Jäger and G. Zanderighi, *Electroweak W^+W^-jj prodution at NLO in QCD matched with parton shower in the POWHEG-BOX*, *JHEP* **04** (2013) 024 [`1301.1695`].

[33] M. Rauch and S. Plätzer, *Parton Shower Matching Systematics in Vector-Boson-Fusion WW Production*, *Eur. Phys. J. C* **77** (2017) 293 [`1605.07851`].

[34] B. Biedermann, A. Denner and M. Pellen, *Large electroweak corrections to vector-boson scattering at the Large Hadron Collider*, *Phys. Rev. Lett.* **118** (2017) 261801 [1611.02951].

[35] B. Biedermann, A. Denner and M. Pellen, *Complete NLO corrections to W^+W^+ scattering and its irreducible background at the LHC*, *JHEP* **10** (2017) 124 [1708.00268].

[36] A. Denner, S. Dittmaier, P. Maierhöfer, M. Pellen and C. Schwan, *QCD and electroweak corrections to WZ scattering at the LHC*, *JHEP* **06** (2019) 067 [1904.00882].

[37] A. Denner, R. Franken, M. Pellen and T. Schmidt, *NLO QCD and EW corrections to vector-boson scattering into ZZ at the LHC*, *JHEP* **11** (2020) 110 [2009.00411].

[38] A. Denner, R. Franken, M. Pellen and T. Schmidt, *Full NLO predictions for vector-boson scattering into Z bosons and its irreducible background at the LHC*, *JHEP* **10** (2021) 228 [2107.10688].

[39] A. Denner, R. Franken, T. Schmidt and C. Schwan, *NLO QCD and EW corrections to vector-boson scattering into W^+W^- at the LHC*, *JHEP* **06** (2022) 098 [2202.10844].

[40] S. Actis, A. Denner, L. Hofer, A. Scharf and S. Uccirati, *Recursive generation of one-loop amplitudes in the Standard Model*, *JHEP* **04** (2013) 037 [1211.6316].

[41] S. Actis et al., *RECOLA: REcursive Computation of One-Loop Amplitudes*, *Comput. Phys. Commun.* **214** (2017) 140 [1605.01090].

[42] A. Denner, S. Dittmaier and L. Hofer, *Collier - A fortran-library for one-loop integrals*, *PoS* **LL2014** (2014) 071 [1407.0087].

[43] A. Denner, S. Dittmaier and L. Hofer, *COLLIER: a fortran-based Complex One-Loop LIbrary in Extended Regularizations*, *Comput. Phys. Commun.* **212** (2017) 220 [1604.06792].

[44] A. Rytz, *Recommended energy and intensity values of alpha particles from radioactive decay*, *Atomic Data and Nuclear Data Tables* **47** (1991) 205.

[45] J. Chadwick, *Intensitätsverteilung im magnetischen Spektrum der β-Strahlen von Radium B + C*, *Verhandl. Dtsc. Phys. Ges.* **16** (1914) 383.

[46] W. Pauli, "Pauli letter collection: letter to Lise Meitner.".

[47] M.E. Peskin and D.V. Schroeder, *An Introduction to quantum field theory*, Addison-Wesley, Reading, USA (1995).

[48] E. Fermi, *Tentativo di una teoria dell'emissione dei raggi beta*, *Ric. Sci.* **4** (1933) 491.

[49] E. Fermi, *Versuch einer Theorie der β-Strahlen. I*, *Z. Phys.* **88** (1934) 161.

[50] F.L. Wilson, *Fermi's Theory of Beta Decay*, *Am. J. Phys.* **36** (1968) 1150.

[51] F. Reines and C.L. Cowan, *Detection of the free neutrino*, *Phys. Rev.* **92** (1953) 830.

[52] F. Reines, C.L. Cowan, F.B. Harrison, A.D. McGuire and H.W. Kruse, *Detection of the free anti-neutrino*, *Phys. Rev.* **117** (1960) 159.

[53] D. Griffiths, *Introduction to elementary particles*, Wiley-VCH (2008).

[54] M. Froissart, *Asymptotic behavior and subtractions in the Mandelstam representation*, *Phys. Rev.* **123** (1961) 1053.

[55] T.D. Lee and C.-N. Yang, *Question of Parity Conservation in Weak Interactions*, *Phys. Rev.* **104** (1956) 254.

[56] C.S. Wu, E. Ambler, R.W. Hayward, D.D. Hoppes and R.P. Hudson, *Experimental Test of Parity Conservation in β Decay*, *Phys. Rev.* **105** (1957) 1413.

[57] E.C.G. Sudarshan and R.e. Marshak, *Chirality invariance and the universal Fermi interaction*, *Phys. Rev.* **109** (1958) 1860.

[58] A. Proca, *Sur la theorie ondulatoire des electrons positifs et negatifs*, *J. Phys. Radium* **7** (1936) 347.

[59] J.M. Cornwall, D.N. Levin and G. Tiktopoulos, *Derivation of Gauge Invariance from High-Energy Unitarity Bounds on the s Matrix*, *Phys. Rev. D* **10** (1974) 1145.

[60] J. Humphreys, *Introduction to Lie Algebras and Representation Theory*, Graduate texts in mathematics, Springer (1972).

[61] A. Wipf, *Symmetrien in der Physik*, Springer (2023).

[62] M. D'Onofrio and K. Rummukainen, *Standard model cross-over on the lattice*, *Phys. Rev. D* **93** (2016) 025003 [1508.07161].

[63] J. Goldstone, A. Salam and S. Weinberg, *Broken Symmetries*, *Phys. Rev.* **127** (1962) 965.

[64] E. Fabri and L.E. Picasso, *Quantum field theory and approximate symmetries*, *Phys. Rev. Lett.* **16** (1966) 408.

[65] S.L. Glashow, *Partial Symmetries of Weak Interactions*, *Nucl. Phys.* **22** (1961) 579.

[66] S. Weinberg, *A Model of Leptons*, *Phys. Rev. Lett.* **19** (1967) 1264.

[67] A. Salam, *Weak and Electromagnetic Interactions*, *Conf. Proc. C* **680519** (1968) 367.

[68] F.J. Hasert et al., *Search for Elastic ν_μ Electron Scattering*, *Phys. Lett. B* **46** (1973) 121.

[69] R. Franken and C. Schwinn, *On-shell constructibility of Born amplitudes in spontaneously broken gauge theories*, *JHEP* **02** (2020) 073 [1910.13407].

[70] C.E. Vayonakis, *Born Helicity Amplitudes and Cross-Sections in Nonabelian Gauge Theories*, *Lett. Nuovo Cim.* **17** (1976) 383.

[71] M.S. Chanowitz and M.K. Gaillard, *The TeV Physics of Strongly Interacting W's and Z's*, *Nucl. Phys. B* **261** (1985) 379.

[72] J.C. Romão, *The need for the Higgs boson in the Standard Model*, 3, 2016 [1603.04251].

[73] B.W. Lee, C. Quigg and H.B. Thacker, *The Strength of Weak Interactions at Very High-Energies and the Higgs Boson Mass*, *Phys. Rev. Lett.* **38** (1977) 883.

[74] B.W. Lee, C. Quigg and H.B. Thacker, *Weak Interactions at Very High-Energies: The Role of the Higgs Boson Mass*, *Phys. Rev. D* **16** (1977) 1519.

[75] G. 't Hooft and M.J.G. Veltman, *Regularization and Renormalization of Gauge Fields*, *Nucl. Phys. B* **44** (1972) 189.

[76] M.D. Schwartz, *Quantum Field Theory and the Standard Model*, Cambridge University Press (3, 2014).

[77] H. Lehmann, K. Symanzik and W. Zimmermann, *On the formulation of quantized field theories*, *Nuovo Cim.* **1** (1955) 205.

[78] J.C. Ward, *An Identity in Quantum Electrodynamics*, *Phys. Rev.* **78** (1950) 182.

[79] F. Bloch and A. Nordsieck, *Note on the Radiation Field of the electron*, *Phys. Rev.* **52** (1937) 54.

[80] T. Kinoshita, *Mass singularities of Feynman amplitudes*, *J. Math. Phys.* **3** (1962) 650.

[81] T.D. Lee and M. Nauenberg, *Degenerate Systems and Mass Singularities*, *Phys. Rev.* **133** (1964) B1549.

[82] P.A.M. Dirac, *Classical theory of radiating electrons*, *Proc. Roy. Soc. Lond. A* **167** (1938) 148.

[83] S. Abreu, R. Britto and C. Duhr, *The SAGEX review on scattering amplitudes Chapter 3: Mathematical structures in Feynman integrals*, *J. Phys. A* **55** (2022) 443004 [2203.13014].

[84] G. 't Hooft, *Dimensional regularization and the renormalization group*, *Nucl. Phys. B* **61** (1973) 455.

[85] S. Weinberg, *New approach to the renormalization group*, *Phys. Rev. D* **8** (1973) 3497.

[86] X.-G. Wu, S.J. Brodsky and M. Mojaza, *The Renormalization Scale-Setting Problem in QCD*, *Prog. Part. Nucl. Phys.* **72** (2013) 44 [1302.0599].

[87] X.-G. Wu, Y. Ma, S.-Q. Wang, H.-B. Fu, H.-H. Ma, S.J. Brodsky et al., *Renormalization Group Invariance and Optimal QCD Renormalization Scale-Setting*, *Rept. Prog. Phys.* **78** (2015) 126201 [1405.3196].

[88] P. Ciafaloni and D. Comelli, *Sudakov enhancement of electroweak corrections*, *Phys. Lett. B* **446** (1999) 278 [hep-ph/9809321].

[89] M. Ciafaloni, P. Ciafaloni and D. Comelli, *Electroweak Bloch-Nordsieck violation at the TeV scale: 'Strong' weak interactions?*, *Nucl. Phys. B* **589** (2000) 359 [hep-ph/0004071].

[90] M. Ciafaloni, P. Ciafaloni and D. Comelli, *Bloch-Nordsieck violation in spontaneously broken Abelian theories*, *Phys. Rev. Lett.* **87** (2001) 211802 [hep-ph/0103315].

[91] S. Frixione, *Initial conditions for electron and photon structure and fragmentation functions*, *JHEP* **11** (2019) 158 [1909.03886].

[92] Y.L. Dokshitzer, *Calculation of the Structure Functions for Deep Inelastic Scattering and e+ e- Annihilation by Perturbation Theory in Quantum Chromodynamics.*, *Sov. Phys. JETP* **46** (1977) 641.

[93] V.N. Gribov and L.N. Lipatov, *Deep inelastic e p scattering in perturbation theory*, *Sov. J. Nucl. Phys.* **15** (1972) 438.

[94] G. Altarelli and G. Parisi, *Asymptotic Freedom in Parton Language*, *Nucl. Phys. B* **126** (1977) 298.

[95] S. Catani and M.H. Seymour, *A general algorithm for calculating jet cross-sections in NLO QCD*, *Nucl. Phys.* **B485** (1997) 291 [hep-ph/9605323].

[96] S. Catani, S. Dittmaier, M.H. Seymour and Z. Trocsanyi, *The dipole formalism for next-to-leading order QCD calculations with massive partons*, *Nucl. Phys.* **B627** (2002) 189 [hep-ph/0201036].

[97] S. Dittmaier, *A general approach to photon radiation off fermions*, *Nucl. Phys.* **B565** (2000) 69 [hep-ph/9904440].

[98] S.L. Adler, *Axial vector vertex in spinor electrodynamics*, *Phys. Rev.* **177** (1969) 2426.

[99] J.S. Bell and R. Jackiw, *A PCAC puzzle: $\pi^0 \to \gamma\gamma$ in the σ model*, *Nuovo Cim. A* **60** (1969) 47.

[100] W.H. Furry, *A Symmetry Theorem in the Positron Theory*, *Phys. Rev.* **51** (1937) 125.

[101] K. Nishijima, *Generalized Furry's Theorem for Closed Loops*, *Progress of Theoretical Physics* **6** (1951) 614
[https://academic.oup.com/ptp/article-pdf/6/4/614/5419315/6-4-614.pdf].

[102] C.Q. Geng and R.E. Marshak, *Uniqueness of Quark and Lepton Representations in the Standard Model From the Anomalies Viewpoint*, *Phys. Rev. D* **39** (1989) 693.

[103] S.L. Adler and W.A. Bardeen, *Absence of higher order corrections in the anomalous axial vector divergence equation*, *Phys. Rev.* **182** (1969) 1517.

[104] R.W. Assmann, *LEP operation and performance with electron positron collisions at 209-GeV*, *Conf. Proc. C* **0101153** (2001) 323.

[105] P. Bambade et al., *The International Linear Collider: A Global Project*, 1903.01629.

[106] Particle Data Group collaboration, *Review of Particle Physics*, *PTEP* **2020** (2020) 083C01.

[107] ATLAS collaboration, *Measurement of the $t\bar{t}$ production cross-section and lepton differential distributions in $e\mu$ dilepton events from pp collisions at $\sqrt{s} = 13$ TeV with the ATLAS detector*, *Eur. Phys. J. C* **80** (2020) 528 [1910.08819].

[108] A. Denner and S. Dittmaier, *Scalar one-loop 4-point integrals*, *Nucl. Phys.* **B844** (2011) 199 [1005.2076].

[109] A. Denner and S. Dittmaier, *Reduction of one-loop tensor 5-point integrals*, *Nucl. Phys.* **B658** (2003) 175 [hep-ph/0212259].

[110] A. Denner and S. Dittmaier, *Reduction schemes for one-loop tensor integrals*, *Nucl. Phys.* **B734** (2006) 62 [hep-ph/0509141].

[111] M. Luscher, *A Portable high quality random number generator for lattice field theory simulations*, *Comput. Phys. Commun.* **79** (1994) 100 [hep-lat/9309020].

[112] F. James, *RANLUX: A FORTRAN implementation of the high quality pseudorandom number generator of Luscher*, *Comput. Phys. Commun.* **79** (1994) 111.

[113] R. Kleiss and R. Pittau, *Weight optimization in multichannel Monte Carlo*, *Comput. Phys. Commun.* **83** (1994) 141 [hep-ph/9405257].

[114] Z. Nagy and Z. Trocsanyi, *Next-to-leading order calculation of four-jet observables in electron-positron annihilation*, *Phys. Rev.* **D59** (1999) 014020 [hep-ph/9806317].

[115] T. Motz, *Generic Monte Carlo event generator for NLO processes*, Ph.D. thesis, University of Zurich, Zürich, 2011.

[116] A. Denner, S. Dittmaier, M. Pellen and C. Schwan, *Low-virtuality photon transitions $\gamma^* \to f\bar{f}$ and the photon-to-jet conversion function*, *Phys. Lett. B* **798** (2019) 134951 [1907.02366].

[117] A. Keshavarzi, D. Nomura and T. Teubner, *Muon $g-2$ and $\alpha(M_Z^2)$: a new data-based analysis*, *Phys. Rev. D* **97** (2018) 114025 [1802.02995].

[118] A. Denner, L. Hofer, A. Scharf and S. Uccirati, *Electroweak corrections to lepton pair production in association with two hard jets at the LHC*, JHEP **01** (2015) 094 [`1411.0916`].

[119] E.W.N. Glover and A.G. Morgan, *Measuring the photon fragmentation function at LEP*, Z. Phys. C **62** (1994) 311.

[120] A. Denner, S. Dittmaier, T. Kasprzik and A. Muck, *Electroweak corrections to W + jet hadroproduction including leptonic W-boson decays*, JHEP **08** (2009) 075 [`0906.1656`].

[121] A. Denner, S. Dittmaier, T. Gehrmann and C. Kurz, *Electroweak corrections to hadronic event shapes and jet production in e+e- annihilation*, Nucl. Phys. B **836** (2010) 37 [`1003.0986`].

[122] A. Denner, S. Dittmaier, T. Kasprzik and A. Muck, *Electroweak corrections to dilepton + jet production at hadron colliders*, JHEP **06** (2011) 069 [`1103.0914`].

[123] ALEPH collaboration, *First measurement of the quark to photon fragmentation function*, Z. Phys. C **69** (1996) 365.

[124] NNPDF collaboration, *Parton distributions for the LHC Run II*, JHEP **04** (2015) 040 [`1410.8849`].

[125] NNPDF collaboration, *Illuminating the photon content of the proton within a global PDF analysis*, SciPost Phys. **5** (2018) 008 [`1712.07053`].

[126] A. Buckley, J. Ferrando, S. Lloyd, K. Nordström, B. Page, M. Rüfenacht et al., *LHAPDF6: parton density access in the LHC precision era*, Eur. Phys. J. **C75** (2015) 132 [`1412.7420`].

[127] A. Denner, S. Dittmaier, M. Roth and D. Wackeroth, *Electroweak radiative corrections to $e^+e^- \to WW \to 4$ fermions in double pole approximation: The RACOONWW approach*, Nucl. Phys. **B587** (2000) 67 [`hep-ph/0006307`].

[128] D.Y. Bardin, A. Leike, T. Riemann and M. Sachwitz, *Energy-dependent width effects in e^+e^--annihilation near the Z-boson pole*, Phys. Lett. **B206** (1988) 539.

[129] S. Heinemeyer, C. Mariotti, G. Passarino and R. Tanaka, eds., *Handbook of LHC Higgs Cross Sections: 3. Higgs Properties*, (Geneva), CERN, 2013. 10.5170/CERN-2013-004.

[130] A. Denner, S. Dittmaier, M. Roth and D. Wackeroth, *Predictions for all processes $e^+e^- \to 4$ fermions $+ \gamma$*, Nucl. Phys. **B560** (1999) 33 [`hep-ph/9904472`].

[131] A. Denner, S. Dittmaier, M. Roth and L.H. Wieders, *Electroweak corrections to charged-current $e^+e^- \to 4$ fermion processes: Technical details and further results*, Nucl. Phys. **B724** (2005) 247 [`hep-ph/0505042`].

[132] A. Denner and S. Dittmaier, *The complex-mass scheme for perturbative calculations with unstable particles*, Nucl. Phys. Proc. Suppl. **160** (2006) 22 [`hep-ph/0605312`].

[133] A. Denner and S. Dittmaier, *Electroweak Radiative Corrections for Collider Physics*, Phys. Rept. **864** (2020) 1 [`1912.06823`].

[134] M. Cacciari, G.P. Salam and G. Soyez, *The anti-k_t jet clustering algorithm*, JHEP **04** (2008) 063 [`0802.1189`].

[135] CMS collaboration, *W^+W^- boson pair production in proton-proton collisions at $\sqrt{s} = 13$ TeV*, Phys. Rev. D **102** (2020) 092001 [`2009.00119`].

[136] ATLAS collaboration, *Measurement of fiducial and differential W^+W^- production cross-sections at $\sqrt{s} = 13$ TeV with the ATLAS detector*, Eur. Phys. J. C **79** (2019) 884 [`1905.04242`].

[137] CMS collaboration, *Measurements of properties of the Higgs boson decaying to a W boson pair in pp collisions at $\sqrt{s} = 13$ TeV, Phys. Lett. B* **791** (2019) 96 [`1806.05246`].

[138] A. Denner and S. Pozzorini, *One loop leading logarithms in electroweak radiative corrections. 1. Results, Eur. Phys. J.* **C18** (2001) 461 [`hep-ph/0010201`].

[139] ATLAS collaboration, *Evidence for the production of three massive vector bosons with the ATLAS detector, Phys. Lett. B* **798** (2019) 134913 [`1903.10415`].

[140] T. Becher, R. Frederix, M. Neubert and L. Rothen, *Automated NNLL + NLO resummation for jet-veto cross sections, Eur. Phys. J. C* **75** (2015) 154 [`1412.8408`].

[141] J.M. Campbell, R.K. Ellis, T. Neumann and S. Seth, *Jet-veto resummation at N^3LL_p + NNLO in boson production processes, JHEP* **04** (2023) 106 [`2301.11768`].

[142] S. Frixione, E. Laenen, P. Motylinski, B.R. Webber and C.D. White, *Single-top hadroproduction in association with a W boson, JHEP* **07** (2008) 029 [`0805.3067`].

[143] W. Hollik, J.M. Lindert and D. Pagani, *NLO corrections to squark-squark production and decay at the LHC, JHEP* **03** (2013) 139 [`1207.1071`].

[144] M. Ciccolini, A. Denner and S. Dittmaier, *Electroweak and QCD corrections to Higgs production via vector-boson fusion at the LHC, Phys. Rev. D* **77** (2008) 013002 [`0710.4749`].

[145] B. Jäger and J. Scheller, *Electroweak corrections and shower effects to Higgs production in association with two jets at the LHC, JHEP* **09** (2022) 191 [`2208.00013`].

[146] F. Campanario, M. Kerner, L.D. Ninh and D. Zeppenfeld, *QCD Induced Di-boson Production in Association with Two Jets at NLO QCD, Nucl. Part. Phys. Proc.* **273-275** (2016) 2212 [`1410.3498`].

Versicherung an Eides statt
gem. der Promotionsordnung vom 04.10.2011

Ich, Robert Franken, Kettengasse 16, 97070 Würzburg, versichere an Eides statt durch meine Unterschrift, dass ich

- die vorliegende Dissertation eigenständig, d. h. insbesondere selbstständig und ohne Hilfe einer kommerziellen Promotionsberatung, angefertigt habe,

- keine anderen als die von mir angegebenen Quellen und Hilfsmittel benutzt habe,

- dass ich die Gelegenheit zum Promotionsvorhaben nicht kommerziell vermittelt bekommen habe

- und insbesondere nicht eine Person oder Organisation eingeschaltet habe, die gegen Entgelt Betreuer bzw. Betreuerinnen für die Anfertigungen von Dissertationen sucht.

- Ich erkläre zudem, dass ich die Regeln der Universität Würzburg über gute wissenschaftliche Praxis eingehalten habe.

- Die Dissertation habe ich weder in gleicher oder anderer Form zur Erlangung eines akademischen Grades in einem anderen Prüfungsfach vorgelegt.

- Ich versichere an Eides statt, dass ich die vorgenannten Angaben nach bestem Wissen und Gewissen gemacht habe und dass die Angaben der Wahrheit entsprechen und ich nichts verschwiegen habe.

- Ich bin mir bewusst, dass falsche oder unwahre Angaben bei der Meldung zu dieser Prüfung den sofortigen Ausschluss von der Prüfung zur Folge haben.

_____   _____

Ort, Datum   Unterschrift

Danksagung

Vollendet ist das große Werk, der Schöpfer sieht's und freuet sich. Um nicht auf den letzten Metern eines Plagiats überführt zu werden: Joseph Haydn, die Schöpfung, Hob. XXI:2. Mit diesem kleinen Ausflug in die klassische Musik soll es genug sein, denn im Gegensatz zu den Taten von Haydns Schöpfer wurden hier deutlich kleinere Werke vollbracht und statt sechs Tagen hat diese Arbeit auch sechs Jahre in Anspruch genommen. Diese sechs Jahre waren eine Zeit voll Höhen und Tiefen, im privaten wie auch im gesellschaftlichen Bereich. Es hätte wohl niemand im Jahr 2018, als diese Arbeit aufgenommen wurde, erahnen können, welche Ereignisse sich Ende 2019 in einem fernen Winkel der Welt anbahnten und bald darauf Einfluss auf unser aller Leben nahmen. Nun ist ein Lebensabschnitt zu Ende und ich möchte diversen Personen danken, die mein Leben in den letzten sechs Jahren begleitet haben. Dabei sind in Richtung des Arbeitsumfelds explizit zu nennen:

- Prof. Dr. Ansgar Denner mit seiner unendlichen Geduld meiner Promotion gegenüber, seiner fachlichen Expertise, die er mit mir geteilt hat, und vielen anregenden Diskussionen über die Dissertation;

- Brigitte Wehner und Karina Zink mit ebenso viel Geduld und vielfach gespendeter Motivation;

- Dr. Timo Schmidt und Dr. Christopher Schwan für inhaltliche Diskussionen über alle Arten von Vektorbosonstreuung;

- die Vorgenannten, sowie darüber hinaus Dr. Benedikt Biedermann, Dr. Mauro Chiesa, Christoph Haitz, Dr. Mathieu Pellen und Dr. Giovanni Pelliccioli für eine gute Atmosphäre in der Arbeitsgruppe; und

- zuletzt Dr. Christian Schwinn für meine Empfehlung nach Würzburg.

Weiterer Dank im Kontext der Physik geht an

- Dr. Sven Feuerbacher und Prof. Dr. Michael Krämer für das Wecken und Aufrechterhalten meines Interesses an physikalischen Fragestellungen.

Darüber hinaus danke ich in meinem privaten Umfeld

- Levi Ostler dafür, dass er mich jeden Tag aufs Neue aushält;

- Julian Meusel, der von meinem Büronachbarn zu meinem Nachbarn wurde;

- Leonie Lindner, Evelyn Scheu und Paulina Vogel, weil es immer vorteilhaft ist, stets mindestens eine Juristin in der WG zu haben; und

- Felix Dietz, Andreas Gößmann-Schmidt, Viktoria Hernandez, Raphael Laufkötter, Marcus Orlandi, Clara Seck und Jan Willmann, weil es noch vorteilhafter ist, nicht nur mit Juristinnen zusammen gewohnt zu haben.

Zuletzt finden nicht namentliche lobende Erwähnung für meine Begleitung in den letzten sechs Jahren generisch: die Hippies, die Pfadfinder und die Zecken. Betreffende Personen wissen, dass sie angesprochen sind, und wie sie sich in eine oder mehrere Kategorien davon einteilen lassen können – oder zumindest, wie ich sie darin einteilen würde.